Doctoral Dissertation

Doctoral Program in Materials Science and Technologies (35th Cycle)

Development of the additively manufactured stainless steel 316L and AlSi10Mg alloys by in situ alloying and post-process treatment

By

Mohammadreza Jandaghi

******

Supervisor:

Prof. Matteo Pavese

Doctoral Examination Committee:

Prof. Sergio Lorenzi, Referee, Università degli Studi di Bergamo
Prof. Zbigniew Karol Brytan, Referee, Silasian University of Technology

Politecnico di Torino
2022

Declaration

I hereby declare that the contents and organization of this dissertation constitute my own original work and does not compromise in any way the rights of third parties, including those relating to the security of personal data.

Mohammadreza Jandaghi

2022

* This dissertation is presented in partial fulfillment of the requirements for **Ph.D. degree** in the Graduate School of Politecnico di Torino (ScuDo).

I would like to dedicate this thesis to my loving wife who supported me in all the hard situations.

Acknowledgment

I want to thank my supervisor Prof. Matteo Pavese for his kindly helps and the open title he defined for my thesis which eventually helped me to evaluate a wide range of materials in additive manufacturing.

I prefer to acknowledge the department of Applied Science and Technology of Politecnico di Torino for provision of the facilities used in this research.

I would like to appreciate my friends Dr. Hesam Pouraliakbar and Prof. Vahid Fallah from Queens university of Canada for the scientific discussions for analyzing the results of different projects of this thesis.

And I would like to acknowledge Prof. Sun Ig Hong and Dr. Sang Hun Shim from the Chungnam National University of South Korea for doing the TEM characterizations and scientific discussion in analyzing the TEM results.

I deeply acknowledge Dr. Leonardo Iannucci and Prof. Sabrina Grassini for their kindly helps in performing the corrosion tests and related analysis.

The helps of Prof. Johan Moverare from Linköping University in Sweden for the provision of the facilities for EBSD and SEM images and scientific discussions is worthy of deepest acknowledgment.

I kindly appreciate the helps of Prof. Ehsan Ghassemali for provision of my access to the electron microscopy center of Jönköping University in Sweden.

Finally, I prefer to acknowledge my wife, my family and all my friends who supported me to keep on my scientific path until reaching the best results.

Abstract

Thanks to their admirable printability, AlSi10Mg and stainless steel 316L are among the alloys that have been repeatedly fabricated by different 3D printing technologies. In this research, some solutions for the development of these alloys through laser powder bed fusion (LPBF) have been examined. To compositional modification of these alloys, a wide range of alloying elements and non-metallic particles have been inoculated into the matrix through in-situ alloying and the effects of the added elements on the modification of the microstructure, on the mechanical properties and on the corrosion behavior of the studied alloys were investigated. To reduce the production cost of the additively manufactured steel, also the feasibility of replacing the gas atomized (GA) powders with water atomized (WA) powders was investigated. Furthermore, the impact of high-temperature rapid annealing of the LPBF fabricated SS316L for rapid stress-relieving the AM samples has been surveyed as a part of this research. According to the obtained results, the typical cellular structure of the additively manufactured alloys has an undeniable role in higher mechanical properties of the AMed parts compared to conventionally fabricated parts. During annealing, this cellular structure disappears before any grain evolution and results in a tangible drop in mechanical properties. Comparison of the fabricated components with GA and WA powders of SS316L revealed that by choosing the right process parameters and particle size distribution, WA samples would show higher mechanical properties, corrosion resistance and better surface roughness. Co-addition of the Ti and Mn to SS316L and Ni to AlSi10Mg by in-situ alloying revealed that activation of the slip systems in brittle phases and formation of the GNDs at matrix would preserve the interface of the particle/matrix from crack formation. Also, addition of the nanoparticles to AlSi10Mg revealed that stacking the nanoparticles on irregular shape particles would create some defects in AMed parts and degrade the mechanical properties.

Table of Content

List of Tables

List of Figures

Chapter 1

Introduction

1.1. Additive Manufacturing

Additive manufacturing methods are established based on the fabrication of objects with layer-by-layer addition of raw material according to the received inputs from a computer-aided design (CAD) model. Compared to the conventional production processes, AM technologies provide more advantages, such as freedom in design of complex shape structures without need of complementary tooling and machining. This technology has revolutionized every area it has reached by improving the design, properties, and production rate of the components. Likewise, reducing the production wastes besides the possibility of the recycling and reuse of the raw materials has made it a desirable choice for environmental sustainability. A growing number of papers have been published on AM of structural materials in recent years (Fig. 1).

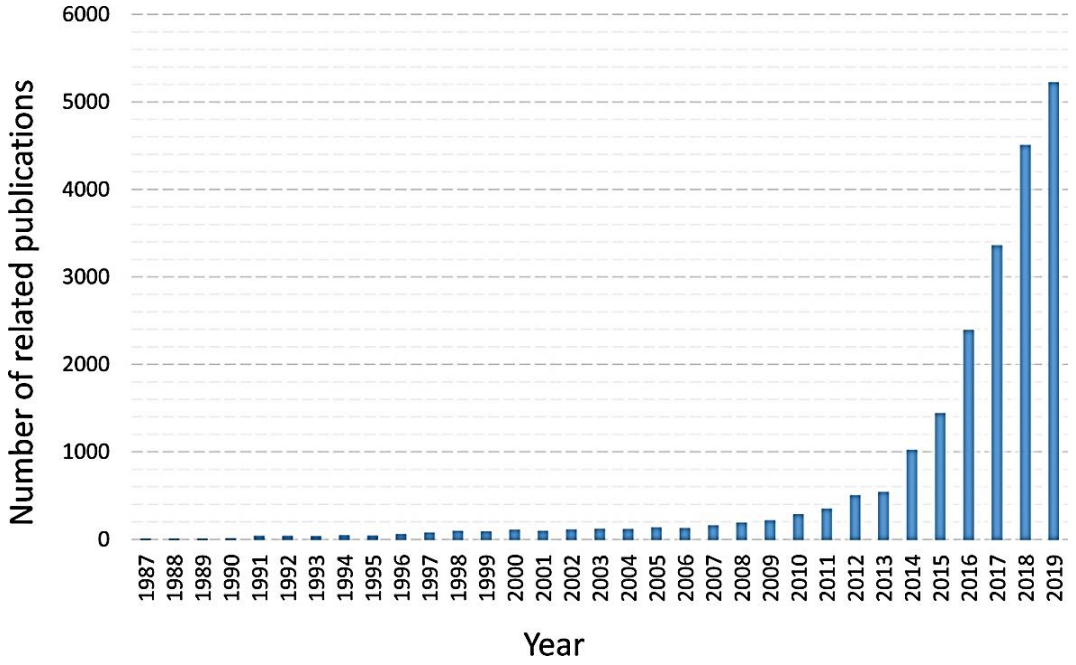

Fig. 1. Statistical data of articles on the topic of "additive manufacturing" published from 1987 to 2019 [1].

Owing to advantages such as the higher mechanical properties of the additively manufactured metallic part, this technology has been frequently employed for the production

and development of metals and alloys, and replaced the conventional manufacturing processes. Fig. 2 shows the investment of different industries in additive manufacturing technologies.

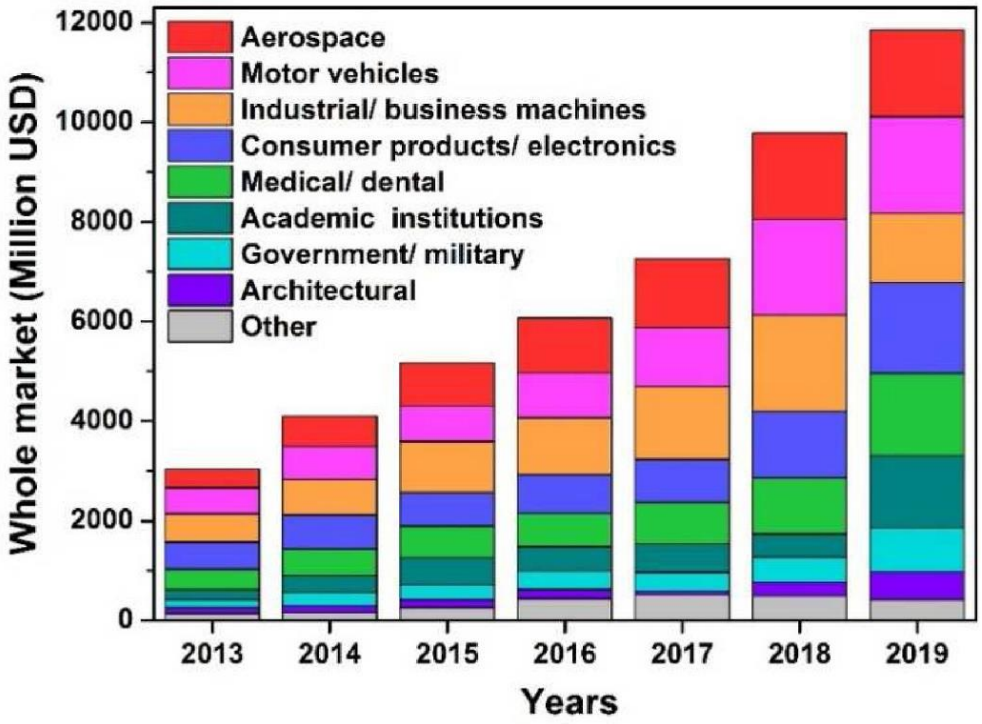

Fig. 2. Additive manufacturing market size by industry sectors between the years 2013–2019 [2]

1.2. Laser powder bed fusion

For 3D printing of the metallic materials, laser and electron beam are usually employed as a high-intensity heat source to melt the particles. Hence, this kind of additive manufacturing methods are called *powder bed fusion*. Making a homogenous solution and an adhesive bonding between subsequent layers is of great importance in powder bed fusion methods. During the powder bed fusion, the temperature locally increases above 2000 °C while the temperature gradient and cooling rate is about 10^7 K/s [3]. In between, vaporization of low melting point or small particles would result in gas entrapment as well as incomplete melting and insufficient interlayer bonding would result in lack of fusion defect. As a result, the processing window for fabrication of intact bulk metallic parts by additive manufacturing is exceptionally narrow. Considering the complications to print a defect-free specimen, achieving desirable properties and homogenous microstructure is very challenging, and having a comprehensive understanding about the microstructural evolution is critical. The schematic illustration of the LPBF method is presented in Fig. 3.

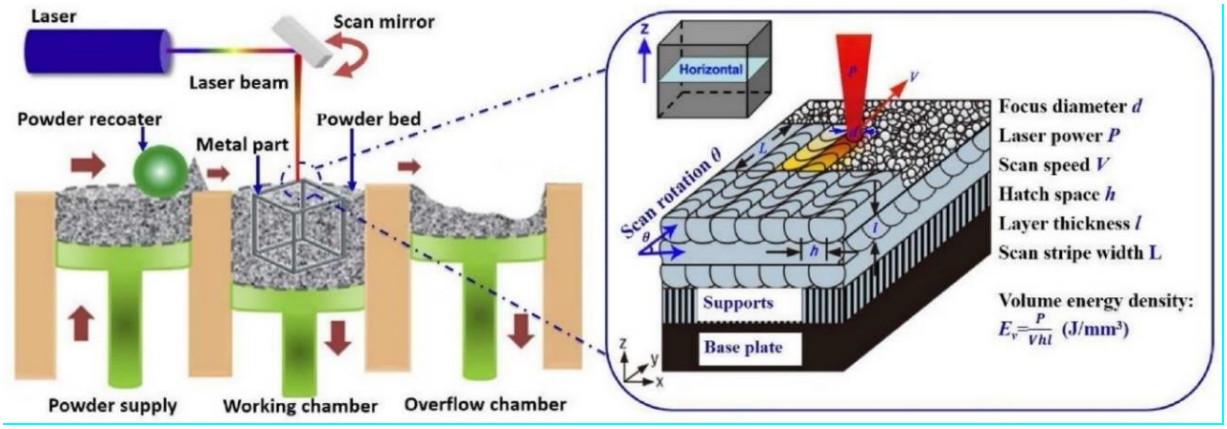

Fig. 3. Illustrations of the laser powder bed fusion technology [2]

The microstructures of LPBF manufactured metallic parts are affected by a wide range of parameters [4]. The laser power, beam radius, scanning speed, hatching distance, and layer thickness are the parameters that could be controlled by the printer machine. Also, the temperature of the building plate, the atmosphere of the printing chamber and the size and morphology of the powders are other parameters that could directly affect the microstructure of the specimens. Since formation of imperfections would significantly degrade the mechanical properties of the metallic components, achieving the highest relative density is the first goal of the additive manufacturing researchers [5]. Most of the previous studies considered the volumetric energy density (VED) as a criterion for the imposed energy per unit volume of powders in powder bed printing methods [6]. The energy density has been introduced as VED = $P / v{\cdot}h{\cdot}t$, where P, v, h, and t are the laser power, scan speed, hatching distance, and layer thickness, respectively. In general, optimum process parameters imply on the best VED which results in minimum porosities in the printed parts. Applying low VED would result in incomplete melting of the particles and residual unmelted chunks and lack of fusion around the melt pool borders [7]. On the other side, applying a significantly high VED, increases the temperature of the melt pool over the boiling point of the metal and results in material evaporation and subsequent trapping the spherical pores in the printed parts [8]. Hence, choosing an optimum VED which could make a sufficiently large and stable melt pool is critical. However, even if VED has been properly adopted, it still has some limitations particularly for in-situ alloying [9]. Some parameters like laser beam focal diameter and printing strategy that directly affect the thermal history are ignored in the VED equation. Consequently, the optimized process parameter might be unique for each printer and cannot exactly give similar results by another machine. Likewise, by changing the printing strategy and rotation angle again another set of the process parameters and VED will give the highest relative density. However, for printing single-phase materials this would not make a major

difference, but due to the different transferred effective energy and heating cycles, the amount of the residual strain and homogeneity of the microstructure for in-situ alloyed materials would be different.

1.3. Powder processing for AM

In the powder-bed systems, a re-coater must carry the powder from a feedstock chamber and spread it on the building plate [10]. The individuation of an ideal metallic powder for AM requires the documentation of its features, namely average particle size, particle size distribution, surface area, flowability, apparent density, tap density, moisture content, and trapped porosities in the powder [11]. Since the spreadability plays an important role in printing a faultless and dense part, often a powder with proper size distribution composed of particles with a spherical shape and smooth surface is known as the ideal feedstock for AM [12]. Moreover, a small friction coefficient between the spherical powders facilitates their spreading [13]. The prevalent processes for fabrication of proper powders for AM are ‘‘plasma atomization”, ‘‘gas atomization” (GA), and ‘‘water atomization” (WA) [14]. Among them, plasma atomization provides the most spherical shape powders. Compared to plasma atomization, gas atomization can produce spherical powders with a lower price and appropriate morphology [15]. Nonetheless, the simplest and cheapest atomization method is water atomization [16]. Due to the high cooling rate in water atomization, the particles adopt an irregular shape [17], while the inert atmosphere of the chamber in gas atomization reduces the solidification rate of the particles and creates a more regular morphology in the final powder [18]. Moreover, the oxygen content of the WA particles is higher than in gas and plasma atomized particles. Oxygen uptake and chemical oxidation during AM directly arise from high oxygen content in the feedstock powder, which not only affects the powder flow but also degrades the mechanical properties of the printed parts [19]. Hitherto, WA powder of different alloys such as Al [20], Zn [21], Ti [22], IN625 [23, 24], IN738 [25], NiTi [18] and high entropy alloys (HEAs) [26] were evaluated for AM applications. It has been expressed that due to the problem of oxygen pickup, water atomization is not an appropriate production route for Al, Ti and the alloys containing such reactive elements, and the most eligible material for water atomizing is steel [27]. According to the cost estimations, using WA powder instead of GA can reduce the production cost from 10 to 80% [28]. To overcome the drawbacks of WA powders, some solutions have been proposed. Schade et. al [11] designed a multi-step process to eliminate the more irregular particles of WA iron powder. Despite increasing the apparent

density and flowability of the powders, wasting about 50% of the initial powder in the separation line reduced the cost-efficiency of this process. Boisvert et. al inoculated magnesium into the melt of SS304 before the atomization to favor the direct formation of more spherical powders with fewer internal pores [12]. Chikosha et al. [29] and Park et al. [30] employed an inductively coupled thermal plasma system for spheroidizing the irregular powders. Consequently, the fine particles were majorly removed and the flowability of the powder significantly improved. Mirzababaei et al. suggested adding a solid lubricant such as zinc stearate to the feedstock for reducing the interparticle friction and enhancing flowability [31]. Calculating the Hausner ratio (tap density/apparent density) is the simplest way to predict the flowability of the powders. Generally, the Hausner ratio and avalanche angle of WA powders is lower than GA ones [32]. Howbeit beyond a threshold, amelioration of the Hausner ratio and sphericity cannot majorly affect the final part density [33]. Nonetheless, some authors declared that the bulk densification of the printed parts with WA powder was close to those built by GA counterpart even by using the same process parameters [34, 35]. Compared to GA powders, irregular WA particles have a rougher surface with a higher surface area to volume ratio and benefit from higher laser absorption and lower reflectivity [3, 36]. So applying similar energy densities would provide higher heat input for melting the WA powder [37]. Fig. 4 properly shows the difference between the laser absorption of the WA and GA powders of stainless steel 316L.

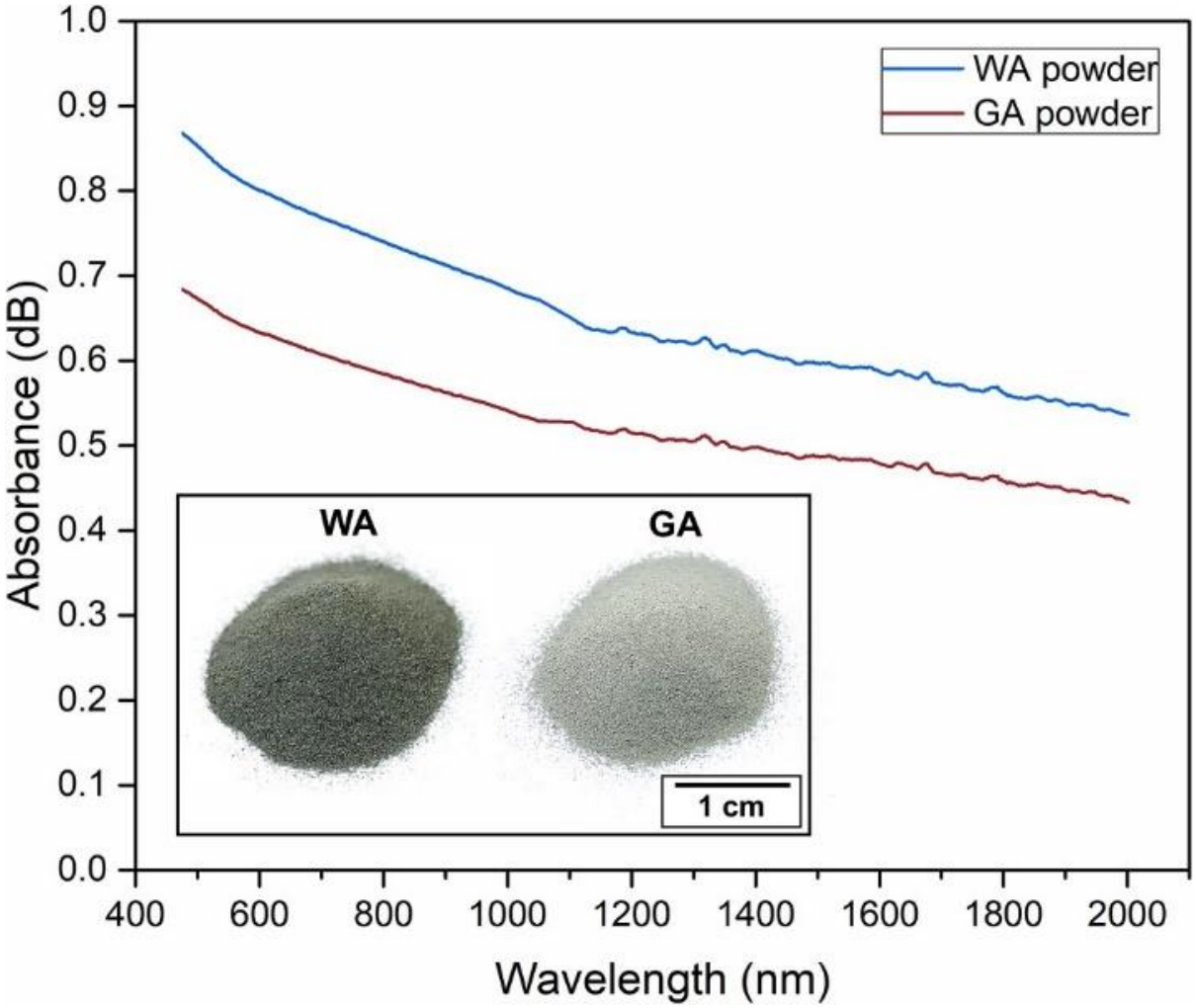

Fig. 4. Laser absorbance of the WA and GA powders acquired from diffuse reflectance measurements in the visible spectrum (wavelength: 400–1050 nm) and near infrared (1100–2000 nm), and an inset photograph of the powders [38].

According to the literature, at low energy densities and similar particle size, the parts produced by GA powder show higher densification and mechanical strength. But, applying higher energy densities result in similar packing density and mechanical properties of WA and GA components [39]. Stainless steel 316L is a favorable alloys for a wide spectrum of applications due to notable corrosion resistance and admirable mechanical properties [40]. It has been revealed that by optimizing the process parameters of the LPBF method, significant similarities can be achieved for the parts produced by WA and GA stainless steel 316L [41]. In the current work, the authors demonstrated that higher laser absorption of WA powder besides pinning effect of fine inclusions result in stronger texture and higher mechanical properties compared to GA samples. In this regard, the morphology, chemical composition, and structure of WA and GA feedstock powders and printed samples were precisely analyzed and compared with the mechanical behavior of the final products.

1.4. Pre-alloying and In-situ alloying

Usually, the elemental proportion of the powders used for LPBF is regulated in a pre-alloying step. However, the substitution of the pre-alloying steps comprising casting and atomization by in-situ alloying would save time and cost, and increase the productivity of AM methods. Inhomogeneous dispersion, evaporation, and incomplete melting of the guest elements are the main challenges of in-situ alloying by AM [9]. Hence, incorporating the elements having close melting points would provide a more reliable feedstock. Many researchers exploited in-situ alloying as a low-cost strategy for structural modification, particularly grain refinement. Hitherto, a significant number of solute elements prone to promote the equiaxed growth of the grains in different alloying systems have been introduced [42]. The refinement mechanism of the inoculants can be assorted into two main categories. (1) affecting the growth restriction factor (Q) and changing the heat flow direction like Cu in Ti alloys [43], (2) making reaction with the matrix to form the phases that can pin the grain boundaries like Zr [44] and Sc [45] in Al alloys and Ni [46] and La [47] in Ti alloys.

1.5. Post-processing treatment

During L-PBF process, the extreme thermal gradients and high cooling rates can result in the generation of large residual stresses and consequently parts distortion [48]. According to the literature, in the rapidly solidified processes such as welding the level of residual stress is proportional to the thermal gradient and cooling rate. This problem becomes more serious in the L-PBF process, mainly owing to its nature as a rapid solidification process. Therefore, so far, several studies have been carried out to control residual stresses and minimize their value in L-PBF fabricated samples [49]. Nonetheless, often it is not possible to significantly reduce the level of residual stress through modification of the process parameters, particularly for laser printed SS316L samples [50, 51]. Hence, the post thermal treatment has been proposed as a low cost and reasonable supplementary process to relieve the residual stresses and improve the performance of the L-PBF SS316L samples.

Predominantly, post-printing annealing of SS316L specimens is performed in a temperature range of 300-1200 °C for 30 minutes to 6 hours [52, 53]. Reijonen et al [54] investigated the effect of applying different stress-relieving procedures and introduced the hot isostatic pressing as the most effective standardized heat-treatment for the 316L built components. Chao et al. [55] examined the annealing temperature of 400 °C and 650 °C for 2

hours and solution annealing at 1100 °C for 5 min. According to their report, applying such an annealing resulted in 24%, 65% and 90% stress relieving, respectively. Riabov et al. [56] declared that during annealing of the SS316L samples at 400, 800 and 1200 °C, oxygen and nitrogen content gradually increases. In addition, by annealing the sample over 400 °C, cellular structure was removed and elemental segregation at the cell walls was no longer detectable. It has also proven that, annealing up to 600 °C has not any major impact on the microstructure [57]. However, annealing between 600-1000 °C activates elemental diffusion and gradually eliminates the cell walls, leading to a sharp decline of mechanical strength. Keeping on annealing above 1100 °C removes all L-PBF microstructure footprints and renders a conventional-like microstructure [58].

However, it is reported that long-term annealing is faced with two major challenges, such as grain growth and significant microstructural changes [59]. In fact, the high cooling rate during the L-PBF process results in a rapid solidification after the laser/material interaction and in the formation of an ultrafine sub-grain structure [60]. It should be highlighted that the presence of this ultrafine structure in the SS316L samples results in its superior properties. However, the long term annealing thoroughly removes such a desirable structure and thwarts the L-PBF supremacy [52]. Furthermore, AM techniques typically benefit from the exclusion of multiple time-consuming steps in the production cycle and combination with a long-term complementary procedure will reduce their productivity. Thus, in this study, the authors applied a rapid annealing heat treatment at elevated temperatures on L-PBF SS316L samples.

1.6. Stainless steel 316L in additive manufacturing

Austenitic stainless steel 316L (SS316L) broad range of biomedical and industrial applications lie on its outstanding resistance against corrosion, oxidation, creep, and fatigue along with proper weldability, formability, and mechanical strength [61]. Nonetheless, the low yield strength (YS) is usually the principal drawback of the SS316L components fabricated by conventional processes. Hitherto, different supplementary processes have been proposed to resolve this longstanding challenge [62]. Till now, numerous efforts were carried out following the purpose of improvement of mechanical strength and extension of the application of stainless steels through thermomechanical processes. The employed strategies often led to sacrificing the ductility in strength-ductility trade-off [63]. Hence, it is believed that a modern production method with more advanced capabilities to extend the mechanical strength of low-carbon austenitic steels should be exploited. For this reason, advanced manufacturing technologies such as Additive Manufacturing (AM) technologies are considered as promising alternatives to conventional manufacturing processes. In fact, through these technologies, it would be possible to not only improve the mechanical performance of the SS316L component but also to produce SS316L components with a high level of complexity. The outstanding merit of AM methods is their capability for fabrication of complex-shape components without any need to final tooling and machining compared with conventional time-consumable procedures. The exclusion of some steps from the production line could make them also more cost-efficient and competitive with respect to other methods [64]. Hence, development of SS316L by the AM techniques has been progressively investigated. Thanks to the notable compactness, fine microstructure, high mechanical strength and proper elongation, Laser Powder Bed Fusion (L-PBF) found a prominent position between the AM methods, applied more often than other AM techniques in the production of SS316L.

1.7. In situ alloying of SS316L by Ti addition

According to the equilibrium phase diagram of Fe-Ti (Fig. 5), the addition of over 10 at.% Ti to iron-based materials would result in the formation of the Fe_2Ti intermetallic compound. Increasing this value to over 30 at.% would result in formation of FeTi beside Fe_2Ti while the addition of a quantity of Ti over 50 at.% would guarantee the formation of FeTi and β-titanium. There are also two eutectic points, at 17 at.% and 70 at.% Ti.

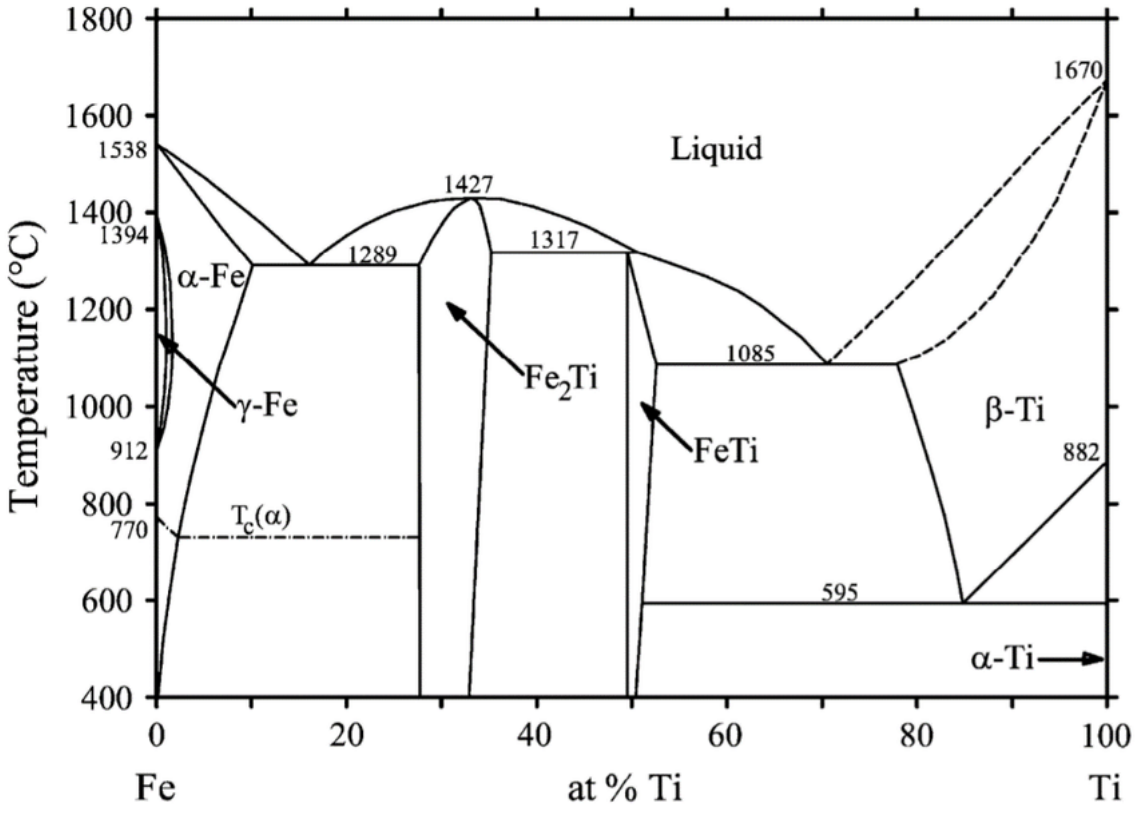

Fig. 5. Fe–Ti phase diagram [65].

In 2020, Requena et al. have investigated the printability of the Fe-Fe_2Ti eutectics through direct energy deposition (DED) method. Based on their observations, 3D printing of pre-alloyed powders with hypereutectic composition (Fe-17.6 at.% Ti) would result in the formation of an ultrafine grain structure without any cracking (Fig. 7). Based on another research performed by this group on Ti-32.5Fe eutectic composition, increasing the Ti value in pre-alloy powders results in formation of a hierarchical microstructure with micro-dendrites of η-$Ti_4Fe_2O_x$ embedded in an ultrafine eutectic β-Ti/TiFe matrix. But again, it did not have the consequence of the formation of brittle phases and cracking in the printed samples with pre-alloyed powder.

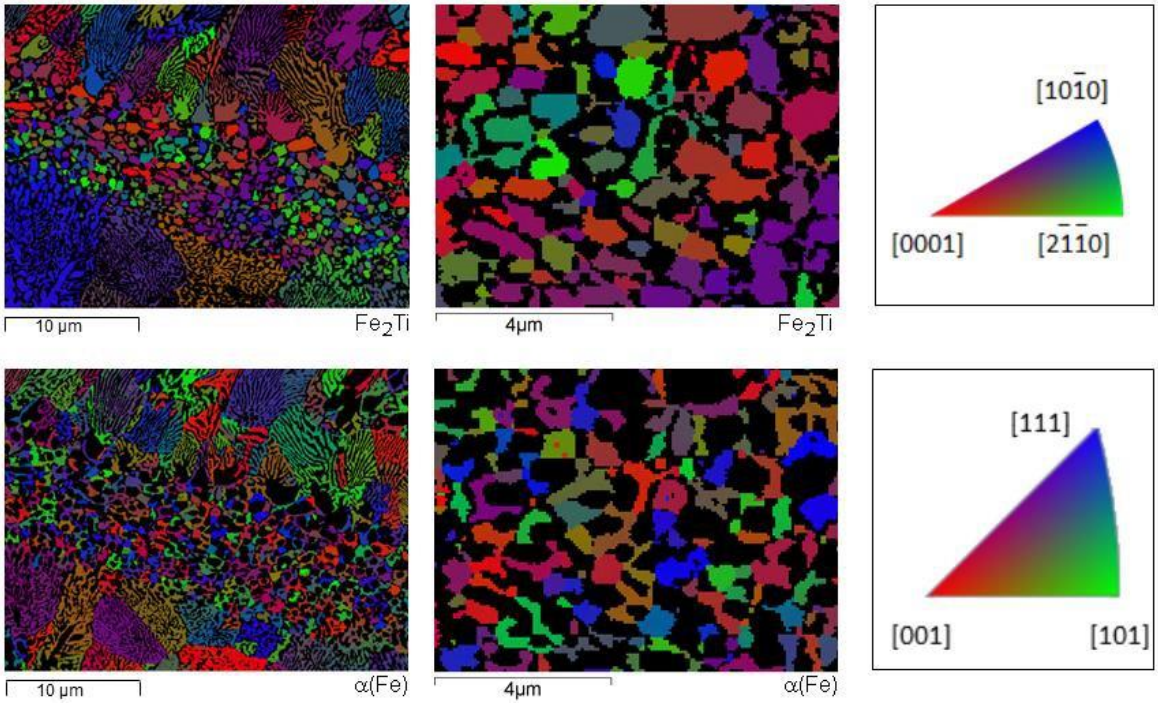

Fig. 6. EBSD color maps and related inverse pole figures of Fe_2Ti and α-Fe in the microstructure of the additively manufactured alloy with pre-alloyed powder [66].

Recently, Nyborg et. al have investigated the effect of inoculation of TiN [67] into steel, revealing that the formation of Ti oxides nanoparticles in the melt pool can hinder the epitaxial growth of grains and the typical severe texturing observed in AM. Similar results has been reported by Jagle et al. on inoculation of Ti into steel. Based on their observations, Ti can react with the pre-existing oxygen in the steel's raw powder and induces the formation of TiO and Ti_2O_3 particles. The important criteria, which is mentioned for the grain refinement impact of an element like Ti in steel matrix and TiC particles in Al matrix [68], is the lattice mismatch/misfit by the matrix. According to the observations on the grain refinement effect of Ti compounds in additively manufactured steel and aluminum alloys, the effective nucleant particles and the formed phases after their addition to a matrix have less than 10% interatomic mismatch with the matrix. The enhancement of interfacial atomic matching between the inoculated particles and host matrix results in lowering the atomic interfacial energy and in the decrement of the critical undercooling for activating heterogeneous nucleation during solidification.

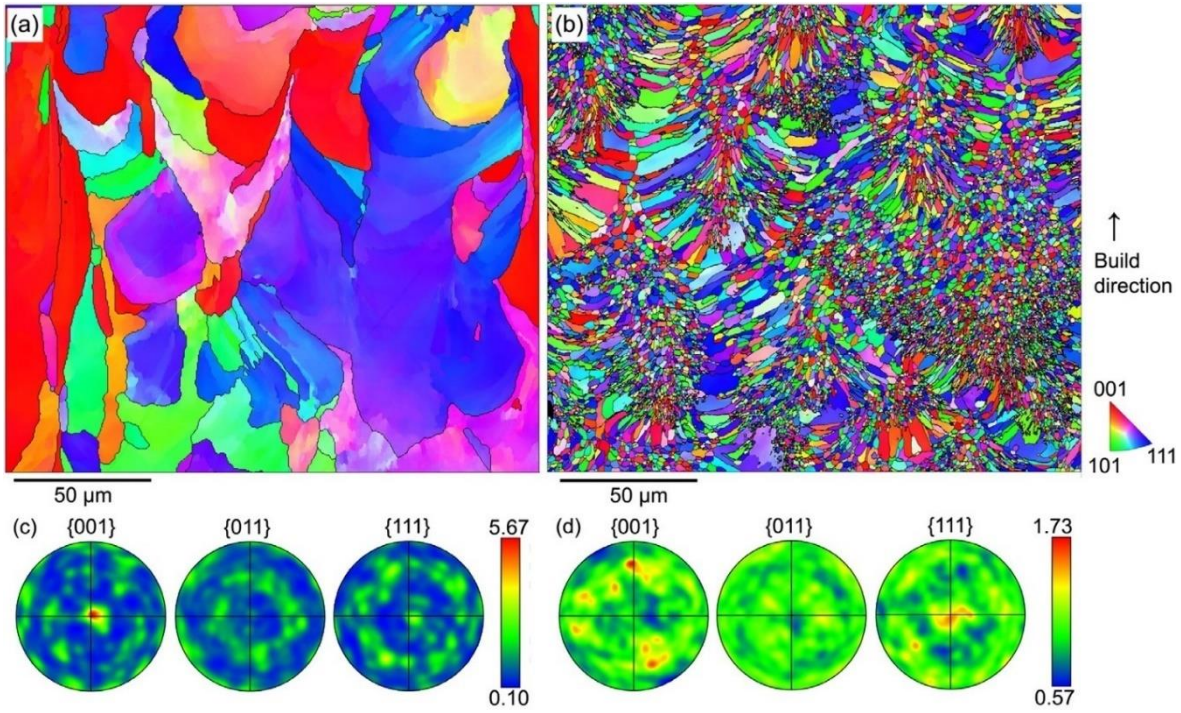

Fig. 7. EBSD IPF colored maps and showing the microstructure of the (a) SS316L and (b) TiN reinforced alloy and correlated pole figures (c, d), respectively [67].

1.8. In situ alloying of SS316L by Mn addition

High-manganese steels (HMnS) are known because of their extraordinary combination of mechanical properties and toughness. In these steels, high Mn value stabilises the austenitic phase and reduces the stacking-fault energy (SFE) to the range of 10 to 50 mJ/m^2. Hence under mechanical loading multiple deformation mechanisms can be activated within these alloys parallel to the dislocation glide. Often, in high manganese steels, activation of transformation-induced plasticity (TRIP) due to low SFE accompanies with activation of twinning-induced plasticity (TWIP). Activation of a variety of deformation mechanisms facilitates the dislocation motion, retards the dynamic recovery and improves the strain hardenability [69]. As a result, TWIP and TRIP steels demonstrate a high simultaneous synergy of tensile strength and elongation at failure (Fig. 8).

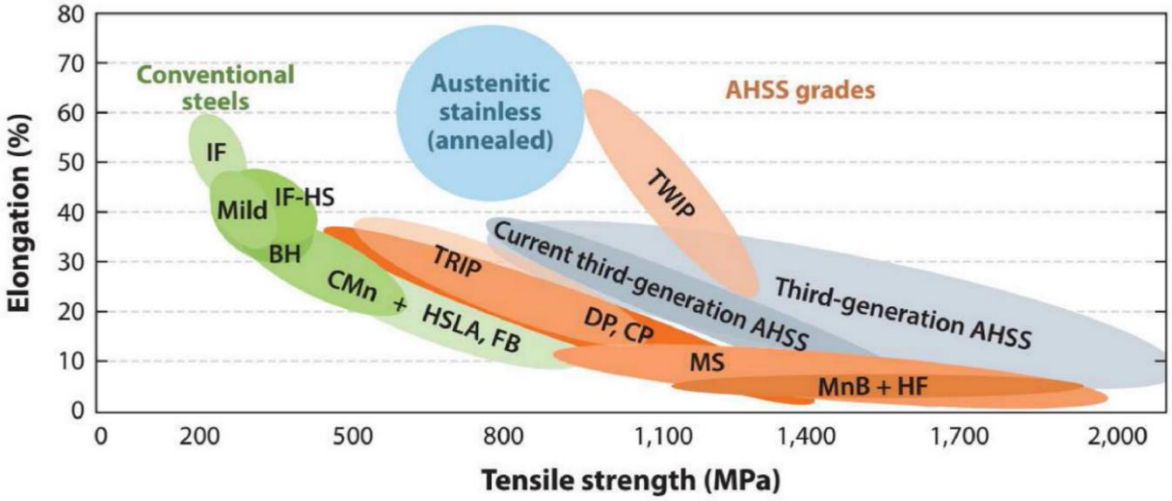

Fig. 8. A property map summarized tensile strength and elongation combinations for conventional steels and high-Mn steels. Abbreviations: interstitial free (IF), interstitial free-high strength (IF-HS), bake hardened (BH), high strength low alloy (HSLA), complex phase (CP), dual phase (DP), ferritic bainitic (FB), hot formed (HF) [2].

Since the mechanical properties of SS316L alloy can be tailored by adjusting the Mn value, authors believed that the synergistic exploiting of the Mn and Ti capabilities could promote the work hardening coefficient and toughness of the AMed stainless steels. Hence, part of this research is focused on exploring the impact of simultaneous inoculation of Mn and Ti in stainless steel 316L by LPBF technique and on the investigation of the microstructural evolution and correlated mechanical properties.

1.9. AlSi10Mg

The LPBF technique offers the possibility of further improvement of the strength-to-weight ratio of aluminum alloys [70]. AlSi10Mg alloy is one of the most investigated alloys processed via the LPBF method [71]. This high level of interest originated from its low melting point and thermal expansion, low susceptibility to solidification cracking as well as good weldability. In addition, the chemical composition of this alloy which is near the eutectic composition, makes it easily processable through laser-based technologies [72, 73]. Moreover, AlSi10Mg belong to the ageing/precipitate hardenable alloys that can reach higher strength when subjected to a specific supplementary heat treatment [74]. For instance, Maamoun et al. [75] and Aboulkhair et al. [76] surveyed the effect of annealing on the structure and mechanical properties of AlSi10Mg. Their outcomes indicated that despite short-term annealing (1-5 h), T6 heat treatment could significantly enhance the hardness of this alloy due to the formation of Mg_2Si and Al_5FeSi precipitates. Previous researchers [77] declared that annealing temperature plays an effective role in the size of the Si particles, and solution treatment below the standard T6

temperature (550 °C) eventuates in finer Si particles and guarantees higher mechanical strength. Kimura et al. [78] revealed that complete disassociation of Si dendritic structure occurs after a long-term solution treatment over 300 °C.

Furthermore, many efforts have been made to improve the mechanical properties of AlSi10Mg alloy through the addition of grain refiners like LaB_6 [79] and BN [80]. However, only some of them were slightly effective, while most of them could not remarkably improve the mechanical strength. Another approach that has been reported so far to improve the mechanical strength of AlSi10Mg alloy is the addition of reinforcing particles to produce AlSi10Mg based composites [81]. For instance, TiB_2 [82, 83], graphene [84], CNT [85], and TiC [86] were found to be promising reinforcements for AlSi10Mg alloy. However, it is well reported that in most of the cases, the interfacial bonding between the Al matrix and reinforcements is rather weak, and consequently, this weak point degrades the mechanical performance of the sample [87, 88]. Another approach that can be effective to improve the mechanical strength of the AlSi10Mg alloy is a slight modification of its chemical composition that can be implemented through the in-situ alloying process.

Nevertheless, based on the authors' knowledge, far too little attention has been paid to the development of new AlSi10Mg alloys through the in-situ alloying process. Hence, the aim of this work is at first to assess the feasibility of producing Ni-modified AlSi10Mg alloy through the LPBF method. The second target in this research is to evaluate the impact of thermal post-processing on the microstructure and mechanical properties of the newly developed alloy. In this regard, the microstructure and phase transformations linked to the addition of nickel were analyzed carefully and their correlation with tensile strength and fracture mechanism of the samples was elucidated.

1.10. Nano-oxide reinforcement

The unique properties of aluminum matrix composites (AMCs) such as outstanding specific strength and wear resistance, and low thermal expansion coefficient have created a collective demand for the development of this family of materials [89]. AMCs were formerly processed through conventional methods like powder metallurgy and casting. The mechanism of composite development by these techniques is leaning on two different approaches: (1) addition of fine ceramic particles to a molten matrix to restrict the grain growth and hinder the dislocation movement; (2) inoculating the potential alloying elements into the Al matrix to induce the formation of strengthening phases during the fabrication process or post thermal treatment [90].

Nevertheless, the slow solidification rate of the traditional processing techniques and confined wettability between the reinforcing phases and Al matrix oftentimes resulted in agglomeration of the reinforcement agents and weak interfacial bonding in the particulate/matrix. The above-mentioned drawbacks can considerably deteriorate the mechanical strength and limit the applications of AMCs [91]. Hence, it seems necessary to find an alternative method that narrows the particulate aggregation and promotes the uniform distribution of nanoparticles within the matrix [92].

Because of the ultrafast cooling rate (10^3-10^7 °C/s) and the turbulence of Marangoni flow which induces a capillary force in molten material, the LPBF process has a high potential for the fabrication of refined microstructures with uniform distribution of reinforcements [93]. The higher laser power usually improves the dispersion of nano-particulates in the Al matrix by enhancing wettability and reducing friction forces between liquid Al and nanoparticles and increasing the solidification rate [94]. Moreover, the addition of nanoscale ceramic particles modifies the laser absorptivity [95], and considering the high thermal diffusivity of aluminum, the parameters needed for the optimum density achievement must be carefully considered. Several researchers have reinforced the AlSi10Mg alloy by addition of different nano/microparticles and using the LPBF technology while it is proven that AlSi10Mg can be significantly strengthened by a wide range of nano/micro particulates and reach notable mechanical properties [96]. Jiang et al. [85] and Luo et al. [97]] evaluated the CNTs-AlSi10Mg composite fabricated by LPBF and argued that during printing, some CNTs reacted with Al and formed Al4C3. The synergistic function of CNT with Al_4C_3 created strong pinning that resulted in an improvement of the mechanical properties. Zhao et al [84] have reported a similar

behavior for graphene when developing an AlSi10Mg-based composite by LPBF. Xue et al. [98] observed that the addition of SiC particles to AlSi10Mg was accompanied by the formation of needle-shaped phases of Al_4SiC_4 and Si particles. Hence, despite the desired effect of the SiC reinforcement on the improvement of the hardness, owing to the weak adhesion between the particles and matrix, the brittleness of the material was increased, and the mechanical strength was degraded. However, Wang et al. revealed that despite the formation of the detrimental phase of Al_4C_3, the tendency of the SiC nanoparticles for distribution at the cell walls led to remarkable grain refinement in AlSi10Mg by spreading the heterogeneous nucleation sites and the Zener pinning effect [99]. He et al. introduced the TiCN as an efficient particulate that owing to its pinning effect on the grain boundaries in AMCs improves the mechanical performance of such additively manufactured components under high-temperature deformation [100].

In between, promising results have been reported about the impact of nano-oxide particles on the grain refinement of aluminum alloys [101]. Seleman et al. have used irregular nano-powder of Al_2O_3 to fabricate Al-based composite with Friction Stir Deposition (FSD) additive manufacturing method. They argued that the uniform distribution of Nano-powder promoted finer grains and improved the wear resistance, hardness, and compressive strength of the AA2011 alloy [102]. Chen et al. investigated the efficiency of Al_2O_3 for in-situ reinforcement of AlSi10Mg through LPBF and announced that Al_2O_3 particles could promote the fine cell-like microstructure, which enhances the hardness. However, choosing the wrong process parameter can make numerous gas pores and frustrate the hardening effect of the Al_2O_3 particles [81]. A Similar refinement effect has been observed for in-situ alloying of stainless steel 304L with yttrium oxide (Y_2O_3) nanoparticles [103], IN718 with $CoAl_2O_4$ nano-powder [104] and commercially pure titanium with La_2O_3 nanoparticles [105] through additive manufacturing. According to the existing literature, the reinforcement impact of the Er_2O_3 and Gd_2O_3 nanoparticles for in-situ alloying of AlSi10Mg alloy has not been studied yet. Initial assessments revealed that in the case of decomposition of Er_2O_3, Er would react with Al and Si and form Al_3Er and Er_5Si_3 compounds [106]. Also, disassociation of the Gd_2O_3 and reaction of Gd with AlSi10Mg would consequence in the formation of Al_2Gd, Al_3Gd, and the ternary compound of Al_4GdMg (τ) in the matrix [107].

To evaluate the effect of nano-oxide particles on structural modification of the AlSi10Mg, the effect of addition of Er_2O_3 and Gd_2O_3 nanoparticles on the microstructure and hardness of

additively manufactured AlSi10Mg alloy was also investigated. Additionally, the correlation between the nonuniform dispersion of nanoparticles and correlated defects was disclosed.

1.11. State of the Art

Thanks to the admirable printability of the austenitic stainless steel 316L (SS316L) and AlSi10Mg alloys, in the current research the authors focused on improvement of the processability, reducing the production cost and structural modification of additively manufactured SS316L and AlSi10Mg alloys. To satisfy this requirement, some potential elements/compounds were inoculated into the SS316L and AlSi10Mg alloys through LPBF in-situ alloying. Also, the feasibility of exploiting the irregular shape particles for 3D printing by LPBF method was investigated by comparison of the water- and gas-atomized powders. Meanwhile, the impact of the rapid annealing as a fast stress relieving step for AMed samples was surveyed. The correlation of the microstructural evolutions and mechanical properties and corrosion resistance of the LPBF fabricated samples has been studied.

Chapter 2

Experimental Method

The samples of this research were manufactured using three different 3D printer machines. A Sharebot METALONE laser printing machine, equipped with a fiber laser with a wavelength of 1080 nm, maximum laser power of 250 W, maximum scanning speed of 5 m/s and spot size of 40 μm. An EOS M270 system with maximum power of 200 W, laser beam diameter of 100 μm and laser wavelength of 1060-1100 nm. Also, a Concept Laser Mlab cusing R equipped with an ytterbium fiber laser source. The maximum power of the laser was 100 W while the wavelength and the spot size of the laser beam were 1070 nm and 70 μm, respectively. The building processes were executed under a flowing inert high purity Ar atmosphere, with the oxygen level below 0.1%. Samples were printed on an SS304L substrate with distinct geometries of (1) cubic samples with a dimension of 10×10×10 mm^3 for microstructural investigations and (2) tensile bars with a gauge dimension of 32×6×4 mm^3 according to the ASTM-E8 sub-size standard. The optical analysis of the microstructure was conducted by a Leica 5000 DMI optical microscope equipped with a polarizing lens and an Olympus DSX1000 digital microscope. Electron backscatter diffraction (EBSD) and scanning electron microscope (SEM) microanalysis was carried out via a JEOL (JSM7001F) and a Carl-Zeiss FE-SEM microscope working at 5-20 kV. The chemical composition of the crystalline phases in the as-printed alloy was investigated by an energy-dispersive x-ray (EDX) spectroscope. Phase identification was realized by an X-Pert Philips x-ray diffractometer (XRD) with $Cu_{K\alpha}$ radiation in a Bragg Brentano configuration in a 2θ range between 10 and 110 (operated at 40 kV, 40 mA, and step size of 0.013 for 25 s per step). Microhardness tests were conducted with five repetitions per sample using a Leica VMHT microhardness tester with an applied load of 100 g for 15 s. Room-temperature quasi-static tensile tests were conducted using a Zwick/Roell Z050 machine at starting strain rate of 2×10^{-3}/s. The acquired EBSD data were analyzed using EDAX OIM Analysis™ software. TEM analysis was carried out on FIB-cut thin foils using a dual-beam FEI Helios-NanoLab FIB and JEOL JEM-2100F TEM operated at 200 kV. The values of oxygen, nitrogen, and hydrogen in LPBF printed samples was measured using the LECO test.

Fig. 9. Different 3D printing systems used in this research

Chapter 3

Development of the SS316L through LPBF

3.1. Evaluation of the rapid annealing

Mohammad Reza Jandaghi*, Abdollah Saboori, Luca Iuliano, Matteo Pavese, "On the effect of rapid annealing on the microstructure and mechanical behavior of additively manufactured stainless steel by Laser Powder Bed Fusion" ***Materials Science and Engineering: A***, November 2021.

Abstract

This work presents an investigation on the effect of rapid annealing on the microstructure evolution and mechanical performance of stainless steel 316L (SS316L) fabricated by Laser Powder Bed Fusion. In this process, it is well documented that the intensive thermal gradient in the heat flux direction leaves remarkable residual stress and promotes strong texture along the building direction (BD). In the current research, to swiftly reduce residual stresses, a short-term heat treatment at 1300 °C for different holding times of 10 to 120 s was designed and studied. Microstructural observation through the optical microscopy and scanning electron microscopy, as well as the X-ray diffraction analysis, revealed that rapid annealing longer than 30 s resulted in the gradual annihilation of the cell walls which are indeed the sub-grain boundaries (SGBs). In addition, electron backscatter diffraction outputs demonstrated that rapid annealing significantly reduced the low angle grain boundaries and attenuated the texture developed along the BD. Moreover, the analysis of grains size and shape illustrated that annealing up to 30 s recovered the structure. In contrast, longer annealing resulted in increasing the aspect ratio of grains along the direction with maximum residual strain (i.e. BD) due to activation of the strain induced grain boundary migration (SIGBM) mechanism. After the rapid annealing, the mechanical performance of the samples also indicated that annealing up to 30 s would not reduce the compressive and tensile strength more than 6%. In comparison, longer annealing resulted in 24% reduction in mechanical properties along with coarsening of dimples in the fracture surface of the samples.

3.1.1. Experimental procedure

3.1.1.1. Samples preparation

In this work, a spherical, gas atomized SS316L powder was used as a feedstock material (Fig. 10**(a)**).

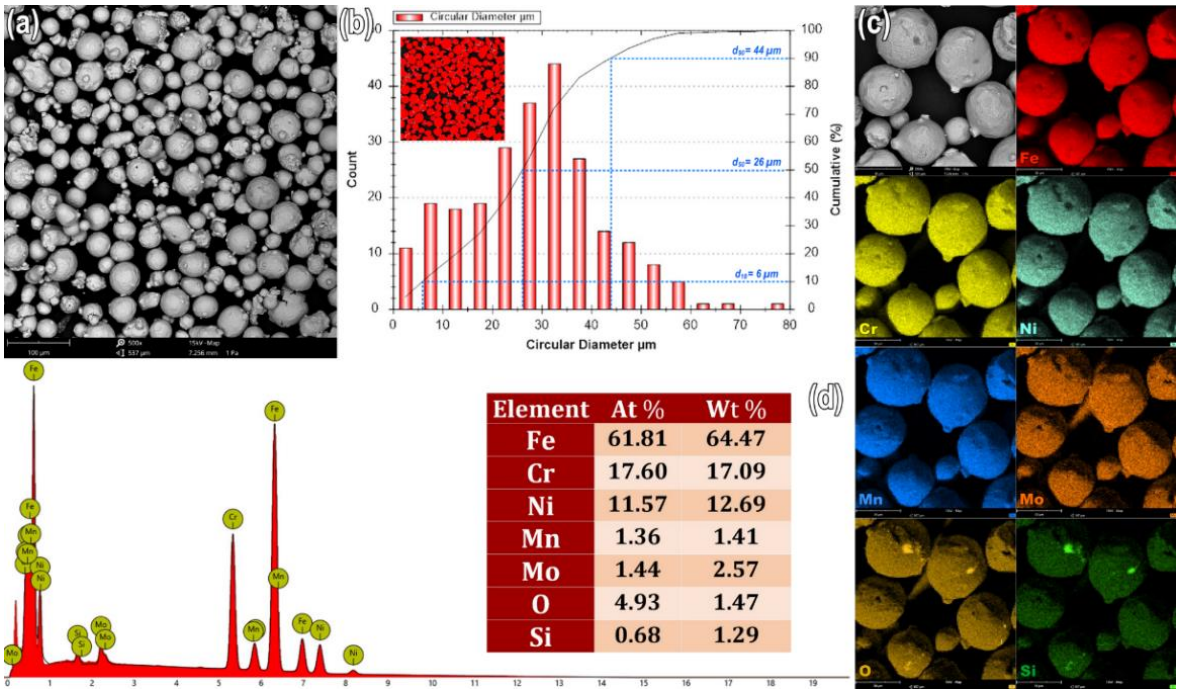

Fig. 10. SEM micrograph (a), size distribution diagram (b), element distribution map (c) and EDS elemental analysis (d) of the steel 316L powder used in L-PBF process.

The PSD of the starting powder was analyzed using PAX-it software, and the result is presented in Fig. 10(b). As can be seen, the particle size range of the starting powder lies in the range of 15-65 µm, which is a typical particle size range for L-PBF. The chemical composition of the atomized powder is presented in Fig. 10(c). The samples were manufactured using a Sharebot METALONE Laser printing machine. The cubic samples with a dimension of 10×10×10 mm was fabricated using stripe pattern and 90° rotation after printing each layer. Schematic illustration of the scanning strategy is shown in Fig. 11.

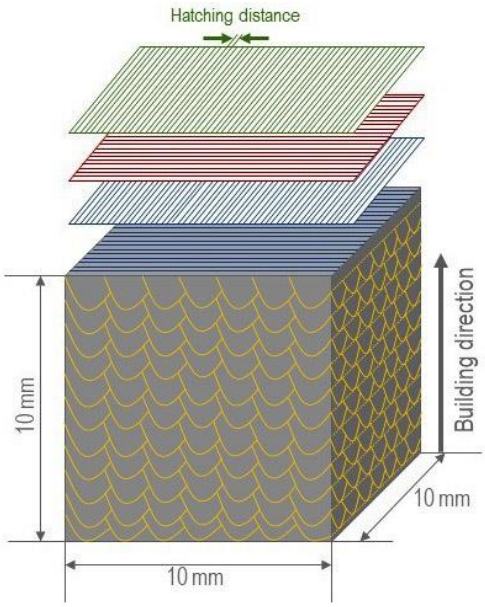

Fig. 11. Schematic representation of the samples fabricated with L-PBF method.

Before producing samples, a Design of Experiments (DoE) considering a different combination of process parameters was performed. As a result, the optimum process parameters to produce dense samples were achieved. In this DoE, several cubes were produced using a constant hatching distance of 100 µm, and a layer thickness equal to 30 µm. The laser power varied between 70 and 100 W, and the scan speed between 300 and 400 mm/s. To evaluate the effect of the combination of process parameters, the Volumetric Energy Density (VED) was considered and calculated using the following equation [108]:

$$E = \frac{P}{v \times d \times t} \qquad (1)$$

where P is the laser power (W); v the scanning speed (mm/s); d the hatching distance (mm) and t the layer thickness (mm). In this work, to facilitate the sample removal and guarantee the mechanical support and heat dissipation, the samples were produced on support structures. After the building, all the cubes were removed from the building platform using Wire Electrical Discharge Machining (EDM). Fig. 12(a-b) shows the images of the as-built cubes for the microstructural analysis and compression test, and flat tensile samples, respectively.

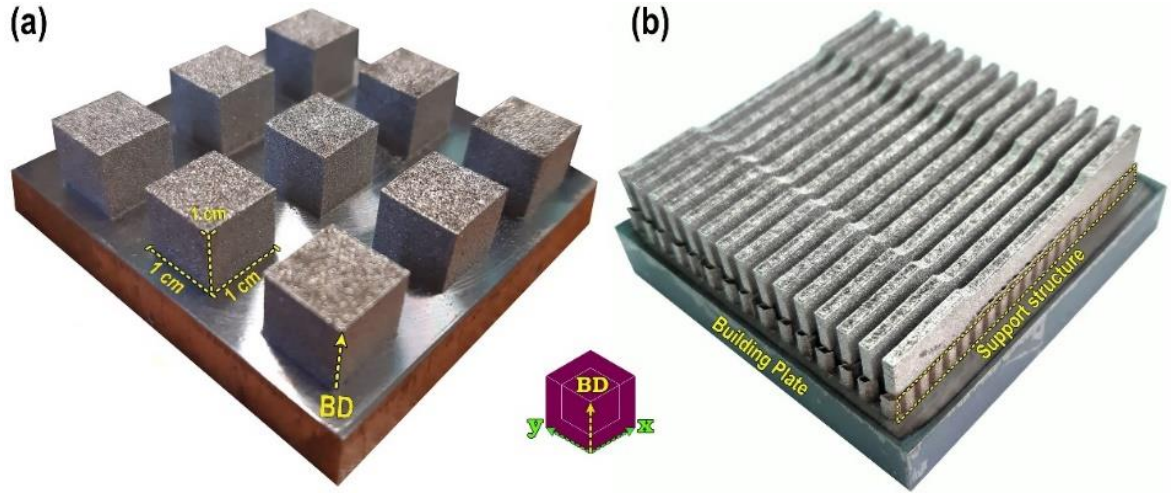

Fig. 12. Image of the 3D printed samples through L-PBF.

According to the literature, a temperature range of 800 to 1200 ºC and an annealing time of 30 to 120 min have been usually considered for the solution treatment of L-PBF stainless steel specimens [27]. Instead, in this work, due to the higher kinetics of restoration at elevated temperatures, the samples were annealed at 1300 ºC for 10 to 120 s followed by air cooling down to room temperature. In fact, the goal of this rapid heat treatment was to relieve the residual stress in a short time with a minimum change in the microstructure and mechanical properties of the as-built SS316L samples.

For the microstructural analysis, both XY and XZ cross-sections of the as-built cubes were cut, ground and polished according to the standard procedure for the metallography of 316L stainless steel [109]. Thereafter, the porosity content of the samples was evaluated on the as-polished samples using Image Analysis method. To reveal the microstructure, all the samples were chemically etched in a solution composed of 50 vol.% hydrochloric acid, 40 vol.% nitric acid and 10 vol.% acetic acid for 10 s. The EBSD measurements were performed at an acceleration voltage of 20 kV and a step size of 1 μm. The AZTEC data acquisition software (Oxford Instruments plc) was employed in this work. The outputs were analyzed by TSL Orientation Imaging Microscopy (OIM) Analysis 7 software from EDAX. EBSD mappings of the as-built and subsequently annealed samples were sectioned along the Building Direction (BD)-Transverse Direction (TD) plane. Mechanical properties of the samples were evaluated via tensile and compression tests with a crosshead velocity of 2 mm/min. For each sample, at least three specimens were examined.

3.1.2. Results and Discussion

3.1.2.1. Process parameters optimization

Fig. 13 displays the OM cross-section of the as-polished SS316L cubes produced using various combination of the process parameters.

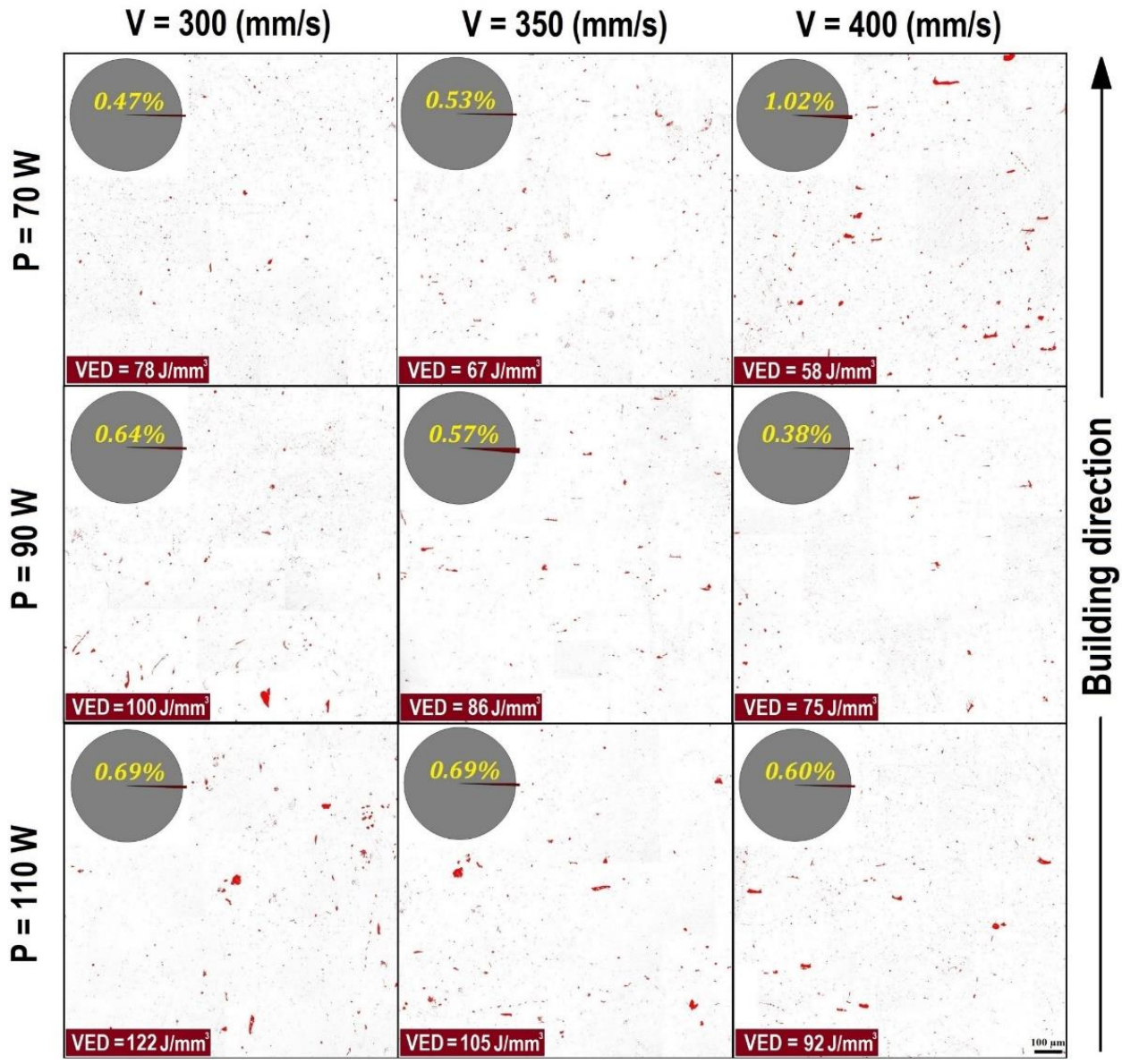

Fig. 13. Effect of different scanning speed (v), laser power (w) and energy density (VED) on the variation of porosity fraction along building direction in BD-TD plane.

As shown in this figure, the samples porosity content calculated through image analysis lies in the range of 0.47-1.02%. Moreover, Fig. 14 exhibits volumetric porosity variation as a function of energy density. It is evident that in the samples produced with the lowest laser power (70 W), the porosity content increases by increasing the laser scanning speed. The presence of irregular shape porosities in these samples suggests that the energy density

provided to the material for melting was insufficient and as a consequence resulted in the formation of process-induced porosity that is also known as lack of fusion porosity (LOF) [110]. It is evident that by increasing the energy density up to a certain level, it would be possible to facilitate the SS316L samples consolidation, leading to a very low porosity content in these samples.

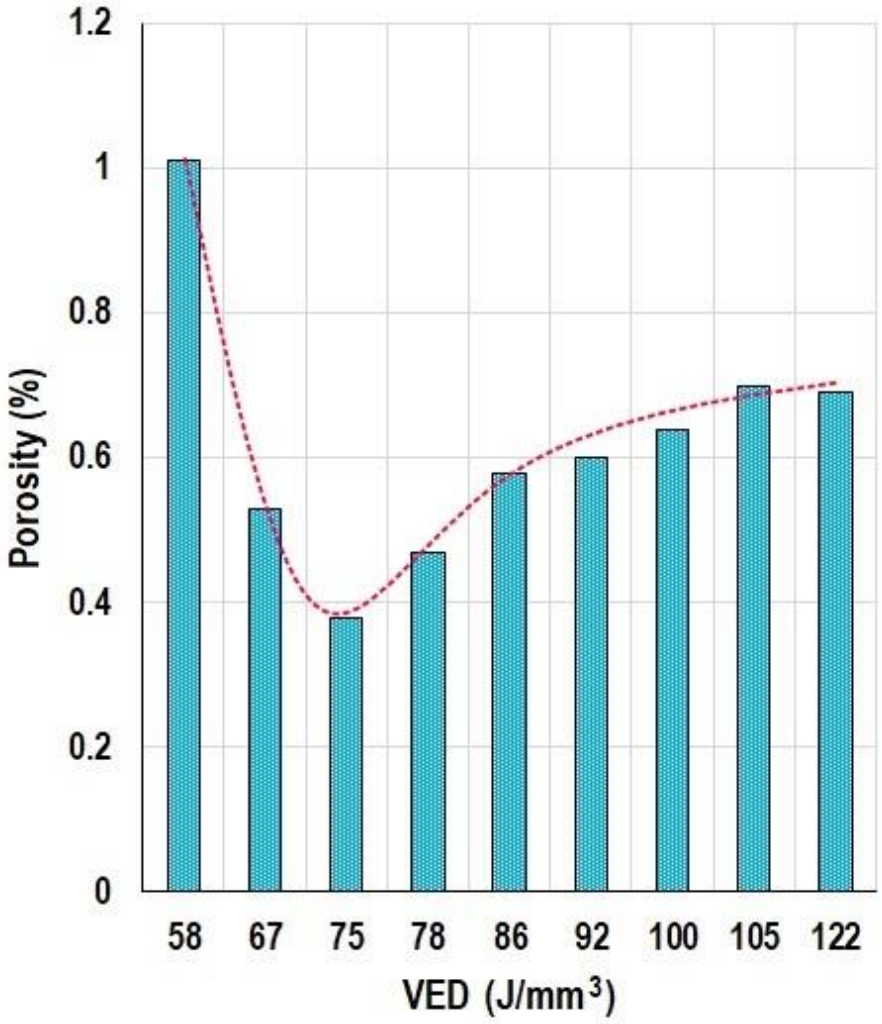

Fig. 14. Variation of porosity fraction as a function of energy density (VED) for samples fabricated by different processing parameters.

On the other hand, it was found that raising the energy density to more than ≈ 80 J/mm^3 was accompanied by the formation of gas induced-pores in the as-built SS316L cubes. Formation of this type of porosity in the as-built samples can be due to evaporation and entrapment of some alloying elements [111]. Fig. 14 indicates that the densest sample, with minimum porosity content, could be achieved utilizing an energy density between 70 to 80 J/mm^3. This optimized range for energy density would be reliable until the other processing parameters remain constant. It means that by any change in the layer thickness, scanning

strategy, laser beam diameter and morphology of feedstock material from the optimized condition, a slight re-optimizing might be required [112].

3.1.2.2. Microstructural evolutions during rapid annealing

Fig. 15 shows the general microstructure of the SS316L cube produced using the optimum process parameters. Accordingly, the grains nucleated on the support structures were finer than those in the middle of the cube. Formation of these fine grains at the bottom of the samples is due to the presence of a cold building platform that acted as a heat sink. Due to the higher cooling rate at the primary layers, the formation of finer grains near the building plate was expectable. After printing the initial layers, gradually the role of the building platform in dissipating the laser heat became less effective, resulting in heat accumulation in the center of the samples. This accumulated heat promotes epitaxial grain growth in the direction of the maximum thermal gradient. Formation of this type of microstructure in the as-built SS316L samples is also consistent with the results reported by Andreau et al. [113]. In fact, they proved that in the first layers, the grains were finer with random orientation while after some initial layers, the grains continue to grow along a preferential direction, creating a strong texture along the BD (Fig. 15(b)).

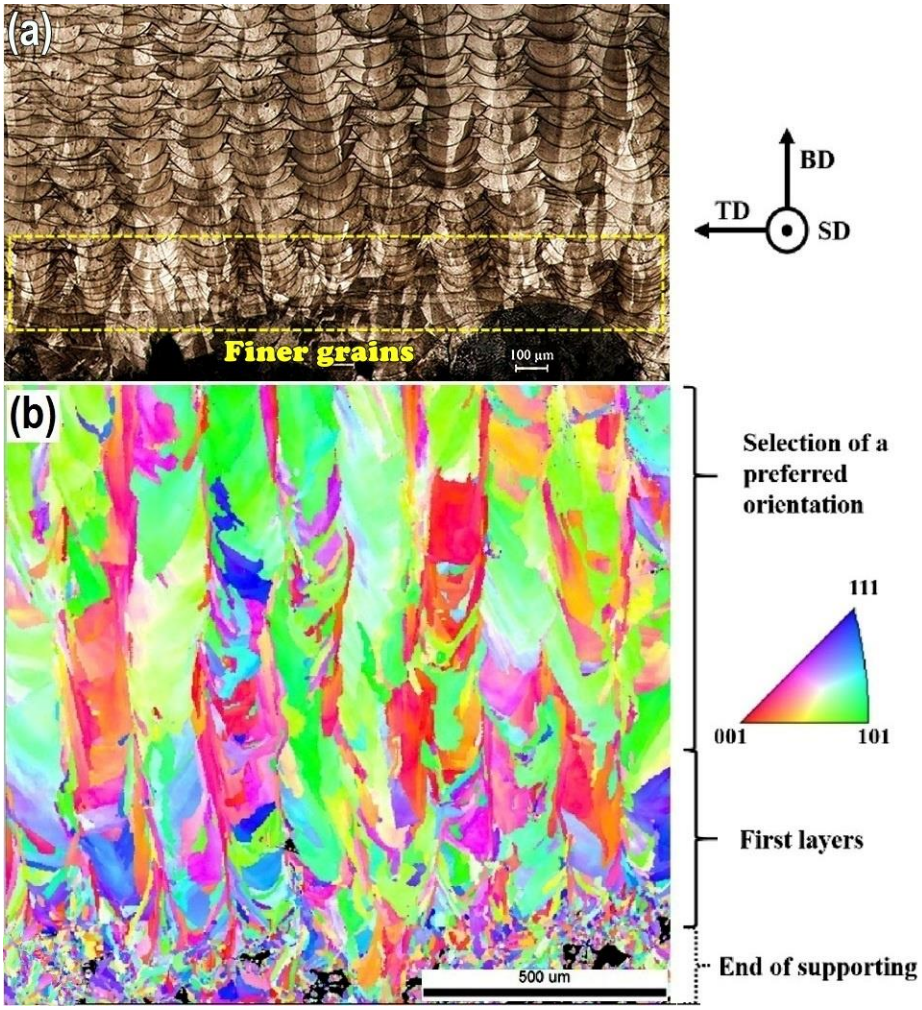

Fig. 15. (a) Optical micrograph, and (b) EBSD color map [113] representing the grains morphology and orientation from bottom to center of the as-built SS316L specimen.

Fig. 16 compares the 3D OM micrographs of the L-PBF SS316L samples before and after the rapid annealing at 1300 ºC for different periods of time, from 10 s to 120 s. The top surface of the specimens (*XY* plane) indicates that laser tracks are intersecting at an angle of 90º, which is equal to the rotation angle per layer during the building process. Besides, fine equiaxed grains observed in the *XY* plane are indeed a transverse section of the columnar grains that have grown along the BD. As already discussed, it is well documented that the formation of the elongated grains along the BD is usually due to the presence of a high thermal gradient along the BD that results in a directional heat dissipation [114]. It is evident that by increasing the annealing time the columnar grains grew, and the melt pool boundaries faded gradually until they completely disappeared after 120 s.

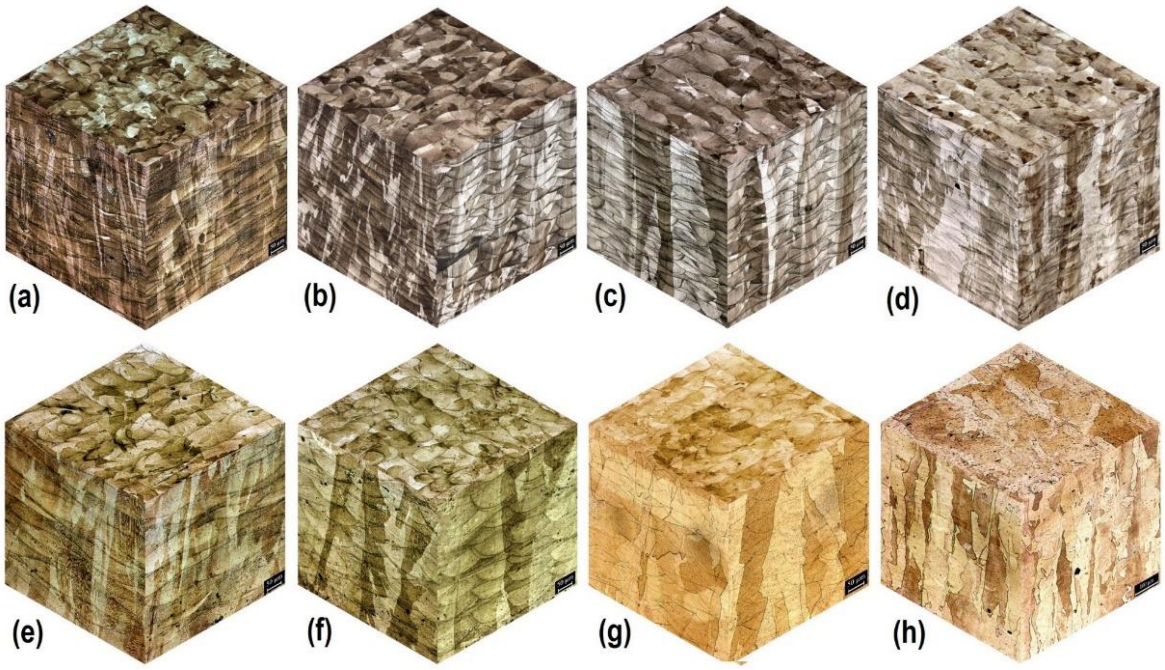

Fig. 16. OM micrographs of the L-PBF SS316L sample, (a) in the as-built state, after heat treatment at 1300°C for (b) 10 s, (c) 20 s, (d) 30 s, (e) 45 s, (f) 60 s, (g) 90 s and (h) 120 s.

FE-SEM micrographs in Fig. 17 represent the effect of heat treatment on the cellular and dendritic structures formed inside the melt pools during the L-PBF process. In fact, as reported in the literature, the final microstructure of an AM sample can be defined by the local solidification rate, the temperature gradient at the solid-liquid interface (G), the growth rate of the solidifying front (R), the undercooling (ΔT) and the alloy composition. In particular, the solidification mode and consequently the morphology of the final microstructure depends on the solidification morphology parameter (G/R) and the cooling rate level ($G \times R$) [115].

Notwithstanding some local variations in the microstructure of the as-built sample, the high cooling rate in the L-PBF process, that can reach 10^5-10^6 K/s, contributes markedly to the microstructure refinement and, as a consequence, to the higher mechanical properties compared to the conventionally manufactured alloy [116]. It is also proved that this kind of cellular-columnar structure can be formed only when G/R is higher than $\Delta T/D$, where ΔT is the solidification undercooling and D is the diffusion coefficient of the printed material. Notwithstanding this knowledge, still the prediction of the microstructural features of SS316L L-PBF samples based on the process parameters is a vital challenge. In particular, the local changes in G and R values during the building process can lead to the formation of columnar or equiaxed microstructures in the as-built samples. Fig. 17(a) illustrates a representative microstructure of the SS316L samples, including cellular and elongated dendrites and the melt pool boundaries in the as-built microstructure of the SS316L samples. Interestingly, as shown

in Fig. 17(b), both the cellular structure and the melt pools boundaries were stable after annealing up to 30 s. Instead, a substantial microstructural transition started after 45 s by the partial coalescence of the melt pool borders (Fig. 17(c-d)). Fig. 17(e-f) indicate that at longer annealing, up to 90 s, the melt pool contours disappeared, resulting in the homogenization of the microstructure.

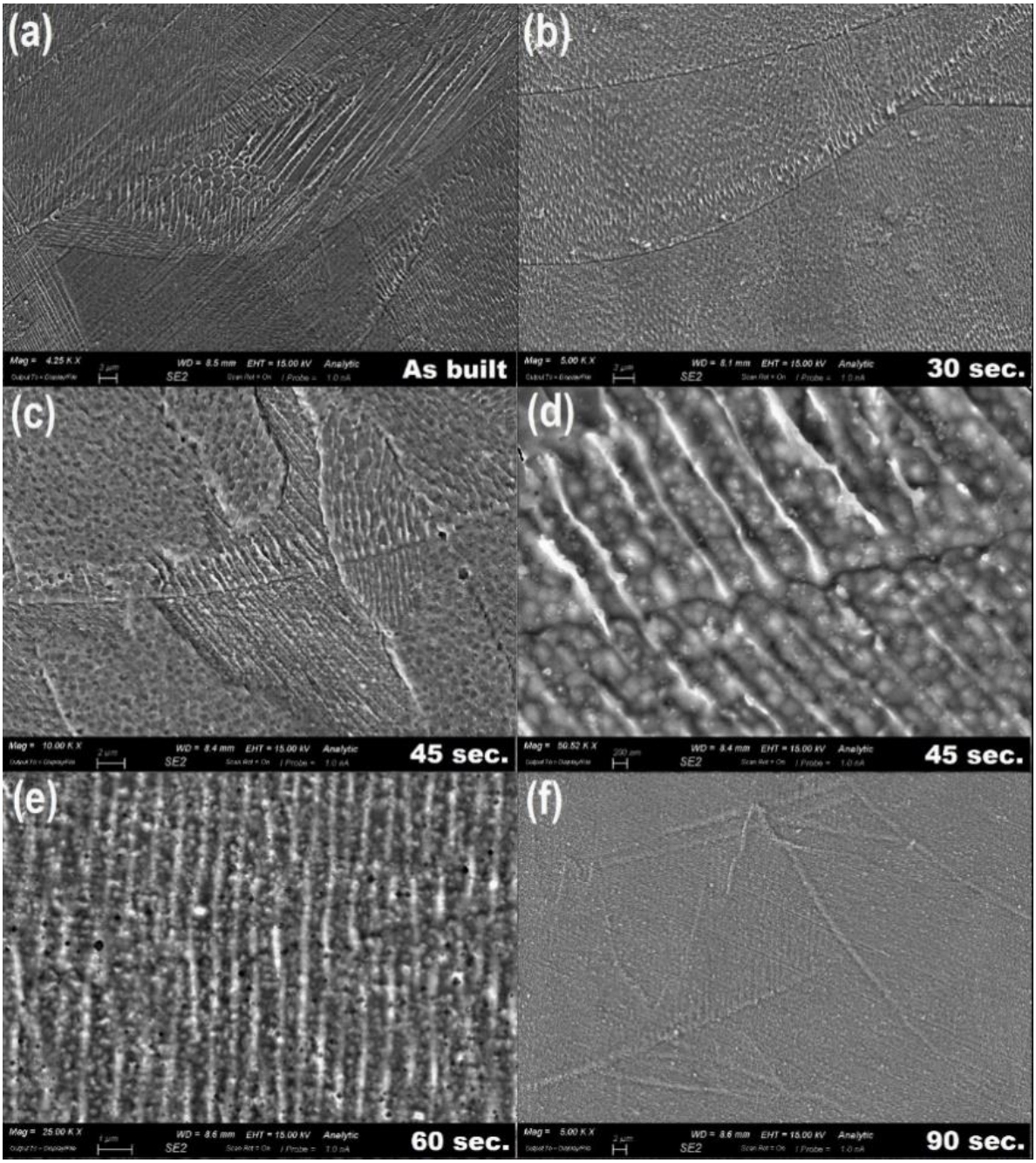

Fig. 17. Melt pools evolution in L-PBF SS316L samples, (a) in the as-built state, after annealing at 1300 °C for (b) 30 s, (c-d) 45 s, (e) 60 s, and (f) 90 s.

Fig. 18 shows the SEM image of the as-built SS316L samples indicating the formation of a zigzag pattern during the epitaxial grain growth by passing through the successive layers. To

minimize the nucleation energy during the solidification, the grains of the new layer preferentially continue the growth path of the previous grains. Moreover, during the building process, because of using 90° rotation per layer, in each new layer the laser trajectory is perpendicular to the previous layer. As a result, the growth orientation of the grains as well as their internal columnar dendrites rotates toward the maximum thermal gradient, which is generated by the heat source. Consequently, cellular structure as elongated tubes with polygonal cross-section were formed along the thermal gradient direction (Fig. 18(b)). Where the laser tracks of the subsequent layers overlap, the grains and dendritic structure resumes the growth pattern of the previous layer (Fig. 18(c)).

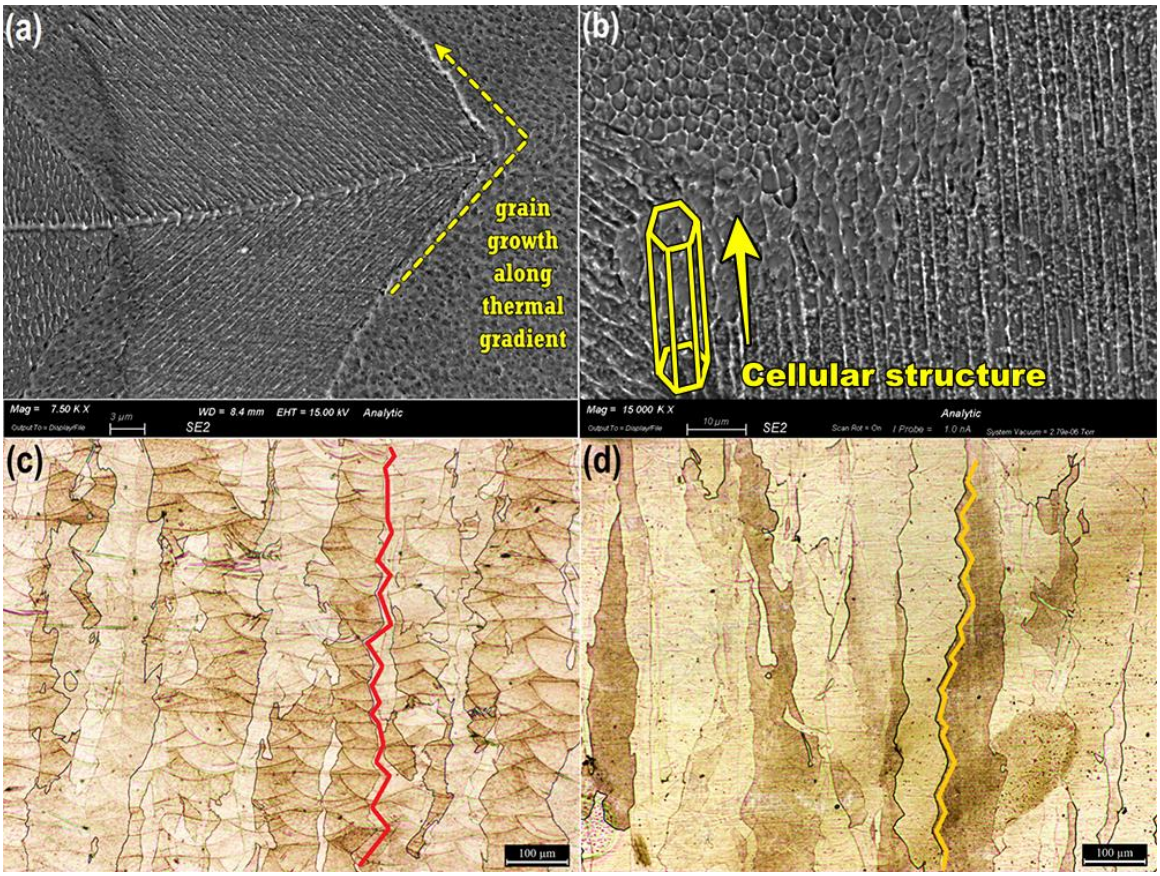

Fig. 18. (a) Zigzag epitaxially grain growth during L-PBF, (b) Schematic of cellular growth during L-PBF, and (c) stability of the fish scale pattern after annealing for (c) 90 s and (d) 120 s.

In general, thus, the fish-scale pattern originates from a successive change in the growth direction of the grains by passing sequential melt pools during the epitaxial growth. It is interesting to point out that this pattern remained stable during the rapid annealing, even after the heat treatments over 45 s that gradually unified the melt pools and eliminated the laser runways (Fig. 18(c-d)).

Fig. 19(a) is a representative SEM micrograph of the as-built SS316L sample produced via L-PBF process. As can be seen, the cell size of the as-built sample that was measured using triangle method [117] is 0.75±0.09 μm. Kim et al. [118] and Yin et al. [119] found that the cooling rate during the solidification is the key parameter that defines the cell size, and their correlation can be expressed as follow:

$$\lambda_1 = A\,\beta^{-D} \qquad (2)$$

Where λ_1 is the cell size, in μm, and β is the cooling rate, in K/s. A and D are two parameters, with values in the range A = 10^2-10^4, and D = 0.25-0.7. In the literature, this equation is well adapted to assess the relationship between the cell size and cooling rate for various stainless steels, with $A = 80$ and $D = 0.33$ [120]. Therefore, here the cooling rate during the solidification was also estimated using this equation and the cell size calculated via image analysis. The outcomes of this evaluation indicated that the formation of 0.752 μm cells resulted from a cooling rate equal to 1.2×10^6 K/s. It is very interesting to notice that the calculated cooling rate in this work is in a good agreement with those of literature [121].

The influence of rapid annealing on the cellular structure is presented in Fig. 19(b-d). The comparison of Fig. 19(a-b) illustrates that the cellular network's size and morphology remained stable during the rapid annealing up to 30 s. As the annealing time extended, the cell walls gradually disintegrated, and after 60 s, they disappeared to a large extent (Fig. 19(c-d)). Because of the high kinetic of lattice transformation at elevated temperatures, rapid annealing even for longer times did not change the initial size of the cellular structures until complete elimination of the cell walls [122]. According to Zhong et al., these cell walls characterized by a high dislocation density are the SGBs [123]. In fact, the aggregated dislocations in the SGBs are essentially immobile and can only move by glide mechanism [58, 124]. Hence, they displayed higher stability during heat treatment and were eliminated at high temperatures only for longer periods.

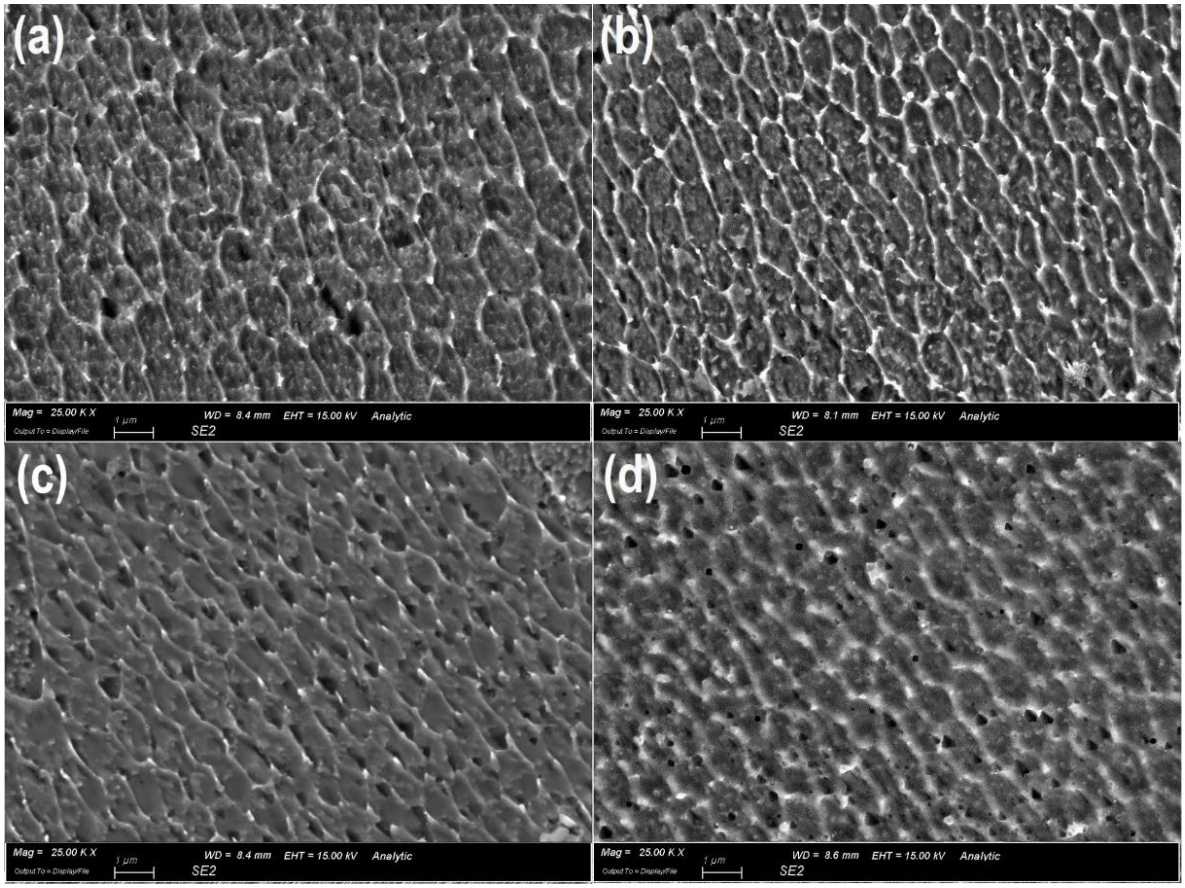

Fig. 19. SEM micrograph of the cellular structures in (a) as-built state, after annealing at 1300 °C for (b) 30 s, (c) 45 s, and (d) 60 s.

Apart from the cell size, it is also believed that the cooling rate has a vital effect on other microstructural features of the as-built samples. In general, standard rapid solidification of an austenitic stainless steel can lead to the formation of two microstructures, according to its chemical composition; austenite (γ) and δ-ferrite [125]. In fact, during the L-PBF process, since the cooling rate is much higher than in the case of conventional manufacturing processes, the molten material solidifies in a non-equilibrium state. As a result, the prediction of the phase composition of the as-built samples are very challenging. In the literature, Schaeffler diagram and pseudo-binary predictive phase diagram have been used to roughly evaluate the phase composition and solidification mode of the SS316L during the rapid solidification [126]. In this work, in order to predict the theoretical gross quantity of δ-ferrite at first Cr and Ni equivalents were calculated using the equations that are presented elsewhere [127]. According to the Schaeffler diagram, pseudo-binary diagrams and equivalent contents of Cr and Ni, it was found that the theoretical residual δ-ferrite content of the as-built samples should lie in the 5-10% range. Moreover, the ratio of $Cr_{eq.}/Ni_{eq.}$ was calculated to be 1.52. According to the pseudo-binary phase diagram and the calculated $Cr_{eq.}/Ni_{eq.}$ of the as-built samples, the SS316L alloy used in this work was placed within the FA region, i.e. that of austenite + lathy ferrite. It

means during the solidification, the primary δ-ferrite solidifies in the melt pool. Thereafter, in the L+δ zone, the last fraction of liquid becomes rich in γ-stabilizer elements such as Ni, N and C, and solidifies later in the γ structure. However, it should be underlined that the presence of a rapid directional solidification together with the reheating of the solidified layers during the building process can promote the segregation of alloying elements and consequently the variation of the microstructural features. SEM images of Fig. 20 confirms the presence of some white phases settled at the SGBs. In particular, EDS elemental analysis revealed that cell boundaries were decorated with Cr and Mo as well as a small amount of Si (Fig. 20 (c)). There are various theories about the presence of Si in the SGBs. Salman et al. [128] suggested that since Si is a ferrite stabilizer, it probably leaves the liquid phase during the solidification and precipitates at the SGBs. Saeidi et al. proved that during solidification, Si and Cr migrate from the adjacent areas to cell walls and form spherical amorphous nano-inclusions [116]. The simultaneous presence of Ni, Mo and Cr-containing silicate nano-inclusions can play a synergistic pinning role at the SGBs. As a result, intertwined stabilized dislocations in cell boundaries will act as a strong barrier to the movement of free dislocations. Recent studies have also confirmed that cellular network can enhance the resistance of materials to deformation by delaying or preventing the migration of free dislocations formed under external force [129].

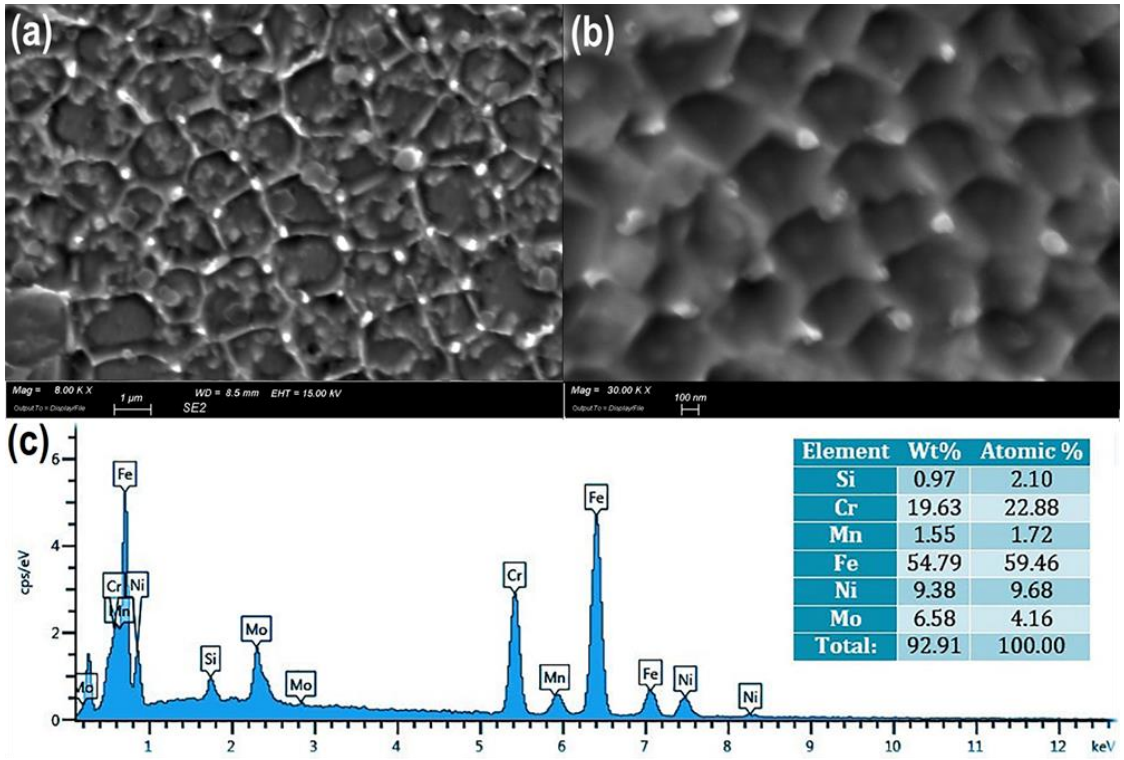

Fig. 20. (a) Accumulation of heavy elements on the cell boundaries (in white color) and (b) at higher magnification; (c) EDS elemental analysis of the white phase depicted in (b).

The comparison of the XRD patterns of the atomized powder with the as-built specimen through L-PBF suggests that the quantity of the primary δ-ferrite in the as-built SS316L sample was slightly lower than in the SS316L powder (Fig. 21(a)). On the other hand, structural analysis via SEM equipped with EBSD detector verified the presence of a slight amount of δ-ferrite on the cell boundaries (Fig. 21(b)). Accordingly, the unevenly distributed green dots in the austenitic substrate (blue background) represent δ-ferrite with body-centred cubic (BCC) arrangement. As shown in Fig. 21(c), a high temperature annealing longer than 120 s could annihilate the cellular structure and facilitate the diffusion of stacked elements from the sub-grain boundaries into the austenitic substrate.

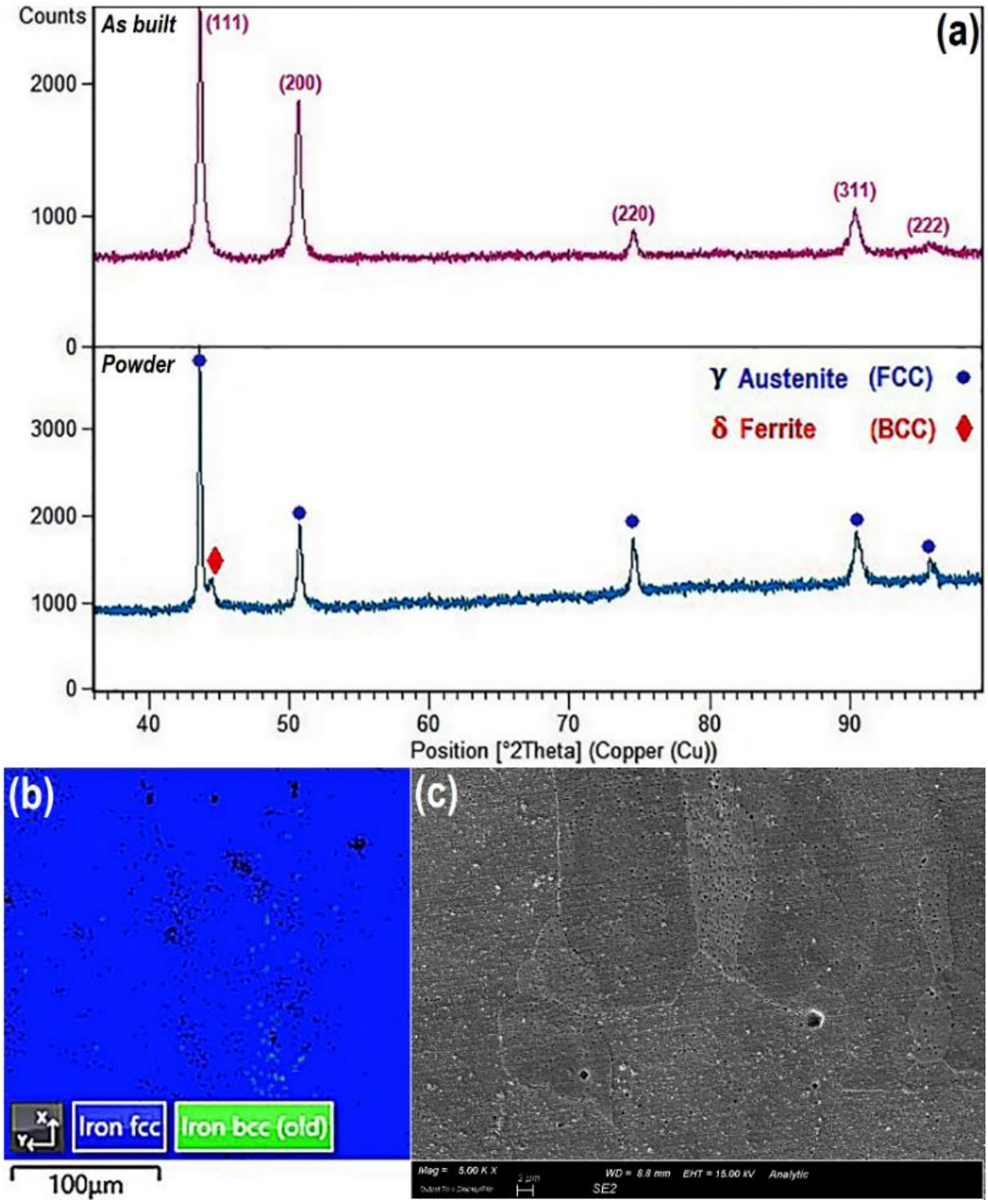

Fig. 21. (a) XRD pattern of initial powder and as-built sample, (b) EBSD output implying on random distribution of remained δ-ferrite by BCC structure in austenite matrix, and (c) complete annihilation of the cellular network after annealing at 1300°C for 120 s.

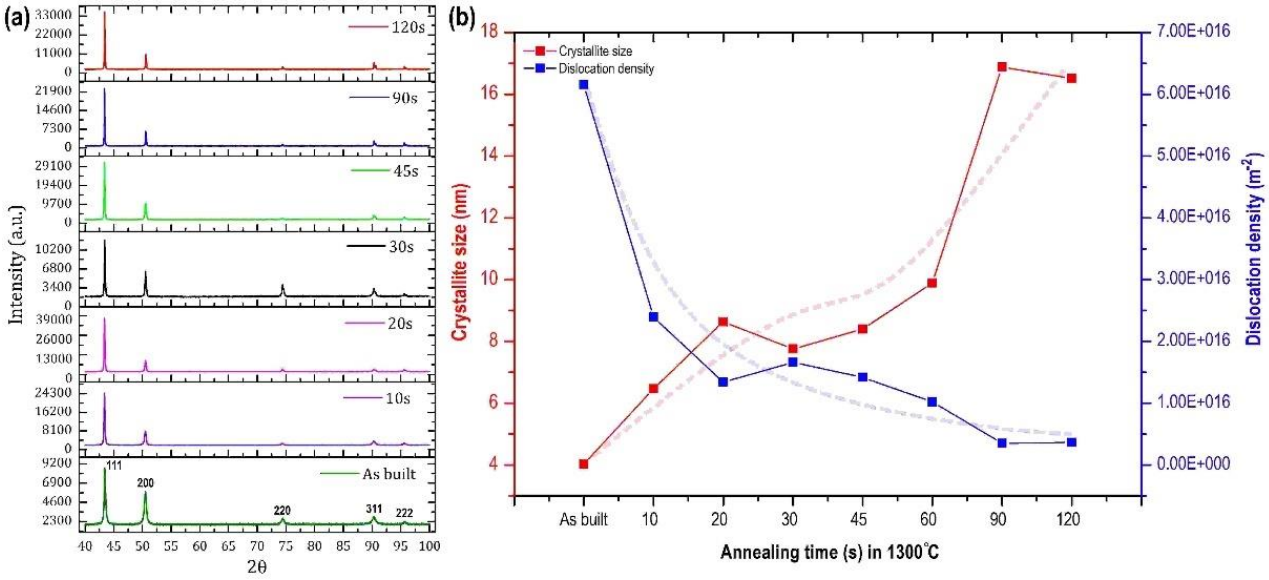

Fig. 22. (a) XRD patterns of the L-PBF fabricated samples after different annealing times and (b) changes of crystallite size and dislocation density during rapid annealing for different times.

XRD analysis that was performed on the samples before and after the heat treatment elucidates the lattice transformations during the rapid annealing **(**Fig. 22**)**. According to Fig. 22**(a)**, owing to the Faced-Centered Cubic (FCC) structure of austenite, regardless of specimen, (111) plane has the maximum peak intensity ratio (I/I_{max}) between atomic planes. Annealing up to 20 s is accompanied by the strong intensification of the (111) plane reflection. But, annealing at 30 s reduces the intensity of (111) plane again, with longer annealing times following the previous intensification uptrend. The calculation of the variation of crystallite size and dislocation density from the XRD spectra was executed by using Williamson-Hall and Scherrer methods, and the results are presented in Fig. 22(b). It is very interesting to highlight that before and after the 30 s annealing, two different trends were revealed. In fact, annealing below 30 s evidently reduced the dislocation density and caused the growth of the crystallite, whereas, annealing for 30 s resulted in a transitory reversion of this trend. This discrepancy can be attributed to the thermal recovery and rearrangement of the free dislocations. As a matter of fact, as the annealing time increased, the twisty dislocations walls were gradually dissipated. This structural evolution emerged as a decrease in dislocation density along with an increase in crystallite size.

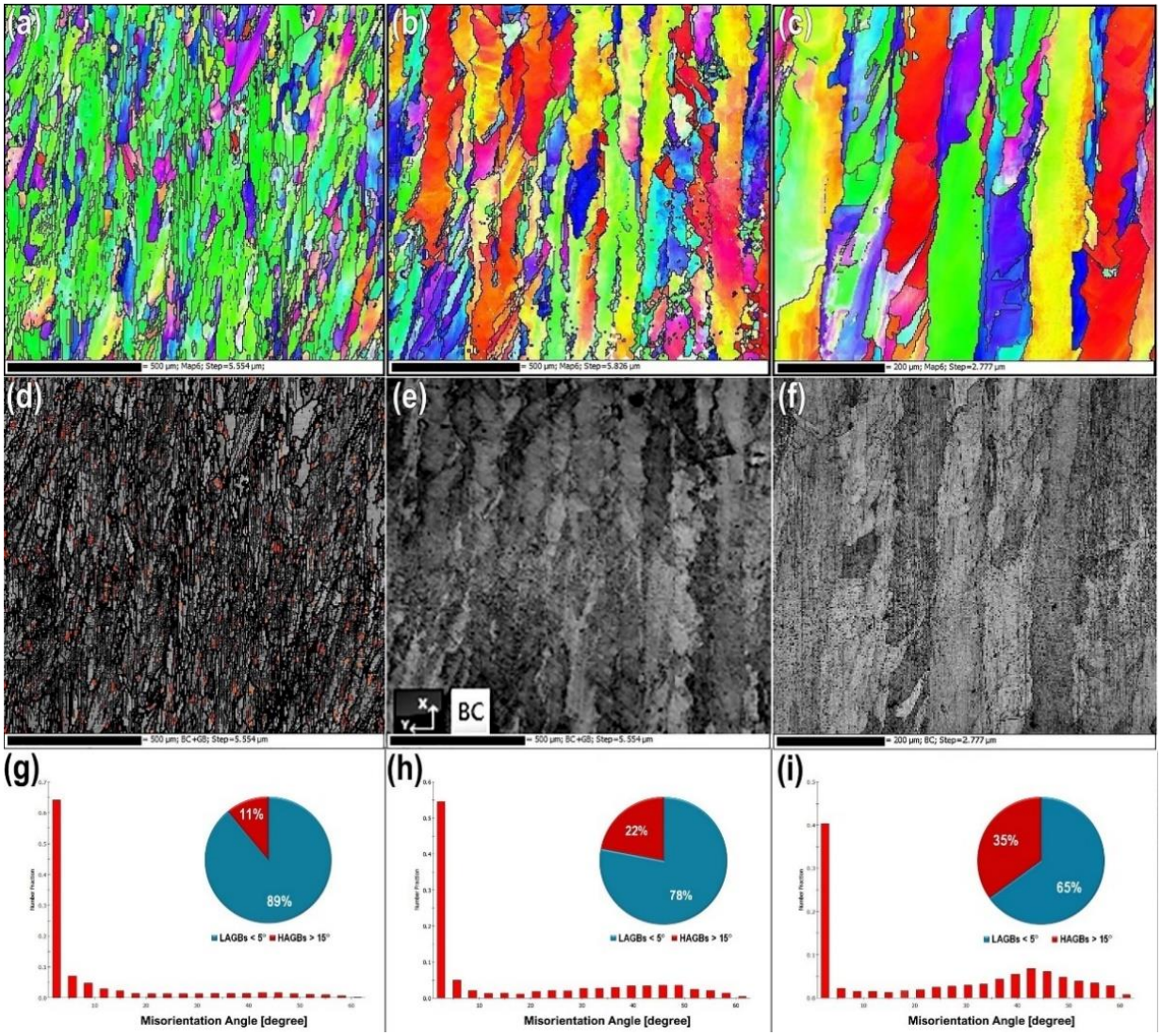

Fig. 23. (a-c) EBSD grain color map, (d-f) band contrast, and (g-i) misorientation profile of L-PBF fabricated SS316L samples after annealing for 45 s and 90 s at 1300 °C.

EBSD grain color maps of as-built SS316L specimen after 45 s and 90 s annealing at 1300 ℃ is displayed in Fig. 23(a-c). Variation of color contrast in discrete grains can be attributed to the intergranular misorientation. Hence, the increment colors variety in the color map of EBSD images implies augmentation of the preferential orientations in many numbers of the grains and depression of the developed texture along the BD. Both small swerved and narrow columnar grains of opposite colors are probably formed in the overlap zone between the adjacent laser tracks. As can be seen in this figure, increasing the annealing time causes an increase of the grain size. The band contrast images of Fig. 23(d-f) reveal that annealing for 45 s has remarkably removed the SGBs and more annealing time could not make impressive changes in the structure. The variation of the misorientation profile for similar distances of specimens after different annealing times is presented in Fig. 23(g-i). As can be seen, annealing for 45 s significantly increased the fraction of high angle grain boundaries (HAGBs), which

means a huge number of low angles grain boundaries (LAGBs) are annihilated. However, doubling the annealing time did not tangibly increase the HAGBs. Comparison of this trend with SEM images of Fig. 19 and Fig. 21 and dislocations trend in Fig. 22 revealed that a continuous reduction in the dislocation density, the annihilation of cellular structure, and downtrend of LAGBs during annealing over the 30s occurred in accordance together.

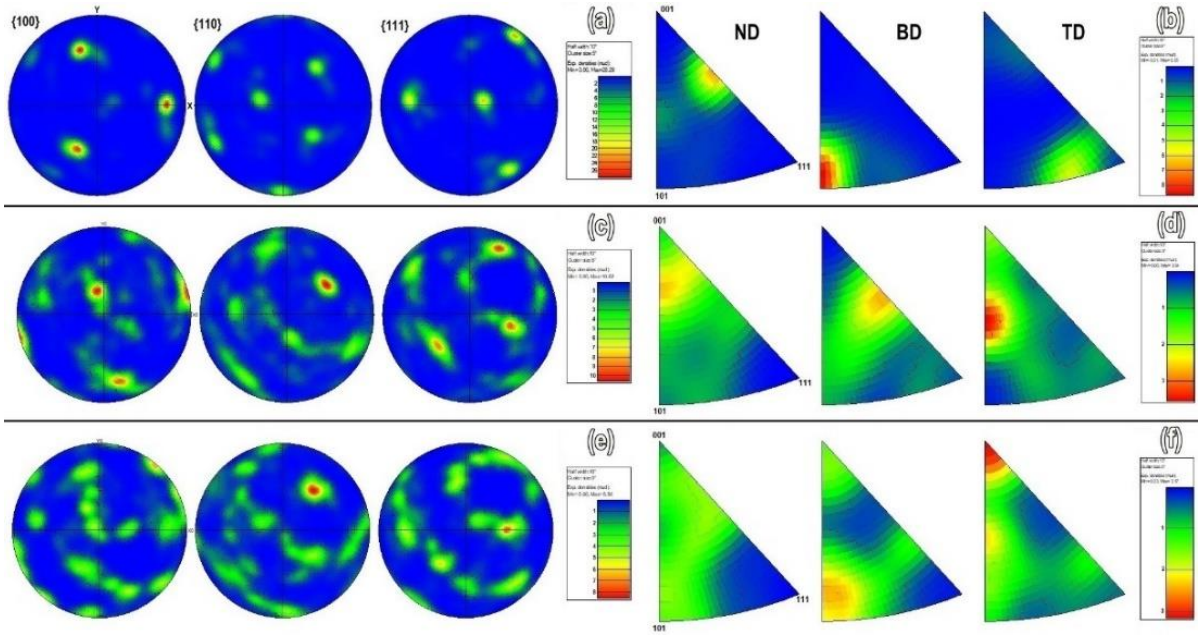

Fig. 24. (a,b) EBSD PF and IPF of the as-built SS316L, and after annealing for (c,d) 45 s and (e,f) 90 s.

To survey the effect of rapid annealing on the crystallographic texture and preferential orientation of the grains, the stereographic texture pole figures (PF) and their corresponding inverse pole figures (IPF) were investigated in the samples before and after the heat treatment (Fig. 24). The center of pole figures is parallel to the building direction (normal to the page), and the scale bar presented beside the pole figures refers to texture intensity of a random distribution [130]. Therefore, the stronger the texture, the greater the intensity. The centralized intensities on pole figure imply preferential orientation of a certain set of grains [131]. The orientation of grains often follows the thermal gradient. High laser VED creates a localized heat accumulation that can make a homogeneous melting and dissolve most of the pre-existing heterogeneities in the former layer. As a result, there would be sufficient time for the grains to be oriented and grow against the heat transfer direction [132]. Therefore, several large and elongated grains with a preferred orientation along the BD, are aligned and developed a predominant texture along (100) <101> (Fig. 24(a, b)). As discussed earlier, in the L-PBF fabricated SS316L samples, the predominant phase is austenite with FCC arrangement. According to solidification theory of FCC materials, <100> is the principal growth direction

of this family of crystals. Since different crystallographic planes in FCC materials have distinct packing densities, solidification occurs along the direction with the least atomic aggregation due to faster heat dissipation [113]. Since the samples were produced using a stripe scanning strategy by 90º rotation, advance orientation of heat source and subsequently solidification direction frequently changes. On the other hand, the solidification of the last deposited layer starts from the bottom of the molten pool, because the transverse section of the already grown columnar grains would be an eligible site for heterogeneous nucleation. Hence, new grains tend to germinate on top of the previously formed grains and continue to grow epitaxially. Oftentimes, the angular deviation between the thermal gradient direction and the epitaxial growth is not substantial for disrupting the vertical growth of the columnar grains. Comparison of PF and IPF of the as-built sample (Fig. 24(a,b)), with annealed samples for 45 s (Fig. 24(c,d)) and 90 s (Fig. 24(e,f)) revealed that by annealing over 30 s, regardless of annealing time, spread texture is majorly attenuated. This effect can be verified through the comparison between the PF patterns before and after the annealing. In fact, after annealing for 45 s, maximum texture intensity is reduced from 28.3 to 10.6, while annealing up to 90 s led to a reduction in the texture intensity to 8.54. On the other hand, the maximum texture intensity of the IPF patterns is reduced from 8.66 in the as-built sample to 3.54 and 3.17 after annealing for 45 s and 90 s, respectively. Likewise, during annealing up to 90 s, the reduction in texture along the BD (100) is accompanied by a change in overall lattice orientation to other directions.

All the evidence implies a remarkable texture attenuation and gradual annihilation of the cellular structure. To find the origin of such behavior, the components of the cellular structures must be investigated as dissociated. According to the literature [133], the cellular structure is composed of tubular columns with polygonal cross-section, with the walls of the tubes made by intertwined dislocations, i.e. SGBs. Most of these intergranular tubes grow parallel to the grain boundaries and sometimes passes through multiple melt pools. Hence, they have a large aspect ratio which means the fraction of accumulated SGBs along the BD is much higher than its value in the perpendicular direction. As a result, gradual annihilation of the cellular structure during annealing leads to the removal of most of the aligned dislocation walls along BD. It must also be considered that the tubes orientation was influenced by the laser source and had different deviation angles with the BD, even if their general orientation was along BD. Sun et al. [134] indicated that the orientation of the grains with respect to growth direction could also contribute to developing the texture in the as-built SS316L samples. According to their observation, a lower deviation angle of the orientation of the grain with respect to BD could

intensify the texture along (100) direction. Compared to zigzag epitaxial growth linked to the change in the growth angle in consecutive melt pools, straight growth of the grains can create more strong texture along the BD. Here, both EBSD patterns in Fig. 23(a-c) and OM micrographs in Fig. 25 show that during annealing, in some melt pool borders, straight GBs evolved into a zigzag shape. This can be attributed to the faster lateral growth of the grains due to horizontal residual stress along the laser path. As a result, the variation of grains morphology from straight to zigzag could also contribute to texture attenuation during the annealing. However, even after annealing for 90 s, the grains kept their elongated shape aligned with the BD, suggesting that the zigzag boundaries were not playing a decisive role on texture debilitation, since after the annihilation of cellular structure over 45 s, the (100) direction was not the strongest anymore.

Indeed, dimensional, and morphological changes of the grains during the rapid annealing were precisely evaluated, and the results are presented in Fig. 25. For a precise assessment of the grain growth mechanism during the high-temperature annealing, an extra sample was subjected to a heat treatment up to 300 s. The horizontal and vertical lengths of the highlighted grains were measured, and the grain size distribution along with the average length and width of the grains after different annealing times was presented. From the morphological insight, the as-built sample (Fig. 25(a)) had thin elongated grains with straight GBs and annealing for 30 s clearly increased the width of grains (Fig. 25(b)). In the following, by annealing for 90 s, 120 s, and 300 s (Fig. 25(c-e)) the grain growth sped up while the fraction of serrated boundaries increased, which can be ascribed to the lateral growth of the grains at the primary stages of the annealing.

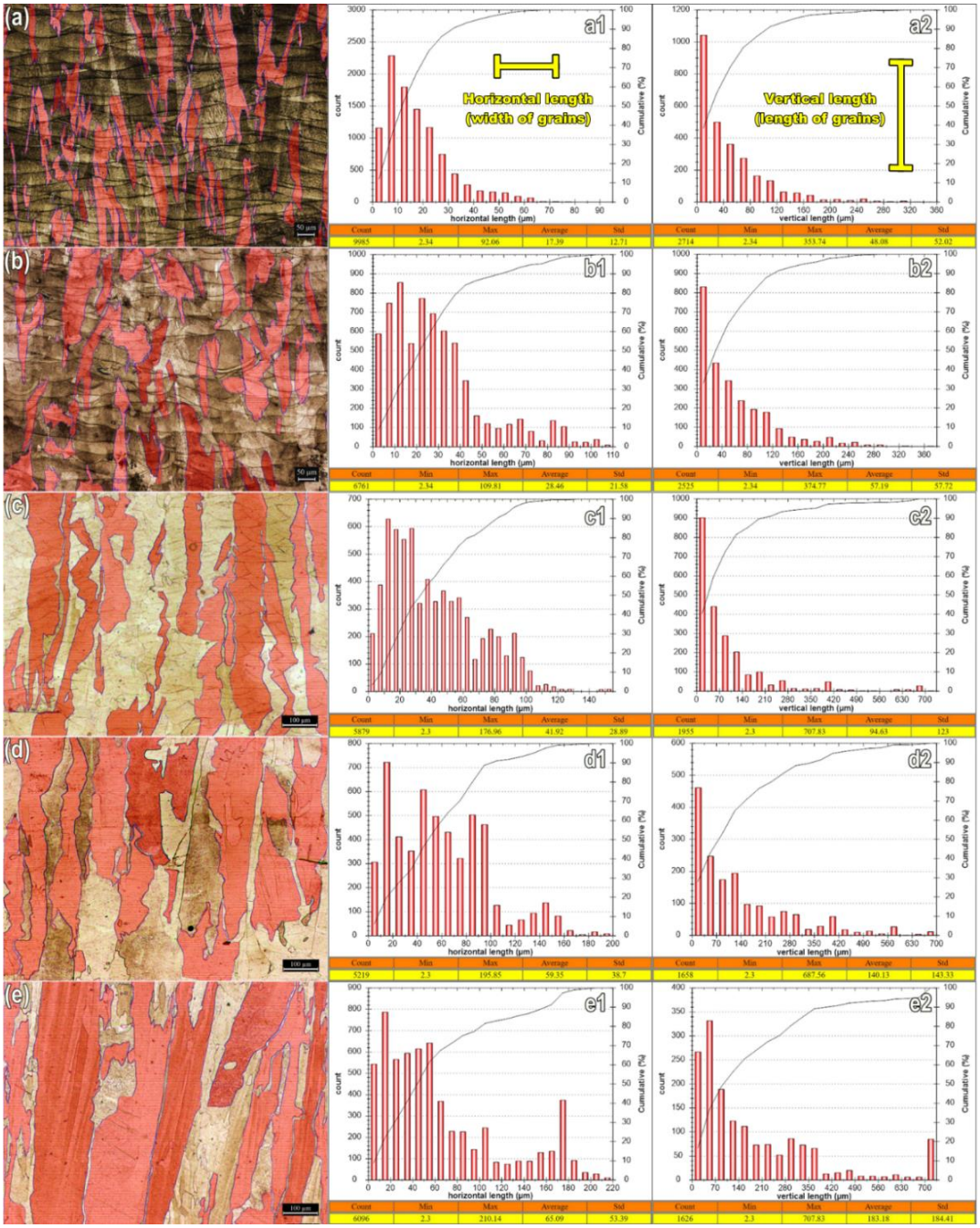

Fig. 25. Variation of the grains morphologies and horizontal and vertical length distribution of the grains in (a) as built sample and after annealing for (b) 30 s, (c) 90 s, (d) 120 s and (e) 300 s.

Variation of average width, length, and aspect ratio of the grains after rapid annealing for different times is presented in Fig. 26.

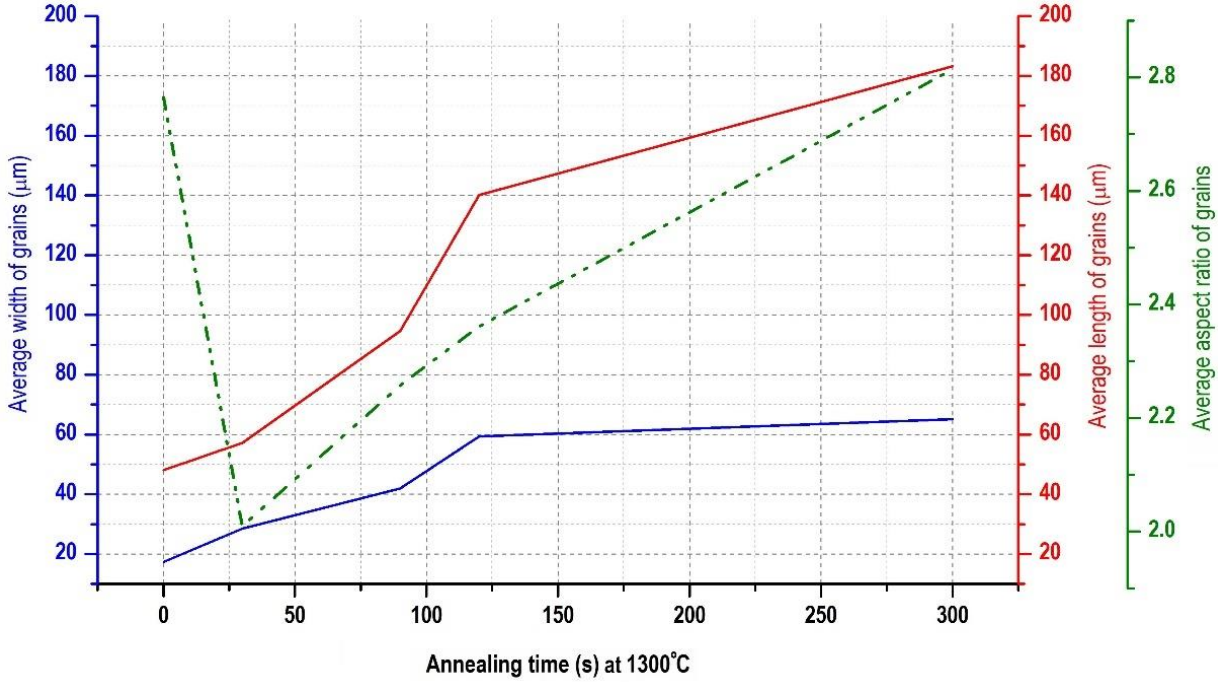

Fig. 26. Variation of the average length, width, and aspect ratio of the grains after annealing at 1300 °C up to 300 s.

As illustrated, annealing up to 300 s was constantly accompanied by horizontal (blue line) and vertical (red line) growth of the grains. At the beginning of the heat treatment, the rate of lateral growth along the laser trajectory surpassed the vertical counterpart. However, keep on annealing for longer times eventuated in greater grain growth along the BD along with annihilation of the SGBs (cell walls) and increment of the average aspect ratio of the grains. The curves show that the annealing for more than 30 s and the consequent annihilation of the cellular structure facilitate the stress relieving along the BD through the activation of the strain-induced grain boundary migration (SIGBM) mechanism. According to the literature [135], during the thermal recrystallization of samples having high residual stress, like in the case of severely strained materials, the grains prefer to grow toward the locations with maximum residual stress and stored energy. As a result, in materials with intensive texture and remarkable stored energy, often during annealing the grain growth along the length of elongated grains surpasses their transversal growth owing to SIGBM phenomenon.

3.1.2.3. Mechanical properties

Fig. 27 shows the effect of annealing time on the mechanical response of the L-PBF SS316L specimens for compression and tensile tests. Uniaxial compression loading was imposed along the building direction of the as-built specimens. As evident from the stress-strain curves in Fig. 27(a-b) and from the values presented in Fig. 27(c), annealing for 10 s

caused no measurable reduction of Yield Tensile Strength (YTS), Ultimate Tensile Strength (UTS), or Yield Compressive Strength (YCS). However, annealing for longer times resulted in an improvement in the elongation and a reduction in the mechanical strength with respect to the as-built specimens. Obviously, annealing up to 30 s has not significantly attenuated the tensile and compression strength of the samples. However, striking collapse in mechanical strength after annealing for 60 s is evident. By annealing of specimens for 30 s, YCS, YTS and UTS, declined from 305 MPa to 285 MPa (6%), from 530 to 455 MPa (14%) and from 681 to 637 MPa (6%), respectively. Instead, annealing for 60 s reduced the YCS, YTS and UTS values to 222 MPa (27%), 405 MPa (24%), and 579 MPa (15%), respectively. A similar downtrend for hardness [136] and tensile strength when increasing the annealing time [52] or temperature [128] was also reported by previous researchers. It is evident that the attenuation of mechanical strength by extending the annealing time concurs with the disintegration trend of the cellular network. Therefore, it is worthwhile to conclude that the interconnected cellular network acts like a scaffold pinned by nano-inclusions and ferrite stabilizer large atoms within the L-PBF printed SS316L sample. As long as this scaffolding network remains stable, the outstanding mechanical strength achieved as an advantage of L-PBF can almost be maintained. Instead, there is no doubt that rapid annealing for more than 30 s would eliminate the subgrains and reduce the strength, however increasing the ductility of the material. Nevertheless, the acquired properties after long-term annealing are not so impressive to suggest the use of longer heat treatments for L-PBF manufactured materials.

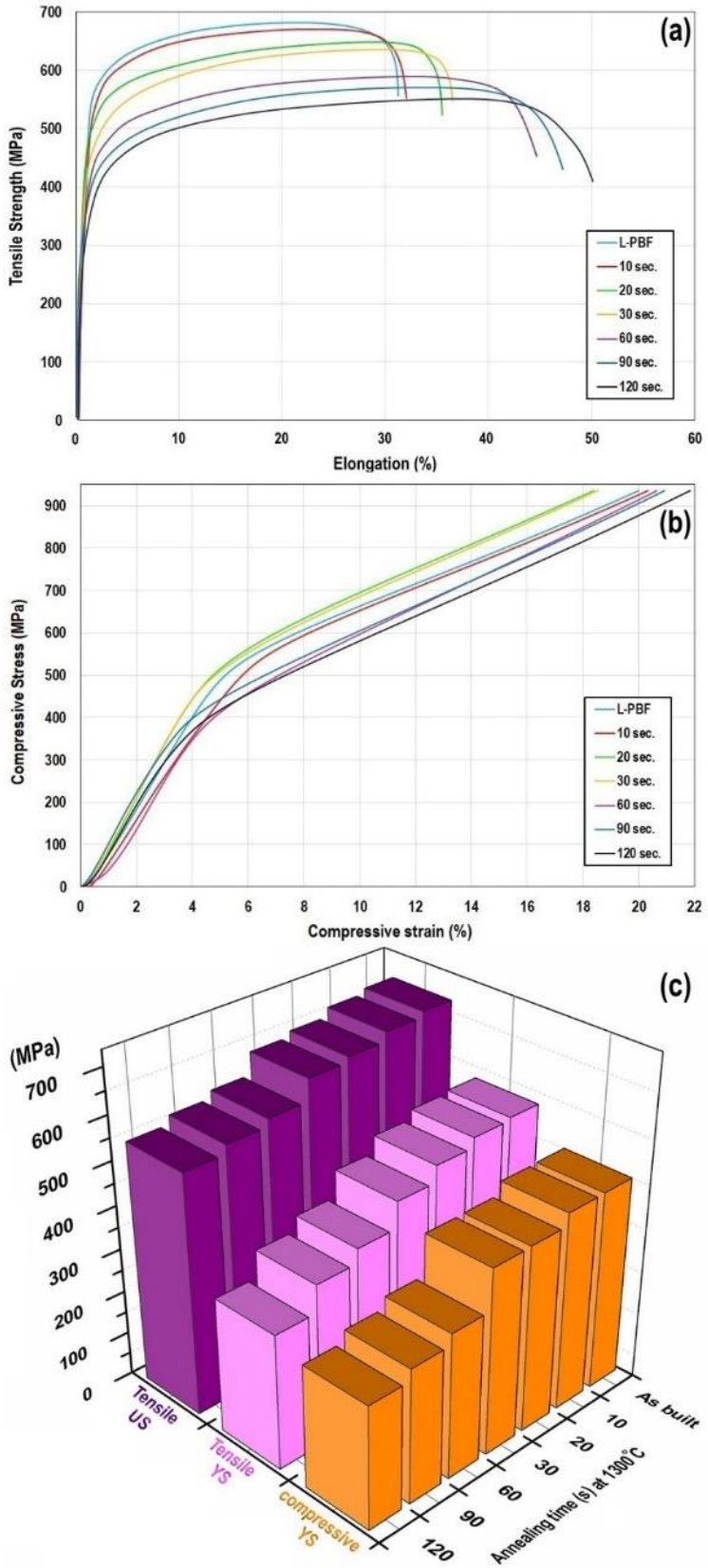

Fig. 27. (a) Tensile, (b) compressive stress-strain curves and (c) variation of the YCS, YTS and UTS by heat treatment at 1300 ºC for different periods.

Fig. 28 shows the fracture surface of the samples after the tensile test. As can be seen, the as-built sample (Fig. 28(a)) had the finest dimples and an increase in annealing time led to a

partial growth of dimples in the fracture surfaces. Evidently, annealing up to 30 s could not majorly affect the size and morphology of dimples (Fig. 28(b-d)) while longer heat exposure increased the dimension of dimples (Fig. 28(e-h)). This behavior confirms that cellular structure can directly affect the strength of the material and its gradual elimination after 45 s reduces the number of dimple walls, which hints at a softer fracture.

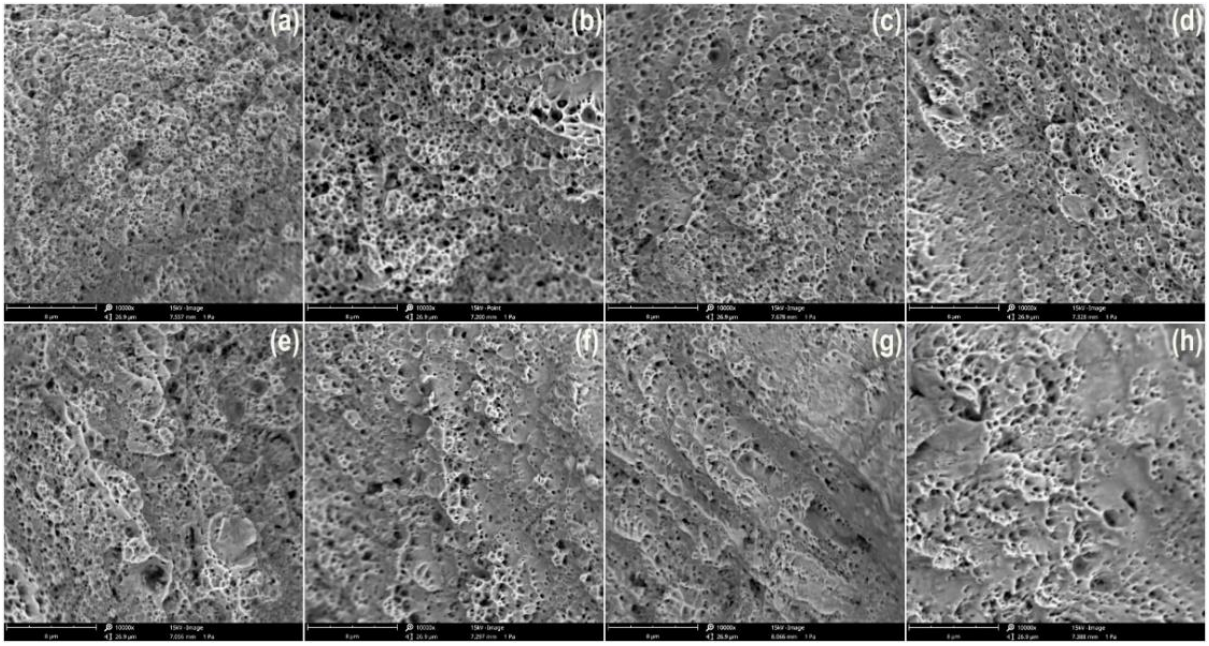

Fig. 28. Fracture surface of the (a) as-built sample, after annealing at 1300 °C for (b) 10 s, (c) 20 s, (d) 30 s, (e) 45 s, (f) 60 s, (g) 90 s, and (h) 120 s.

In-depth Characterization of the fracture surface (Fig. 29) shed light on the destructive role of some defects in the failure of the material. Fig. 29(a) shows that a long area has ruptured with a slip facture mode, which is a soft failure mechanism. Since the heat-affected zone (HAZ) of a laser track is the weakest point in the LPBF fabricated samples, probably this area was the HAZ of a laser track that has insufficient interfacial bonding and acted as crack origin under tensile loading. Fig. 29(b) shows that some inclusions were the origin of coarse dimples and contribute as one of the failure originations points. Similarly, some non-metallic inclusions with similar size and morphology were observed in OM micrographs during microstructural investigations (Fig. 29(c)). SEM analysis of the primary powder revealed that similar inclusions were present on the surface of the particles from the beginning. The elemental distribution maps of Fig. 29(d) revealed that these inclusions were enriched in O and Si and probably have SiO_2 composition. It is proved that these large oxide inclusions inside the precursor powder formed during inert gas atomization were distinguished as the main origin of the formation of micro/nano inclusion in LPBF fabricated SS316L components. But owing to

have a melting point (about 1710 °C) below the temperature of the laser beam, most of them were dissolved in molten pools under laser irradiation and formed again by re-oxidation/re-precipitation [137, 138]. Eventually, they remained in the steel matrix in the form of precipitates with negligible coherency and during the tensile test they could easily detach and create a void much larger than the typical dimple.

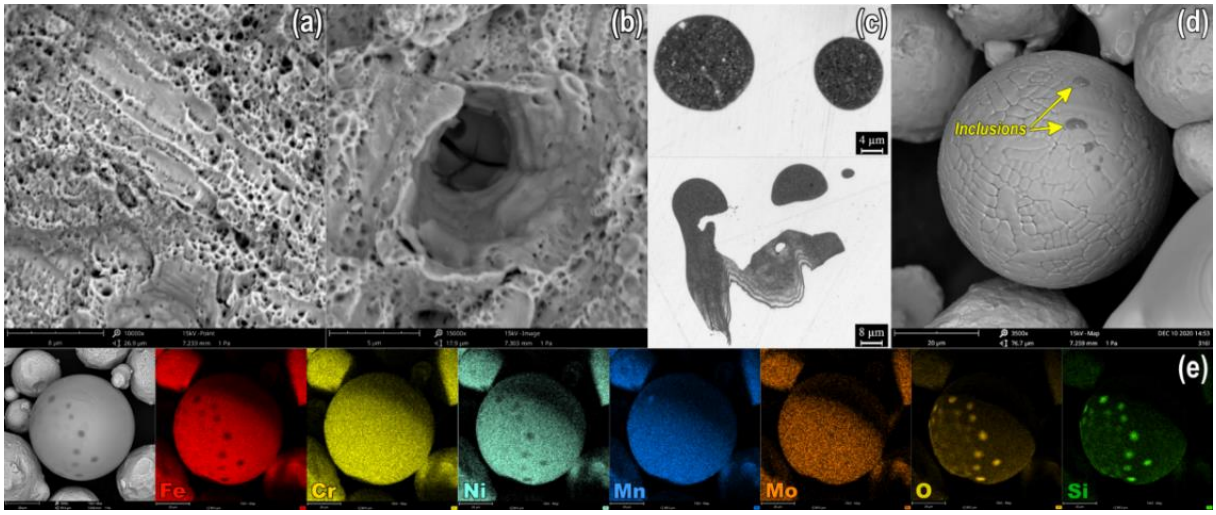

Fig. 29. (a) Trace of laser tracks on the fracture surface, and (b) the presence of SiO_2 inclusions in a dimple, (c) OM micrograph of as-built sample, (d) Surface of the initial powder, and (e) element distribution map of the primary powder.

3.1.3. Summary and conclusions

In the current study, samples of 316L austenitic steel were produced using the L-PBF technique. To identify a fast process to counteract strong texture formed due to the rapid solidification of fused layers, samples were treated via a short-term annealing (10-120 s) at 1300 °C. The effect of annealing time on the microstructure and mechanical strength of the samples was evaluated. The main achievements of this research can be summarized as follows:

- An increment of the annealing time gradually causes the borders of melt pools to vanish and merged them together. SEM characterization revealed that the disappearance of the borders began after annealing for 45 s, and over 90 s most the laser footprints were removed, and grain growth accelerated.
- The monitoring of the disintegration of the cellular structure during rapid annealing indicated that the cell walls were stable up to 30 s and then were gradually annihilated. Thermal stability of the SGBs can be attributed to the presence of Mo, Cr, silicate

inclusions, and a small amount of δ-ferrite, whose presence were validated by EDS and EBSD evidence.

- The severe thermal gradient from the surface to the depth of melt pools, and the change in the heat source direction during the buildup of samples, resulted in intensive epitaxial grain growth along the BD. EBSD outputs showed that a strong texture developed along the BD, that was largely thwarted by rapid annealing for more than 30 s. Since after annealing over 45 s the grains were still elongated, the texture reduction is instead attributed to the annihilation of the cellular structure as well as to the disordered transformation of straight GBs to zigzag shape.
- According to the analysis of the size and shape of the grains, by annealing over 30 s the grains started to grow faster along their length (BD), and their aspect ratio constantly increased. Due to remarkable residual stress along the BD, it can be attributed to the activation of SIGBM mechanism.
- Analysis of tensile and compressive properties of samples revealed that annealing up to 30 s would not significantly reduce the YCS (6%), YTS (14%) and UTS (6%). Whereas, annealing for 60 s lowered them about 27%, 24% and 15%, respectively. Comparing the mechanical outputs with the structural evolutions disclosed the undeniable scaffold-like role of SGBs on the mechanical strength of L-PBF fabricated SS316L samples.

3.2. Comparison of Water- and Gas atomized powders

Abstract

In the current research, the microstructure and mechanical properties of laser powder bed fusion (LPBF) manufactured stainless steel 316L with water atomized (WA) and gas atomized (GA) powders were compared together. Due to the irregular shape and higher laser absorption of WA particles, when using powders with similar dimension, samples obtained from GA powder present usually better performance. Hence, in the current work, WA powders with finer size compared to GA were employed. According to the obtained results, using the same process parameter resulted in higher tensile strength (UTS), yield strength (YS), elongation (El%), and toughness in the WA sample (728 MPa, 580 MPa, 31.8%, and 215 J/m3), compared to GA sample (602 MPa, 503 MPa, 25.2%, 145 J/m3). Likewise, the WA sample showed a superior work-hardening rate. The overplus oxygen in the WA sample combined with Mn, Si, and Cr caused the formation of multiple inclusions that resulted in non-uniform hardness distribution. A higher solidification rate of melt pools in the WA sample left more intensive residual stress with distorted grains, showing a remarkable orientation spread (GOS). To save the lattice continuity, a multitude of geometrically necessary dislocations (GNDs) formed around the grain boundaries and the interface of particles/matrix, which emerged as higher kernel average misorientation (KAM) in the WA sample. Measurement of the dislocation density from XRD patterns validated the higher KAM and GNDs in the WA sample. Also, higher dislocation density in the WA specimen appeared as a smaller cellular structure in SEM images, which implies more sub-grain boundaries. The columnar growth of the grains along the building direction created a stronger texture in the WA sample compared to the GA counterpart.

3.2.1. Materials and processing

3.2.1.1. processing

Gas atomized (GA) and water atomized (WA) powders of stainless steel 316L used in the current study were supplied by Höganäs AB and Pometon S.p.A (Italy), respectively. Both samples were printed by a Concept Laser Mlab Cusing with a laser spot size of 50 μm and a laser power of 95 W, scanning speed of 500 mm/s, layer thickness of 25 μm, hatching distance of 74 μm, and rotation angle of 67° as the optimum parameters.

3.2.1.2. Corrosion

All electrochemical measurements were performed in 3.5 wt% NaCl solution. Samples were mounted in epoxy resin and polished mirror-like before each corrosion test. The exposed area was 0.9 cm^2 and all presented results were normalized for this value. Electrochemical measurements were carried out in a 3-electrode electrochemical cell, where the sample was the working electrode, a platinum wire was the counter electrode, and the reference was an Ag/AgCl electrode. All corrosion tests were performed at room temperature, using the Ivium-n-Stat potentiostat. Before each measurement, the sample Open Circuit Potential (OCP) was measured for 30 min. Cyclic-Potentiodynamic Polarization (CPP) measurements were carried out from -0.2 V vs OCP toward anodic voltage values. The scan rate was equal to 10 mV/min, at potential steps of 1 mV. The scan direction was reversed when the measured anodic current density was equal to 1 mA/cm^2 and the measurement finally ended at -0.2 V vs OCP. Electrochemical Impedance Spectroscopy (EIS) was carried out by applying a sinusoidal stimulus of 10 mV around the OCP. Measurements were performed in the frequency range of 10^{-2} Hz to 10^5 Hz, acquiring 10 points per frequency decade. Each electrochemical measurement was repeated three times.

3.2.2. Results and discussions

3.2.2.1. Powder analysis

The morphology and size distribution of the GA and WA powder was characterized by a digital optical microscope (Fig. 30(a, b)) and SEM (Fig. 30(c, d)). Also, characterizing the cross-section of the GA and WA particles after etching reveals that WA powder is more resistant to the corrosive media of the solution etchant. A comparison of the circular diameter and circularity of the WA and GA powders used in this study (Fig. 30(e-h)) indicates that WA powder has finer particles with lower circularity. Previous researchers demonstrated that the particle size of the powders is strongly correlated with the flowability, and finer particles usually show lower spreadability [37]. The average circular diameter of the GA and WA powders was 29 μm and 22 μm, respectively; these values are in the optimal size distribution range for LPBF (ranging from 10 μm to 45 μm) [12].

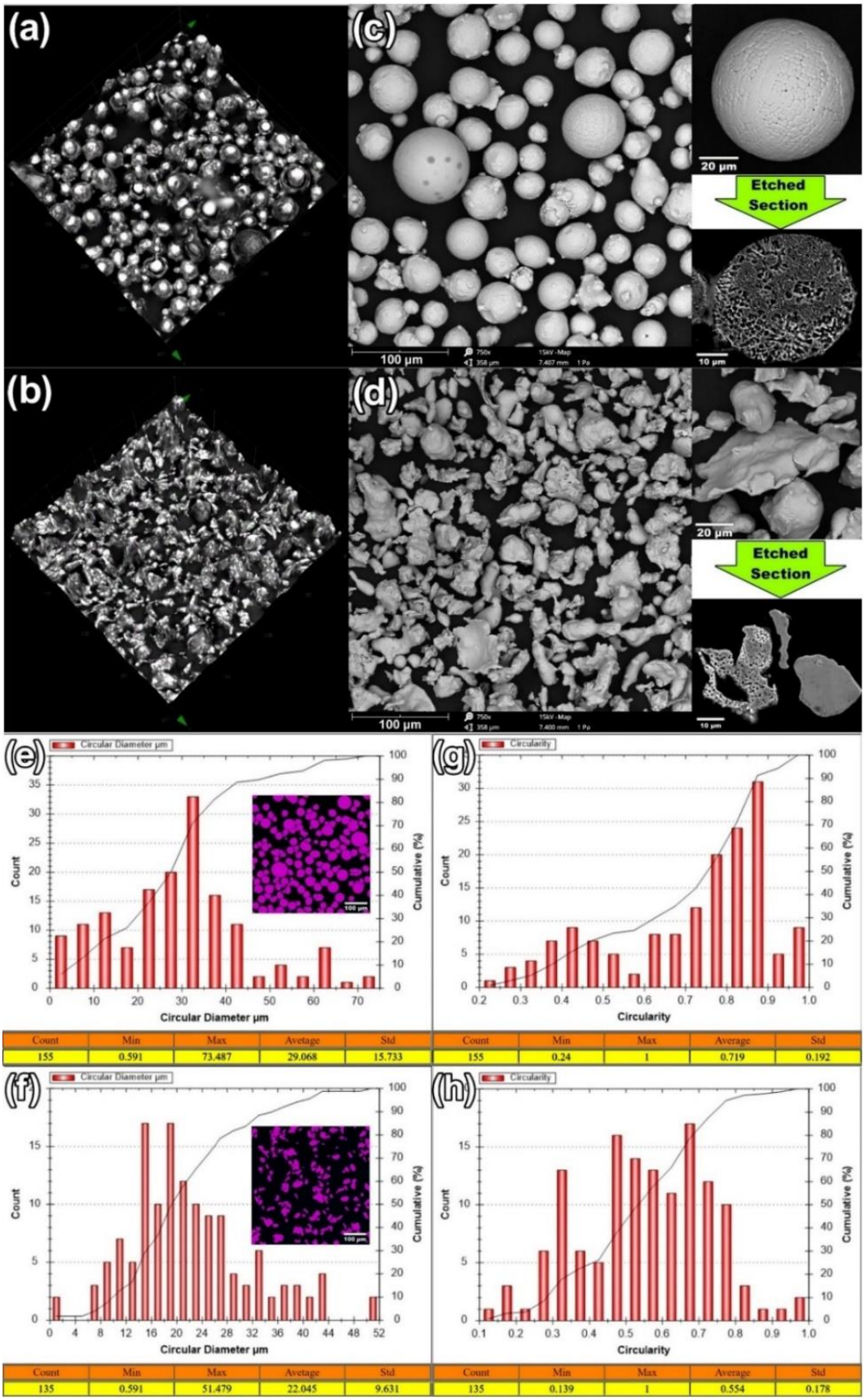

Count	Min	Max	Avetage	Std
155	0.591	73.487	29.068	15.733

Count	Min	Max	Average	Std
155	0.24	1	0.719	0.192

Count	Min	Max	Avetage	Std
135	0.591	51.479	22.045	9.631

Count	Min	Max	Average	Std
135	0.139	1	0.554	0.178

Fig. 30. Optical 3D micrographs and SEM images of GA (a, c) and WA (b, d) samples and distribution histograms of size and circularity of GA (e, g) and WA (f, h) samples.

The selection of true layer thickness can directly affect the productivity of industrial applications. The optimum layer thickness that results in maximum compactness and proper bonding between successive layers in AM fabricated samples was often determined as a value between D(50) and D(90) of the powder feedstock [34]. In the current work, both the GA and WA samples were printed with a layer thickness of 25 µm. The particle size distribution (PSD) of the GA powder is wider than the WA powder and usually could make higher packing density since the fine particles fill the voids between large adjacent particles [15]. Apart from powder morphology, the surface roughness of the printed samples improves proportionally to the powder flowability [139]. Also, it has been proven that reduction of the particles size will increase the laser absorption (Fig. 31).

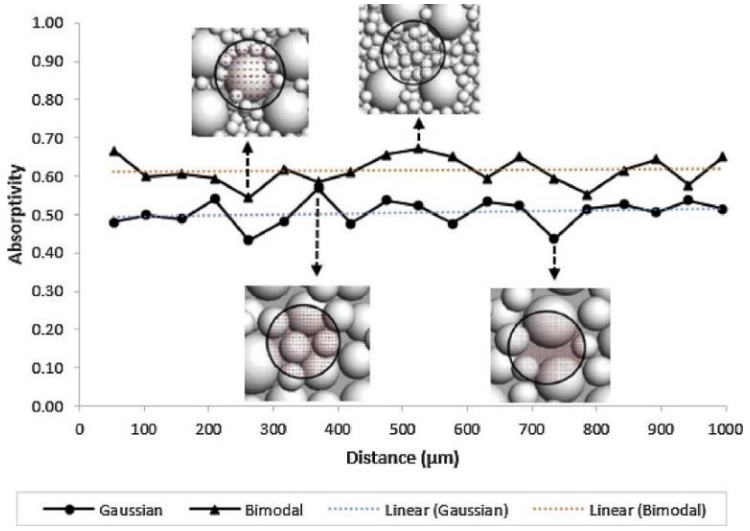

Fig. 31. Thermal absorptivity Comparison of Bimodal and Gaussian powder [140].

The chemical composition and elemental distribution map of the GA and WA powders are presented in Fig. 32(a, b) and Fig. 32(c, d), respectively. According to the chemical composition tables of Fig. 32(a) and Fig. 32(c), GA powder has higher Mn and lower Si content compared to the WA powder. Such a difference was repeatedly detected over multiple powder particles indicating a consistent difference in the Mn value of the GA compared to WA powder, as also has already been reported for the same alloy [141], as well as for 4130 [142] and 17-4 PH [32] steels. Furthermore, WA powder has a higher Si content with relatively large Si-rich inclusions, whereas smaller particles can be spotted on the surface of GA particles. Such a difference in the Si amount, together with the higher oxygen content of the WA powder, would result in the formation of more inclusions in the WA sample during printing.

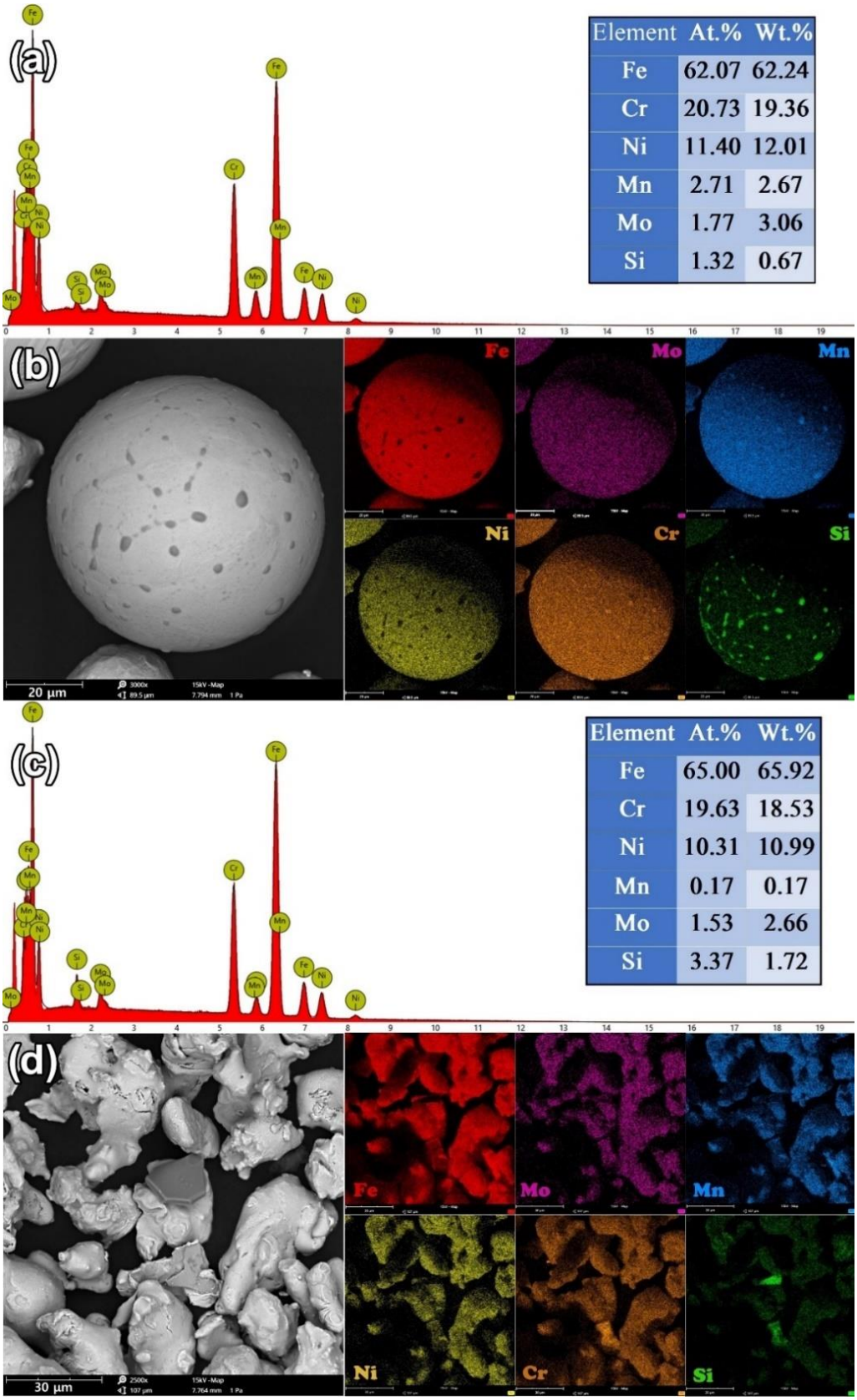

Fig. 32. EDS and elemental distribution map analysis of GA (a, b) and WA (c, d) samples.

The EBSD analysis of the GA and WA particles is presented in Fig. 33. According to the orientation maps of Fig. 33(a) and Fig. 33(b), both types of particles have a polycrystal

structure while phase maps of the Fig. 33(c) and Fig. 33(d) imply the formation of a ferritic phase during water atomization of SS316L. It means some fully ferritic particles and some austenitic-ferritic (partially ferritic) particles were formed due to faster solidification in water media. According to the elemental distribution map of Fig. 33(e), ferritic particles had a higher fraction of Fe and lower amounts of Ni, Cr, and Mo. These particles are identified as δ-ferrite, formed during the molten steel's rapid solidification [143].

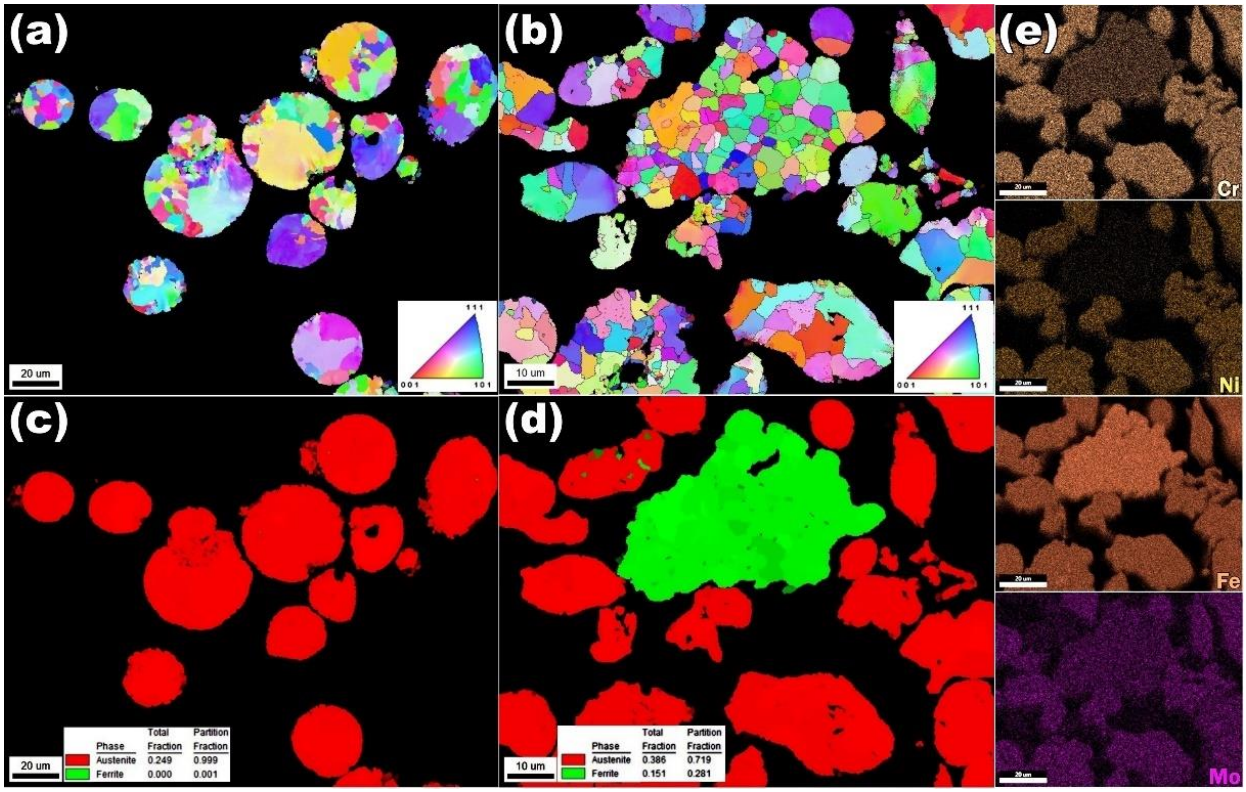

Fig. 33. EBSD orientation maps (a, b) and the corresponding phase maps (c, d) of GA and WA powders and elemental distribution map of the WA powder (e).

3.2.2.2. Microstructural characterization

Microstructure and lattice parameters of the LPBF fabricated samples by GA and WA powders has been compared together using different analysis methods. The acquired are presented in the following.

3.2.2.3. XRD

Fig. 34(a) and Fig. 34(b) show the XRD patterns of the GA and WA powders, and the as-printed samples, respectively. Fig. 34(a) properly shows that in both the GA and WA powders, there is a peak of δ-ferrite with BCC structure at $2\theta = 44°$. However, this peak is rather sharper

for WA powder compared with GA powder. It shows that some ferritic particles will indeed form in both atomization media, though with a higher fraction in WA as could be also seen in the EBSD maps (Fig. 33(c) and Fig. 33(d)). Fig. 34(b) reveals that, after printing the samples, the peak of δ-ferrite could not be found, which could be attributed to either the complete dissolution of ferritic particles or the formation of a low volume of ultrafine ferritic phases that the XRD could not detect.

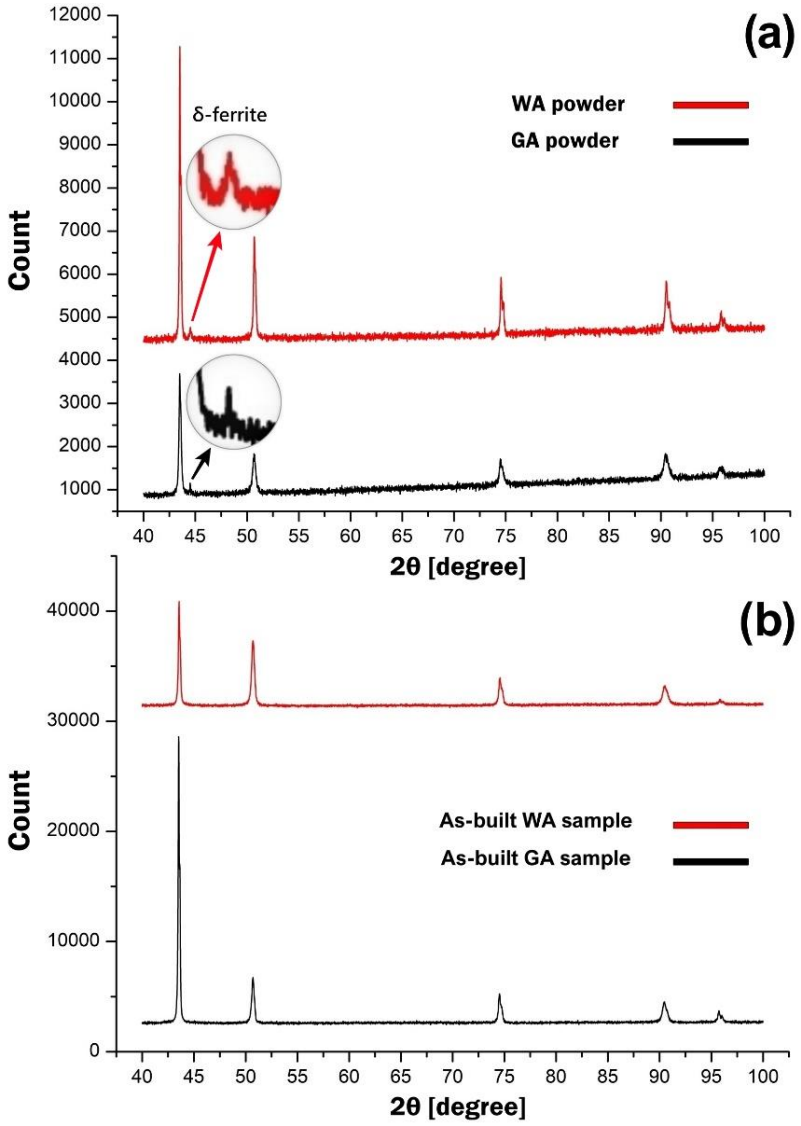

Fig. 34. XRD patterns of the GA and WA powders (a) and 3D printed samples (b).

The lattice parameters of the GA and WA powders and as-printed samples are presented in Table 1. As shown, not only in the powder state but also after printing the samples the lattice constant of the austenite phase in the WA specimen was lower than the GA counterpart. Also, WA samples exhibited a smaller crystallite size and a higher dislocation density compared with

the GA sample in the as-printed state. A similar difference was established in the lattice parameters of δ-ferrite in the WA and GA powders.

Table 1. Lattice parameters of the GA and WA powders and as-printed samples

XRD output	Phase	GA powder	WA powder	GA sample	WA sample
Lattice constant	ϒ-austenite	3.5992	3.5975	3.5986	3.5976
	δ-ferrite	2.8129	2.8772	-	-
Crystallite size	ϒ-austenite	351	626	474	408
	δ-ferrite	2209	378	-	-
Dislocation density	ϒ-austenite	1.52E+13	3.14E+12	5.68E+12	7.53E+12
	δ-ferrite	2.05E+11	7.00E+12	-	-

3.2.2.4. LECO test

The amounts of oxygen, nitrogen, and hydrogen (ONH) in the as-printed samples by GA and WA samples have been measured and the results are presented in Table 2. Since the atmosphere of the printing chamber for GA and WA samples was similar (argon), the difference in ONH can be attributed to the atomization media. Accordingly, GA has a higher N value because of atomization in nitrogen inert gas, while WA powder has higher O and H values due to the atomization in water. It has repeatedly been proven in the literature that atomization in the nitrogen atmosphere directly affects the chemical composition by stabilizing the austenite phase [27, 144]. Albeit, a high nitrogen content could cause problems such as solidification cracking [145]. On the other side, a higher oxygen content can negatively affect the processing by disrupting layer adhesion, i.e., via splitting the continuous laser track into multiple molten segments and spreading more inclusions [140].

Table 2. The results of the LECO test

Material	Oxygen (%)	Nitrogen (%)	Hydrogen (ppm)
GA sample	0.0736 ± 0.0066	0.0633 ± 0.0012	39.6 ± 10
WA sample	0.185 ± 0.011	0.0222 ± 0.0005	95.4± 6.9

3.2.2.5. Microscopy investigation

Fig. 35(a) and Fig. 35(b) show the OM micrographs of the as-printed samples with GA and WA powders, respectively. It is well depicted that the GA sample consists of a grain structure with a fish-scale pattern, while the WA sample is composed of columnar grains along the BD. The smaller particle size of the WA compared to GA powder besides the higher laser absorption of WA powder has created better bonding between deposited layers, which is in accordance with the reported results by previous researchers [146]. Indeed, higher laser heat input would provide the condition for a deeper penetration of the laser beam, partial remelting of the last deposited layer and stronger orientation of the grains along the BD with nucleation on the epitaxially grown grains. Compared to the components made with gas-atomized, those printed with the water–atomized counterpart benefit from the superior surface finish, uniformity in deposition and stronger layer bonding [32]. The higher laser absorption of WA compared with the GA powder results in the creation of hotter melt pools with a faster solidification rate that in turn can promote a finer dendritic structure [147].

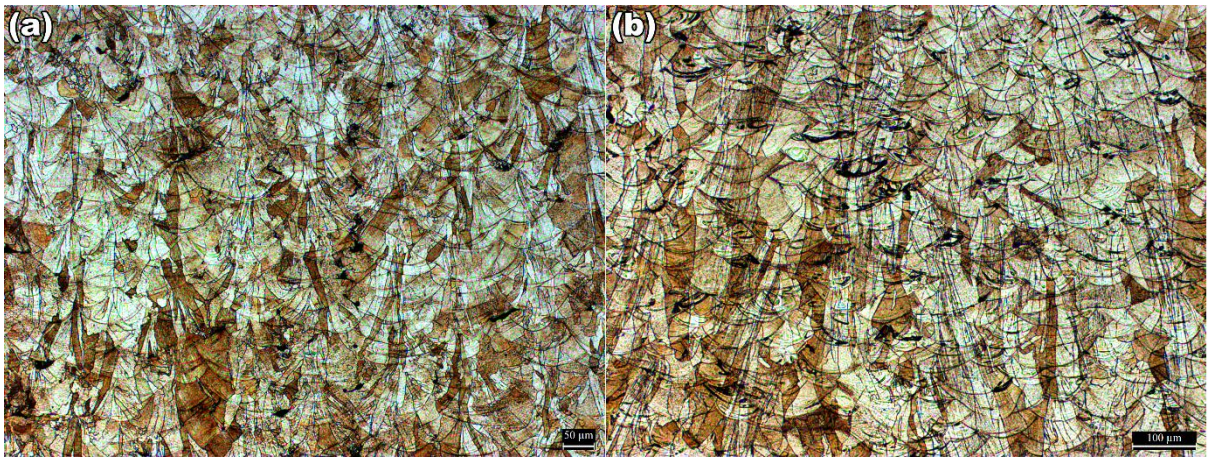

Fig. 35. 3D optical micrograph of GA (a) and WA (b) samples.

Fig. 36 shows the shows the 3D surface topology of the GA and WA samples. As can be seen, the WA sample exhibits lower fluctuations on the top surface. The values of the surface

roughness for WA sample were varied from 0 to 16.63 while for GA counterpart these values have changed between 0 to 46.21. Evidently, the WA specimen represented the lowest surface roughness which implies on smoother surface of the printed part.

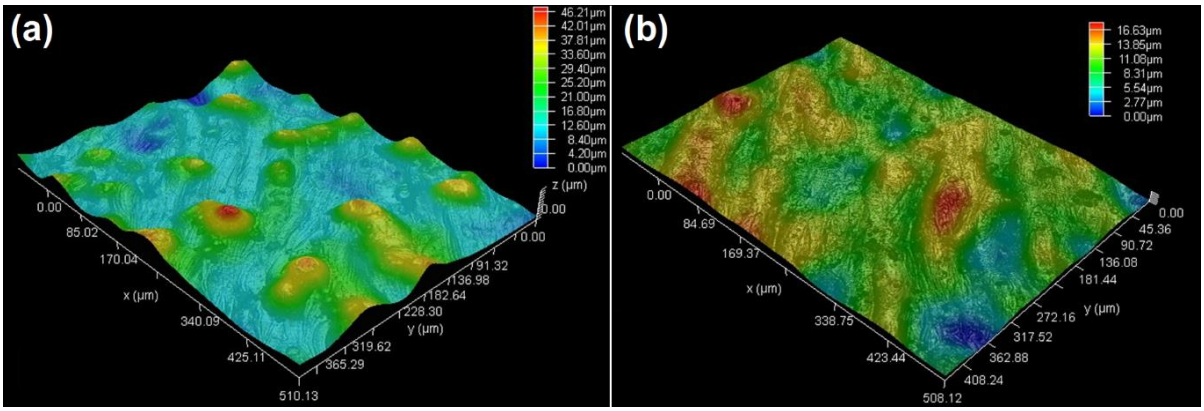

Fig. 36. Surface topography of GA (a) and WA (b) samples.

The EBSD maps in Fig. 37 properly shows the differences between the grain morphology of the GA and WA samples. Similar to the OM observations, the WA sample shows more elongated grains along the BD. Fig. 37(c, d) display the corresponding IQ maps along with histograms of grain misorientation wherein the solid red lines represent the low angle grain boundaries (LAGBs) with misorientation angle (θ) between 2 and 15° and the blue lines represent the high angle grain boundaries (HAGBs) with misorientation angle (θ) over 15°. The measurement of misorientation angle in AM fabricated samples points to the formation of a larger fraction of LAGBs ($2° \leq \theta \leq 15°$) in WA as opposed to more HAGBs ($15° < \theta$) in GA samples (as can be inferred from the misorientation angle histograms shown in Fig. 37(e, f)).

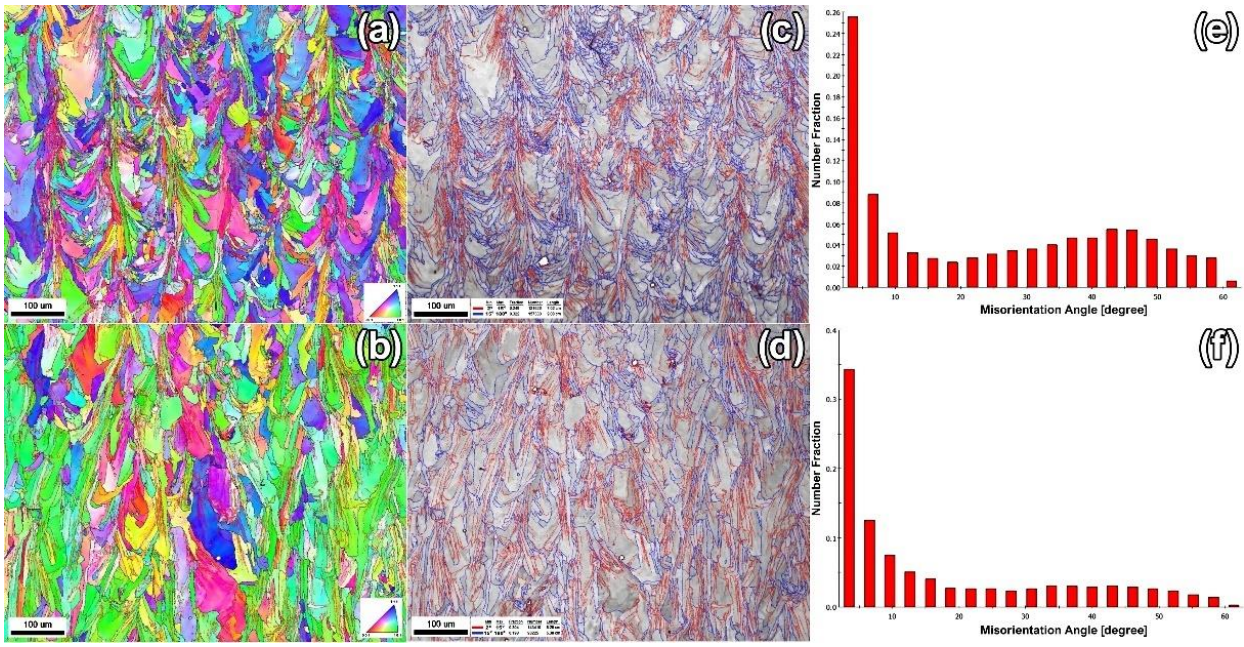

Fig. 37. EBSD orientation pattern, IQ map, and misorientation angle histogram of GA (a, c, e) and WA (b, d, f) samples.

The EBSD phase analysis of the GA and WA samples is exhibited in Fig. 38(a, b). As shown, the GA sample exhibits an almost fully austenitic structure. However, some ferritic zones are formed in the WA sample. The corresponding elemental distribution map of the WA sample (Fig. 38(c)) implies Fe enrichment of the ferritic zones. Obviously, multiple fine inclusions containing Si, Cr, and Mn have been formed in the WA sample. The high amount of residual oxygen in the water atomized powder led to its reaction with the Si, Mn, and Cr and form submicron oxides [56]. The formation of these particulates can directly affect the mechanical properties [148]. Kong et al. have illustrated that the formation of nano-twins around these inclusions in additively manufactured SS316L samples could improve the resistance against crack propagation [149]. However, their coarsening during annealing would have a reverse effect and degrade the mechanical properties [55].

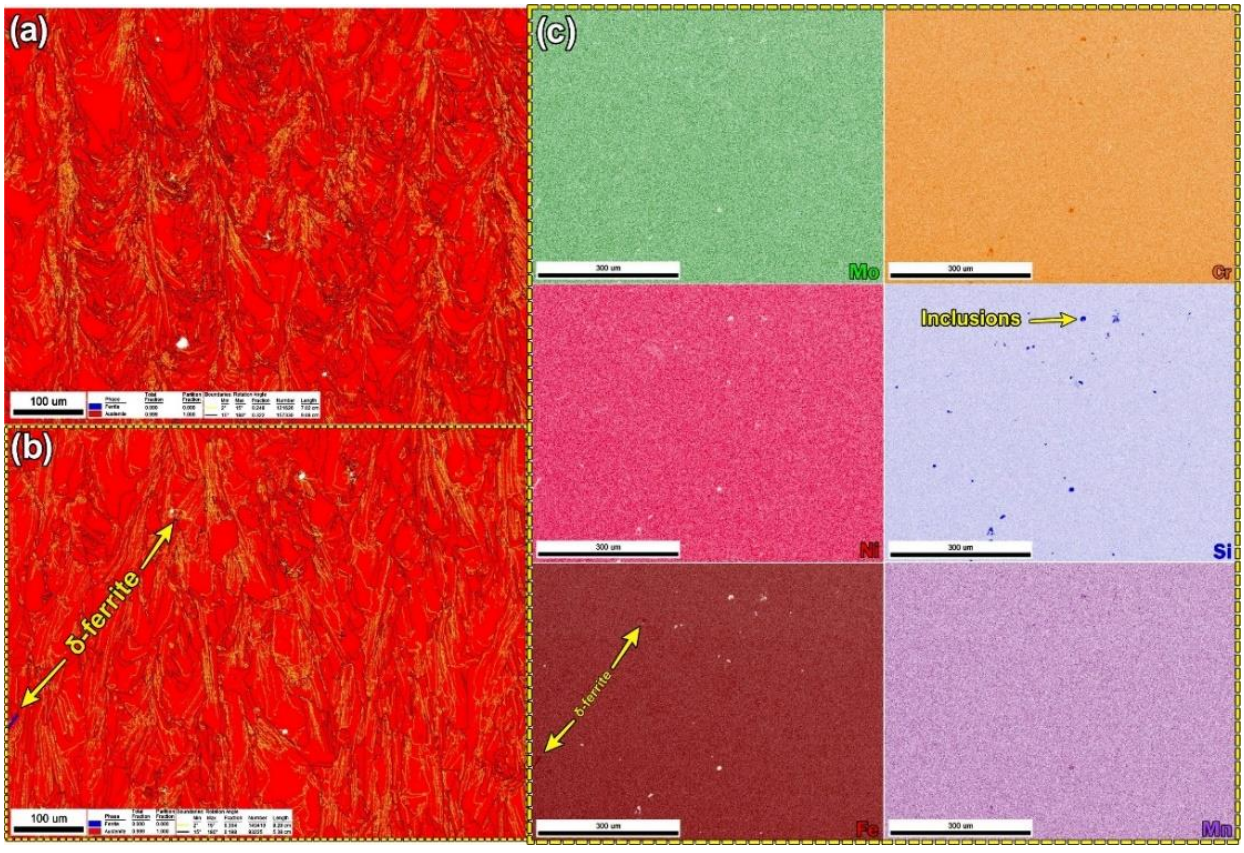

Fig. 38. Phase map of GA and WA samples (a, b), and elemental distribution map of WA sample (c).

The Kernel Average Misorientation (KAM) distribution maps are employed to compare the local orientation differences between GA and WA samples (Fig. 39(a, b)). As shown, the WA sample shows a rather higher KAM value than the GA specimen. It can be attributed to the generation of more dislocations due to the higher solidification rate of the WA sample.

During the AM process, remelting/reheating of the successive layers results in an inhomogeneous spreading of the dislocations by continuous re-orientation of the grain boundaries [133]. Since the KAM map represents the extent of the misorientation between a certain point (kernel) of grain with its surrounding points (typically below 5°), the higher KAM value implies higher dislocation motion and localized plastic deformation [150]. The strain accumulation occurs predominantly near the grain boundaries and often the grains interiors, particularly in the GA sample, are stress-free [151]. The stress localization around the GBs forced the adjacent grains to increase their misorientation and to maintain the continuity between the grains; thereby, more geometrically necessary dislocations (GNDs) will form around the GBs [152]. The GNDs can be calculated according to the strain gradient theory with the following equation:

$$\rho GND = \frac{2\theta}{\mu b} \tag{1}$$

where ρ_{GND} is the GND density at the point of analysis, θ represents the local misorientation angle, μ is the unit length of the point ($\mu = 2x$, where x is the step size used when taking the EBSD images), and b is the Burger's vector [153]. Furthermore, the formation of more inclusions enriched with Si, Cr, and Mn in WA samples, in turn, contributes to the promotion of GNDs being generated around their interface with the austenitic matrix. The proliferation of dislocations is correlated with the misorientation distribution in grains and analyzing the grain orientation spread (GOS) aids in quantifying this misorientation [154]. The grain orientation spread (GOS) pattern shows the average deviation in orientation of each pixel of grain from the average orientation of that grain [155] and is representative of the residual stress in a single grain. Hence, greater distortion in a grain result in higher GOS while approaching the recrystallized state appears with a lower GOS value. The GOS map of the GA and WA samples is presented in Fig. 39(c) and Fig. 38(d), respectively. As shown, faster solidification led to greater residual stress and higher GOS value in the WA sample [156]. The high concentration of this residual stress on GBs responded by activation of slip systems around the interface and generation of more GNDs [157]. Also, the GA sample has a higher fraction of fine recrystallized grains, as can be inferred from Fig. 39(c,d) and Fig. 39(e,f), which mostly are formed at the hatching and melt pool boundaries, where laser tracks had an overlap. So, remelting of the previously printed layers facilitated the recrystallization of the new grains. However, the recrystallization can be distinguished through the combined analysis of GOS and grain size [158]. Ergo, comparing the grain size distribution of the GA and WA samples (Fig.

39(e, f)), a narrower distribution and the smaller average size of the grains in GA can be observed compared with the WA sample, i.e., implying a more recrystallized structure.

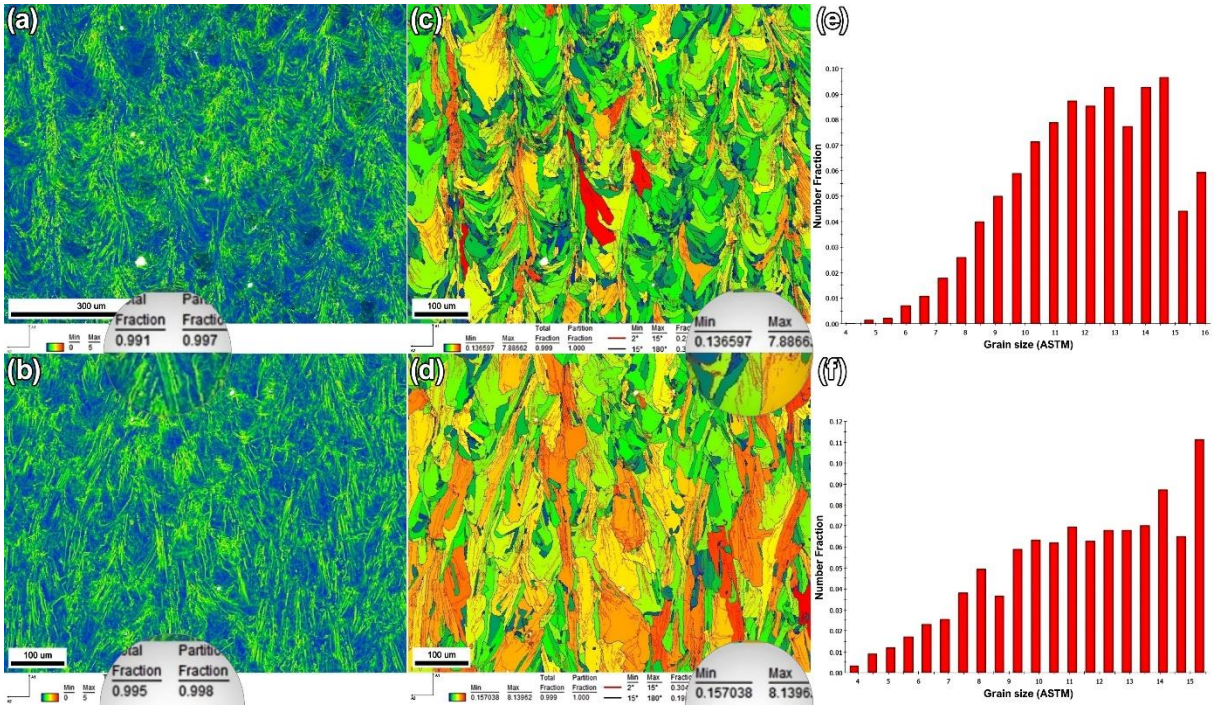

Fig. 39. KAM (a, b), GOS (c, d), and grain size distribution (e, f) in GA and WA samples.

The pole figures (PFs) and inverse pole figures (IPFs) of Fig. 40(a, b) shows that the formation of aligned columnar austenitic grains vertically oriented along the BD has created a strong crystallographic texture in the <001> direction. The higher texture index of the PF and IPF implies the stronger orientation of the grains and more anisotropic properties in the WA sample. The PF and IPF are planar stereographic illustrations of spatial structural orientation. Hence, a detailed analysis of the orientation distribution in 3D space can be explored by the orientation distribution function (ODF) maps. Fig. 40(c) and Fig. 40(d) display the ODF map of texture in GA and WA samples, respectively. Tracing the crystal orientation in different Euler angles (φ_1, φ_2, Φ) through rotation of the φ_2 angle from 0 to 90° validated the stronger texturing in the WA sample and lower anisotropy in the GA sample.

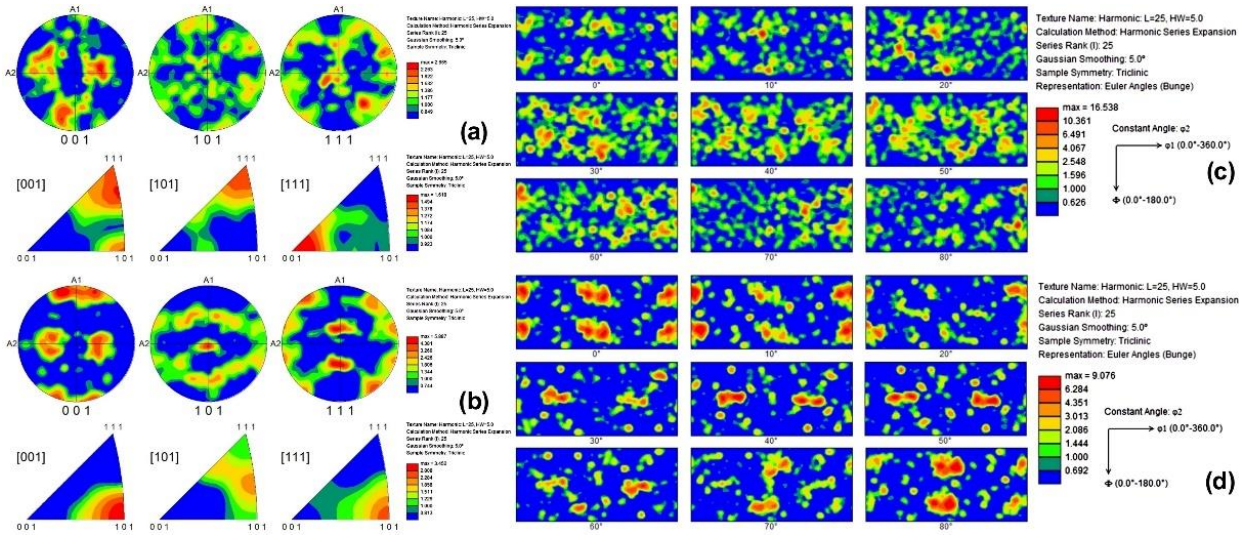

Fig. 40. Pole figures (PF) and inverse pole figures (IPF) of GA and WA samples (a, b), and correlated orientation distribution function (ODF) at Euler angle Φ2=0-90 (c, d).

SEM micrographs of Fig. 41(a, b) show that due to rapid solidification during AM, a noticeable amount of residual δ-ferrite has formed on the cellular structure of both the GA (Fig. 41(a)) and WA (Fig. 41(b)) samples. Likewise, lower average particle size of the powder and more penetration depth of the laser beam in the WA sample have created more cohesive bonding at the melt pool boundaries (Fig. 41(c, d)). A comparison of the cell size in WA and GA samples (Fig. 41(e, f)) manifested more delicate and rather smaller cells in the WA sample. It can be attributed to the higher under-cooling and solidification rate of the WA compared to the GA sample. A similar observation has already been reported for fabricated samples with both the LPBF and electron beam melting (EBM) additive manufacturing methods. Therein, it is demonstrated that a lower solidification rate due to pre- and post-sintering of the deposited layers by EBM resulted in a coarser cellular structure with thicker cell walls [159]. Formation of finer cells means a larger density of cell walls which in essence are sub-grain boundaries, consisting of twisted dislocations. This result is in accordance with the XRD and EBSD outputs that showed a higher dislocation density and GNDs in the WA sample, respectively.

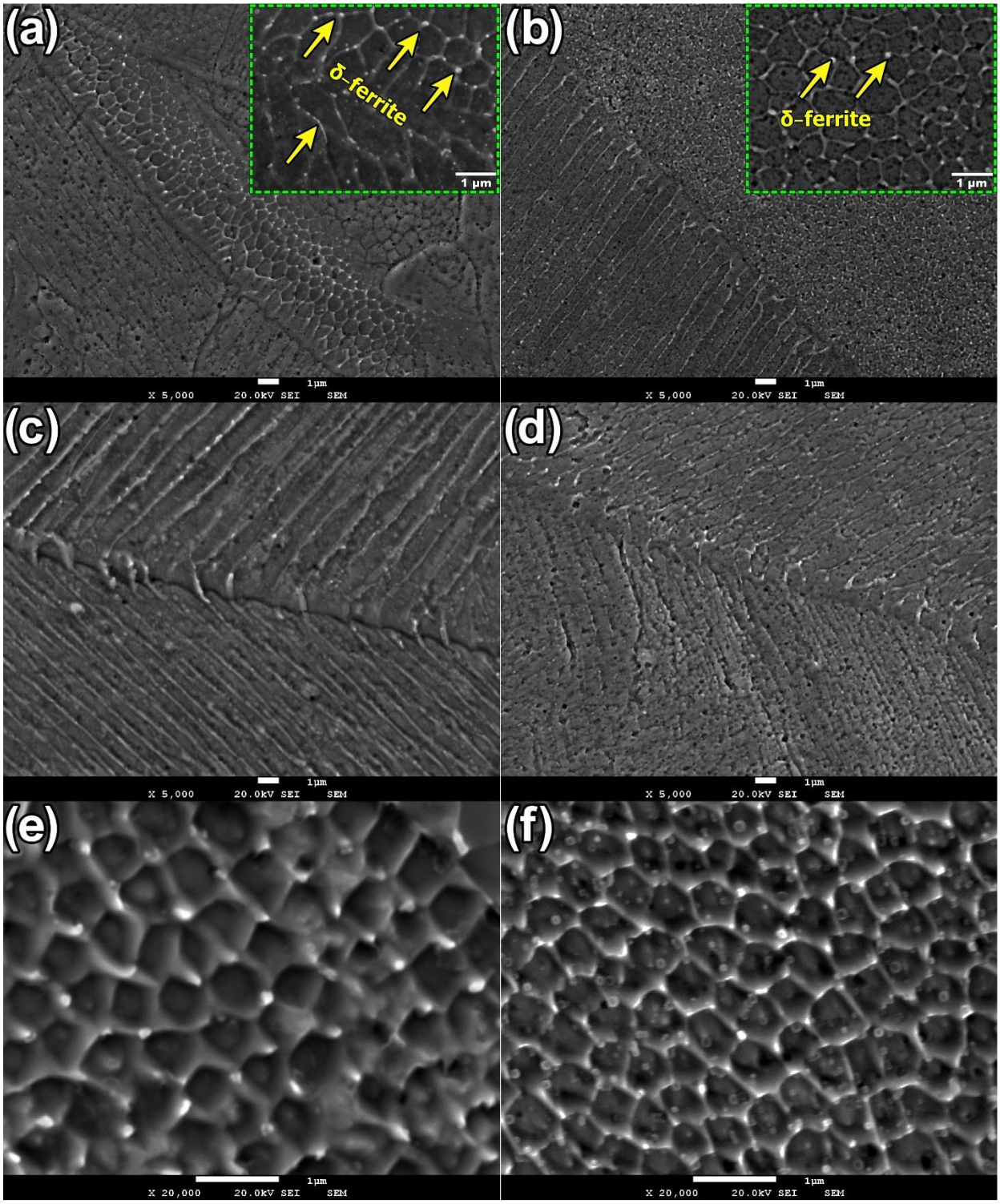

Fig. 41. SEM micrographs of GA (a, c and e), and WA (b, d, and f) samples.

3.2.2.6. Mechanical properties

Mechanical properties of the WA and GA samples have been evaluated, and the results are presented in Fig. 42. Stress-strain curves of Fig. 42(a) clearly show the superior tensile strength of the WA sample. The extracted data from the stress-strain curves are presented in Fig. 42(b). As reported, the WA sample has shown higher ultimate tensile strength (728 MPa vs 602 MPa), yield strength (580 MPa vs 503 MPa), toughness (215 J/m^3 vs 145 J/m^3), and elongation (31.8% vs 25.2%) compared with GA sample. It has been reported in the literature that for coarse particles, the processability and circulation in the molten pool of GA track were more suitable, while in the smaller size range of the powders, WA feedstocks give a better performance [160]. The work hardening rate micrographs of Fig. 42(c) points to easy glide of dislocations at stage I of deformation. The main difference between WA and GA samples is in transition stage II, where hardening attenuated with a lower rate in the WA sample. The behavior of the material in the second stage is the result of a trade-off between hardening and softening phenomena including partial glide of dislocations, generation of the new GNDs, and annihilation of dislocations through dynamic recovery. In between, the formation of the dislocation tangles could hinder the movement of free dislocations and limit the nucleation of new dislocations. So, the formation of the stress field around these dislocation clogs plays a pinning effect that eventually increases the tensile strength of the material [161]. The higher work hardening rate of the WA compared to the GA sample can be attributed to the faster annihilation of dislocations and dynamic recovery in the WA sample. As depicted in Fig. 42(d), the GA sample shows a more uniform distribution as well as a rather higher average microhardness compared to the WA sample (237 vs. 229, respectively). The more fluctuation of the hardness values in the WA sample can be ascribed to the higher percentage of defects and inclusions as hard brittle phases [41]. The SEM images of Fig. 42(e) and Fig. 42(f) display the fracture surface of GA and WA samples, respectively. As can be seen, the average size of dimples in the WA sample was lower than GA, which is in accordance with the higher strength and finer cellular structure in the WA sample.

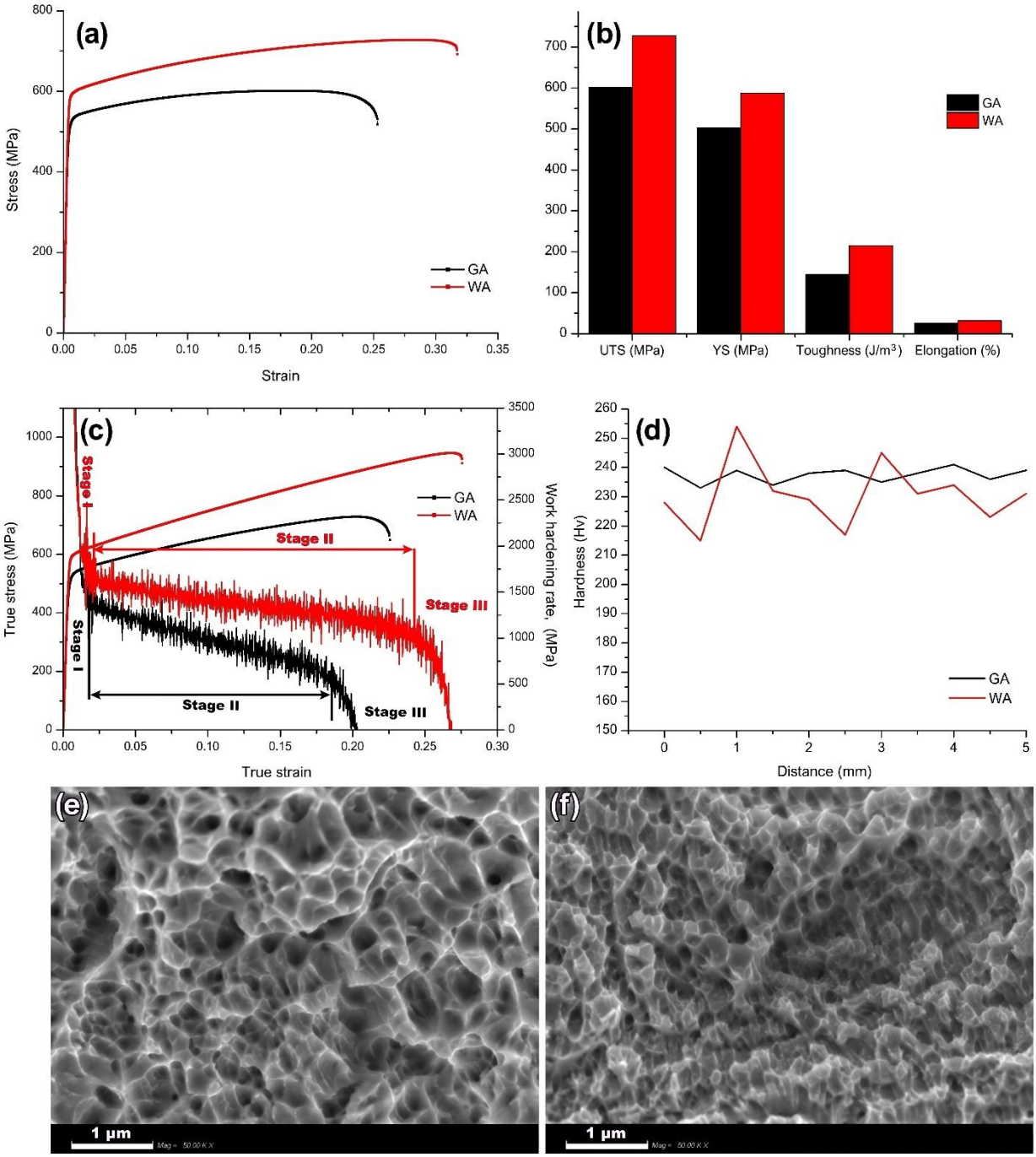

Fig. 42. Engineering stress-strain curves (a) and extracted data from the engineering stress-strain curves (b), true stress-true strain curves and variation of work hardening rate (c), Vickers microhardness (d), and fracture surface of GA (e), and WA (f) samples.

3.2.2.7. Corrosion

The electrochemical behavior of the samples was investigated using CPP and EIS measurements. The CPP curves of the GA and WA samples are presented in Fig. 43. At the beginning, both specimens showed similar values for OCP. Likewise, the cathodic branches of the curves were marginally different for the GA and WA samples. Basically, in the cathodic branch, oxygen reduction occurs on the electrode surface and the kinetics is determined by the oxygen diffusion rate from the solution. However, in the anodic part of the curve different behaviors were observed. The GA samples exhibit higher current density values in the anodic part, which also reflects on the corrosion current density ($i_{corr.}$) computed through the Tafel interpolation.

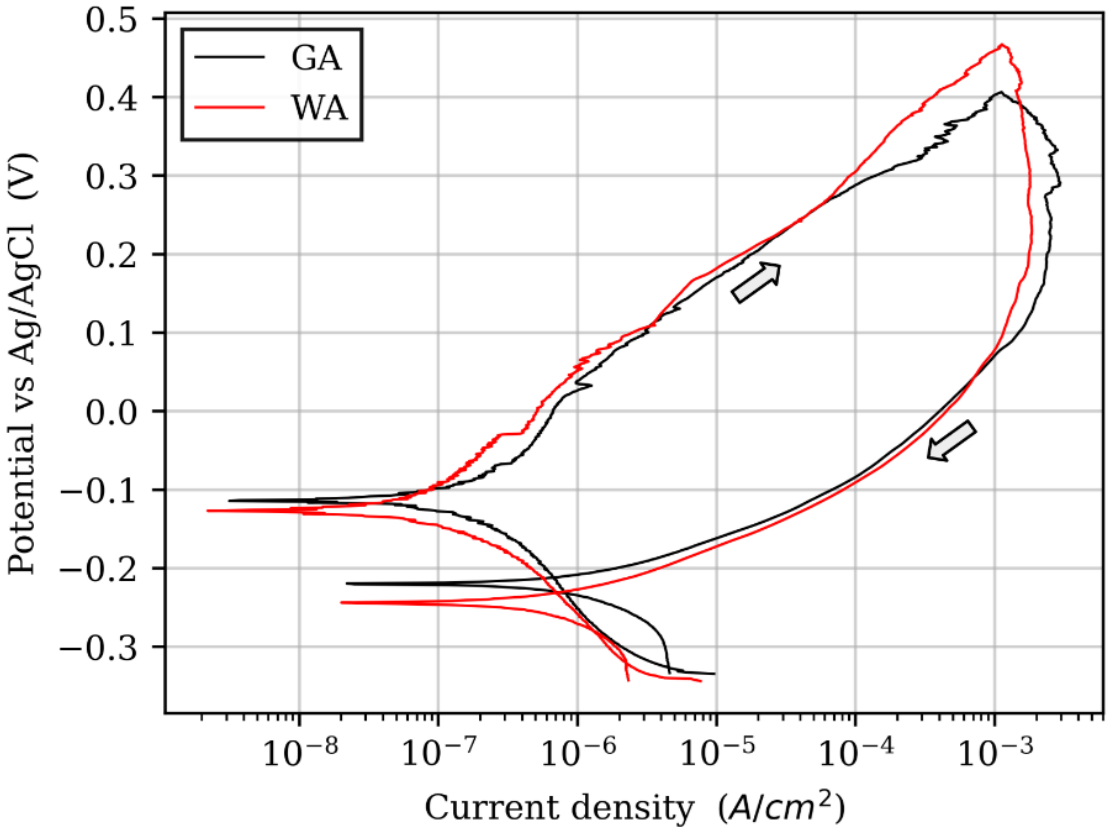

Fig. 43. Cyclic potentiodynamic polarization (CPP) curves of the GA and WA samples acquired in 3.5 wt% NaCl solution. Scan direction is indicated by arrows.

As reported in Table 3, $I_{corr.}$, which changes proportionally to the corrosion rate, was three times higher for the GA sample. The higher corrosion potential ($E_{corr.}$) of the GA sample reflects the OCP values, implying a slightly nobler behavior of the GA sample.

Table 3. Comparison of the most important parameters derived from CPP measurements for the GA and WA samples.

	OCP (mV vs Ag/AgCl)	E corr. (mV vs Ag/AgCl)	I corr. (A/cm^2)	E pass. (mV vs Ag/AgCl)
GA	-113.3 ± 20.6	-114.8 ± 6.4	$13.8 \cdot 10^{-8} \pm 7.98 \cdot 10^{-8}$	-242.0 ± 18.7
WA	-138.3 ± 24.0	-134.3 ± 29.6	$4.63 \cdot 10^{-8} \pm 2.64 \cdot 10^{-8}$	-249.0 ± 11.5

In the anodic branch of the curve, both samples exhibited an active behavior that appeared as increasing current density along higher applied potentials. Moreover, current peaks in the anodic branch can be attributed to metastable pitting. The lack of a passive region made it difficult to identify the pitting potential, which is generally an important parameter to describe the behavior of stainless steel. After reaching the cycle vertex at a current density of 1 mA/cm^2, the scan has been reversed. Therein, the current density values remained high in a wide range of potential that points to the formation of stable pitting. Re-passivation occurs at applied potentials below the corrosion potential (about -242.0 mV for the GA sample and at -249.0 mV for the WA one).

EIS measurements corroborated the electrochemical behavior observed with CPP curves. As can be seen in Fig. 44, the superficial oxide layer is slightly more protective against the chloride solution for the WA sample. From a graphical interpretation of Bode diagrams, this can be recognized by looking at the maximum value in the phase that reaches higher values for WA samples. Moreover, the impedance modulus at low frequency is higher for the WA sample, showing better protective efficiency and a lower corrosion rate than the WA sample.

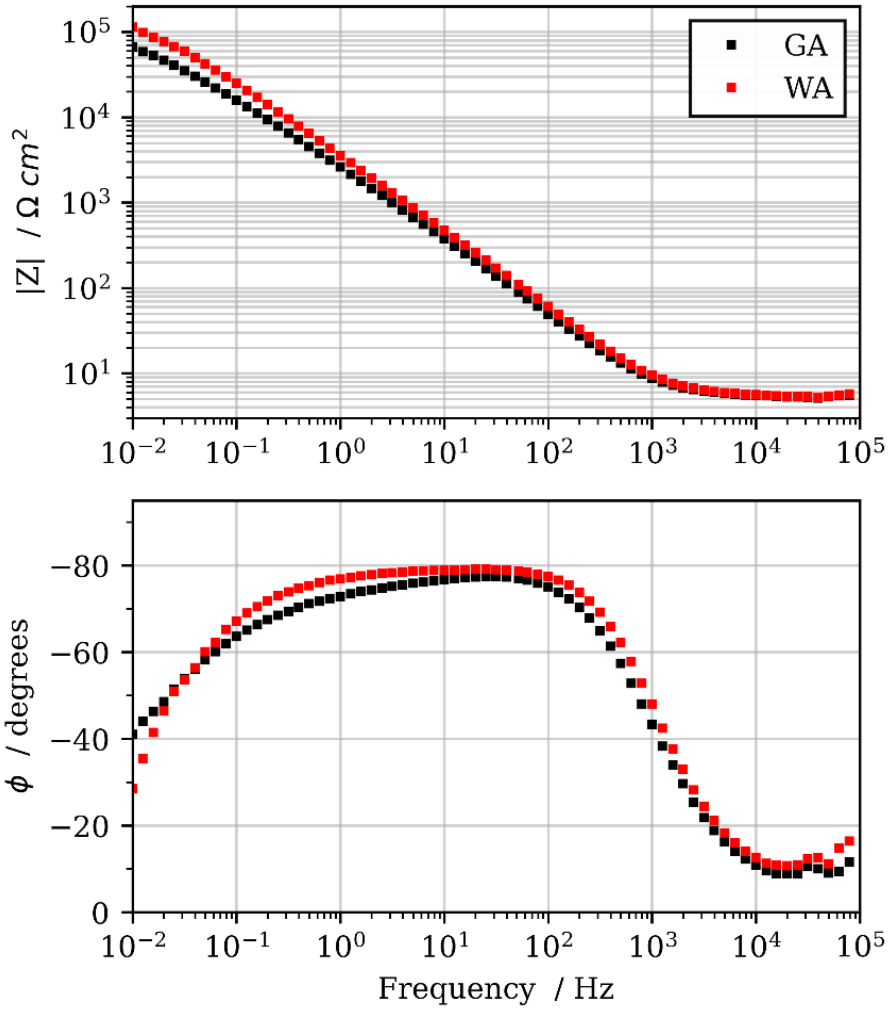

Fig. 44. Two representative EIS spectra reported as Bode diagrams were acquired on the GA and WA samples in 3.5 wt.% NaCl solution.

These considerations were further confirmed by the modeling of the EIS spectra by means of equivalent electrical circuits (EEC). The used circuit shown in Fig. 45 comprises the solution resistance (R_s), the resistance to charge transfer (R_{ct}), and the capacitance of the double layer (CPE_{dl}).

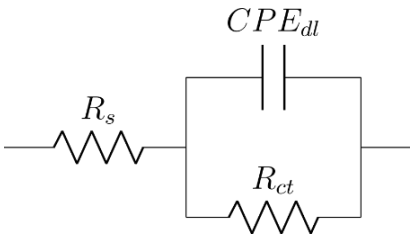

Fig. 45. Equivalent Electrical Circuit (EEC) used to model the impedance spectra.

This last parameter was modeled using a Constant Phase Element (CPE) to consider time constant dispersion on the electrode surface [162]. The value for solution resistance is taken from the high-frequency impedance where the phase is close to 0° and, as expected, it is

constant for both samples. Minor but statistically significant differences were observed in the values of R_{ct}, which is proportional to the corrosion rate, and CPE_{dl}, which models the non-faradaic processes associated with double-layer capacitance (Table. 4). Indeed, in the WA sample, higher values for both parameters were computed by means of EEC fitting. This confirms the superior corrosion resistance of the WA sample. For both samples, the CPE parameter (n) has values close to unity, indicating a behavior close to the pure capacitor for this circuit element.

Table 4. Comparison of the EEC elements values for the GA and WA samples.

	R_s ($\Omega \cdot cm^2$)	R_{ct} ($\Omega \cdot cm^2$)	CPE_{dl} ($s^n/(\Omega \cdot cm^2)$)	n
GA	5.5 ± 0.2	$1.24 \cdot 10^5 \pm 0.78 \cdot 10^5$	$8.5 \cdot 10^{-5} \pm 8.0 \cdot 10^{-6}$	0.86 ± 0.01
WA	5.5 ± 0.2	$1.15 \cdot 10^5 \pm 0.16 \cdot 10^5$	$6.23 \cdot 10^{-5} \pm 1.2 \cdot 10^{-5}$	0.88 ± 0.01

SEM images of Fig. 46 show the surface of the GA and WA samples after the potentiodynamic polarization test. As can be seen, the GA sample exhibited a higher vulnerability against aggressive ions in the corrosive media. Despite the greater number of inclusions in the WA sample, they are strongly bonded to the austenitic matrix and did not result in more pitting cavities. Higher corrosion resistance could be also attributed to smoother surface of the WA sample. Often samples with lower roughness act as better barrier to penetration of the aggressive electrolyte to the metal substrate. This is mainly due to the fact that the stable passive layers which usually forms on the surface significantly reduces further mass loss. Obviously, the more surface damages and local breakdown of the protective oxide layer and oxidation of the substrate metal in the anodic zones result in the local pit formation.

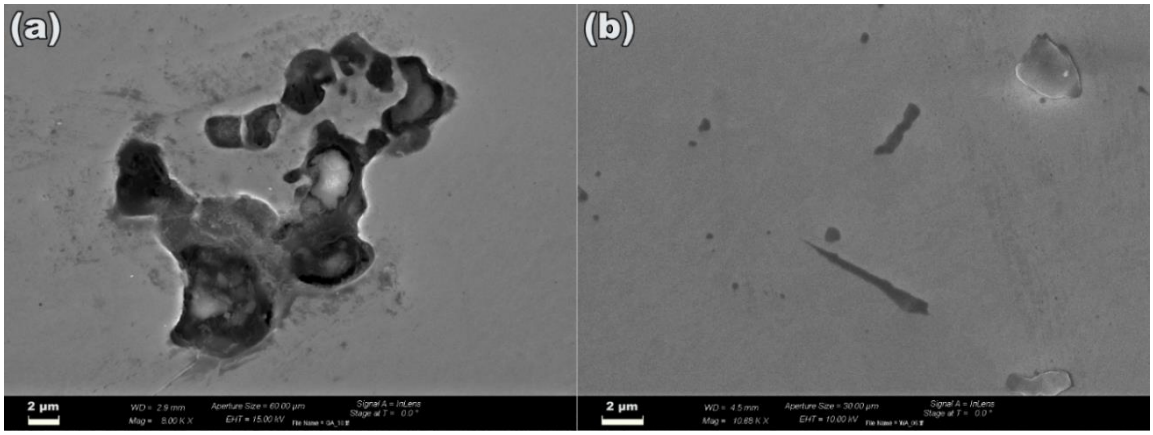

Fig. 46. SEM images from the surface of the GA (a) and WA (b) samples after the CPP test.

Effect of Co-addition of Ti and Mn

Mohammad Reza Jandaghi*, Hesam Pouraliakbar, Sang Hun Shim, Vahid Fallah, Sun Ig Hong, Matteo Pavese, " In-situ alloying of stainless steel 316L by co-inoculation of Ti and Mn using LPBF additive manufacturing: Microstructural evolution and mechanical properties", **Materials Science and Engineering: A**, September 2022.

Abstract

Recently, Ti has been introduced as a grain refinement agent in additively manufactured steels. Also, the outstanding formability of high-Mn TWIP/TRIP steels owing to low stacking fault energy has been proved. In the current work, Ti and Mn were inoculated simultaneously to the stainless steel 316L by LPBF in-situ alloying. Added elements locally formed complexes of brittle phases that improved strength at the expense of elongation. Microstructural observations revealed intermetallic masses comprised FeTi (*bcc*), σ, and C14 laves phase (*hcp*) surrounded by ferritic grains. The ultrafast solidification of the molten tracks induces significant thermal stress, which was followed by the generation of geometrically necessary dislocations (GNDs) at the interface of austenite and ferritic grains. The lattice response in the intermetallic zone was activation of synchroshear mechanism in the C14 laves phase and heat-dependent slip systems in FeTi and generation of twin-like structures and dislocation forest within them, respectively.

3.2.3. Experimental method

Commercial gas atomized SS316L powder with particle size distribution ranging from 15 to 50 μm was blended with 1 wt.% Ti and 2 wt.% Mn and used as feedstock material. The elemental distribution map of the feedstock is presented in Fig. 47.

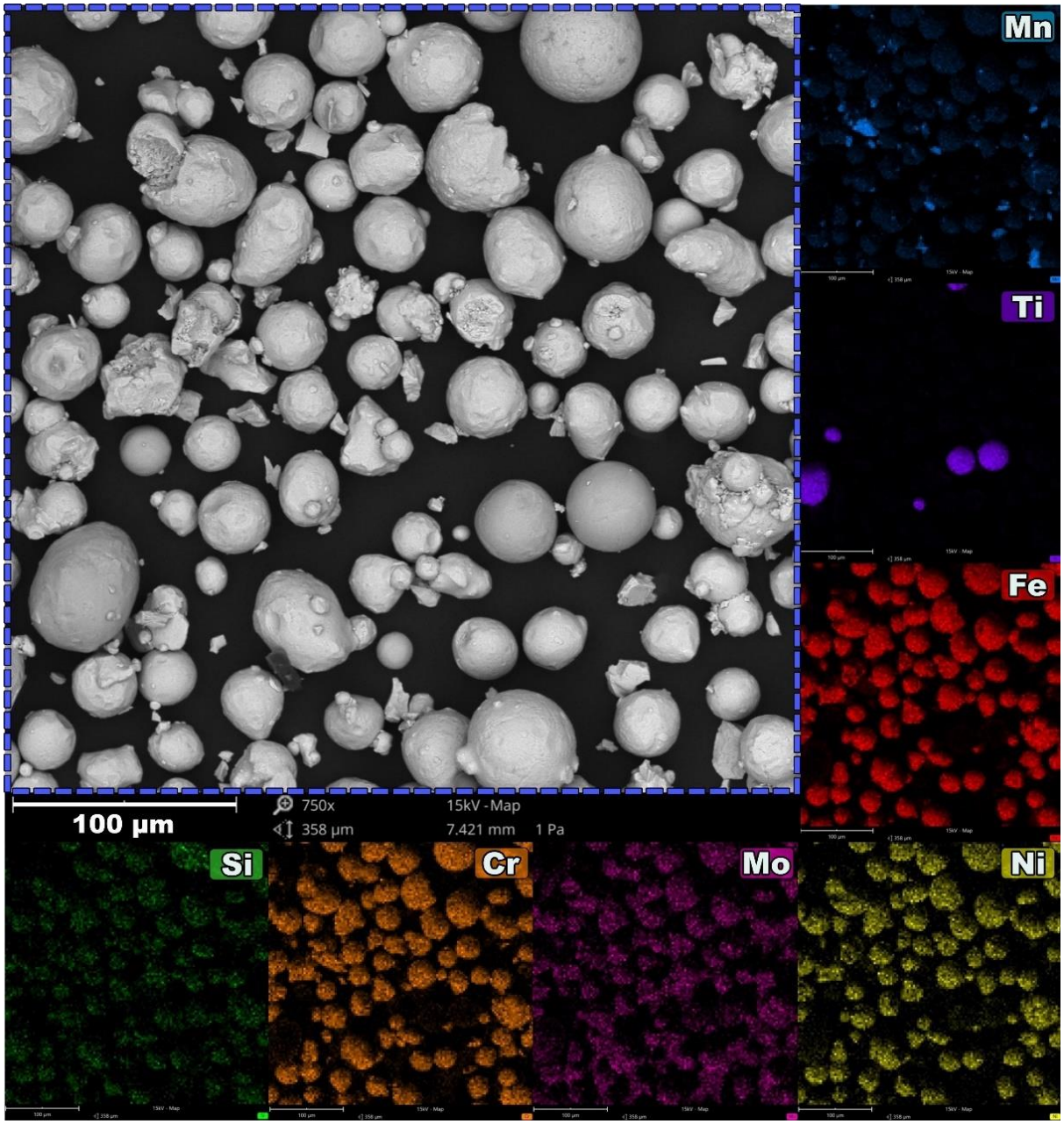

Fig. 47. Elemental distribution map of the particles used as the feedstock.

A Sharebot METALONE Laser with a spot size of 40 µm was employed to print the specimens under an argon atmosphere (O2<100 ppm) with the optimized process parameters of 90 W, 400 mm/s, 30 µm layer thickness, 70 µm hatch spacing, and 67° scan rotation between layers (i.e., the set of parameters that obtained the highest relative density). Samples were printed with two geometries: cubic samples with a dimension of 10×10×10 mm^3 for microstructural investigation and tensile samples with a gauge dimension of 32×6×4 mm^3. To reveal the grains, mirror polished specimens were etched by a solution composed of HCl, HNO_3, and acetic acid with volume ratio of 15:10:1.

3.2.4. Results and discussions

The OM, SEM, and EBSD micrographs of the as-built SS316L and reinforced sample are presented in Fig. 48. Samples were chemically etched for OM and SEM characterization. As shown, despite applying the optimized process parameters, the guest elements have not uniformly distributed inside the austenitic matrix. OM (Fig. 48(a, f)) and EBSD color patterns (Fig. 48(b, g)) show a bimodal structure in the reinforced sample, including ultrafine grains around the staked phases and coarse columnar grains at regions far from the created phases signalizing the epitaxial growth. According to the SEM micrographs of Fig. 48(c) and Fig. 48(h), these undesired phases are mostly formed at the melt pool borders as well as vast areas in some melt pools. The formation of these phases has limited the typical cellular structure of additively manufactured SS316L. Likewise, the intensive vulnerability of these phases at corrosive media of etching (white districts in SEM) arises from a difference in their chemical composition with the substrate. An analysis of the phase map revealed that alloying elements localized in the austenitic matrix have resulted in the formation of some *bcc* and *hcp* phases compared to conventional SS316L (Fig. 48(d, i)). The partial refinement of the grains besides the formation of some phases that have hindered the epitaxial growth of the columnar grains could attenuate the typical texturing along the buildup direction of additively manufactured SS316L alloy (Fig. 48(e, j)).

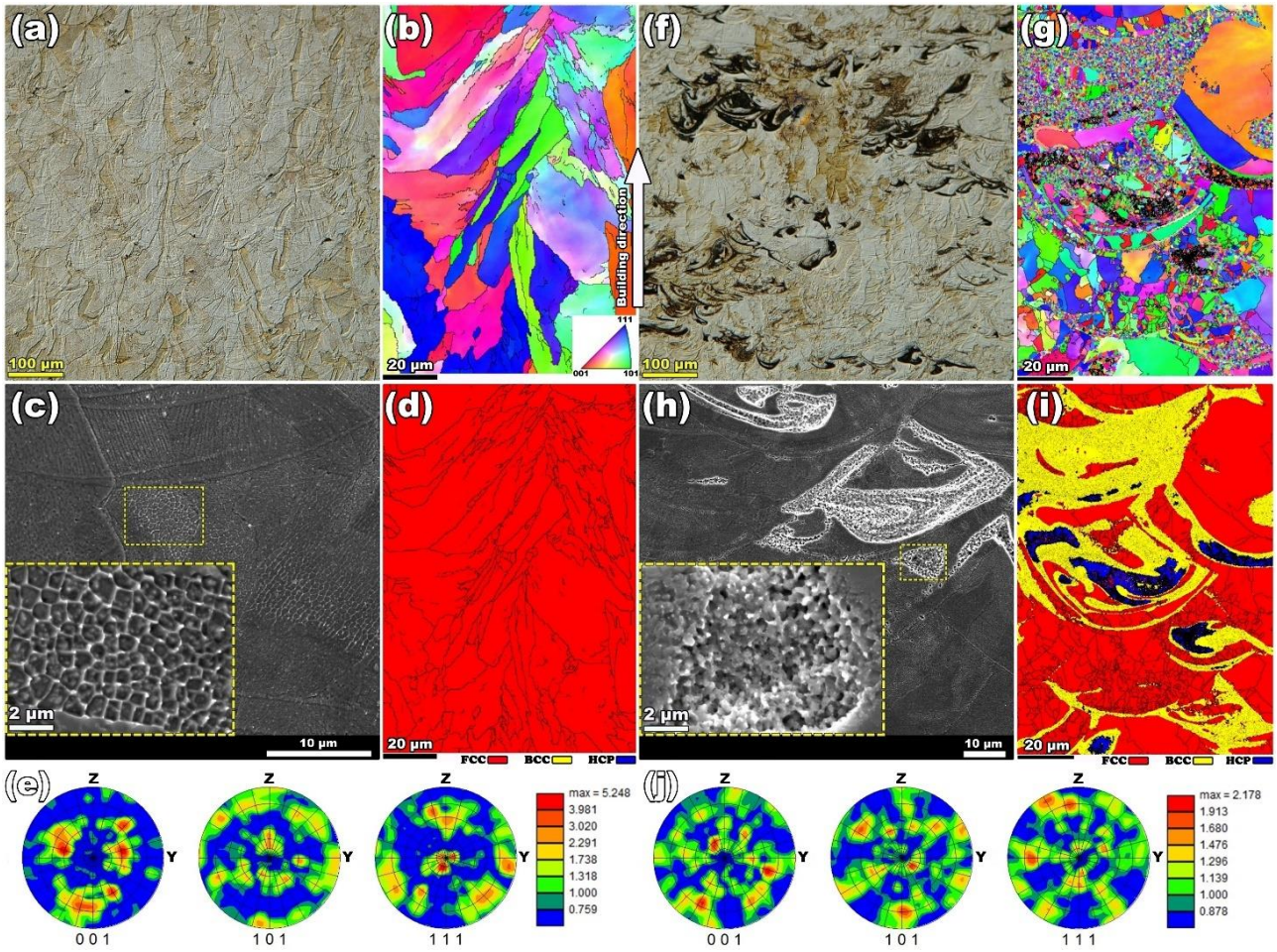

Fig. 48. OM micrographs, EBSD IPFs, SEM images, phase maps, and PFs of (a-e) unreinforced and (f-j) reinforced AMed SS316L alloys.

Fig. 49 displays the typical stress-strain curve and the corresponding fracture surface of the LPBF manufactured SS316L and reinforced specimen through in-situ alloying with Ti and Mn addition. Although the yield strength (σ_y) and ultimate strength (σ_{UTS}) of reinforced alloy were higher, the formation of fragile phases significantly degraded the elongation (ε_f) and resulted in brittle failure of the reinforced alloy. It appeared as ruptured areas on the fracture surface of the reinforced sample whereas the dimpled fracture surface of the customary counterpart. Fig. 50 presents the effect of in-situ alloying with Ti and Mn on the true stress-strain curves and work-hardening rate of the SS316L alloy. The reinforced alloy had a lower slip in the first stage of work hardening. In the second stage, brittle phases that could hinder the dislocation's motion have limited the plastic deformation. As a result, the applied stress overcame the strain field induced by accumulated dislocations around the brittle phases and caused the failure (stage III). According to the microhardness variation profile of Fig. 50 and corresponding OM micrographs of the examined points, the reinforced sample showed local

hardness values about two times higher than nominal values for SS316L alloy when passing the indenter on brittle phases.

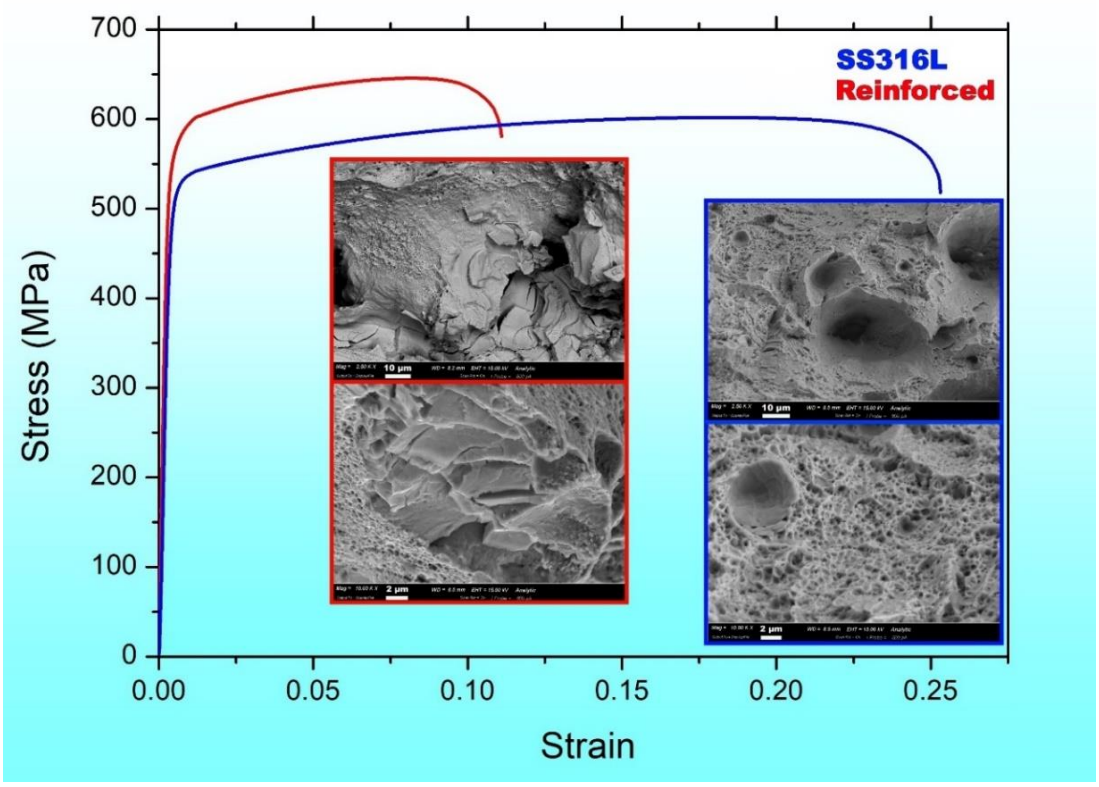

Fig. 49. Engineering stress-strain curves and corresponding fracture surfaces

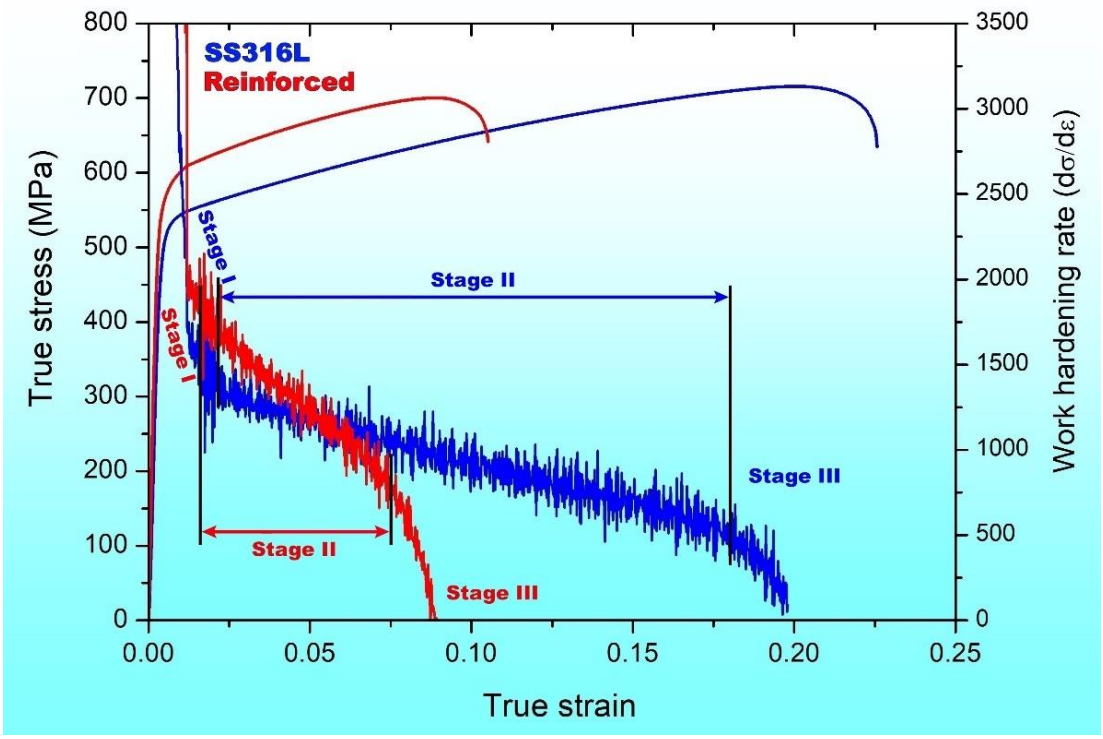

Fig. 50. true stress-strain and work-hardening rate

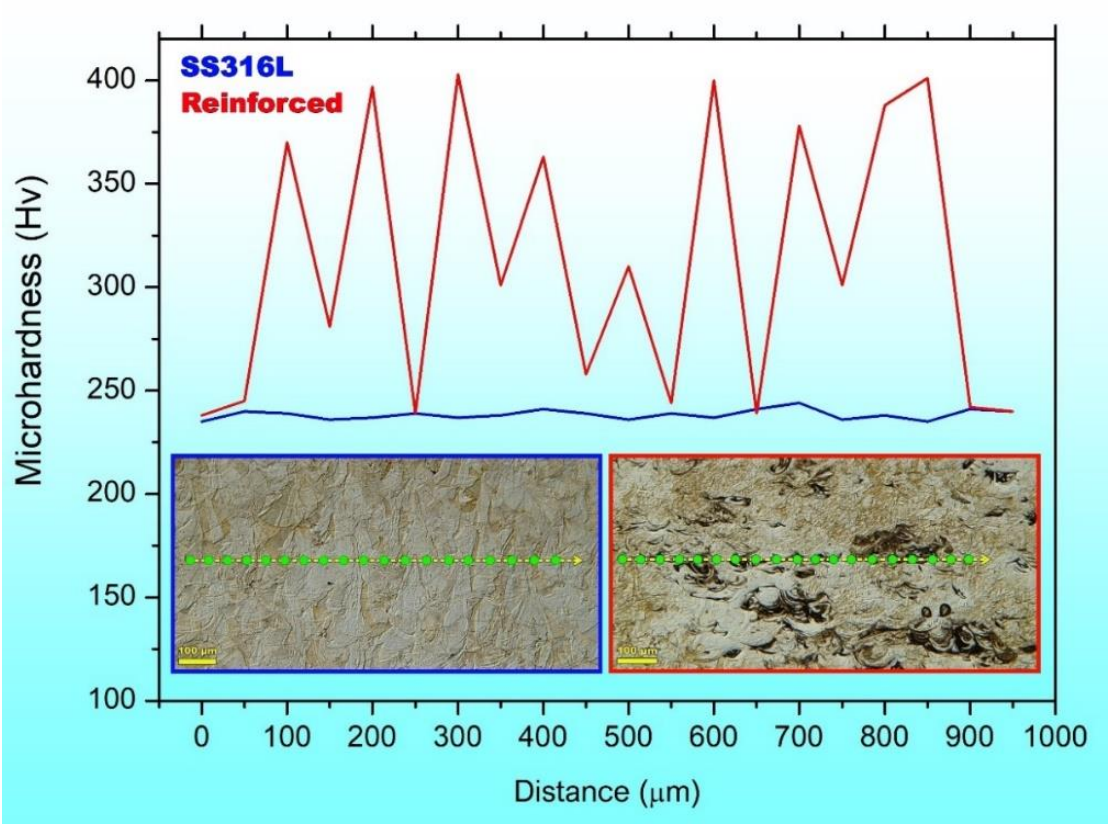

Fig. 51. microhardness profile of SS316L and reinforced alloy with Ti and Mn addition.

STEM image of Fig. 52(a) is provided from the border of a melt pool enriched of accumulated phases. According to the elemental distribution map of Fig. 52(b) and the TEM image of Fig. 52(c) and its corresponding SAED patterns, despite addition of 1 wt.% of Ti, its aggregation has locally changed the proportion of Ti/Fe to higher values. As a result, FeTi (that according to the Fe-Ti phase diagram must form at 50 wt.% Ti) has been formed at the center of the stacked phases with a superlattice *bcc* structure [163]. XRD patterns of Fig. 52(d) validated the existence of these *bcc* phases in the reinforced sample. SAED patterns proved that the FeTi pieces are surrounded by C14 laves phases with *hcp* structure and lower Ti and higher Cr and Mn contents. Since Ti is a ferrite stabilizer element, a ferritic interlayer with *bcc* structure is formed between the intermetallic phases and austenitic substrate with *fcc* structure. The ferritic grains have higher Cr and lower Ni and Ti values compared to the adjacent C14 laves phase. Rapid solidification of the deposited layers leaves remarkable residual stress which in the austenitic zone has been responded by the generation of remarkable geometrically necessary dislocations (GNDs) at the interface of austenitic and ferritic grains (Fig. 52(c)). The strain gradient between the hard intermetallic zone and austenitic matrix led to GNDs pill up at the intermediate soft area [164]. Likewise, the EDS map of Ni distribution indicates some Ni-rich branches in FeTi and Laves phase.

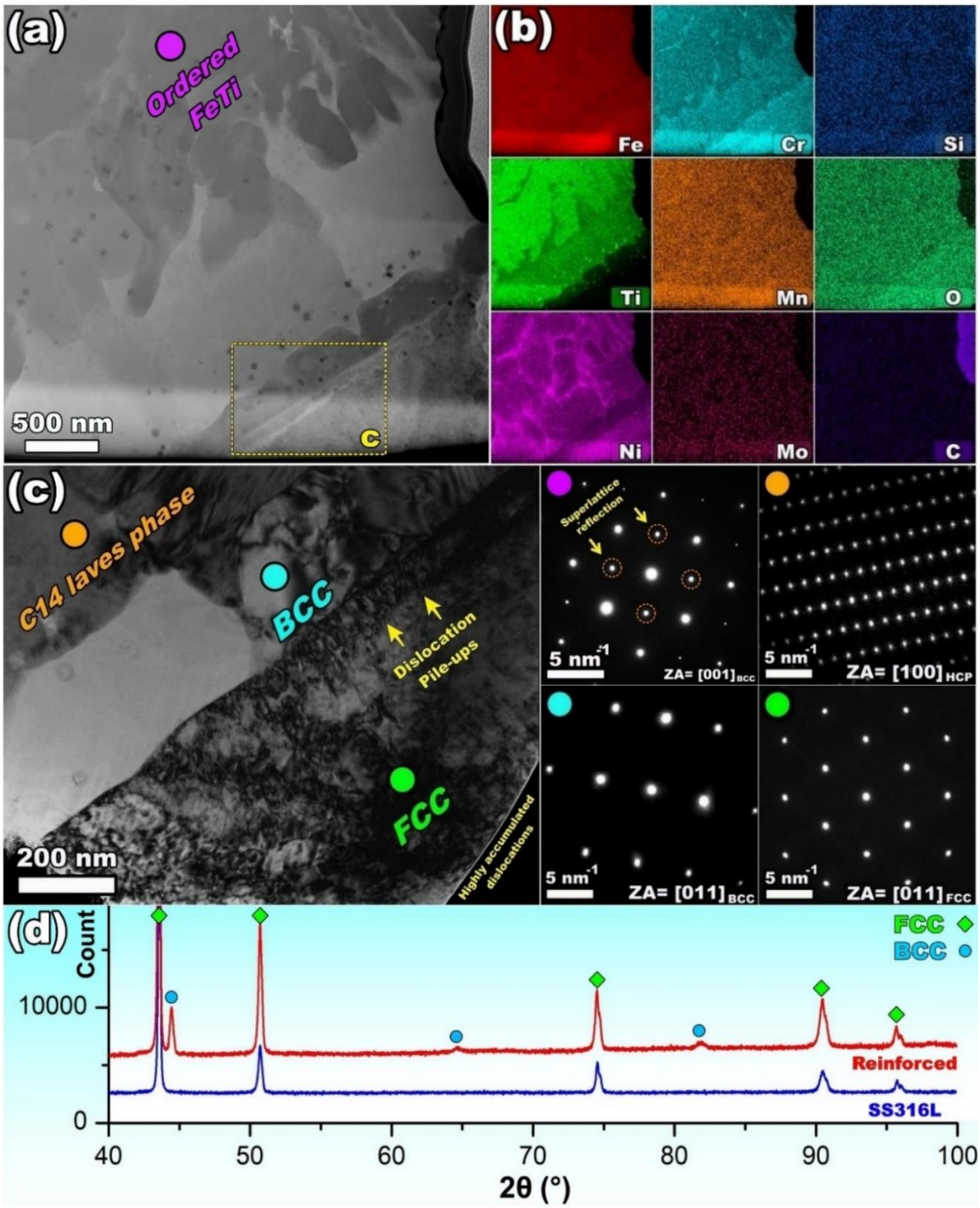

Fig. 52. (a) STEM image obtained from the interface of stacked phases and austenitic matrix, (b) corresponding EDS elemental maps, (c) TEM image and SAED patterns of different regions of the reinforced sample, and (d) recorded XRD patterns for the AMed SS316L alloys.

According to the line-scan and EDS map analysis of Fig. 53(a), these regions were enriched from Cr, Ni, and Mn. Comparing the SAED pattern of Fig. 53(c) with the lattice parameters of the σ phase in the literature (Table 5), shows a high similarity between the detected phase and reported lattice constants for the σ phase. Lee et al. [165] have also examined the Mn variation in austenitic steels on precipitation behavior of the σ phase and found that Mn replaces Mo in the σ phase. Also, it has been proven that the addition of ferrite stabilizer elements like Cr, Mo, and Ti immediately leads to the formation of the σ phase [166]. So, Mn addition not only could not improve the formability but also played an inverse role by reacting with Cr and Ni and creation of the destructive σ phase. According to Fig. 52 and Fig. 53, some TiO nanoparticles were also formed inside the *bcc*, Laves and FeTi phases. These particles have been introduced as the main refinement factor in Ti reinforced steels [167].

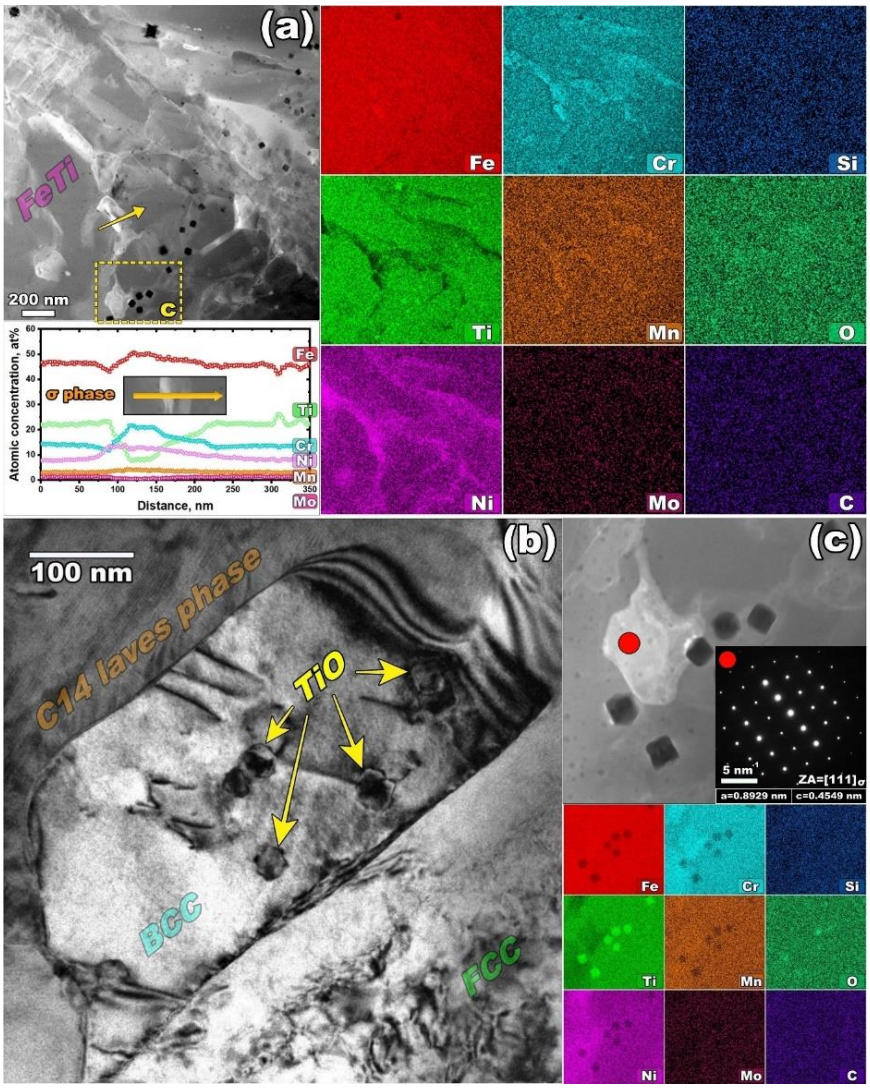

Fig. 53. (a) STEM image, EDS line scans, and corresponding EDS maps acquired from the branched matrix, (b) TEM image and corresponding EDS maps along with SAED pattern exhibiting the formation of the TiO nanoparticles and σ phase, (c) TEM image illustrating the magnified view of TiO nanoparticles embedded in a ferrite grain and (d).

Table 5. collected lattice parameters of σ phase from the literature [166].

Alloy	Lattice parameters of the σ phase (Å)
Fe-Cr	a = 8.799, c = 4.544
Fe-Mo	a = 9.188, c = 4.812
Steel 316	a = 8.28~8.38, c = 4.597~4.599
Steel 316L	a = 9.21, c = 4.78
20Cr-25-34Ni-6.5-8Mo	a = 8.87, c = 4.61

Although TiO nanoparticles have not preferentially settled at the grain boundaries to pin them. As depicted in Fig. 53(b) they will act as an obstacle against dislocations motion and in turn will enhance the tensile strength of the reinforced alloy. The Cr-containing silicates are the most prevalent oxides in SS316L alloy. These inclusions are a constituent part of the feedstock particles and often dissociate and reform during additive manufacturing of stainless steel [138]. Compared to the titanium oxides, the formation enthalpy of the silicates is substantially lower [168]. So, from a thermodynamic standpoint, silicon oxides are more likely to form, and the constitution of TiO nanoparticles may result from the higher kinetic of Ti reaction with oxygen.

Fig. 54(a) depicts an overview of microstructural evolution from the boundary toward the center of a melt pool including complex regions formed due to Ti and Mn accumulation. As can be seen in the top-right corner, the FeTi phase and adjacent Laves phase have no distinguishable boundaries. Also, comparing Fig. 54(b) and the obtained chemical compositions (given in Table 6), illuminate that the Laves phases formed between the ferrite grains and FeTi phase exhibit two distinct morphologies and compositions. The Laves phase closer to the melt pool center contains higher Ti and lower Cr contents than the one beside the ferrite grains. This phase appears to have responded to thermal stresses during rapid solidification of the melt pool by activating the synchroshear mechanism, as can be inferred from Fig. 54(c, d). Owing to the low activation energy, synchroshear is the most prevalent mechanism for the basal slip in the Laves phase with *hcp* crystallography [169]. Indeed, the twin-like structures in Fig. 54(d) are formed by multiple synchroshears and acted as slip planes in the structure of the Laves phase under the applied thermal stresses. The magnitude of synchronous glide of partial dislocations on adjacent parallel atomic planes is equal to the length of Burgers vector [170]. As depicted in the SAED pattern of Fig. 52, FeTi has a superlattice *bcc* structure and the slip systems in *bcc* require sufficient heat to activate. During solidification, the synergetic effect of activation of slip systems in FeTi and the decreased SFE by Mn addition (which facilitates the dissociation of dislocations), generated numerous

statistically stored dislocations (SSDs). It could be inferred that the absence of interface microcracks in the presence of brittle phases (i.e., intermetallic) denotes higher interface cohesion which can be in direct correlation with the feasibility of dislocations dissociation by Mn addition. Hence, the stacked phases in the center of the melt pools are recognizable from their morphology, i.e., the regions with highly accumulated dislocations contain the FeTi phase, whereas the smooth phases containing twin-like structures represent the Laves phase. Compared to SSDs, GNDs are more effective in the improvement of work hardening and mechanical strength of the alloys [171]. It has been revealed that having the same dislocation density, the yield stress and work hardening of the high-GND steels will be much higher than high-SSD ones due to the higher heterogeneous deformation-induced strengthening. However, the role of GNDs is more highlighted in the early stage of work hardening, where the plastic strain is small, but SSDs dominate in the later stages where the strain is significant [162].

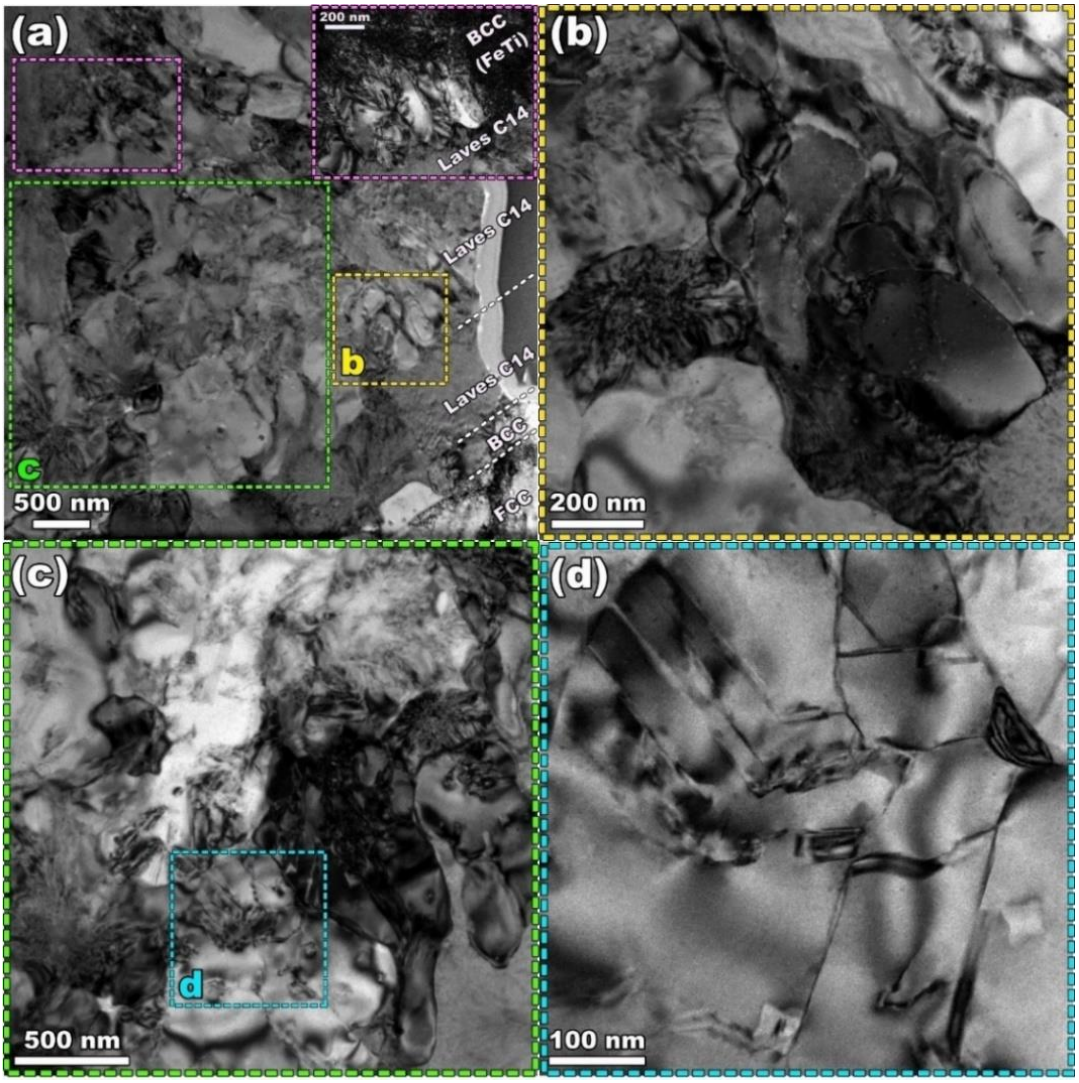

Fig. 54. TEM images of (a) various phases formed inside a melt-pool, (b) Laves phase, (c, d) the synchroshear phenomenon within the Laves phase

Table 6. EDS point analysis acquired from different phases.

Element	FCC, (at%) Austenite	BCC, (at%) Ferrite	Laves C14, (at%) $Fe_2(Ti,Cr)$	Laves C14, (at%) Fe_2Ti	BCC, (at%) FeTi
Si	0.74	0.67	0.79	0.73	0.28
Ti	0.24	3.93	16.76	23.7	50.7
Cr	19.54	21.95	15.72	13.97	4.84
Mn	3.6	3.06	3.12	2.8	1.39
Fe	62.15	60.31	50.84	48.74	31.89
Ni	12.23	8.35	11.24	8.69	10.37
Mo	1.52	1.74	1.53	1.36	0.52

3.2.5. Conclusions

In summary, to exploit the refinement impact of Ti and reduce stacking fault energy by Mn, Ti and Mn were inoculated simultaneously to the stainless steel 316L by LPBF in-situ alloying. Nonuniform distribution of the additives created complex intermetallic phases that led to higher mechanical strength and brittle failure of reinforced alloy. In-depth analysis revealed that stacked phases consist of FeTi (*bcc*) and C14 laves phase (*hcp*) are surrounded by ferritic grains. Rapid solidification leaves remarkable thermal stress that was responded by the generation of GNDs at the interface of austenite/ferrite and activation of synchroshear mechanism and heat-dependent slip systems at C14 laves phase and FeTi, respectively.

Chapter 4

Development of AlSi10Mg alloy

4.1. Addition of Ni to AlSi10Mg

Mohammad Reza Jandaghi*, Alberta Aversa, Diego Manfredi, Flaviana Calignano, Luca Lavagna, Matteo Pavese, "In situ alloying of AlSi10Mg-5 wt. % Ni through laser powder bed fusion", **Journal of Alloys and Compounds**, available online, 2 February 2022.

Abstract

In the current study, the effect of in-situ alloying of AlSi10Mg with 5 wt.% Ni (pseudoeutectic composition) through the LPBF additive manufacturing technique was investigated. Fabricated samples underwent supplementary annealing treatment at 300 °C for 15 and 120 min, eventually. During the thermal treatment, the fish-scale grains created after printing inside the melt pools after printing vanished gradually. In the as-built sample, molten Ni particles settled as big chunks of Al_3Ni in the center and a thin strip of tiny Ni-rich masses in the borders of the melt pools. FIB/SEM and AFM images revealed that after 15 min annealing, silicon cellular dendrites fragment into fine Si particles, and during annealing for 120 min, the aluminum matrix expels out the supersaturated solute silicon atoms. Consequently, Si atoms leave the substrate and diffuse to pre-existing Si particles in cell walls and the triple junctions. Such a collective diffusion of Si atoms leads to the formation of coarse Si particles widespread in the Al matrix. Based on the XRD outputs, annealing for 15 min had not any major effect on Ni-rich phases. However, after 120 min, a more brittle intermetallic shell of a Ni-rich phase formed on pre-exist coarse phases. The comparison of the mechanical properties of the Ni-reinforced AlSi10Mg alloy with those reinforced via the addition of other elements/compounds revealed that in a size range close to AlSi10Mg particles, Ni could not be an appropriate candidate for in-situ alloying through the LPBF method. Furthermore, spheroidization of the silicon particles and formation of fragile Ni-rich intermetallic shells

having weak interfacial bonding to the Al matrix during the long-term annealing results in a significant reduction in mechanical strength of the specimens.

4.1.1. Experimental procedures

4.1.1.1. Materials

To prepare the feedstock materials a gas atomized AlSi10Mg powder (supplied by EOS GmbH) sieved under 45 µm was mixed with 5 wt. % atomized Ni powder (supplied by Sigma Aldrich Co.) with a size range below 20 µm. The size distribution histogram of the mixed powder is presented in Fig. 55. The size of the Ni powder was chosen fine enough to facilitate their complete melting and ensure the homogeneity of the chemical composition all over the sample. However, due to the significant difference between the melting point of Ni (1455 °C) and AlSi10Mg (near 570 °C), optimization of the building parameters would be very critical. Likewise, this proportion was chosen close to the eutectic point to reduce the solidification cracking possibility. The chemical composition of the used powder determined by Energy Dispersive Spectroscopy (EDS) analysis is given in Table 7. The elemental distribution map analysis of the as-mixed AlSi10Mg/Ni powder, shown inFig. 56, adequately confirms that the Ni particles were distributed uniformly within the AlSi10Mg powder.

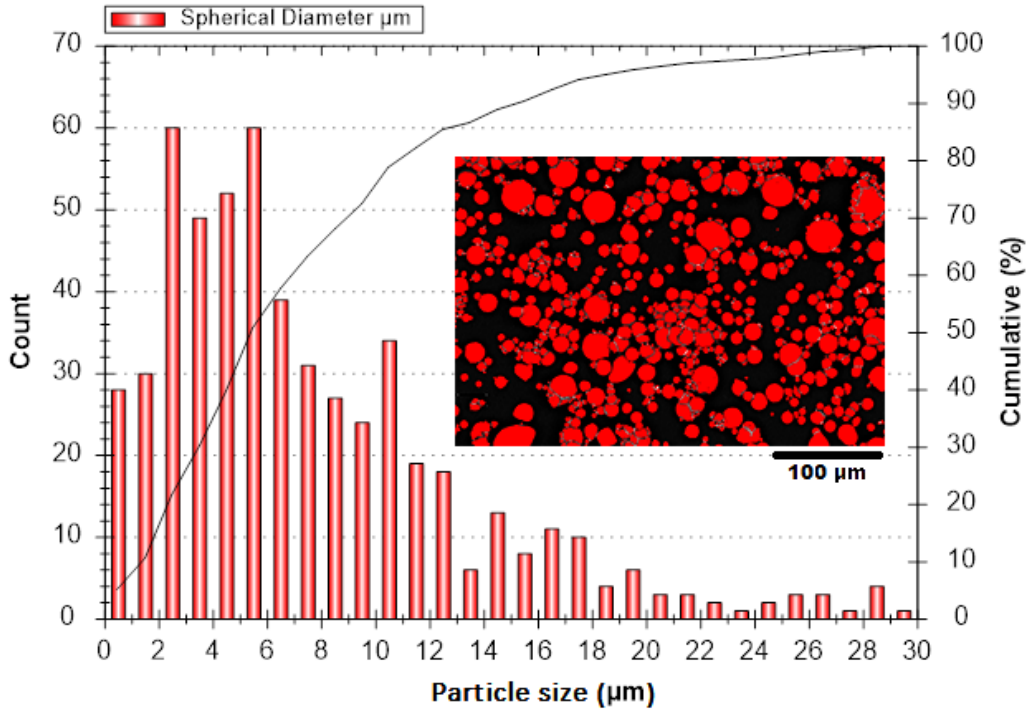

Fig. 55. The particle size distribution of the prepared AlSi10Mg+5%Ni powder.

Table 7. Chemical composition by EDS of the mixed powder

Element	Al	Si	Mg	Mn	Ti	Cu	Ni
AlSi10Mg+Ni	Bal.	8.5-10.5	0.18-42	<0.55	<0.15	<0.05	5.1

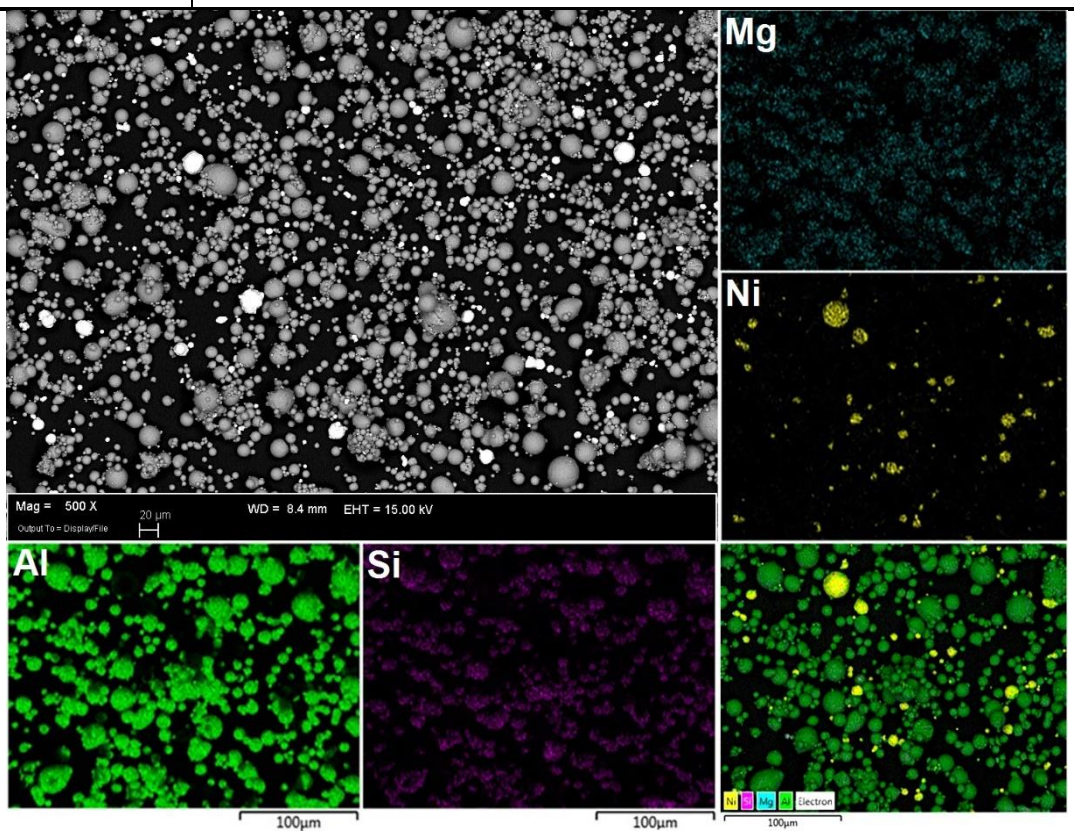

Fig. 56. Elemental distribution map of the prepared AlSi10Mg+5%Ni powder.

4.1.1.2. Sample production

The specimens were printed using an EOS M270 system (maximum power, 200 W; beam spot diameter, 100 µm; laser wavelength, 1060-1100 nm) with the optimum process parameters identified in an earlier study [172]. The building process was executed under a flowing inert high purity Ar atmosphere, with the oxygen level kept below 0.1%, while the temperature of the building platform was 100 °C. The as-prepared specimens were annealed at 300 °C for 15 min and 120 min and air-cooled eventually. In order to trace the phase evolutions in higher temperatures by XRD, one of the sample was annealed at 400 °C for 120 min.

4.1.2. Characterization and mechanical evaluation

All samples for microstructural investigation were cut along the building direction (BD) and mechanically ground and polished using SiC papers and diamond suspension, respectively.

In the following, as-polished surfaces were electro-etched using Barker etchant **[173]** for optical analysis and chemically etched using Keller's solution for SEM analysis. A ZEISS Supra 40 Field Emission Scanning Electron Microscopy (FE-SEM) equipped with an Oxford EDS microanalysis (Liquid-N_2 cooled Si(Li) detector and Helios NanoLab 600i Dual-Beam focused ion beam scanning electron microscopy (FIB-SEM) equipped with 4 gas injection systems for deposition (Pt, Au, SiO_x) and etching (XeF_2) were employed for detecting the evolution of the particles. In order to trace the surface topography, Atomic Force Microscopy (AFM) was employed.

Samples for the tensile test were machined according to ASTM E8 Standard [174]. The tensile tests were carried out at room temperature using a Zwick/Roell Z050 testing machine with a 2 mm/min crosshead velocity. The presented data are the average of at least three specimens processed using similar conditions to ensure the reproducibility of the results.

4.1.3. Results and Discussion

4.1.3.1. Microstructural characterization

The 3D micrograph of an as-built sample, shown in Fig. 57(a), reveals the melt pools orientation along the BD and laser traces on the top surface. Fig. 57(b) and Fig. 57(c) adequately show the different phase evolutions in the center and border of the melt pools. According to these images, the interface of the melt pools comprises a coarse dendritic silicon structure with varying thicknesses. Likewise, the Marangoni effect appears as a circular flow inside some of the melt pools.

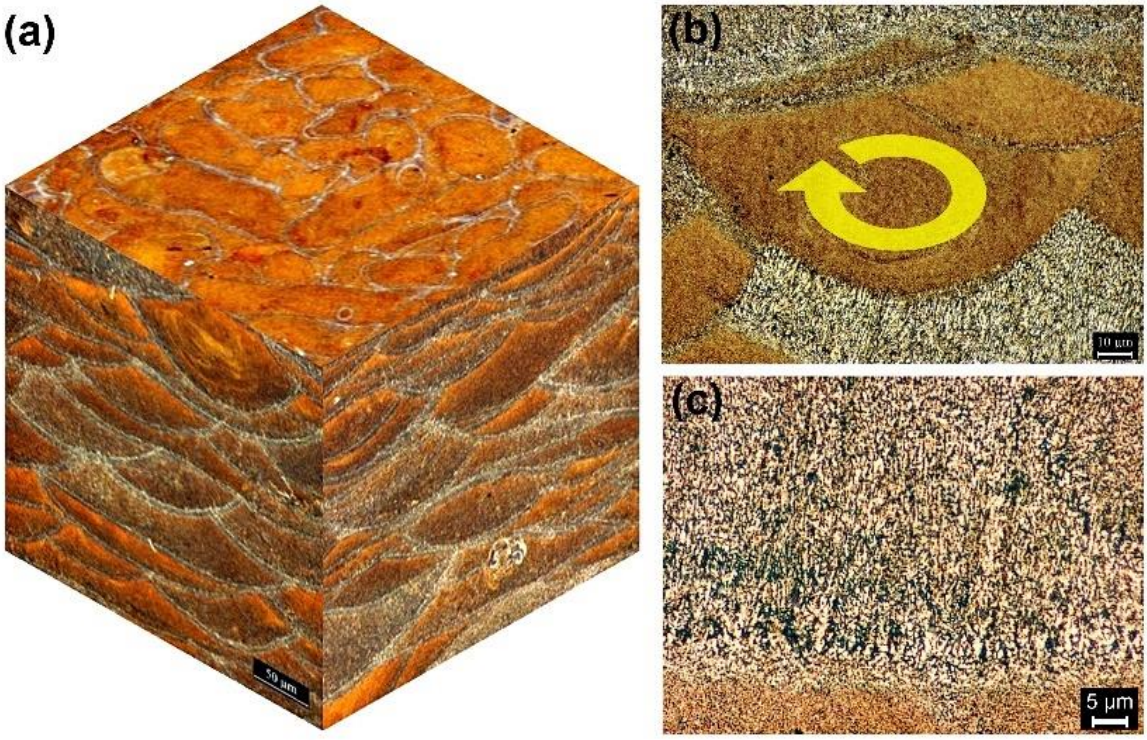

Fig. 57. Microstructure of an as-built sample in (a) 3D view and cross-section (b,c) in two different magnifications.

The optical micrographs of the AlSi10Mg/Ni samples after short-term and long-term annealing are displayed in Fig. 58. Based on Fig. 58(a), the as-built specimen comprised the elongated grains perpendicular to the melt pool boundaries due to the Gaussian distribution of the laser beam energy [175]. Epitaxial grain growth that generally results in the formation of elongated columnar grains in an individual melt pool and an overall zigzag pattern along the BD is a typical phenomenon in the LPBF fabricated samples [176]. It is well documented that this epitaxial grain growth originates from directional solidification in the reverse direction to the heat transfer in LPBF manufactured parts. According to the top surface image of the as-built sample, some Ni-rich phases are pushed to the fusion borders. Likewise, some unmelted phases are stacked inside the melt pools. Accumulation of these phases in the melt pool borders, in turn, contributes to the formation of elongated grains from the borders toward the center of the melt pools. In general, it is reported that the G/R ratio at the solid-liquid interface (G and R are the thermal gradient and solidification rate, respectively) is the key solidification parameter in the formation of specific grain morphologies in different regions of a sample [177]. As this value decreases, planar, cellular, columnar dendritic, and equiaxed dendritic structures can be formed, respectively [72]. Therefore, when Ni phases settle in the melt pool boundaries, many small grains can heterogeneously nucleate at the borders due to the large value of G.

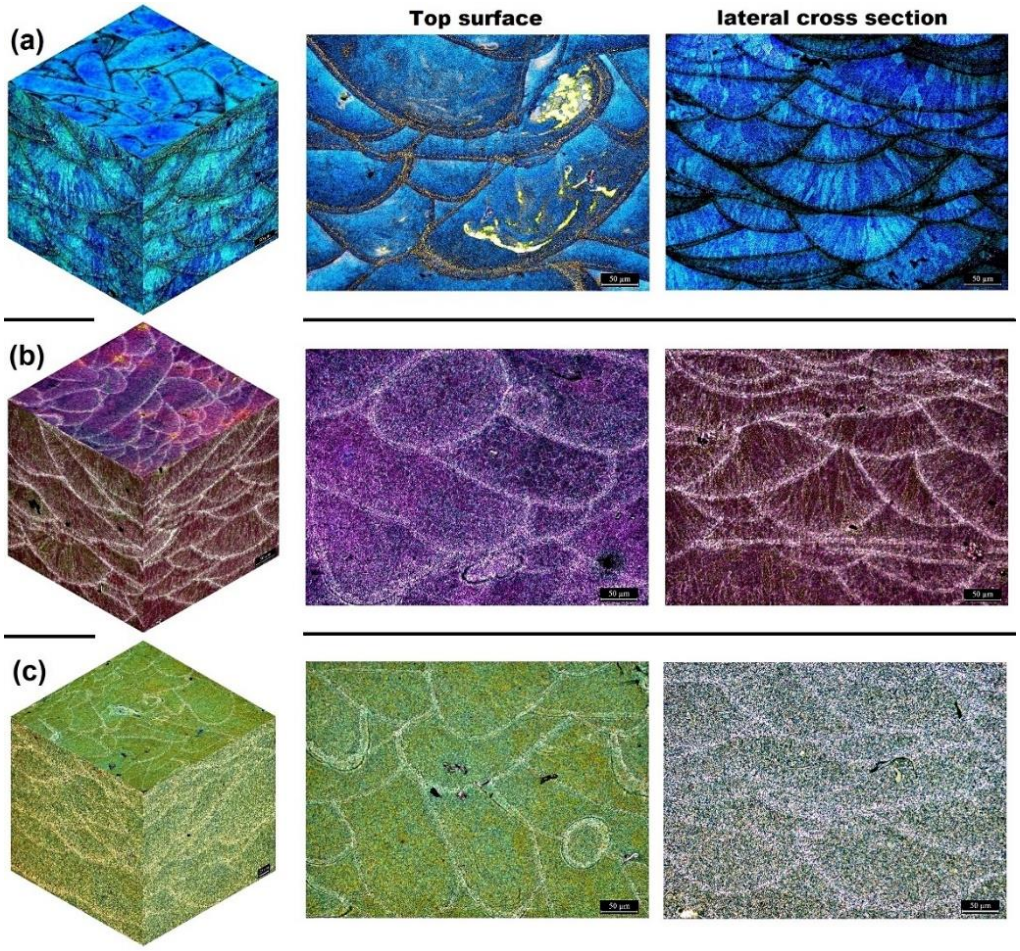

Fig. 58. LOM microstructure of the (a) as-built sample and after annealing at 300 °C for 15 min (b) and 120 min (c).

Owing to the high magnitude of G/R, most of the nucleated grains on borders compete to grow as columnar grains, whereas few of them can grow towards the center of the melt pool. Fig. 58(b) shows the microstructure of the as-built sample after annealing for 15 min at 300 °C. As can be seen, the morphology and size of the grains are still stable and have not significantly changed. The fine grains on the top surface of the sample are cross-sections of elongated grains along the building direction. According to Fig. 58(c), by annealing over 120 min at 300 °C, the fish scale pattern has almost vanished, and the melt pool boundaries gradually merged. Furthermore, despite annihilating the grain structure after long-term annealing, the phases formed in the borders did not leave their initial location completely and appeared with different contrast.

Comparing the EBSD micrographs of Fig. 59(a) and Fig. 59(c) reveals that Ni addition could not majorly refine the microstructure. Also, the band contrast image of the as-printed Ni-reinforced sample (Fig. 59(d)) properly shows the non-uniform distribution of the Ni-rich phases in the aluminum matrix. EBSD images of Figs. Fig. 59(e, f) and Fig. 59(g, h) shows the

grains evolution after annealing at 300 °C for 15 min and 2h, respectively. As can be seen, during annealing the recrystallization started from the fine-grain zones around the melt pool boundaries. However, even after annealing for 2h the grains were not significantly grown, and the morphology of the grains were remained the same. Likewise, applying post annealing led to reaction of the unmelted Ni-rich zones with Al matrix which is clearly observable from the band contrast.

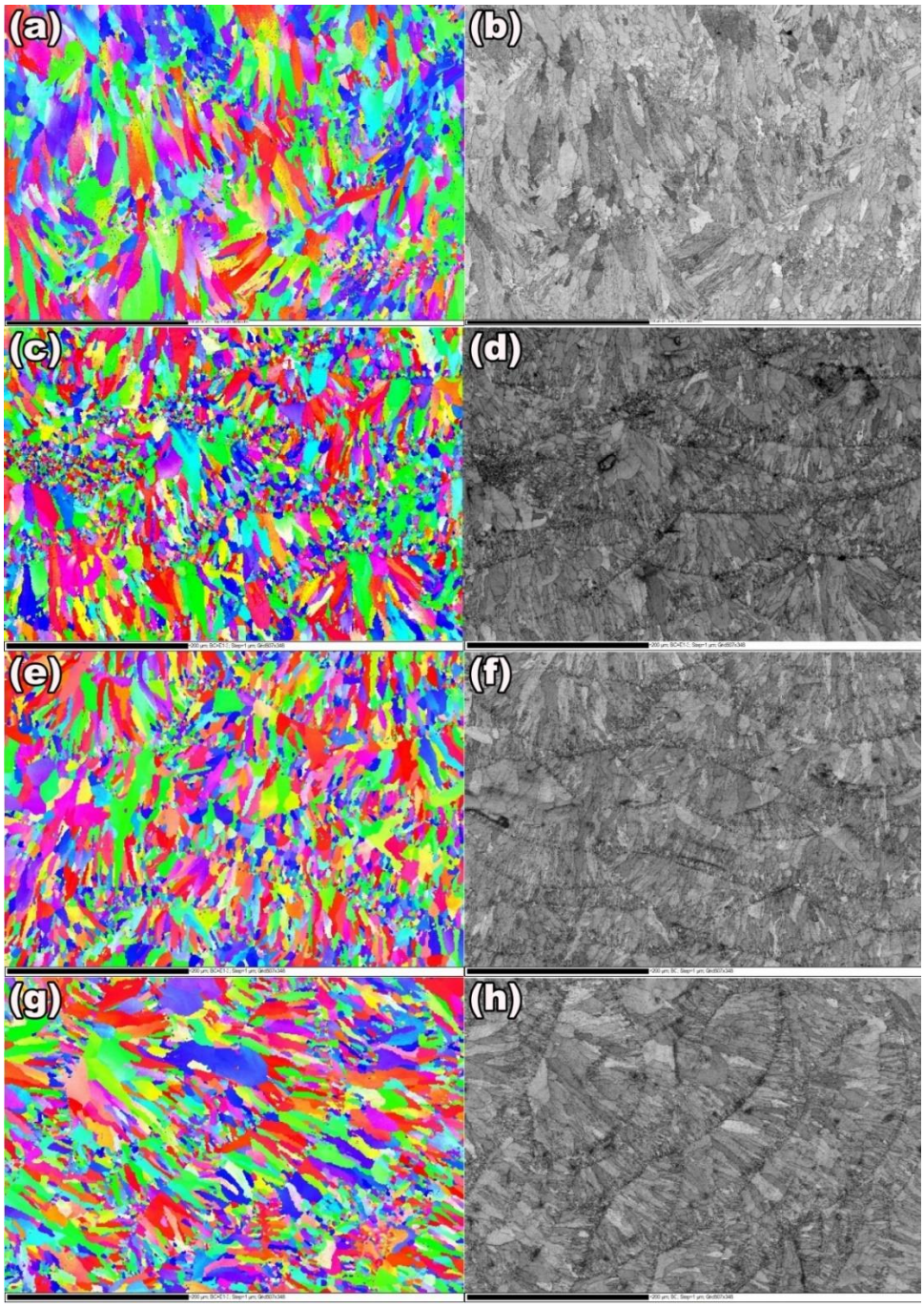

Fig. 59. EBSD IPF color map and band contrast image of (a,b) AlSi10Mg, (c,d) Ni-reinforced and after annealing at 300 °C for 15 min (e,f) and 120 min (g,h).

To better assess the structural transition in the as-built samples during annealing, FIB/SEM imaging was employed at different magnifications, and the results are presented in Fig. 60. According to Fig. 60(a,b), in the as-built specimen, a network of interconnected silicon dendrites is widespread in the supersaturated α-Al matrix. After 15 min treatment at 300 °C, most of the linkages between eutectic Si cellular structures were detached, and the conjunct silicon phases were dissociated into the ultrafine particles (Fig. 60(c) and Fig. 60(d)). As the annealing time increases, supersaturated α-Al tends to repulse the excessive dissolved silicon into the matrix and reach a stable thermomechanical condition. In the following, by diffusion and agglomeration of silicon into the spheroidized precipitated phases due to Ostwald ripening phenomenon [2, 25], fine particles became coarser and significantly reduced their number (Fig. 60(e) and Fig. 60(f)). During this thermodynamically driven spontaneous phenomenon, to reduce the lattice stored energy, the less-stable atoms located on the surface of the smaller particles diffuse to the larger ones with higher volume to surface proportion. Consequently, the smaller particles gradually shrink and/or coalesce to form bigger particles.

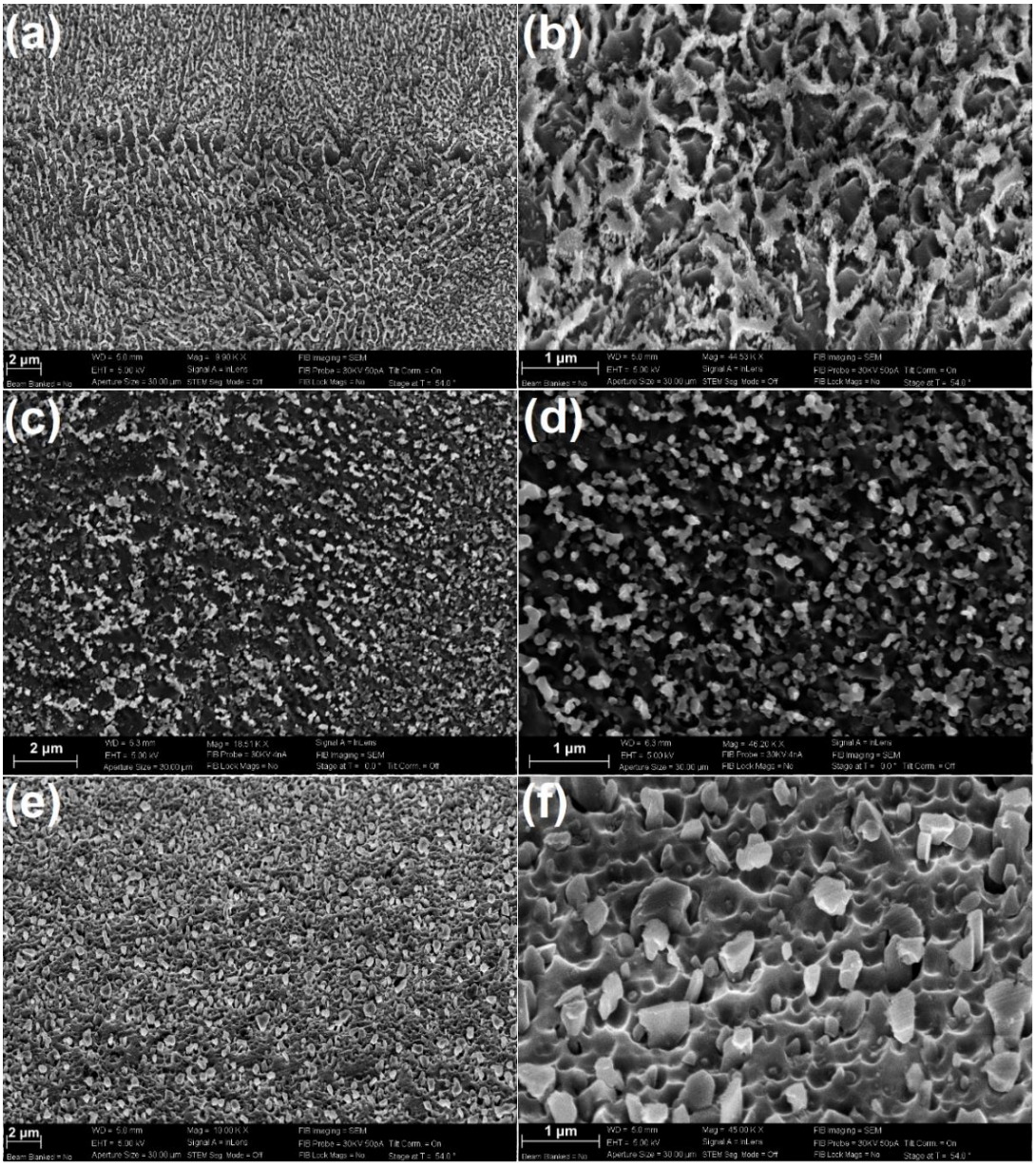

Fig. 60. FIB/SEM micrograph of the (a,b) as-built sample and after annealing at 300 °C for 15 min (c,d) and 120 min (e,f).

The acquired evidence after topography analysis of the surface through the AFM analysis validated the FIB/SEM results (Fig. 61). As shown in the as-built sample, the walls of the cellular dendrites are composed of delicate needle silicon particles, while triple junctions contain coarser silicon particles (Fig. 61(a-c)). According to the literature, triple junctions have higher stored energy, and during the thermal treatments, they start to melt at a temperature below the standard melting point [178]. Since the cell walls are indeed the sub-grain boundaries, probably higher diffusion kinetics has led to partial coarsening of the silicon particles in the triple junctions (Fig. 61(c)). These coarse particles can be the destination of the migrated solute atoms of silicon when leaving the supersaturated Al matrix during the heat

treatment process. Consequently, after annealing at 300 °C for 120 min, numerous coarse silicon particles were uniformly distributed in silicon-free Al matrix (Fig. 61(d,e)).

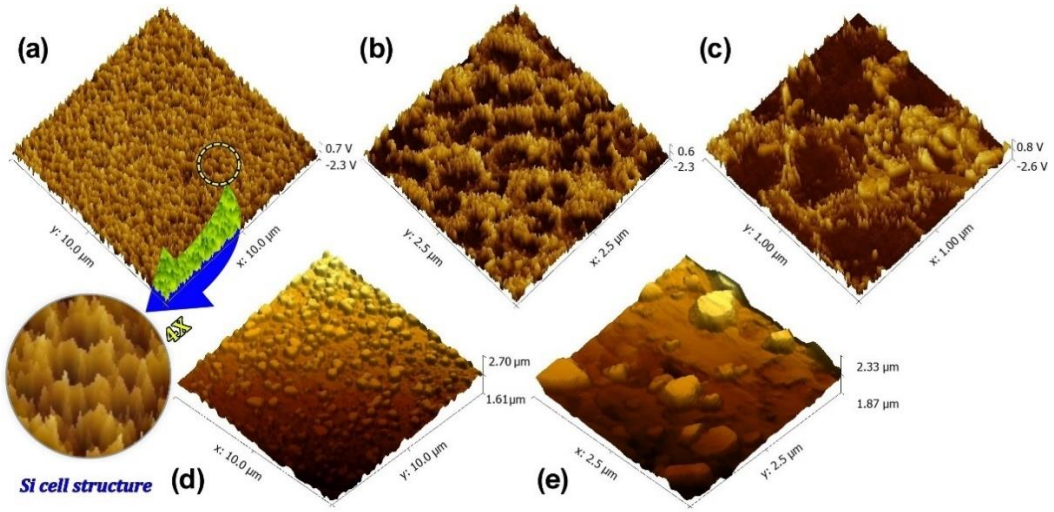

Fig. 61. AFM images show the cross-section of the as-built sample (a-c) after annealing at 300 °C for 120 min (d,e).

Exposure to different thermal treatments leads to the formation of three different zones in terms of morphology and size of the cellular dendrites across the melt pools (Fig. 62(a)). The fine zone (MP fine) in which the size of the cellular dendrites does not exceed 500 nm [179]. The grains in MP fine zone are partially oriented toward the center of the melt pool. The coarse zone at the melt pool border (MP coarse), which has more equiaxed cells with bigger size (2-3 times) compared to the fine area due to a partial remelting and subsequent heat accumulation at the bottom of the melt pool and symmetrical growth of the cells [180, 181]. The third batch of the dendrites is in the Heat Affected Zone (HAZ) that forms on the outskirt of the melt pool below the MP coarse strip. This layer is where during melting of the last deposited powder bed, laser penetration depth was not sufficiently high to remelt it and only was exposed to a temperature between 280-560 °C below a second. Although this temperature was not sufficiently high to propel the long-range diffusion of solute Si to contribute to the particle coarsening there, but the heat transfer of the laser could fragment the Si cellular dendrites. During annealing at 300 °C, the cellular walls gradually collapsed and broke into equiaxed particles. Consequently, after 15 min exposure to this temperature, in fine-grain regions disintegrated Si networks were decorated like the HAZ strip (Fig. 62(b)). As exhibited in Fig. 62(c), the size of the silicon particles upon fragmentation of silicon dendrites and nucleation of new particles from supersaturated Al matrix was in nanoscale. It was proved that the center of the melt pools that benefits from interconnected silicon cells shows higher hardness compared to the borders while HAZ displays the minimum hardness value [70]. Hence, regardless of Ni

addition and related transformations under thermal treatment, complete dissociation of Si cellular dendrites after annealing, in turn, can reduce the mechanical strength of this alloy.

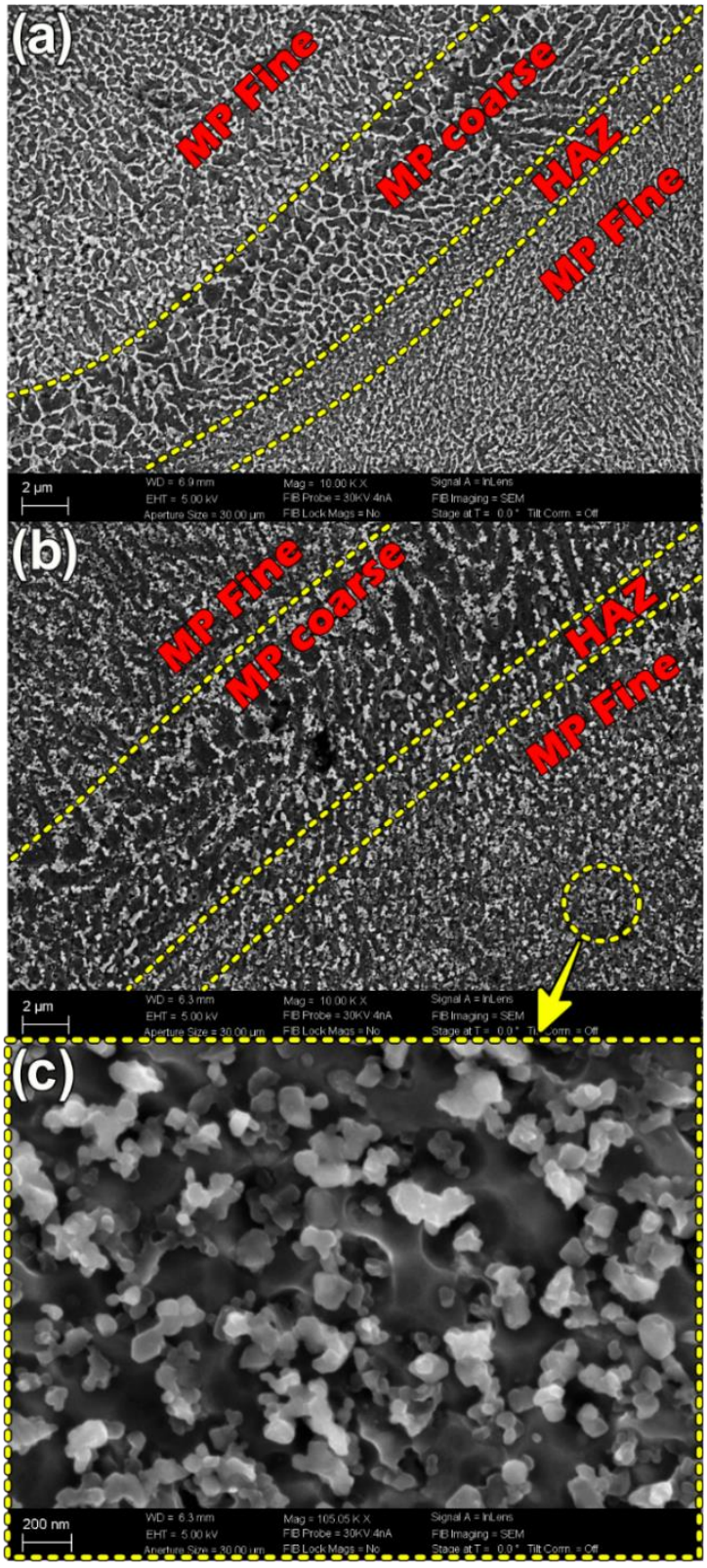

Fig. 62. SEM micrographs of the as-built sample (a) after 15 min annealing at 300 °C (b) and formation of the silicon nanoparticles in the fine-grained zone after annealing at 300 °C for 15 min (c).

The elemental distribution map of Fig. 63(a-d) properly shows that during solidification of a new layer, a significant portion of the Ni particles was driven to the melt pool boundaries and stacked there as Ni-rich streaks (like Fig. 63(a)). Despite the gradual breakdown of the Si dendrites during annealing at 300 °C for 15 min (Fig. 63(e-h)) and 120 min (Fig. 63(i-l)), Ni-rich intermetallics were not majorly affected by heat treatment and preserved their initial locations in melt pool boundaries. Comparison of Fig. 63(c), Fig. 63(g) and Fig. 63(k) revealed that during annealing, supersaturated silicon atoms leave the Al matrix and form individual particles or precipitate on pre-existing particles and coarsened them. As a result, gradually, the Al substrate was depleted from the solute silicon atoms, and after 120 min most of the coarsened Si particles were surrounded by the Al atoms.

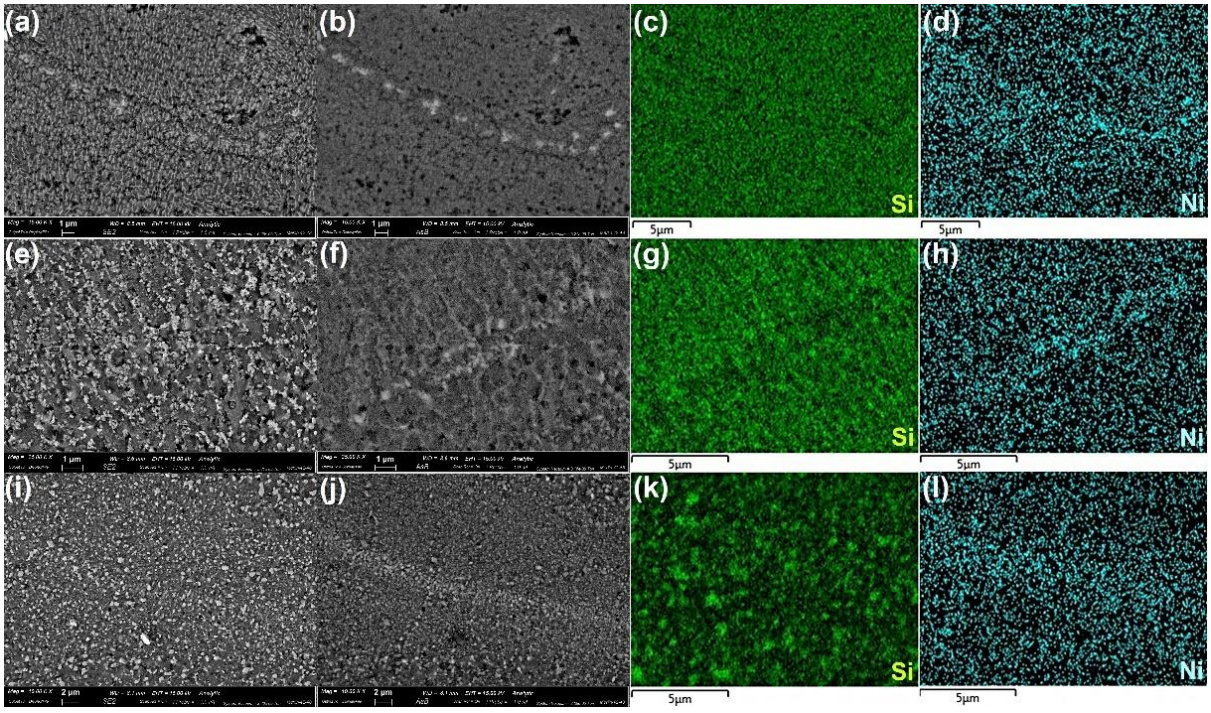

Fig. 63. Secondary and backscatter SEM images and distribution map of Si and Ni elements in the as-built sample (a-d), and after annealing at 300 °C for 15 min (e-h) and 120 min (i-l).

Line-scan patterns of Fig. 64 were taken perpendicular to the melt pool borders after short-term and long-term annealing. Accordingly, differently from the spheroidization of the silicon dendrites and coarsening of the silicon particles through the atomic diffusion from the supersaturated Al matrix, Ni-rich phases are thermodynamically stable up to 300 °C. These results show that the atoms belonging to Ni lumps could not undergo a long-range diffusion in the Al matrix even after 120 min annealing.

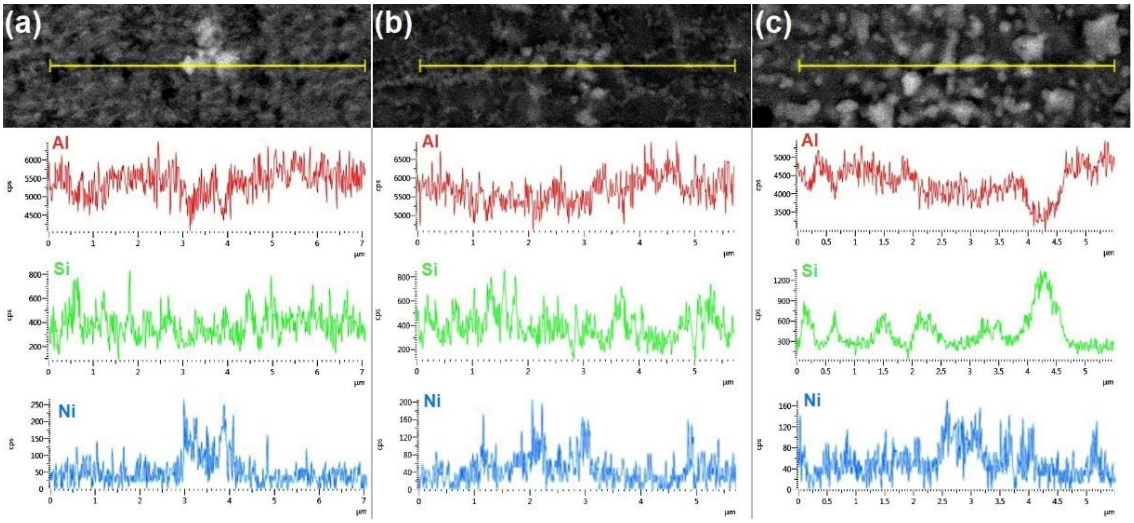

Fig. 64. EDS line scan perpendicular to the melt pool boundaries in (a) as-built sample after annealing at 300 °C for 15 min (b) and 120 min (c).

Fig. 65 shows the destructive role of Ni-rich intermetallics stacked at the melt pool boundaries. As depicted in Fig. 65(a), the accumulation of the molten nickel particles does not limit to the melt pool borders, and some Ni-rich phases were formed at the center of melt pools. Nonetheless, owing to the weakness of the melt pool borders at the interface of MP coarse and HAZ [182], precipitation of the Ni-rich phases made the borders drastically unstable (Fig. 65(b)). Consequently, even thermal shock during rapid solidification of the fused layers can cause the crack initiation at melt pool borders and spontaneous failure of the specimen (Fig. 65(c)).

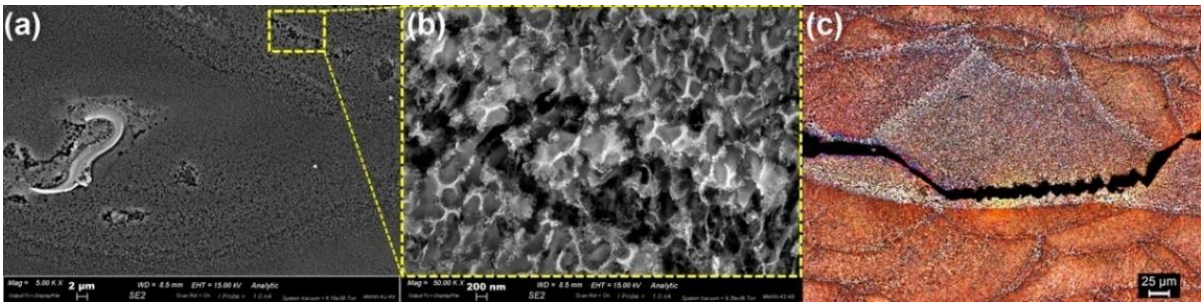

Fig. 65. SEM images of stacked Ni-rich phases at the center (a) and melt pool borders (b) and OM micrograph showing the spontaneous failure of the as-built sample from melt pool boundary.

The XRD patterns of Fig. 66 represent the phase evolutions during short-term and long-term annealing of Ni-reinforced specimens. As shown in the as-built sample, the high temperature of the laser irradiation could melt most of the Ni particles and make a reaction between the molten Ni and aluminium matrix. Consequently, Ni is transformed into Al_3Ni intermetallic chunks. As shown, annealing at 300 °C for 15 min had no influence neither on the AlSi10Mg matrix nor on Ni_3Al phases formed in the printing step. Annealing at 300 °C

for 120 min pulled the trigger of reactivity between the present Ni in the substrate as unmelted particles or coarse Ni_3Al chunks with surrounded Al atoms. Consequently, the peak intensity of the Ni_3Al phase is rather intensified. To trace the probable further phase evolutions, long-term annealing at a higher temperature also was examined. As can be seen, annealing at 400 °C for 120 min has enhanced the intensity of the Al_3Ni and Si peaks in the XRD pattern of the specimens. It shows that annealing at a higher time and temperature however would increase the reactivity of the Ni-rich phases but accompanies by dissociation of the Si branches formed during the LPBF process and migration of the Si from supersaturated Al matrix toward the pre-exist Si particles and eventually formation of coarse brittle Si particles.

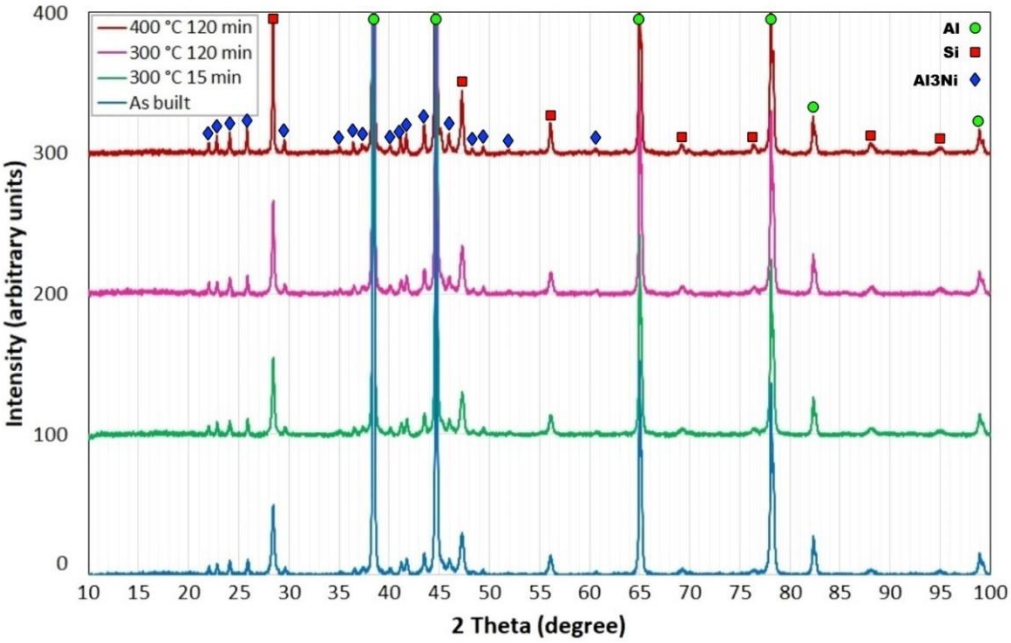

Fig. 66. XRD pattern of the as-built specimen after annealing at 300 °C for 15 min and 120 min and 400 °C for 120 min.

Fig. 67 shows the effect of annealing at 300 °C for 120 min on residual Ni-rich phases. According to the optical micrograph of Fig. 67(a), which is taken from the as-built sample, the chemical composition of coarse Ni-rich chunks is not uniform from surface to center of these regions. It seems that however the heat of laser has evolved most of the Ni particles into Ni_3Al masses, but still the center of these chunks is composed of unreacted Ni. In the following, after 120 min heat treatment at 300 °C, a thin layer of another intermetallic phase has formed around them (Fig. 67(b)). The formation of such a thin shell of intermetallic compounds on the Ni-rich lumps implies that despite the destructive influence of Long-term annealing on dendritic silicon structure, it had a slight effect on aggregated Ni-rich phases. However, even after the formation of this shell, the center of the Ni-rich zones remained as unreacted (brown stripe). Regarding

the difference between the melting point of AlSi10Mg and Ni (570 °C and 1455 °C), the size range of Ni particles must be considerably smaller to achieve a uniform distribution of Ni_3Al intermetallic particles in the Al substrate. Fig. 67(c) and Fig. 67(d) are provided from the fracture surface of the as-built sample and annealed sample at 300 °C for 120 min, respectively. Likewise, EDS analysis of Fig. 67(e) and Fig. 67(f), are related to the exhibited phases in the fracture surface of these two samples. As can be seen, the stacked white phase of Fig. 67(c) is enriched from Ni, while a thin gray layer of intermetallic is formed on it. After long-term annealing, a dark crust of intermetallic was formed on it. The smooth surface of this phase is representative of its weak adhesion to the matrix and easy separation under tensile loading. In the meantime, the formation of some cracks on this intermetallic shell points to the brittle nature of this phase.

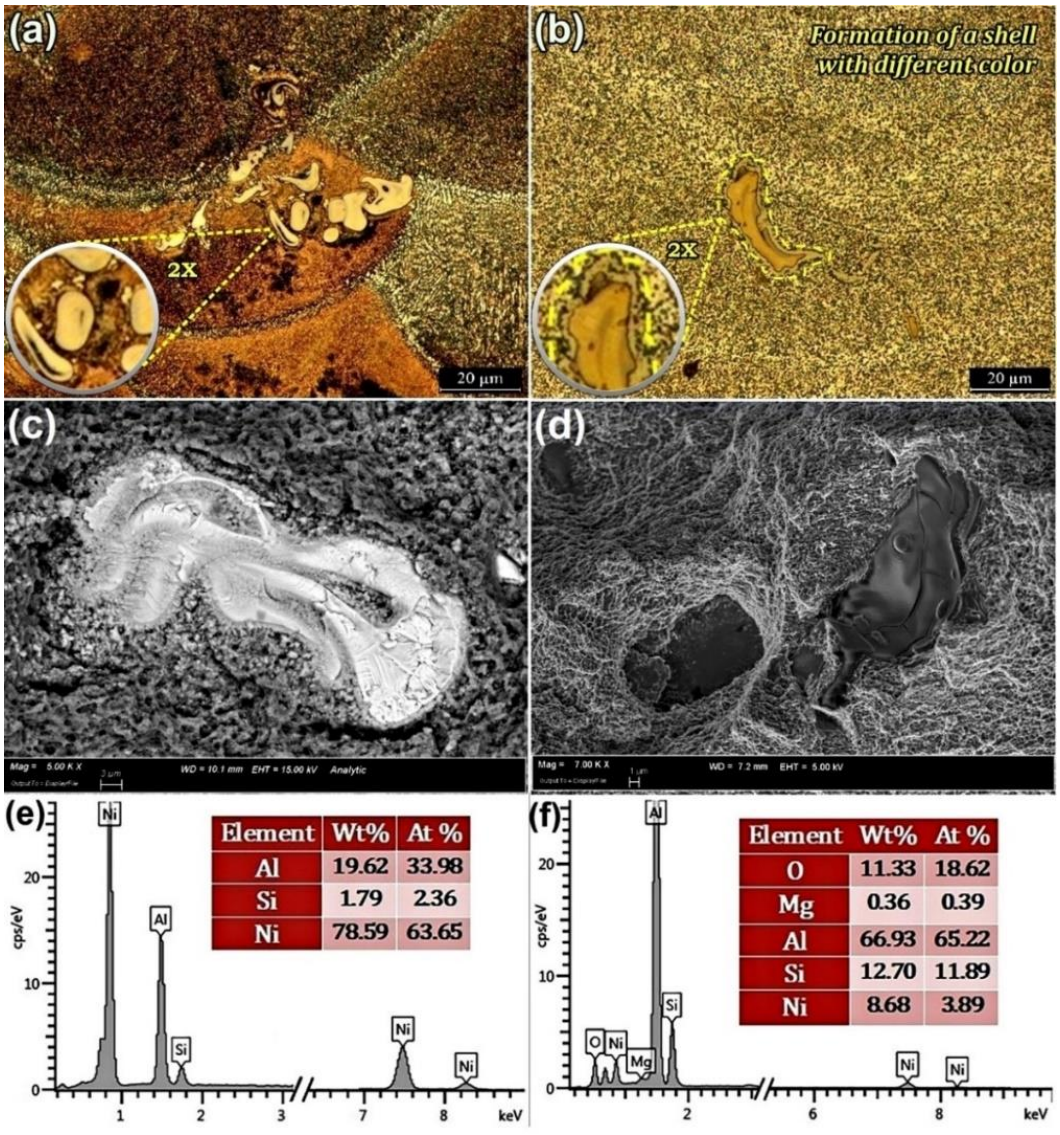

Fig. 67. Optical micrograph, SEM image of the fracture surface and EDS analysis of the accumulated phases in the fracture surface of as-built (a, c, e) and annealed samples at 300 °C for 2h (b, d, f).

The elemental distribution map of Fig. 68, referring to an as-built specimen, also confirms the presence of coarse Ni-rich chunks in the fracture surface of the as-built specimen. As depicted by arrows, many cracks are formed at the interface of Ni-rich lumps with the aluminium matrix. It can be attributed to the difference in thermal expansion coefficient between Al and the thin intermetallic crusts formed on Ni-rich lumps that detach from the matrix during rapid solidification of the fused layers and act as a failure initiation point during the tensile test.

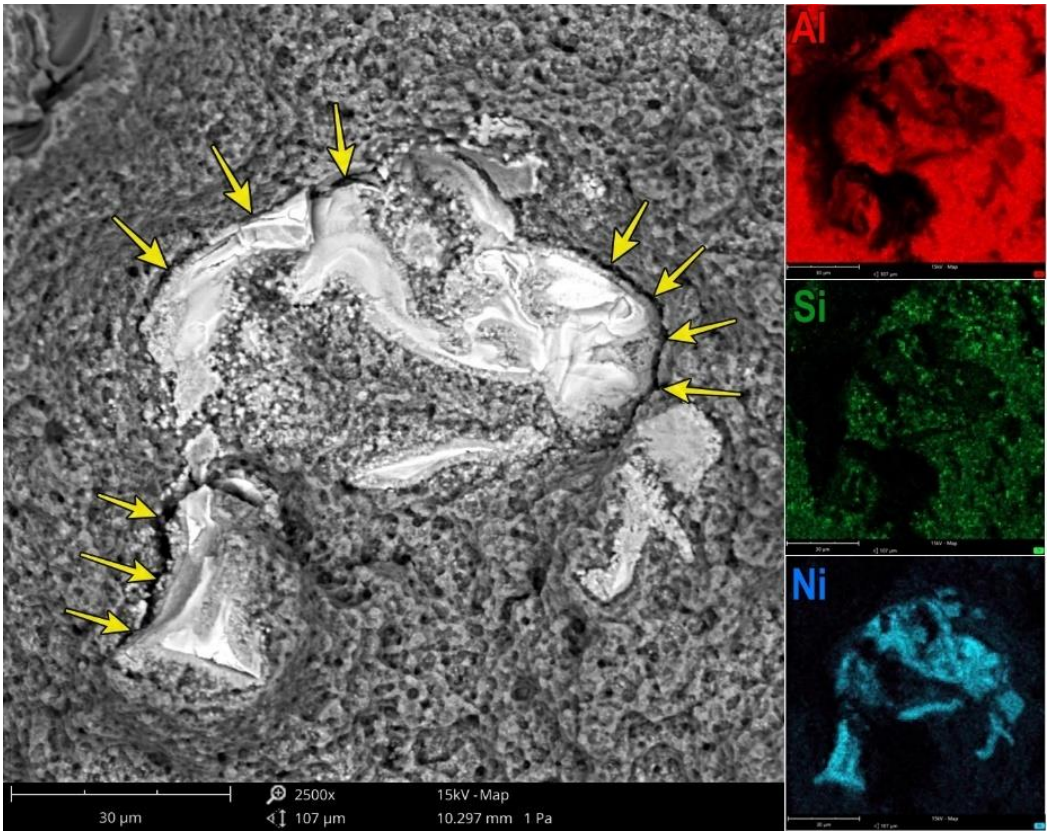

Fig. 68. Element distribution map of the aggregated Ni-rich mass in fracture surface of the as-built specimen.

Nonetheless, Ni-rich chunks were not the only origin of the failure under tensile loading. To analyze the fracture mechanism in the samples, the fracture surface of the as-built specimen (Fig. 69(a-c)) and of the ones annealed at 300 °C for 120 min (Fig. 69(d-f)) was investigated by stereo microscope and SEM. According to Fig. 69(a, b), coarse Ni-rich lumps are uniformly distributed in the fracture surface of the as-built sample and play the main role in the formation of coarse dimples. Likewise, poor metallurgical bonding between the Ni_3Al and Al matrix induced the lack of fusion imperfection (Fig. 69(c)). The spherical hole of Fig. 69(d) shows that some gas bubbles were also entrapped inside the melt pools during LPBF printing of the samples. Such a round shape pores having smooth inner walls often form in the center of melt

pools. Because regardless of the origin of the gas entrance in the molten pool, namely as evaporation of smaller Al particles by a high laser energy density, hollow powders or absorbed gas from the ambient atmosphere around the melt pool, rapid solidification does not allow it to escape from the molten phase [183]. Fig. 69(e, f) shows the high magnification SEM images of the finer dimples in the fracture surface of the long-term annealed specimen. The settlement of the spheroidized silicon particles at the bottom of the fine dimples shows that these fine irregular shape particles can also act as crack nucleation sites under tensile loading.

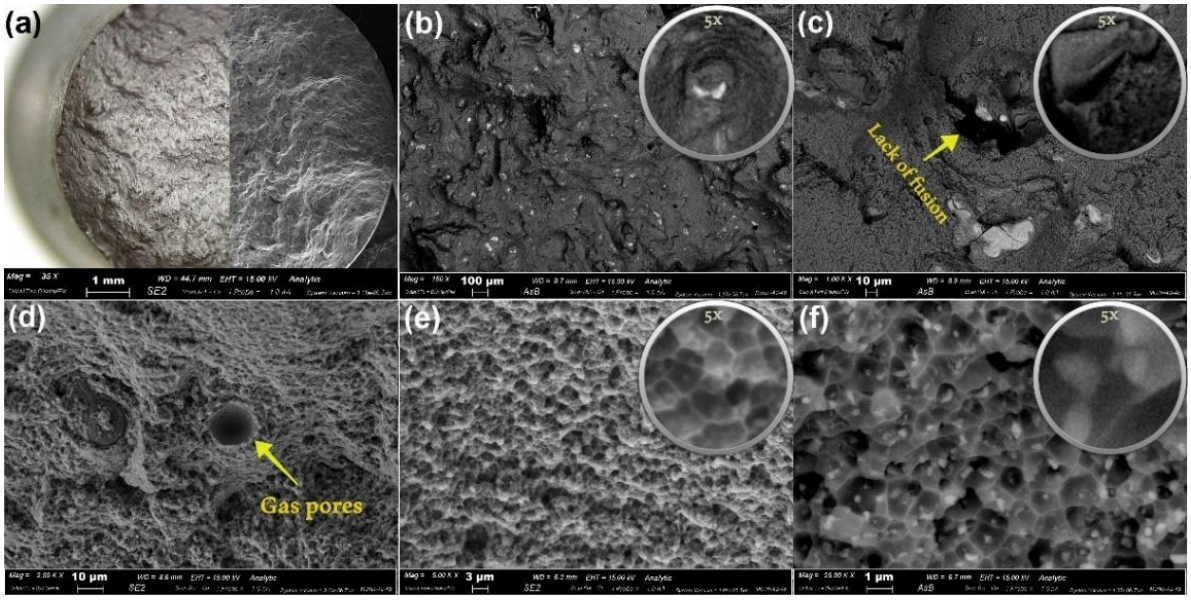

Fig. 69. Stere/SEM (a) and SEM images were provided from the fracture surface of the as-built sample (b, c) after annealing at 300 °C for 120 min (d-f).

4.1.3.2. Mechanical properties

To evaluate the effect of short-term and long-term annealing on the mechanical performance of the AlSi10Mg/Ni samples, tensile and compression tests were executed, and the results are presented in Fig. 70. According to Fig. 70(a), annealing at 300 °C for 15 min could not significantly attenuate the compressive yield strength, even if it is evident that the as-built samples break in a brittle fashion, while the treated samples (in particular the one annealed for 120 min) have a more ductile behaviour. In fact, to keep on the annealing up to 120 min has remarkably reduced the compressive yield strength, from about 330 MPa to near 220 MPa. According to the tensile stress-strain curves of Fig. 70(b), dissociation of the silicon branches into fine particles after short-term annealing could not remarkably reduce the tensile strength of the samples. But after annealing for 2 hours, coarsening of the silicon particles played a destructive role and degraded the tensile properties. In Fig. 70(c), the tensile behaviour of the AlSi10Mg/Ni samples after short- and long-term annealing is compared by AlSi10Mg alloy in

a pure state and after reinforcing with different metallic and non-metallic reinforcements. As illustrated, compared to the non-reinforced AlSi10Mg, Ni-reinforced alloy shows lower tensile strength and a lower elongation to failure. Although short-term annealing could not majorly attenuate the tensile resistance, the synergistic effect of spheroidized silicon particles and promotion of brittle Al_3Ni shell around the Ni-rich lumps after annealing for 120 min resulted in a notable collapse in the mechanical properties. Furthermore, as shown, Cu-reinforced AlSiMg alloy [184] has also shown a similar tensile behavior and rather lower strength compared to the average strength of the 3D printed AlSi10Mg alloy. The noticeable point is that according to the extracted results in the literature (Table 2), compared to metallic elements, improvement of the mechanical strength of AlSi10Mg alloy through the addition of ceramic nanoparticles and carbon allotropes was more favorable. This suggests that to achieve a finer cell structure in the AlSi10Mg components manufactured through the LPBF process, the addition of pre-synthesized fine ceramic particles is more effective than the addition of alloying elements. In fact, the high solidification rate of the molten tracks hinders the long-range diffusion of the solute elements, and for the complete dissolution of the additive metallic particles, they must be very fine. Otherwise, applying an insufficient laser power for dissolving a couple of the particles having a significant difference in melting point (like Ni particles in Al matrix) only according to the optimum parameters for LPBF fabrication of a component cannot properly spread the guest elements among the host matrix. On the other side, exposure of the powder bed to intensive laser irradiation can lead to the formation of some pores due to the Marangoni effect [185] and vaporization of some particles of the low-melting-point ingredient.

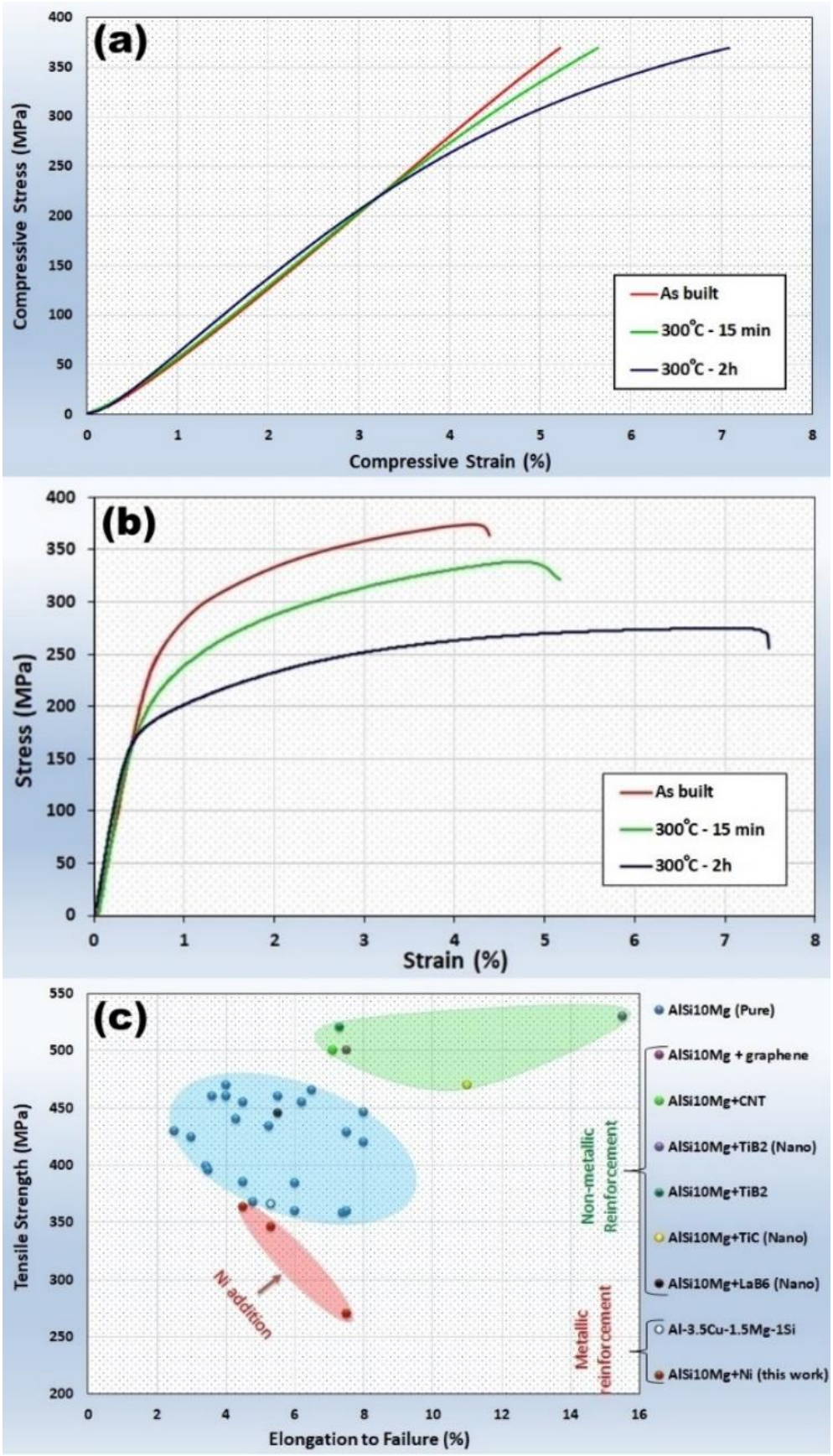

Fig. 70. Variation of compressive (a) and tensile (b) stress-strain curves and comparison of tensile behavior of Ni-reinforced AlSi10Mg alloy after annealing at 300 °C for 15min and 120 min with pure AlSi10Mg and reinforced alloys/composites by other additive agents (c).

Table 8. Overview of tensile properties of AlSi10Mg alloys reinforced by different reinforcements.

Source	Matrix	Reinforcement material	Particle size matrix/reinforcement (µm)	Additive fraction (Wt.%)	Beam diameter (µm)	Laser power (W)	Hatching distance (µm)	Layer thickness (µm)	Scan speed (mm/s)	UTS (MPa)	El. at break (%)
This work	AlSi10Mg	Ni	<45/<20	5	100	195	170	30	800	270-370	4.4-7.5
[186]	AlSi10Mg	TiC	30/1.5	5	70	100	50	50	150	470	11
[82]	AlSi10Mg	TiB_2	53/15	5.6	75	210	100	30	1000	520	7.3
[187]	AlSi10Mg	Nano-TiB_2	<40/nano-sized	11.6	75	300	105	30	1000	530	15.5
[79]	AlSi10Mg	LaB_6	40/100 nm	0.5	70-100	300	130	30	1650	445	5.5
[188]	AlSi10Mg	Graphene	15-45/-	0.1-0.2	73	400	90	30	2250	500	7.5
[184]	AlSiMg	Cu	41	3.5	70-250	190	80	40	165	366	5.3
[85]	AlSi10Mg	CNT	<45/10-30 nm	1	70-500	370	105	30	1300	500	7.1
[189]	AlSi10Mg (Pure)	-	-	-	-	-	-	-	-	358-470	3-8

4.1.4. Summary and conclusions

In the current study, the AlSi10Mg powder was combined with 5 wt.% gas atomized powder of pure Ni and then processed using the LPBF additive manufacturing method. Samples were eventually annealed at 300 °C for different times, and their microstructure and mechanical properties were surveyed. The main achievements of this research are summarized as follows:

- The as-built sample had a fish-scale pattern in which the grains were oriented from the center toward the borders of the melt pools. After annealing the samples at 300 °C for 15min, both the GBs and melt pools were gradually faded while keeping on the annealing for 120 min resulted in the complete disappearance of the melt pools.
- During the printing process, most of the Ni particles reacted with the Al matrix and formed Al_3Ni phase and shoved towards the bottom of the melt pools and located there. During annealing, the cellular dendritic structure formed in the as-built sample gradually spheroidized into fine (after 15 min) and coarse (after 120 min) silicon particles, but the Ni-rich zones did not majorly affect from annealing and preserved their initial positions.

- Microstructural investigation revealed that the high tendency of the Ni particles to accumulation stimulated them to form coarse Ni-rich lumps in the center of the melt pools. However, annealing at 300 °C for 15 min could not majorly affect the stacked Ni-rich chunks and the residual pure Ni but after 120 min, a thick fragile shell of Al_3Ni was formed on Ni-rich masses. The creation of such a brittle crust on numerous Ni-rich lumps having weak interfacial bonding with Al matrix and transformation of silicon cellular dendrites to the coarse particles with sharp edges resulted in a significant drop in tensile strength and a slight reduction in compressive resistance after long-term annealing.
- Comparison of the tensile strength of the AlSi10Mg/Ni alloy with tensile behavior of the AlSi10Mg alloy and reinforced alloys by other materials revealed that compared to metallic elements, the addition of ceramic nanoparticles and carbon nano-compounds has a higher impact on the improvement of mechanical properties.

4.2. Comparison of the Er_2O_3 and Gd_2O_3 Nanoparticles

Mohammad Reza Jandaghi*, Matteo Pavese, " Additive Manufacturing of nano-oxide decorated $AlSi_{10}Mg$ composites: A comparative study on Gd_2O_3 and Er_2O_3 additions", **Journal of Materials characterization**, available online, October 2022.

Abstract

AlSi10Mg-based nanocomposites have been fabricated by laser powder bed fusion (LPBF) additive manufacturing with the addition of 1 wt.% Gd_2O_3 and Er_2O_3 nanoparticles. The effect of different process parameters and remelting strategies on the densification of the samples was evaluated. Results showed that applying remelting by printing successive layers could reduce the imperfections. The microstructural survey revealed that regardless of particle type, stacking the nanoparticles on uneven surfaces of irregular AlSi10Mg particles beside van der Waals attractive force between the adjacent nanoparticles leads to the formation of coarsened clusters in printed samples. The XRD patterns disclosed the partial reaction between the nano-oxides and the aluminum matrix and the formation of some interfacial intermetallic layers, which also were detected by SEM. The measurement of grain size and microhardness implied that Er_2O_3 had a more refining impact and could uniformly enhance the hardness compared to Gd_2O_3. However, due to more localization of the Gd_2O_3 nanoparticles and reciprocally more faulty areas, hardness values had a wider deviation range. In addition, the average hardness of the Gd_2O_3 and Er_2O_3 reinforced specimens was greater than the average reported for LPBF fabricated AlSi10Mg composites. EBSD micrographs revealed that due to the pinning effect of nanoparticles, the particle-rich zones had a higher KAM value and grain orientation spread (GOS) which pointed to the formation of more GNDs at the Al/nanoparticles interfaces.

4.2.1. Materials and Methods

4.2.1.1. Materials

A gas atomized AlSi10Mg stock powder with a diameter range of 15-53 µm was provided by EOS GmbH Co. The powder was composed of Si (9.4 wt.%), Mg (0.31 wt.%), Fe (0.16 wt.%), Mn (0.11 wt.%), Ti (0.10 wt.%), and Al (balance). High purity (99.9 %) Er_2O_3 (density of 8.64 g/cm^3) and Gd_2O_3 (density of 7.41 g/cm^3) nanoparticles with a mean size of 100 nm, supplied from Sigma Aldrich Co., were used as reinforcement agents. The AlSi10Mg feedstock

powder containing 1 wt.% (0.86 At. % Er_2O_3 and 0.93 At. % Gd_2O_3) nanoparticle decorated AlSi10Mg, was prepared by mechanical mixing in ceramic jars with a rotational speed of 60 rpm for 24 h. Fig. 71 shows the characteristics of the particles employed in the current research.

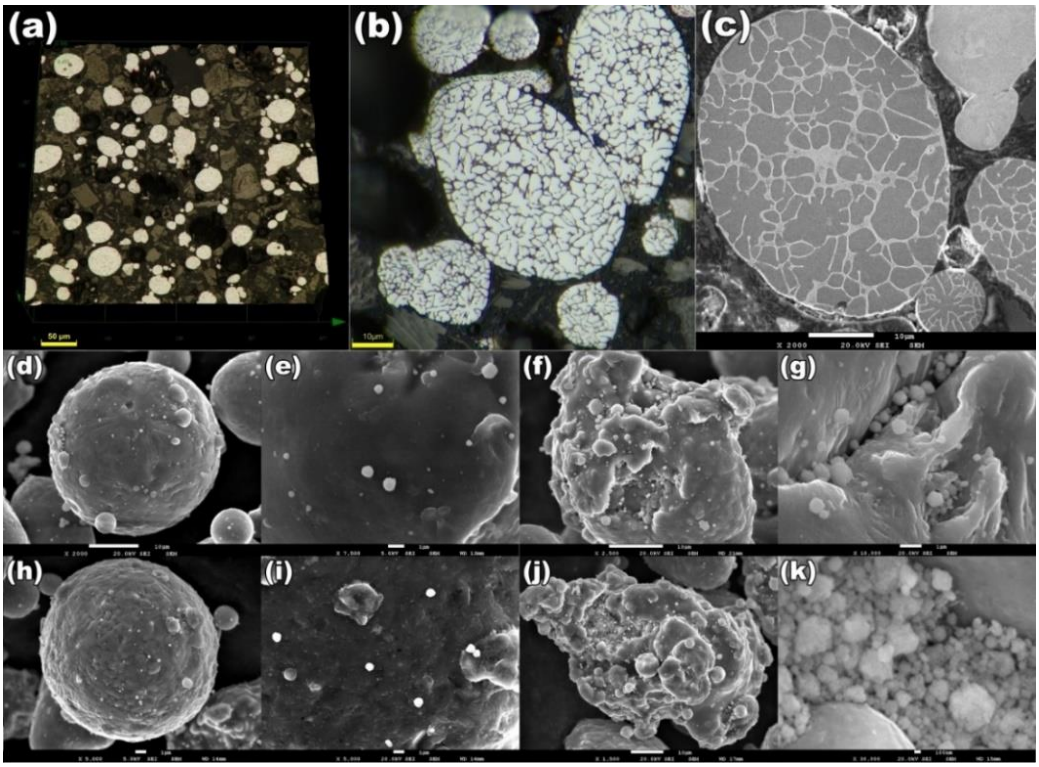

Fig. 71. OM (a, b) and SEM (c) micrographs of the AlSi10Mg particles and SEM images of the Gd_2O_3 (d-g) and Er_2O_3 (h-k) decorated AlSi10Mg particles.

Fig. 71(a,b) represents the AlSi10Mg particles that were mounted, polished, and chemically etched. The size distribution of the particles can be distinguished from Fig. 71(a). Both the optical micrograph of Fig. 71(b) and SEM image of Fig. 71(c) properly manifest the silicon dendrites in the gas atomized AlSi10Mg particles. Fig. 71(d-g) and Fig. 71(h-k) show the distribution of Gd_2O_3 and Er_2O_3 nanoparticles on the surface of AlSi10Mg particles, respectively. According to Fig. 71(d,e) and Fig. 71(h,i), the distribution of the nano-oxide particles on the AlSi10Mg particles having a spherical shape and a rather smooth surface was uniform. On the other hand, comparing Fig. 71(f,g) and Fig. 71(j,k) revealed that significant quantities of the fine oxide particles are aggregated in the cavities formed on the rough surface of the irregular particles. Such a high tendency for agglomeration of nanoparticles can be attributed to the high surface area of nanoparticles that favors the van der Waals interaction among them [190]. Hence, to avoid this problem, some previous researchers have suggested designing supplementary preparation processes like pre-alloying or electrostatic assembly, that involves the coating of matrix powders with nanoparticles [79].

4.2.1.2. Processing

The SLM process was conducted by a commercial system of Concept Laser Mlab cusing R (Germany) equipped with an ytterbium fiber laser source. The maximum power of the laser was 100 W while the wavelength and the spot size of the laser beam were 1070 nm and 70 µm, respectively. The building chamber was filled with high-purity argon, and, during the printing, the oxygen content inside the chamber was kept below 10 ppm. The layer thickness (15 µm) and laser power (95 W) were kept constant while the hatch spacing (95-105 µm) and scanning speed (700-1100 mm/s) were variable during the processing. The laser scanning strategy was based on stripes, with 67° rotation for each successive layer, to minimize the residual stress. The densification and melt pool geometry of the LPBF fabricated specimens can directly be affected by the applied energy density (φ) [191].

$$\varphi = P/ (v \cdot h \cdot t).$$

where P is the laser power, v is the scanning speed, h is the hatching distance, and t is the layer thickness. Applying different processing parameters gives various energy densities, as shown in Table 9Table 1. The fabricated composite samples had a cubic shape with a side length of 10 mm.

Table 9. Processing parameters for LPBF additive manufacturing of AlSi10Mg nanocomposites

Sample code	scan speed (mm/s)	hatching distance (mm)	Laser Power (W)	Layer Thickness (mm)	Energy density (J/mm3)	Gd_2O_3 (R.D %)	Gd_2O_3 (Remelt) (R.D %)	Er_2O_3 (R.D %)	Er_2O_3 (Remelt) (R.D %)
1	1100	0.105	95	0.015	55	96.66	96.3	93.7	96.3
2	1100	0.095	95	0.015	60	95.74	96.77	93.8	96.4
3	900	0.105	95	0.015	67	95.4	95.97	95.2	95.6
4	900	0.095	95	0.015	74	96.21	96.35	95.9	96.7
5	700	0.105	95	0.015	86	95.92	96.22	96.4	97.6
6	700	0.095	95	0.015	95	96.61	96.86	98.8	99

4.2.1.3. Experimental evaluation

The optical analysis of the microstructure was conducted by a Leica 5000 DMI optical microscope equipped with a polarizing lens and an Olympus DSX1000 digital microscope. Electron backscatter diffraction (EBSD) and scanning electron microscope (SEM) microanalysis was carried out via a JEOL (JSM7001F) microscope working at 5-20 kV. The chemical composition of the crystalline phases in the as-printed alloy was investigated by an energy-dispersive x-ray (EDX) spectroscope. Phase identification was realized by an X-Pert Philips x-ray diffractometer (XRD) with $Cu_{K\alpha}$ radiation in a Bragg Brentano configuration in a 2θ range between 10 and 110 (operated at 40 kV, 40 mA, and step size of 0.013 for 25 s per step). Microhardness tests were conducted with five repetitions per sample using a Leica VMHT microhardness tester with an applied load of 100 g for 15 s.

4.2.2. Results and discussion

4.2.2.1. Process parameter optimization

Fig. 72 shows the results of using different process parameters during LPBF printing of Er_2O_3 and Gd_2O_3 reinforced AlSi10Mg alloys on the relative density of the specimens. For Gd_2O_3 reinforced nanocomposite, the increase of laser energy density (VED) could not majorly change the relative density, while for Er_2O_3 reinforced AlSi10Mg the increase of VED improved the densification of the samples and reduced the defects, particularly the lack of fusion [192]. Applying supplementary remelting after printing successive layers minorly affects the Gd_2O_3 composites. Whereas remelting could significantly improve the relative

density of the Er_2O_3 decorated composites, particularly at lower VEDs. Applying the remelting step reduces the thermal gradient within the melt pool and improves the dispersion and reactivity of nano-oxides within the Al matrix [193]. According to Fig. 72, the VED = 95 J/mm^3 as well as supplementally remelting was considered the optimum parameter for printing the densest nanocomposite samples.

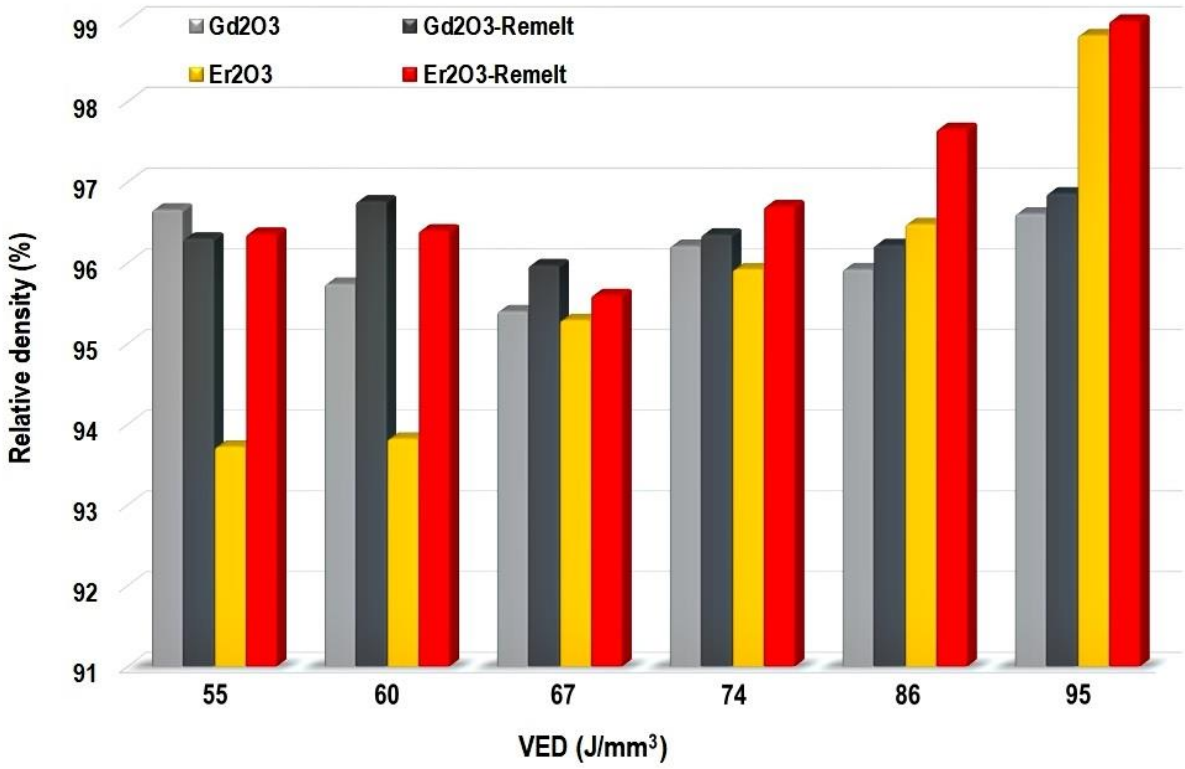

Fig. 72. Variation of the relative density as a function of applied process parameters.

4.2.2.2. Microstructure analysis

Fig. 73 shows the optical micrographs of the non-reinforced AlSi10Mg (Fig. 73(a), Fig. 73(b)) and the reinforced samples by the addition of Er_2O_3 (Fig. 73(c), 73(d)) and Gd_2O_3 (Fig. 73(e), Fig. 73(f)) at different magnifications. As shown, compared with LBPF fabricated AlSi10Mg, the addition of nano-oxide particles could not majorly refine the grain structure but created some defects in the reinforced samples. Optical micrographs of the oxide inoculated samples show that the Er_2O_3 reinforced samples included fewer and finer pores. Likewise, the Er_2O_3 reinforced sample has rather narrower grains than the Gd_2O_3 counterpart does. However, the average size and shape of the melt pools are similar.

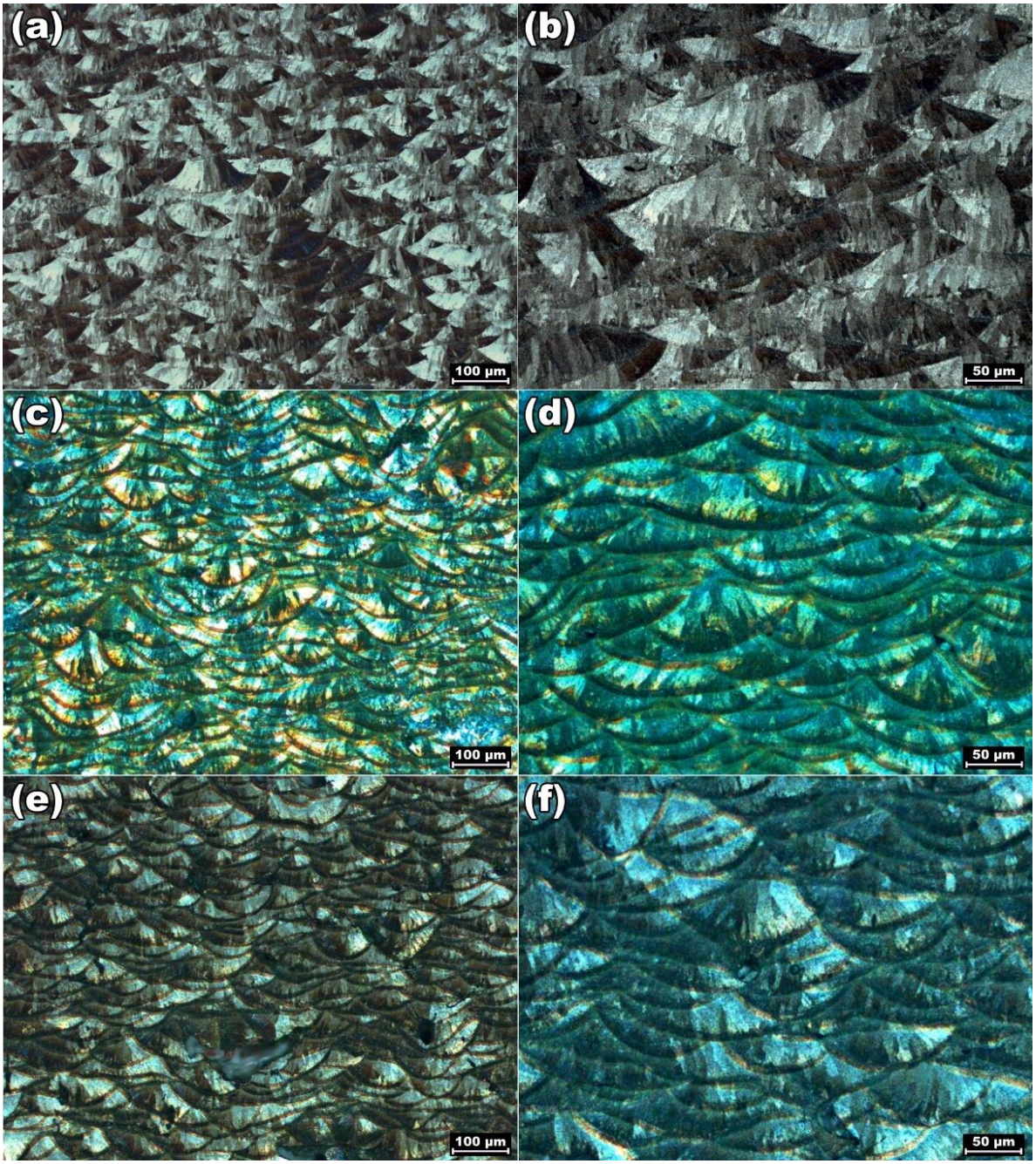

Fig. 73. OM micrographs were taken at two different magnifications from the AlSi10Mg alloy (a, b), and reinforced samples by Er_2O_3 (c, d) and Gd_2O_3 (e, f) fabricated by the VED of 95 J/mm^3.

Fig. 74 shows the microstructure of the reinforced samples at the interface by the building plate. As can be seen, both the Er_2O_3 (Fig. 74(a)) and Gd_2O_3 (Fig. 74(b)) reinforced specimens had a contiguous interface with the Al building substrate. SEM micrographs of Fig. 74 (c, d) also confirm the perfect adhesion of the Er_2O_3-containing nanocomposites to the building plate at the primary printed layers. Fig. 74(e) and Fig. 74(f) display the EBSD analysis of the Er_2O_3 reinforced specimen at the interface with the building plate. According to Fig. 74(e), the first 10 µm of the printed composite is composed of fine equiaxed grains, which do not have any

preferential orientation. Choosing AA6013 as the building plate having constituent alloying elements close to the AlSi10Mg alloy (Mg, Si, and Cu) reduced the possibility of the formation of undesired phases at the first layers. Nevertheless, the higher thermal conductivity of AA6013 (170 W/m.K) [194] compared with AlSi10Mg (110-120 W/m.K) [195] would increase the rate of heat dissipation and accelerate the solidification at the first layers and eventually contribute to the creation of finer grains. Also, the thermal conductivity of Er_2O_3 and Gd_2O_3 is 6.5 W/(m·K) and 6.2 W/(m·K), respectively [196]. Consequently, the addition of these nano-oxides would reduce the overall heat conductivity of the AlSi10Mg-based composites and intensify the heating gradient at their interface with the AA6013 plate. So numerous grains could heterogeneously nucleate on the building plate and solidify in a fraction of a second [197]. Meanwhile, according to the EBSD color patterns, the penetration depth of the laser was so negligible, that it could not affect the grain structure of the AA6013 substrate. In the subsequent layers, the grains became coarser and oriented along the building direction (BD). According to the grain orientation spread (GOS) shown in Fig. 74(f), the finer grains that are formed in the initial layer have a lower GOS value. The GOS is the average angular deviation of each point of a single grain from the average orientation of the grain [198]. Hence, a higher GOS value for a grain implies higher strain accumulation within a grain and vice versa. Therefore, the finer grains formed at the primary layers have a minimum GOS value and a residual strain like with the recrystallized grains. As the further layers were printed, local deviation from the average orientation of the grains increased, and only the regions which had local strain accumulation and heat localization points such as hatch areas were partially recrystallized [199]. These zones can be distinguished as small green grains between the coarse grains of Fig. 74(f).

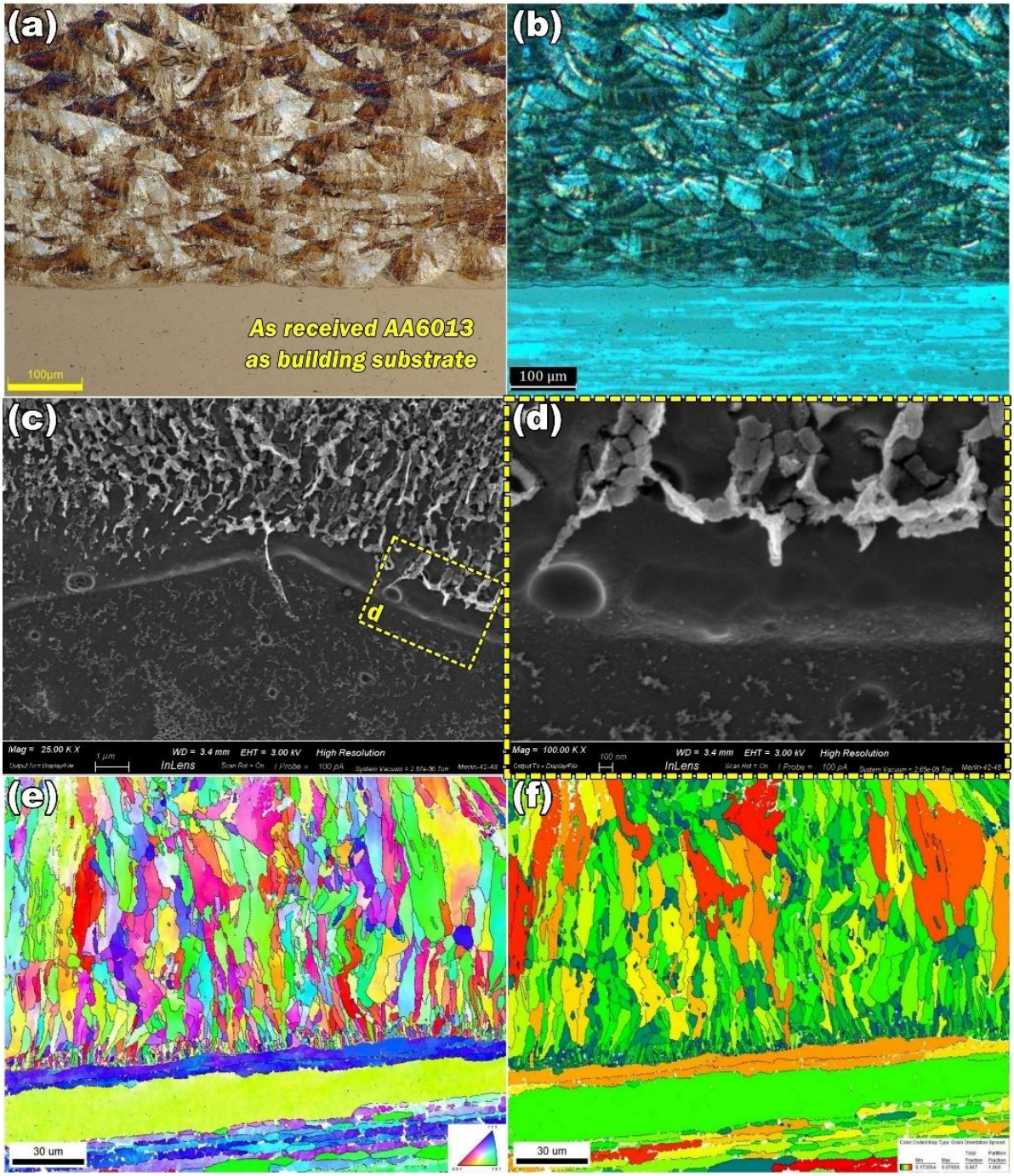

Fig. 74. OM images were provided from the interface of the AA6013 building plate and the Er_2O_3 reinforced (a) and Gd_2O_3 reinforced (b) composites, and SEM (c, d) and EBSD (e, f) analyses were performed on the interface of the Er_2O_3 decorated AlSi10Mg alloy with building plate.

Fig. 75 shows the EBSD analysis of the reinforced samples by the Er_2O_3 (Fig. 75(a-e) and Fig. 75(a1-e1)) and Gd_2O_3 (Fig. 75(f-j) and Fig. 75(f1-j1)) which are printed by the optimum process parameters. Comparing the color map of Fig. 75(a) and Fig. 75(f) illustrates the random orientation of the grains in both reinforced samples by different agents. Additionally, the misorientation angle profiles of Fig. 75(a1) and Fig. 75(f1) points to a higher value of high angle grain boundaries (HAGBs) (15° < misorientation angle) in Er_2O_3 reinforced samples.

Meanwhile, there are a lot of missing points (black dots) in EBSD micrographs, particularly in Gd_2O_3-containing samples, that probably could not be read by the EBSD due to the accumulation of the nanoparticles. Micrographs of Fig. 75(b) and Fig. 75(g) are representing the aspect ratio of grains along the horizontal direction. Since the grains are grown along the building direction (BD), the aspect ratio is lower than one, and the more elongated grains showed a lower aspect ratio (horizontal length/vertical length) and are colored blue. As the morphology of the grains approached the equiaxed shape, the grain's color inclines into green and yellow. As can be seen, the grains are more elongated at the center of melt pools, while the melt pool borders mostly include fine equiaxed grains. According to Fig. 75(b1) and Fig. 75(g1), the distribution histograms of aspect ratio in both samples are almost identical. However, comparing the grain size distribution in Fig. 75(c, c1) and Fig. 75(h, h1) revealed that the Er_2O_3 reinforced specimen has a more uniform grain size distribution with rather finer grains (the higher the ASTM grain size number, the finer the grains). Here again, the presence of finer grains near the melt pool boundaries (blue grains) is evident. Fig. 75(d, d1) and Fig. 75(i, i1) display the difference in GOS micrographs and distribution histogram of the reinforced samples by Er_2O_3 and Gd_2O_3, respectively. As shown, the extent of the distorted grains (with higher GOS) in Er_2O_3 reinforced samples is lower than the Gd_2O_3 counterpart. The GOS histograms also confirm that the average GOS in the Er_2O_3 reinforced sample is slightly lower than the Gd_2O_3 decorated alloy. Variation of kernel average misorientation (KAM) and its related histogram in the reinforced samples by Er_2O_3 and Gd_2O_3 is presented in Fig. 75(e, e1) and Fig. 75(j, j1), respectively. Many researchers argue that the KAM pattern could be used as a criterion to distinguish the distribution of geometrically necessary dislocations (GNDs) [153]. As presented, the regions where the particles are more aggregated (around the melt pool boundaries) have higher KAM levels due to the pinning effect of the nanoparticles and finer microstructure there. Indeed, the accumulation of the nanoparticles increases the dislocation density locally and absorbing the laser heat results in the formation of fine grains in melt pool borders and the rest of the particulate accumulated sites. Furthermore, comparing the GOS micrographs and KAM patterns revealed that the grains with lower KAM and GNDs show a rather lower GOS. Because the generation of GNDs is a lattice response to high thermal stress during to rapid solidification of the molten material [157]. So, in regions that are more affected by the pinning effect of nano-oxides, the lattice must generate more GNDs at the interface of the nanoparticles with the matrix to keep its continuity. So Higher KAM values can be seen in these zones. According to the KAM histograms of Fig. 75(e1, j1) and misorientation profile of

Fig. 75(a1) and Fig. 75(f1) the fraction of low angle grain boundaries (LAGBs) in the Gd_2O_3 reinforced sample is significantly higher.

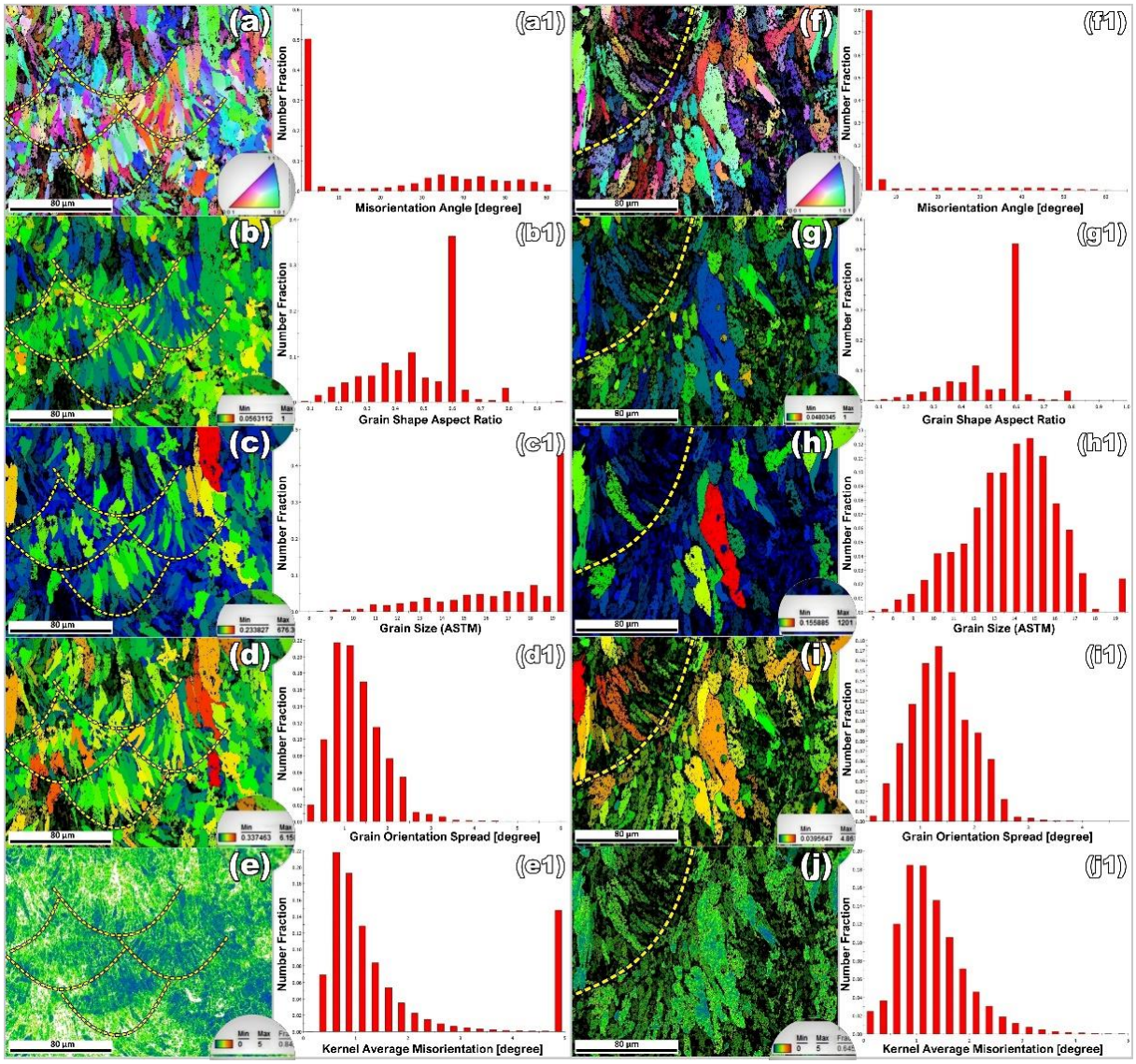

Fig. 75. EBSD maps and their related histograms for Er_2O_3 (a-e and a1-e1) and Gd_2O_3 (f-j and f1-j1) reinforced samples: EBSD color map (a, f), grain shape aspect ratio (b, g), Grain size (c, h), grain orientation spread (GOS) (d, i) and kernel average misorientation (KAM) pattern (e, j).

Fig. 76shows the misorientation profile at the particle-free and particle accumulated zones of Er_2O_3 (Fig. 76(a-c)) and Gd_2O_3 (Fig. 76(d-f)) reinforced samples. According to the indicated arrows in the unique grain color patterns and the related misorientation histograms, in areas with scarce nanoparticles, the major deviation points are the HAGBs. On the other side, the local aggregation of nanoparticles in some regions is accompanied by a successive deviation in orientation. It can be attributed to the passing from the nano-oxide-rich zones or crossing finer grains (more HAGBs) formed because of the refining effect of the nanoparticles.

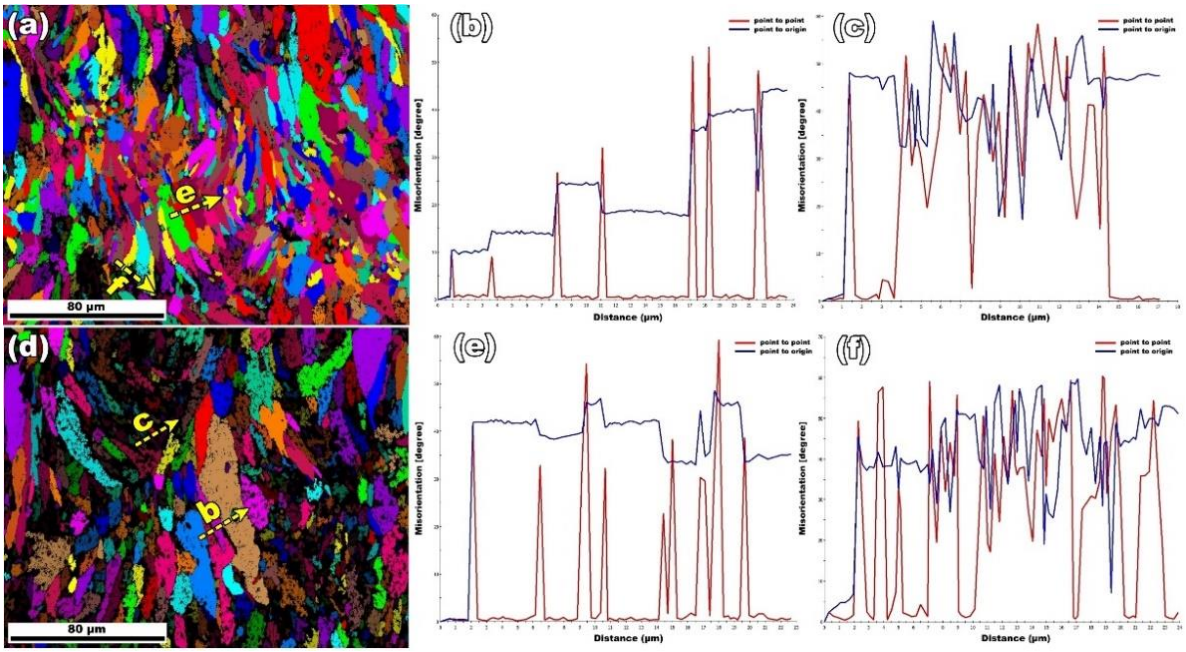

Fig. 76. Unique color pattern and misorientation profile of the particle-free and particle-accumulated zones indicated by arrows Er2O3 (a-c) and in Gd2O3 (d-f) reinforced samples.

Fig. 77 shows the pole figure (PF) and inverse pole figure (IPF) of the reinforced samples with the addition of Er_2O_3 (Fig. 77(a) & Fig. 77(b)) and Gd_2O_3 (Fig. 77(c), Fig. 77(d)), respectively. As can be seen, the Er_2O_3 reinforced sample showed a stronger texture along the BD (001). This result was in accordance with the other EBSD outputs. Because, due to lower particles accumulation, KAM value, and GOS, the orientation of the grains along the BD would be easier.

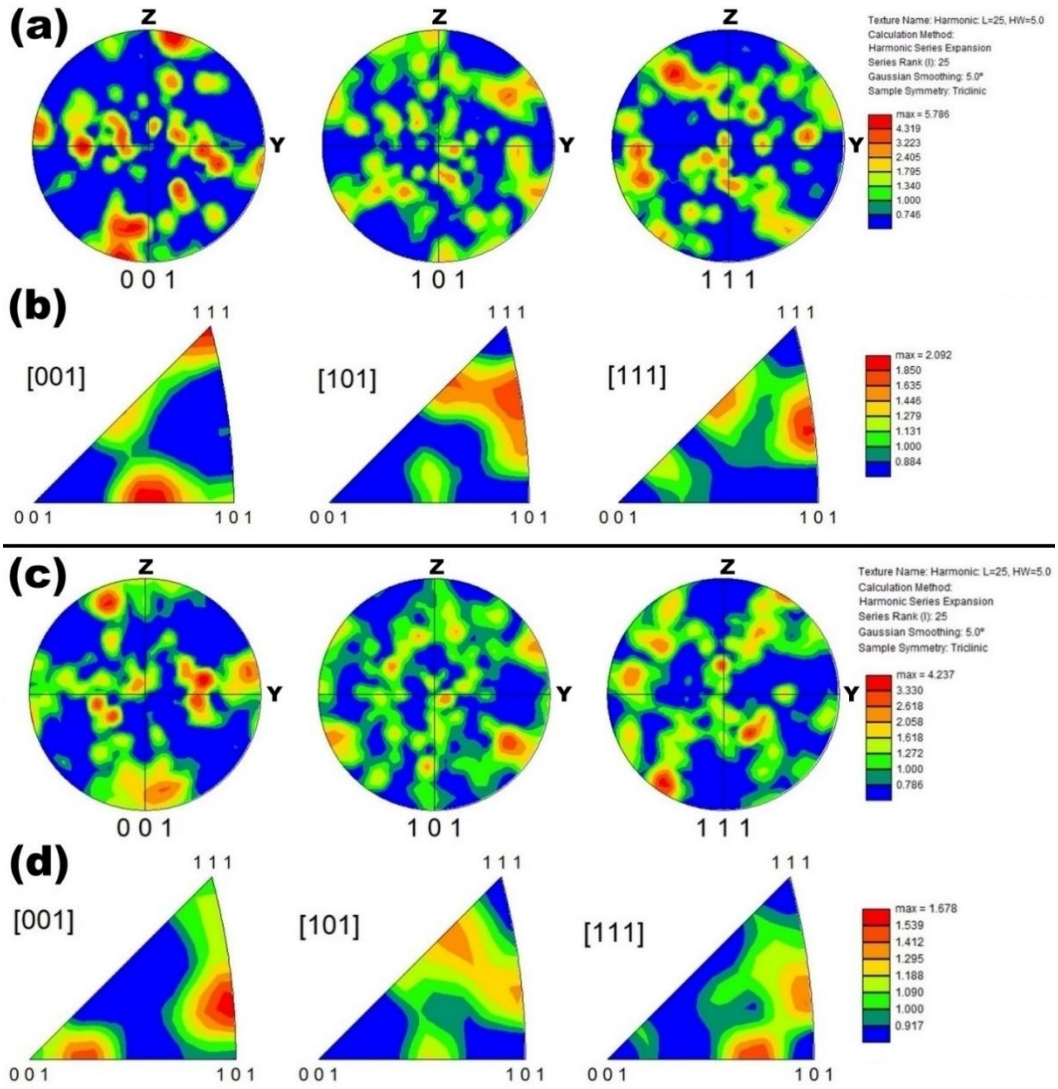

Fig. 77. Pole Figure (PF) and inverse pole figure (IPF) of the reinforced AlSi10Mg alloy with Er_2O_3 (a, b) and Gd_2O_3 (c, d) nanoparticles.

Fig. 78 shows the XRD analysis of the pure nano-oxide powders and the LPBF fabricated nanocomposites. According to Fig. 78(a, c), Er_2O_3 did not make any reaction with the aluminum matrix. On the other side, according to the XRD patterns of Fig. 78(b, d), laser printing of Gd_2O_3 reinforced AlSi10Mg alloy followed by reaction of nano-oxide and aluminum matrix. Resultantly some negligible Al_3Gd phase is formed that the related peaks are labeled in the XRD graph of Fig. 78(d). According to the literature, the melting points of Er_2O_3 (2344 °C) [200] and Gd_2O_3 (2420 °C) [201] are close together, while both of Er and Gd elements have a eutectic point in their phase diagram by Al at 649 °C (Fig. 78(e)) and 634 °C (Fig. 78(f)), respectively. Thus, if the laser beam could partially melt the nano-powders, probably they will react with the aluminum matrix and form eutectic phases. Such a difference in the XRD pattern of the reinforced samples can be attributed to more uniform distribution of

the Er_2O_3 in Al matrix and the finer size of the Er-rich phases so that the XRD could not detect them.

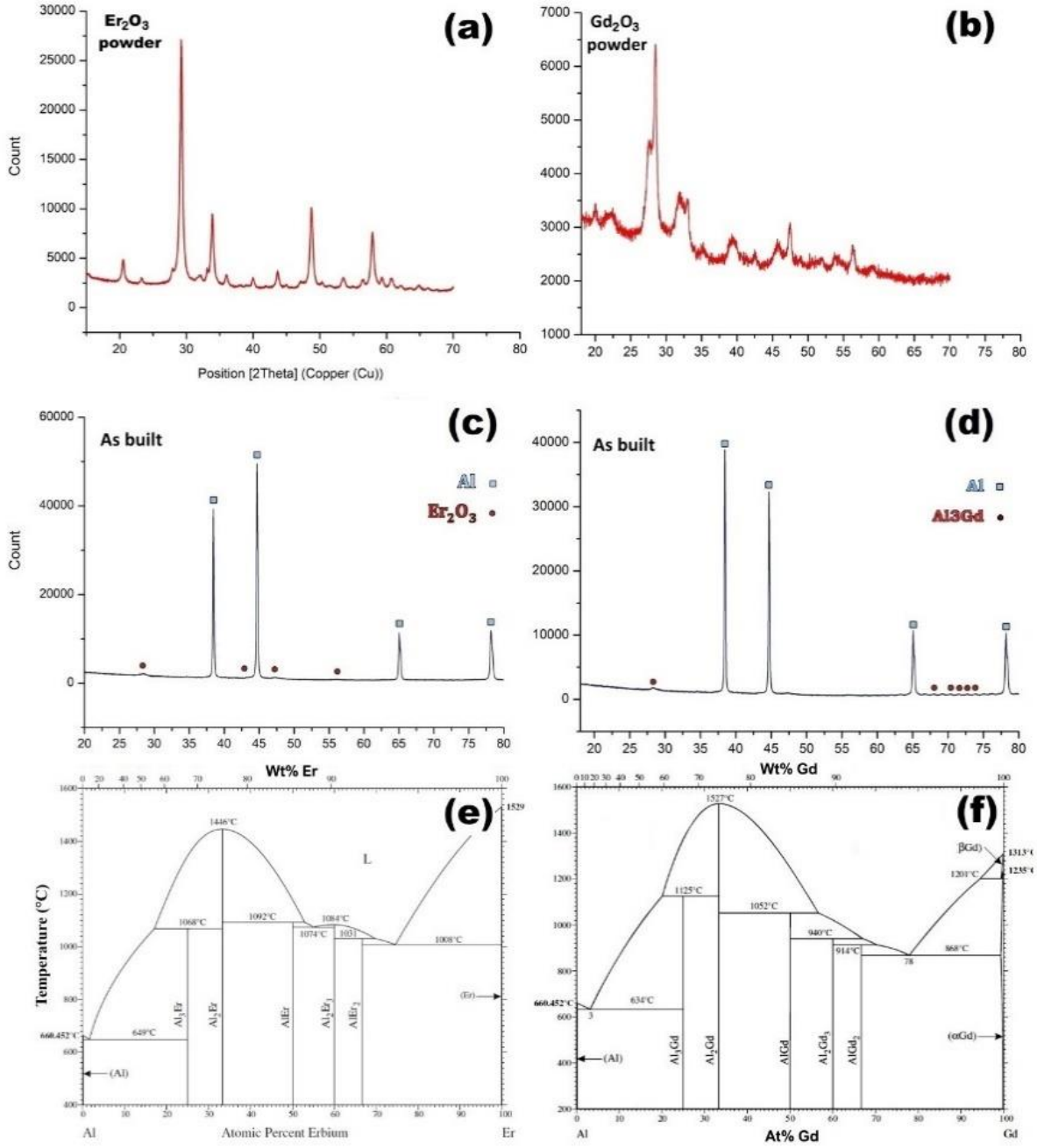

Fig. 78. XRD spectra of the pure powder of Er2O3 (a) and Gd2O3 (b), the reinforced AlSi10Mg alloy by addition of these nano-powders (c and d) and the phase diagrams of the Al-Er [200] (e) and Al-Gd [201] (f).

To find the refinement impact of the nano-oxide particles on silicon cellular structure, SEM characterization was employed, and the results are presented in Fig. 79.

SEM micrographs of Fig. 79(a-f) show the cellular structure in the reinforced sample by Er_2O_3 nano-oxides. As depicted in Fig. 79(a, b), in the Er_2O_3 reinforced sample the local

accumulation of the nanoparticles was not limited to the center of melt pools. But also, in both the border and center of the molten pools, aggregation of the nanoparticles was evident. The EDS point analysis of Fig. 79(b) confirms the accumulation of Er_2O_3 particles at some melt pools. The analogy of the SEM micrographs of Fig. 79(c-f) indicates that when the Er_2O_3 particles swept into the melt pool border, because of high local supercooling, primary cellular dendrites of Si could not find time to grow and form the elongated cellular dendrites. Hence, the melt pool boundaries composed of the finest grains. Additionally, according to Fig. 79(f), uniform dispersion of the Er_2O_3 nanoparticles in the AlSi10Mg matrix would have a prominent refinement effect on the cell structure in MP fine zone alike with our observation on Gd_2O_3 (Fig. 79(l)). SEM micrographs of Fig. 79 (g-l) are related to Gd_2O_3 reinforced sample. According to the Fig. 79 (g, h) the average size of the Si dendrites in the center of the melt pools is finer than at the melt pool boundaries. But at regions with more dispersed nanoparticles, their refinement is intensified (Fig. 79(i, j)). As exhibited in Fig. 79(j) the difference in the size of the Si dendrites at Gd_2O_3-rich zones and the surrounding areas is remarkable (EDS of Fig. 79(i)). It can also be concluded that the laser beam could not uniformly disperse the nano-oxide particles in the Al matrix. Applying higher energy density might enhance the circulation of the molten material but can exacerbate the formation of defects [202, 203]. According to Fig. 79(k, l), the melt pool structure can be subdivided into three different zones according to the morphology and size of the silicon dendrites. The MP fine zone (MP fine) comprises a fine cellular structure, the MP coarse zone (MP coarse) which includes coarse Si cells and the heat-affected zone (HAZ) [9]. MP fine zone and MP coarse zone are located inside the melt pool while the HAZ is a transitional band below the melt pool border as a part of the previous solidified layers [204, 205]. In HAZ, the connected Si branches were broken into fine particles through laser heat [206]. The solidification mode and thickness of the cellular arms depend on the temperature gradient (G) and growth rate of the solid/liquid interface (R) in the molten pool. Different points at the border of the melt pool have diverse thermal gradients (G) and growth rates of the solid/liquid interface (R). The temperature gradient (G) at the surface of the molten metal is lower than in the melt pool depth. Also, the maximum growth rate (R_{max}) equals the scanning speed of the laser at the centerline of the melt pool while R is near zero at the melt pool lateral boundaries. The G/R value determines the solidification mechanism as reduction of the G/R ratio results in activation of the planar, cellular, columnar dendritic, and equiaxed dendritic modes, respectively. Likewise, the $G*R$ value controls the thickness of the cellular structure at different points of the melt pool. The minimum $G*R$ value,

at the bottom of the molten pool, makes a coarse arm spacing while increasing the G^*R value from the molten pool border to the top surface of the melt pool results in the gradual refinement of the arm spacing. Si has a large growth restriction factor (Q) which means Si can strongly restrict the growth of α(Al) grains at the interface of solid/liquid [207]. During solidification of the molten track of AlSi10Mg alloy, Si rapidly provided the required undercooling for the growth of equiaxed dendritic and subsequently started to pile up to extend the supercooling zone. But the epitaxial growth of the cellular dendrites was blocked by the equiaxed grains formed at the center of the melt pools [208]. But comparing Fig. 79(k) and Fig. 79(l) reveals that in some regions, MP fine zone consists of finer Si cells. It could be attributed to the uniform dispersion of the Gd_2O_3 nano-oxides in the Al matrix there. Because, regarding the high melting point of the oxide particles, they could serve as inoculants for the heterogeneous nucleation of new equiaxed grains.

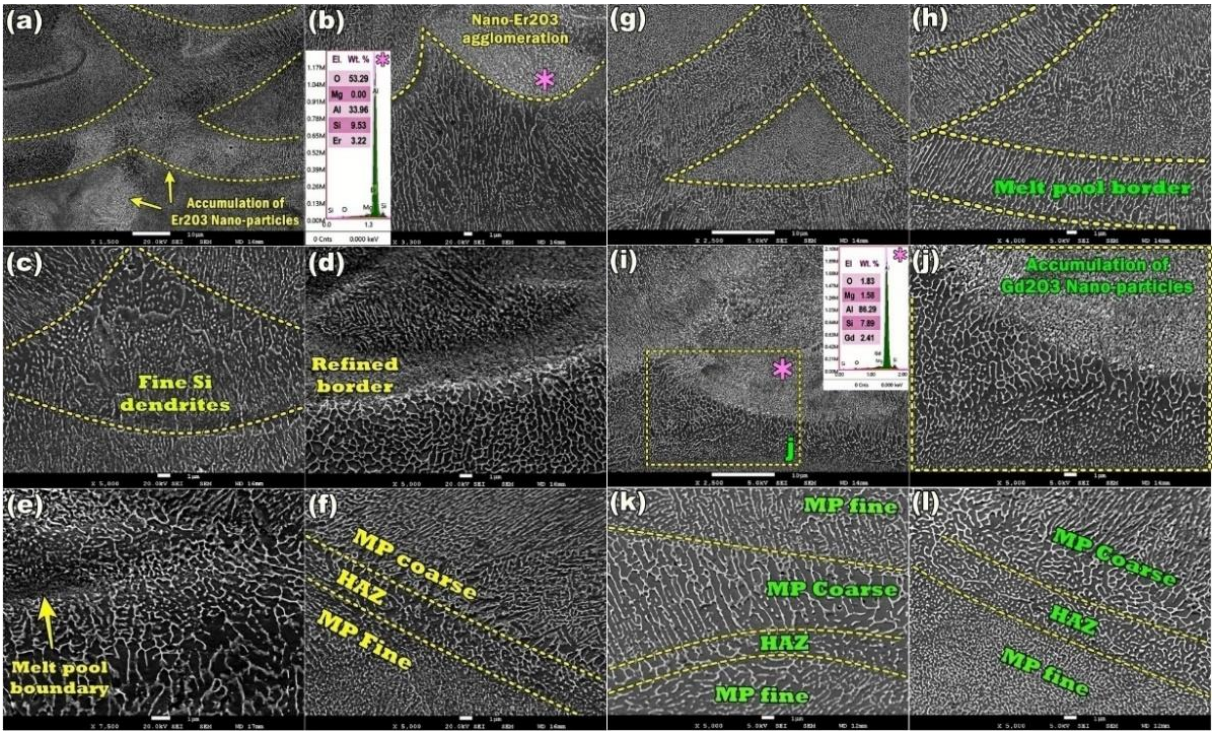

Fig. 79. SEM micrographs of the Er_2O_3 (a-f) and Gd_2O_3 (g-l) reinforced samples.

Nevertheless, the non-uniform distribution of nano-oxide particles could also cause various imperfections which are explained in Fig. 80. Fig. 80(a-c) and Fig. 80(d-i) are related to the Er_2O_3 and Gd_2O_3 reinforced samples, respectively. According to Fig. 80(d), in some regions, the aggregated particles created unreacted coarse chunks. It is well known that significant van der Waals attractive force between the adjacent nanoparticles pushes the nanoparticles to merge and form coarsened masses [92, 197].

Due to the weak adhesion of these phases to the Al matrix, creation of lack of fusion (LOF) defect at these positions is possible. Also, because of the difference in thermal expansion coefficient, during rapid solidification of the laser tracks, some cracks formed close to the oxide-rich locations. Also, according to Fig. 80(e, f), laser heat can cause partial melting of the Gd_2O_3 masses. But these stacked compounds have poor adhesion to the Al matrix and are weak points that can degrade the mechanical strength. Fig. 80(g) shows that uniform dispersion of Gd_2O_3 nanoparticles in the aluminum matrix could remarkably refine the Si cellular structure. However, the accumulation of the nanoparticles in this area resulted in cracking and in the formation of a lack of fusion cavity. Also, weak adherence of the Gd_2O_3 and Al_3Gd masses to the Al matrix could create the LOF during the solidification of molten material (Fig. 80(h)). Fig. 80(i) is taken from the edge of a LOF cavity. As can be seen, a lot of tiny scraps of Gd-rich phases were stuck to the crater and sidewall of the holes and the surrounding faulty area. Comparison of Fig. 80(a, b) with the Gd-rich clusters obviously shows that Er-rich masses had better adhesion with the Al matrix. Additionally, the average size and extent of the LOF defects and destructive impact of stacked particles on adjacent areas were also lower in the Er_2O_3 reinforced specimen (Fig. 80(c)).

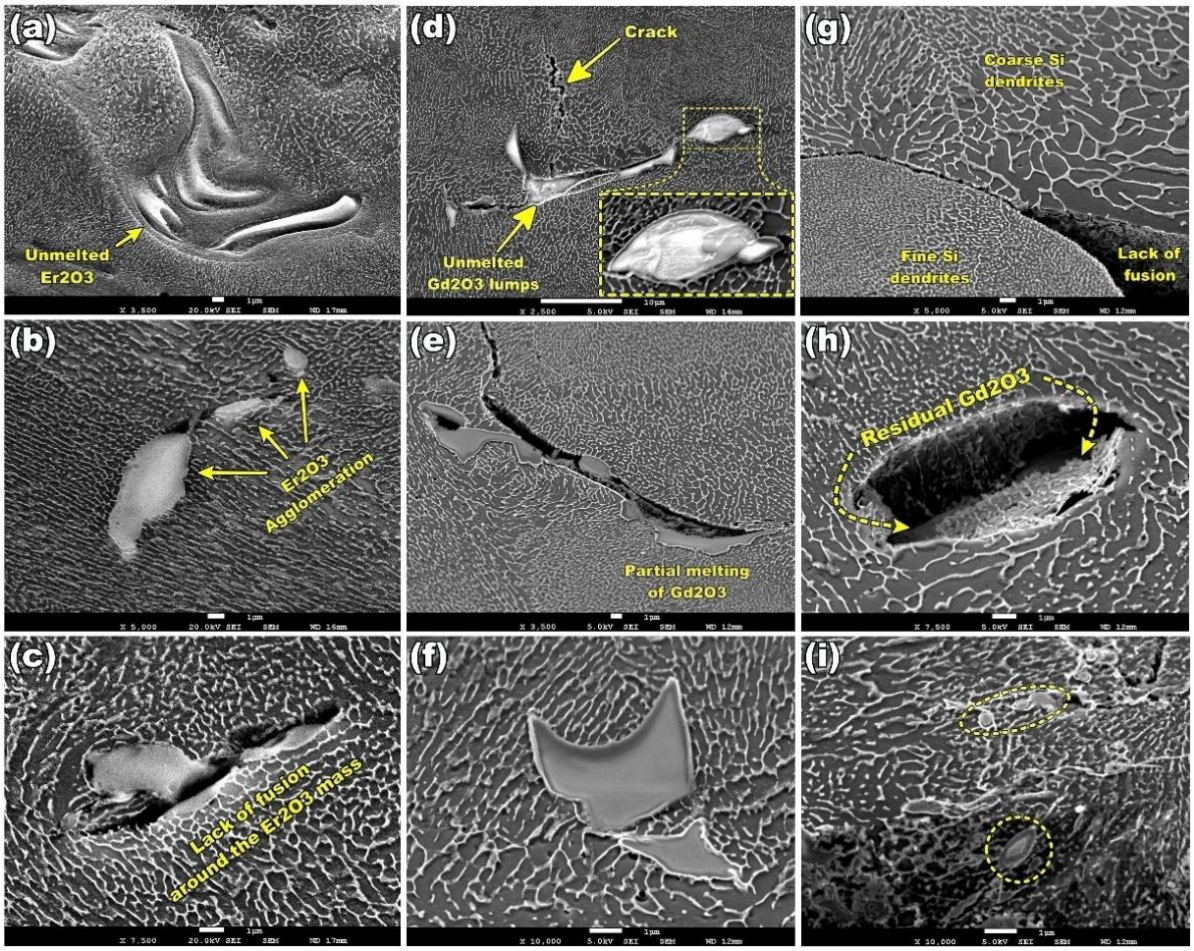

Fig. 80. SEM images taken from various defects and aggregated nanoparticles in the Er_2O_3 (a-c) and Gd_2O_3 (d-i) reinforced specimens.

Fig. 81 shows the elemental distribution map of the Er_2O_3 (Fig. 81(a)) and Gd_2O_3 (Fig. 81(b)) stacked phases in the AlSi10Mg matrix. As can be seen, Gd_2O_3 was less reacted with the Al matrix. Likewise, it seems that existent Mg atoms in the AlSi10Mg matrix showed high affinity to react with the Gd-rich phases. On the other side, the distribution map of the Er_2O_3 reinforced sample implies more homogenous dispersion of the Er-rich phases in the matrix. The color difference between the outer stripe and central part of the stacked phases can be attribute to the local reaction of the oxide nanoparticles with the Al matrix. Furthermore, it is well depicted that compared to the Gd_2O_3 reinforced sample, Er_2O_3 clusters are free of Mg atoms.

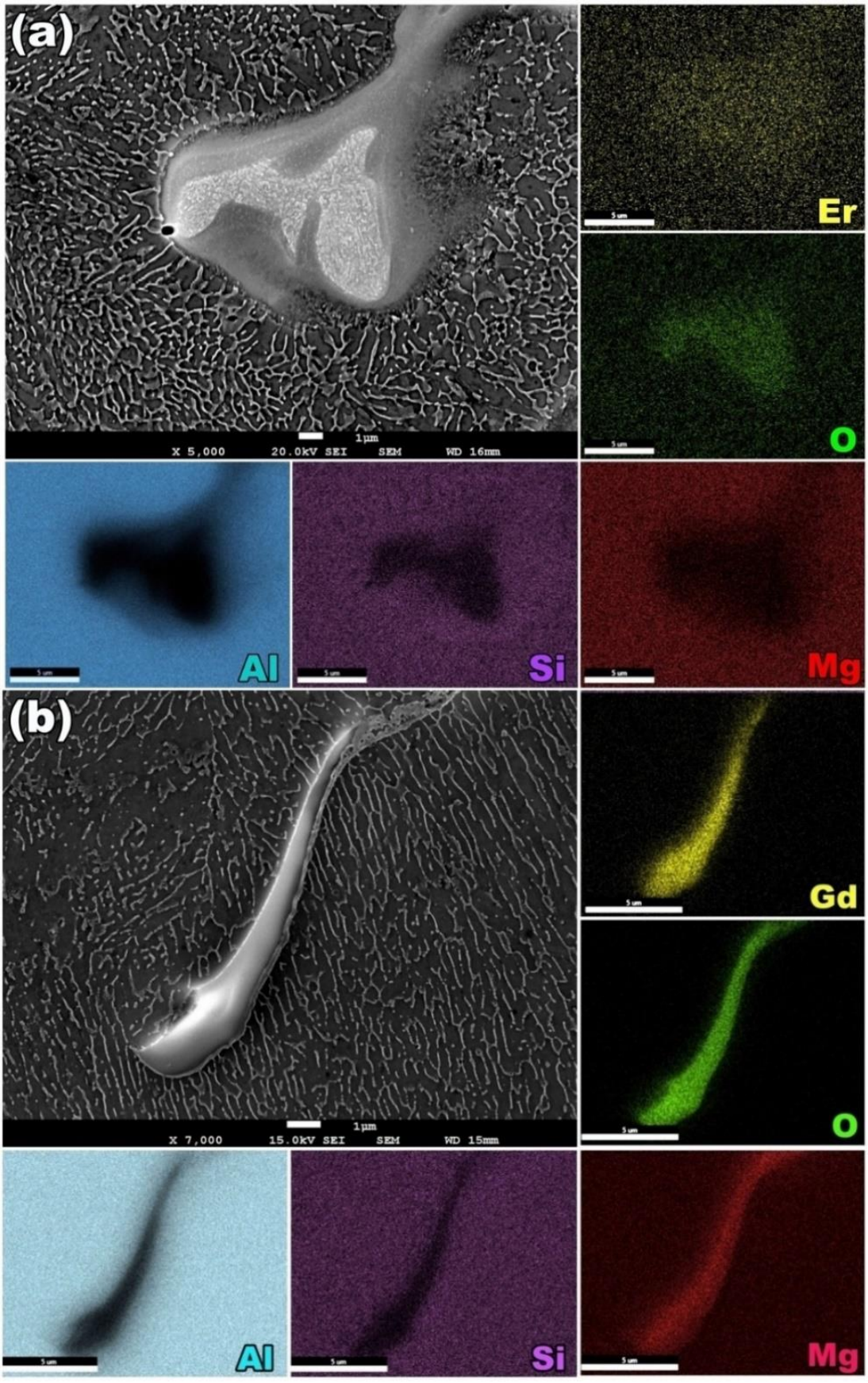

Fig. 81. SEM image and related elemental distribution map of the stacked nanoparticles in AlSi10Mg alloy reinforced by Er_2O_3 (a) and Gd_2O_3 (b).

Fig. 82 properly shows that the accumulation of the nanoparticles and formation of coarse phases cannot play the desired refining role. Besides, however distribution KAM around these phases indicates higher GNDs at their interface with the matrix, GOS distribution patterns do not show any highlighted effect on the recovery of microstructure around them.

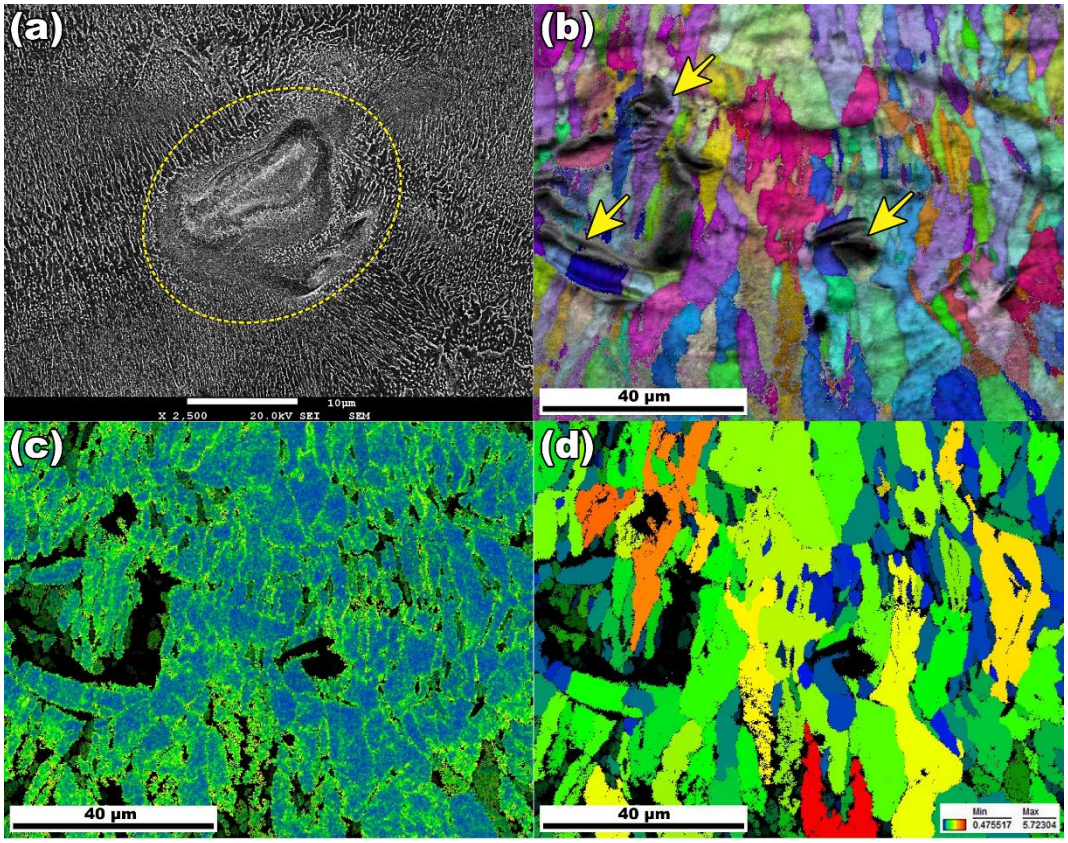

Fig. 82. SEM image (a) and related EBSD color pattern (b), KAM (c) and GOS (d) of microstructural evolutions around the accumulated phases in the Er_2O_3 reinforced sample.

4.3. Hardness evaluation

To evaluate the effect of nano-oxide reinforcement on the mechanical strength of the AlSi10Mg alloy, the microhardness of reinforced samples from the building substrate up to the middle of the specimens was measured and presented as a hardness distribution map (Fig. 83(a, b)). The microhardness of the reinforced AlSi10Mg alloy with other reinforcements was extracted from the literature and compared with the results achieved in the current work (Fig. 83 (c)). Moreover, the details of the process parameters along with size and fraction of different reinforcement agents employed in previous works are presented in the Table 2. According to Fig. 83(a, b), the impact of the Gd_2O_3 on the local enhancement of the hardness was higher than Er_2O_3. This means that Gd-rich clusters are more concentrated and show higher hardness than the Er-rich zones. But the hardness distribution is more uniform in the Er_2O_3 reinforced

sample. The presence of more blue zones in the hardness map of the Gd_2O_3 reinforced sample implies more defective sites with unfavorable strength. This result was in accordance with the VED-relative density graph (Fig. 72) which showed lower relative density (more defects) in Gd_2O_3 reinforced sample after printing by VED = 95 J/mm^3. It has been proved that however uniform dispersion of the nano-particles could majorly refine the microstructure, but the formation of such undesired defects directly degrades the tensile properties of AM fabricated samples [209]. Moreover, apart from the reinforcement agent, additively manufactured AlSi10Mg composites show higher hardness than wrought AlSiMg (AA6013) substrate. The comparative hardness graph in Fig. 73(c) revealed that the introduced nano-oxide particles could improve the hardness of AlSi10Mg alloy more than the average values achieved by several other employed additives. Increment of the hardness through reinforcement by the ceramic particles often resulted in higher yield strength and finally brittle fracture under tensile loading [210]. The significant deviation (scale bars) from the average hardness (solid rectangles) alludes to the fact that obtained values have a wide range of variations. So probably reducing the mass fraction of used nanoparticles or exploiting another preparation method to better disperse the reinforcing particles would ameliorate their strengthening impact on LPBF fabricated AlSi10Mg alloy.

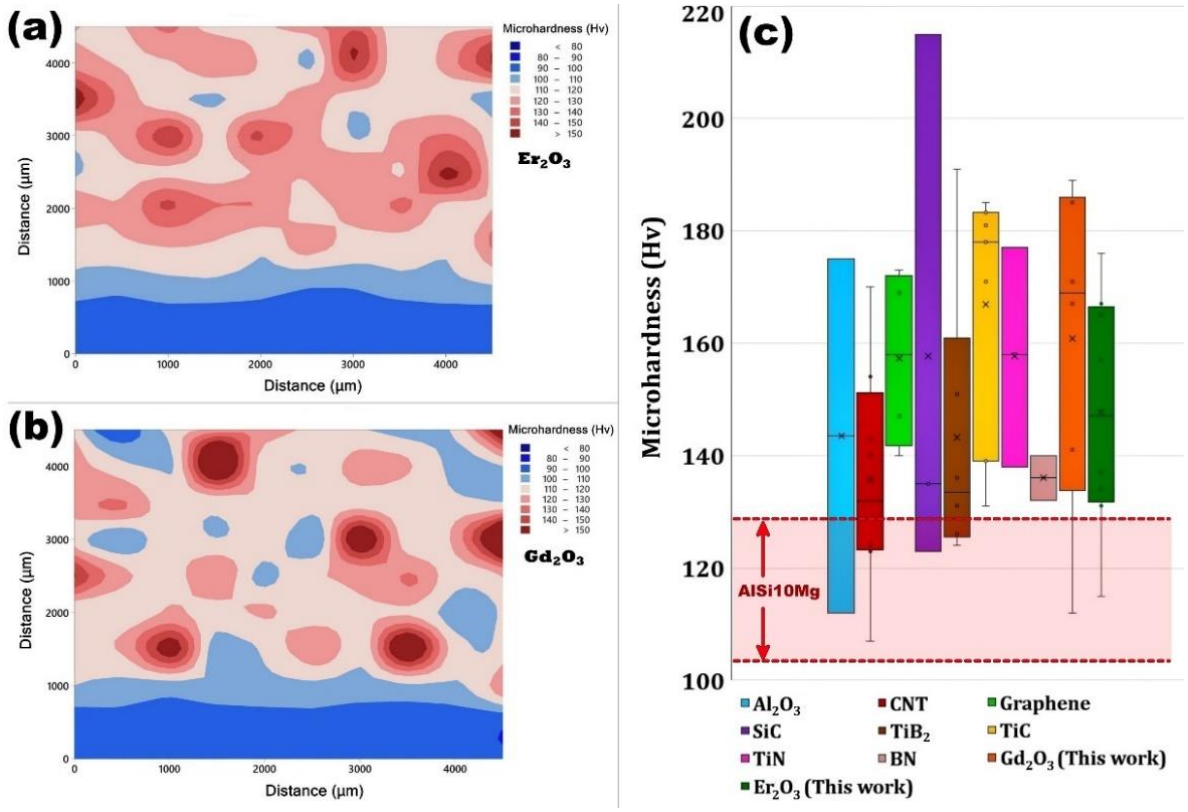

Fig. 83. Microhardness map of reinforced samples by Er_2O_3 (a) and Gd_2O_3 (b) and (c) comparison of the reinforcement's impact of different agents used for development of AlSi10Mg composites.

Table 10. Literature on AlSi10Mg matrix composites fabricated by LPBF additive manufacturing

Ref code	Reinforce Agent (RA)	Wt %	Particle size of the RA	Part. size AlSi10Mg (µm)	Laser diam. (µm)	Layer thickness (µm)	Power (W)	Hatch Dist. (µm)	scan Speed (mm/s)	VED J/mm3	rot. Deg.	Hardness (Hv)
This work	Gd2O3	1	100 nm	15-53	70	15	95	95	700	95	67	112-189
"	Er2O3	1	"	"	"	"	"	"	"	"	"	115-176
[81]	Al2O3	3	3.5 µm	5-120	-	30	240	60	400	333	90	100-112
[211]	Al2O3	10	-	-	-	-	-	-	-	-	-	48.5
[212]	Al2O3	20	-	-	-	-	-	-	-	-	-	175
[213]	CNT	1	8-15 nm	30.7	80	30	360	80	550	273	-	124
[214]	CNT	0.1		15-45	73	-	400	-	-	-	67	125-140
[84]	Graphene	1	20-30 nm	-	-	30	400	130	1200	85	67	169
[85]	CNT	-	-	-	-	30	370	105	1300	90	90	143
[215]	CNT	0.5	25 µm	75-135	-	-	-	-	-	-	-	107
[216]	CNT	0.5	-	25-112	90	30	450	170	2000	44	45	124
[217]	Graphene	0.5	-	20-63	-	30	330	130	-	-	67	173
[218]	CNT	0.5	10-20 nm	5-70	70	50	350	50	2000	70	37	154
[213]	CNT	0.5	8-15 nm	30.7	80	30	360	80	550	273	-	123
[219]	Non-oxidized Graphene	0.1	-	63-150	-	-	-	-	-	-	-	147
[209]	Graphene oxide	0.3	-	27.88	-	30	95	60	200	264	-	101
[214]	Graphene	0.2	-	15-45	73	30	400	90	2250	65.8436	67	140
[220]	CNT	-	8-15 nm	10-50	70	20	160	70	800	143	67	170
[98]	SiC	15	-	44	-	40	490	120	900	114	90	215
[99]	Nano SiC	2	40 nm	39	80	30	150	60	250	334	67	135
[221]	SiC	2	2-10 µm	45-105	-	-	1400	-	1000	-	-	123
[187]	nano TiB2	-	-	-	-	30	275	105	900	97	-	191
[222]	TiB2	-	4 µm	26.5	70	50	350	50	1200	117	37	131
[223]	TiB2	1	-	35.91	-	50	450	50	1800	100	37	126
[224]	TiB2	3.4	3-5 µm	20-63	-	30	275	80	-	-	-	151
[225]	TiB2	-	-	-	70	30	200	70	1200	79	67	136
[226]	TiB2	1	-	-	70	50	400	-	2000	-	37	124
[227]	Nano-TiC	5	50 nm	30	70	50	110	50	150	294	-	181
[86]	TiC	5	45-53 µm	15-53	4mm	-	3000	-	500-800	-	-	183
[228]	TiC	5	25-53 µm	15-53	2mm	-	3500	2000	600	-	-	139
[229]	TiC	5	1.5 µm	30	70	50	100	50	150	267	-	185
[92]	Nano-TiC	5	50 nm	30	70	50	100	50	143	280	-	178
[190]	Nano-TiC	5	50 nm	17-53	100	30	320	130	1100	75	67	131
[230]	TiC	5	1 µm	30	70	30	300	100	1600	62.5	-	171
[231]	Nano-TiN	5	15 nm	30	70	50	200	100	200	200	-	177
[232]	Nano-TiN	2	80 nm	25.7	70	30	100	80	200	208	-	138
[233]	Nano-TiN	4	80 nm	25.7	-	30	200	90	1200	62	15	158
[80]	BN	1	2-5 µm	20-60	-	30	380	200	1300	49	67	138
[234]	AlSi10Mg	-	-	20–63	80	30	350	130	830	108	67	116
[235]	AlSi10Mg	-	-	40	-	30	400	190	1300	54	-	105
[236]	AlSi10Mg	-	-	-	118	25	400	130	-	-	67	130
[237]	AlSi10Mg	-	-	40	50	40	370	150	1900	32.5	-	125

4.3.1. Summary and conclusions

In this work, an identical amount (1 wt.%) of two different nanoparticles of Gd_2O_3 and Er_2O_3 were separately inoculated to the AlSi10Mg powder, and 3D printed by the LPBF additive manufacturing technique. A wide range of processing parameters was evaluated and the microstructure and mechanical properties of the fabricated specimens by optimum parameters were compared together. The results can be summarized as follows:

- Applying the remelting step after printing successive layers could significantly improve the densification of the nanocomposite samples.
- Aggregation of the nanoparticles on the uneven surfaces of irregular shape particles of AlSi10Mg alloy after initial mixing led to the local formation of nanoparticle clusters in printed samples. Due to insufficient adhesion of these coarse chunks to the Al matrix, these areas were prone to the propagation of other types of defects like cracks and lack of fusion cavities.
- Both the XRD and SEM analysis showed some minor intermetallic phases in both the printed nanocomposites. Since both the Gd and Er have a eutectic point in their phase diagram with Al at about 650 °C, even negligible disassociation of the nanoparticles by the laser heat could induce the formation of intermetallic phases.
- EBSD micrographs illustrated that Er_2O_3 was dispersed more uniform than Gd_2O_3 EBSD micrographs illustrated that Er_2O_3 was dispersed more uniform than Gd_2O_3 nanoparticles in the Al matrix and played a more favored role in grain refinement. Also, a comparison of the kernel average misorientation (KAM) patterns with grain orientation spread (GOS) micrographs revealed that particle accumulated zones have higher KAM and lower GOS values. It showed that apart from the pinning role of the nanoparticles on grain refinement, in particle aggregated areas the grains have less freedom to grow and deviate from the average orientation of the grains.
- The microhardness measurement indicated that although the microhardness of the Gd_2O_3 reinforced sample was locally higher than the Er_2O_3 counterpart, due to a rather more uniform distribution of the Er_2O_3 in the Al matrix and less defective areas, it showed a narrower hardness variation range. Also, compared to the other reinforcement agents employed in previous papers, the average hardness of the reinforced samples in the current work was rather higher.

Chapter 5

Conclusion

- In recent years, the focus of additive manufacturing researchers was on finding promising solutions for the challenges of AM and paving the way for replacing conventional production methods with AM. In between, the main concerns were minimizing defects in AM-fabricated parts, reducing production costs, stress relieving the AM-fabricated parts, increasing the strength-to-weight ratio of the printed components, and developing sustainable materials. In the current research, the rapid annealing technique, which involves short-term annealing at temperatures close to the melting point, is employed to speed up the production rate of LPBF-fabricated SS316L samples. To reduce the production cost, water-atomized powders of SS316L with proper particle size satisfying desirable flowability printed with a suitable printing system and fully dense sample compared with the gas-atomized counterpart. To synergistically exploit stacking fault energy reduction of Mn and grain refinement of Ti, co-inoculation of them into SS316L with LPBF in-situ alloying was performed to improve the toughness of the material. Additionally, Ni microparticles and nanoparticles of Er2O3 and Gd2O3 were inoculated into AlSi10Mg by in-situ alloying for structural modification. The main achievements can be summarized as follows:

- The Cellular structures act like a scaffold in additively manufactured materials and removing the cellular structure after 30 seconds annealing at a temperature close to the melting point would result in drop in mechanical properties up to 30%. Also, removing the cellular structure is the first restoration step occurs before recrystallization, while strong texturing in as-printed parts would result in grain growth along the direction with highest strain accumulation (BD) due to the SIGBM phenomenon.

- Higher flowability of the particles would lead to getting a more faultless sample, but it does not mean that using shapeless particles like water atomized powders will eventuate in a spoiled part. Obtained results on 3D printing of the WA and GA powders of ss316L

revealed that due to higher laser absorption, more pinning inclusions, and finer cellular structure, WA sample showed stronger texture along the BD, higher GOS and KAM, higher mechanical properties and finer dimples in fracture surface, superior transvers surface roughness and higher corrosion resistance.

- Addition of ferrite stabilizer elements such as Ti to SS316L induced the formation of the σ phase while Mn addition would replace the Mo in lattice structure of the σ phase. Likewise, agglomeration of the Ti in steel substrate follows by formation of the FeTi and Fe_2Ti intermetallic phases with bcc and hcp structures, respectively. Hence, co-inoculation of the Ti and Mn would lead to formation of a wide range the brittle phases. But due to the activation of the basal slip systems in generated intermetallic phases and formation of numerous GNDs at the interface of the intermetallic chunks and austenitic matrix under intensive thermal shock during the solidification, the interface was preserved from cracking and the reinforced SS316L showed higher strength.

- Ni addition to AlSi10Mg by in-situ alloying resulted in formation of coarse intermetallic chunks of Al_3Ni and partial refinement of the microstructure. Due to the brittleness of the Al_3Ni chunks and weak adhesion of them with the aluminum matrix, the reinforced alloy showed weaker mechanical properties compared to non-reinforced alloy. During short- and long-term annealing of the reinforced samples, the cellular dendrites which were made of Si gradually dissociated while part of the dissolved Si in supersaturated Al matrix were expelled and formed the new Si particles. Due to the Oswald repelling phenomena the fine particles gradually merged and formed coarse polygonal particles of Si and acted as new crack initiation sites. Hence, annealing not only could not spread the Ni in Al matrix, but also worsened the condition and degraded the mechanical properties.

- So far, addition of the lanthanide nano-oxides has been introduced as a promising way for refinement of the microstructure and improvement of the mechanical properties of Al alloys. But the results of the current research on addition of the Gd_2O_3 and Er_2O_3 nano-oxides to AlSi10Mg revealed that stacking the nanoparticles on the surface of the irregular shape particles would result in the formation of the coarse unmelted chunks and lack of fusion defects in reinforced samples. However, applying a remelting could improve the densification and reduce the imperfections. Eventually, due to non-uniform dispersion of

the inoculated particles, in agglomeration points the hardness locally increased while in defective zones the hardness dropped.

References

[1] G. Liu, X. Zhang, X. Chen, Y. He, L. Cheng, M. Huo, J. Yin, F. Hao, S. Chen, P. Wang, Additive manufacturing of structural materials, Materials Science and Engineering: R: Reports, 145 (2021) 100596.

[2] C. Tan, F. Weng, S. Sui, Y. Chew, G. Bi, Progress and perspectives in laser additive manufacturing of key aeroengine materials, International Journal of Machine Tools and Manufacture, 170 (2021) 103804.

[3] U.S. Bertoli, G. Guss, S. Wu, M.J. Matthews, J.M. Schoenung, In-situ characterization of laser-powder interaction and cooling rates through high-speed imaging of powder bed fusion additive manufacturing, Materials & Design, 135 (2017) 385-396.

[4] M. Ali, N. Sabyrov, E. Shehab, Powder bed fusion–laser melting (PBF–LM) process: latest review of materials, process parameter optimization, application, and up-to-date innovative technologies, Progress in Additive Manufacturing, (2022) 1-28.

[5] J. Voigt, T. Bock, U. Hilpert, R. Hellmann, M. Moeckel, Increased relative density and characteristic melt pool. signals at the edge in PBF-LB/M, Additive Manufacturing, (2022) 102798.

[6] Q. Guo, C. Zhao, M. Qu, L. Xiong, L.I. Escano, S.M.H. Hojjatzadeh, N.D. Parab, K. Fezzaa, W. Everhart, T. Sun, In-situ characterization and quantification of melt pool variation under constant input energy density in laser powder bed fusion additive manufacturing process, Additive Manufacturing, 28 (2019) 600-609.

[7] A. Sola, A. Nouri, Microstructural porosity in additive manufacturing: The formation and detection of pores in metal parts fabricated by powder bed fusion, Journal of Advanced Manufacturing and Processing, 1 (2019) e10021.

[8] R. Snell, S. Tammas-Williams, L. Chechik, A. Lyle, E. Hernández-Nava, C. Boig, G. Panoutsos, I. Todd, Methods for rapid pore classification in metal additive manufacturing, JOM, 72 (2020) 101-109.

[9] M.R. Jandaghi, A. Aversa, D. Manfredi, F. Calignano, L. Lavagna, M. Pavese, In situ alloying of AlSi10Mg-5 wt% Ni through laser powder bed fusion and subsequent heat treatment, Journal of Alloys and Compounds, 904 (2022) 164081.

[10] H. Qin, V. Fallah, Q. Dong, M. Brochu, M.R. Daymond, M. Gallerneault, Solidification pattern, microstructure and texture development in Laser Powder Bed Fusion (LPBF) of Al10SiMg alloy, Materials Characterization, 145 (2018) 29-38.

[11] T.F. Murphy, C.T. Schade, Measurement of powder characteristics and quality for additive manufacturing in aerospace alloys, Additive Manufacturing for the Aerospace Industry, (2019) 99-142.

[12] M. Boisvert, D. Christopherson, P. Beaulieu, G. L'Espérance, Treatment of ferrous melts for the improvement of the sphericity of water atomized powders, Materials & Design, 116 (2017) 644-655.

[13] S. Zhang, Q.S. Wei, G.K. Lin, X. Zhao, Y.S. Shi, Effects of powder characteristics on selective laser melting of 316L stainless steel powder, in: Advanced Materials Research, Trans Tech Publ, 2011, pp. 3664-3667.

[14] K. Kassym, A. Perveen, Atomization processes of metal powders for 3D printing, Materials today: proceedings, 26 (2020) 1727-1733.

[15] T. Fedina, J. Sundqvist, J. Powell, A.F. Kaplan, A comparative study of water and gas atomized low alloy steel powders for additive manufacturing, Additive Manufacturing, 36 (2020) 101675.

[16] M. Abdelwahed, R. Casati, A. Larsson, S. Petrella, S. Bengtsson, M. Vedani, On the Recycling of Water Atomized Powder and the Effects on Properties of L-PBF Processed 4130 Low-Alloy Steel, Materials, 15 (2022) 336.

[17] J.P. Kruth, P. Mercelis, J. Van Vaerenbergh, L. Froyen, M. Rombouts, Binding mechanisms in selective laser sintering and selective laser melting, Rapid prototyping journal, (2005).

[18] M. Elahinia, N.S. Moghaddam, M.T. Andani, A. Amerinatanzi, B.A. Bimber, R.F. Hamilton, Fabrication of NiTi through additive manufacturing: A review, Progress in Materials Science, 83 (2016) 630-663.

[19] E. Vasquez, P.-F. Giroux, F. Lomello, M. Nussbaum, H. Maskrot, F. Schuster, P. Castany, Effect of powder characteristics on production of oxide dispersion strengthened Fe14Cr steel by laser powder bed fusion, Powder Technology, 360 (2020) 998-1005.

[20] E. Olakanmi, Selective laser sintering/melting (SLS/SLM) of pure Al, Al–Mg, and Al–Si powders: Effect of processing conditions and powder properties, Journal of Materials Processing Technology, 213 (2013) 1387-1405.
[21] A. Demir, L. Monguzzi, B. Previtali, Selective laser melting of pure Zn with high density for biodegradable implant manufacturing, Addit. Manuf. 15 (2017) 20–28, in.
[22] P. Moghimian, T. Poirié, M. Habibnejad-Korayem, J.A. Zavala, J. Kroeger, F. Marion, F. Larouche, Metal powders in additive manufacturing: A review on reusability and recyclability of common titanium, nickel and aluminum alloys, Additive Manufacturing, 43 (2021) 102017.
[23] A. Mostafaei, J. Toman, E.L. Stevens, E.T. Hughes, Y.L. Krimer, M. Chmielus, Microstructural evolution and mechanical properties of differently heat-treated binder jet printed samples from gas-and water-atomized alloy 625 powders, Acta Materialia, 124 (2017) 280-289.
[24] R. Jiang, L. Monteil, K. Kimes, A. Mostafaei, M. Chmielus, Influence of powder type and binder saturation on binder jet 3D–printed and sintered Inconel 625 samples, The International Journal of Advanced Manufacturing Technology, 116 (2021) 3827-3838.
[25] R. Engeli, T. Etter, S. Hövel, K. Wegener, Processability of different IN738LC powder batches by selective laser melting, Journal of Materials Processing Technology, 229 (2016) 484-491.
[26] A.O. Moghaddam, N.A. Shaburova, M.N. Samodurova, A. Abdollahzadeh, E.A. Trofimov, Additive manufacturing of high entropy alloys: A practical review, Journal of Materials Science & Technology, 77 (2021) 131-162.
[27] D. Herzog, V. Seyda, E. Wycisk, C. Emmelmann, Additive manufacturing of metals, Acta Materialia, 117 (2016) 371-392.
[28] J. SCHRAGE, J.H. SCHLEIFENBAUM, INFLUENCE OF POWDER APPLICATION PARAMETERS ON POWDER BED PROPERTIES AND ON PRODUCTIVITY OF LASER POWDER BED FUSION (L-PBF).
[29] S. Chikosha, L.C. Tshabalala, H. Bissett, M. Lesufi, N.K. Mnguni, T.M. Motsai, T. Manama, S. Hoosain, Spheroidisation of Stainless Steel Powder for Additive Manufacturing, Metals, 11 (2021) 1081.
[30] J.-Y. Park, K.B. Park, J.-W. Kang, H.G. Kim, N.-M. Hwang, H.-K. Park, Spheroidization behavior of water-atomized 316 stainless steel powder by inductively-coupled thermal plasma, Materials Today Communications, 25 (2020) 101488.
[31] S. Mirzababaei, S. Pasebani, A review on binder jet additive manufacturing of 316L stainless steel, Journal of Manufacturing and Materials Processing, 3 (2019) 82.
[32] S. Pasebani, M. Ghayoor, S. Badwe, H. Irrinki, S.V. Atre, Effects of atomizing media and post processing on mechanical properties of 17-4 PH stainless steel manufactured via selective laser melting, Additive Manufacturing, 22 (2018) 127-137.
[33] L. Haferkamp, A. Spierings, K. Wegener, K. Riener, S. Ziegelmeier, G. Leichtfried, The Influence of Particle Shape, Powder Flowability, and Powder Layer Density on Part Density in Laser Powder Bed Fusion, Metals, 11 (2021).
[34] S. Cacace, Q. Semeraro, Influence of the atomization medium on the properties of stainless steel SLM parts, Additive Manufacturing, 36 (2020) 101509.
[35] I. Rishmawi, A. Rogalsky, M. Vlasea, A. Molavi-Kakhki, Comparison of the master sinter curves of water- and gas-atomized AISI 4340 low-alloy steel in binder jetting additive manufacturing, Additive Manufacturing, 48 (2021) 102381.
[36] N. Tepylo, X. Huang, P.C. Patnaik, Laser-based additive manufacturing technologies for aerospace applications, Advanced Engineering Materials, 21 (2019) 1900617.
[37] J.S. Weaver, J. Whiting, V. Tondare, C. Beauchamp, M. Peltz, J. Tarr, T.Q. Phan, M.A. Donmez, The effects of particle size distribution on the rheological properties of the powder and the mechanical properties of additively manufactured 17-4 PH stainless steel, Additive Manufacturing, 39 (2021) 101851.
[38] A. Hatem, C. Schulz, T. Schlaefer, J.T. Boobhun, N. Stanford, C. Hall, Influence of laser absorption by water- and gas-atomised powder feedstock on Laser Metal Deposition of AISI 431 stainless steel, Additive Manufacturing, 47 (2021) 102242.
[39] H. Irrinki, J.S.D. Jangam, S. Pasebani, S. Badwe, J. Stitzel, K. Kate, O. Gulsoy, S.V. Atre, Effects of particle characteristics on the microstructure and mechanical properties of 17-4 PH stainless steel fabricated by laser-powder bed fusion, Powder Technology, 331 (2018) 192-203.

[40] M. Jandaghi, A. Saboori, L. Iuliano, M. Pavese, On the effect of rapid annealing on the microstructure and mechanical behavior of additively manufactured stainless steel by Laser Powder Bed Fusion, Materials Science and Engineering: A, 828 (2021) 142109.
[41] S. Hoeges, A. Zwiren, C. Schade, Additive manufacturing using water atomized steel powders, Metal Powder Report, 72 (2017) 111-117.
[42] H. Ikehata, E. Jägle, Evaluation of microstructure and tensile properties of grain-refined, Ti-alloyed ferritic stainless steel fabricated by laser powder bed fusion, Materials Science and Engineering: A, 818 (2021) 141365.
[43] D. Zhang, D. Qiu, M.A. Gibson, Y. Zheng, H.L. Fraser, D.H. StJohn, M.A. Easton, Additive manufacturing of ultrafine-grained high-strength titanium alloys, Nature, 576 (2019) 91-95.
[44] Y. Guo, W. Wei, W. Shi, B. Zhang, X. Zhou, S. Wen, X. Wu, K. Gao, L. Rong, H. Huang, Effect of Er and Zr additions and aging treatment on grain refinement of aluminum alloy fabricated by laser powder bed fusion, Journal of Alloys and Compounds, 912 (2022) 165237.
[45] Q. Jia, P. Rometsch, P. Kürnsteiner, Q. Chao, A. Huang, M. Weyland, L. Bourgeois, X. Wu, Selective laser melting of a high strength AlMnSc alloy: Alloy design and strengthening mechanisms, Acta Materialia, 171 (2019) 108-118.
[46] Z. Xiong, X. Pang, S. Liu, Z. Li, R. Misra, Hierarchical refinement of nickel-microalloyed titanium during additive manufacturing, Scripta Materialia, 195 (2021) 113727.
[47] P. Barriobero-Vila, J. Gussone, A. Stark, N. Schell, J. Haubrich, G. Requena, Peritectic titanium alloys for 3D printing, Nature communications, 9 (2018) 1-9.
[48] A. Charmi, R. Falkenberg, L. Ávila, G. Mohr, K. Sommer, A. Ulbricht, M. Sprengel, R.S. Neumann, B. Skrotzki, A. Evans, Mechanical anisotropy of additively manufactured stainless steel 316L: An experimental and numerical study, Materials Science and Engineering: A, 799 (2021) 140154.
[49] E. Liverani, S. Toschi, L. Ceschini, A. Fortunato, Effect of selective laser melting (SLM) process parameters on microstructure and mechanical properties of 316L austenitic stainless steel, Journal of Materials Processing Technology, 249 (2017) 255-263.
[50] Q. Zeng, K. Gan, Y. Wang, Effect of Heat Treatment on Microstructures and Mechanical Behaviors of 316L Stainless Steels Synthesized by Selective Laser Melting, Journal of Materials Engineering and Performance, 30 (2021) 409-422.
[51] J. Kluczyński, L. Śnieżek, K. Grzelak, A. Oziębło, K. Perkowski, J. Torzewski, I. Szachogłuchowicz, K. Gocman, M. Wachowski, B. Kania, Comparison of different heat treatment processes of selective laser melted 316L steel based on analysis of mechanical properties, Materials, 13 (2020) 3805.
[52] D. Kong, C. Dong, X. Ni, L. Zhang, J. Yao, C. Man, X. Cheng, K. Xiao, X. Li, Mechanical properties and corrosion behavior of selective laser melted 316L stainless steel after different heat treatment processes, Journal of Materials Science & Technology, 35 (2019) 1499-1507.
[53] T. Ronneberg, C.M. Davies, P.A. Hooper, Revealing relationships between porosity, microstructure and mechanical properties of laser powder bed fusion 316L stainless steel through heat treatment, Materials & Design, 189 (2020) 108481.
[54] J. Reijonen, R. Björkstrand, T. Riipinen, Z. Que, S. Metsä-Kortelainen, M. Salmi, Cross-testing laser powder bed fusion production machines and powders: Variability in mechanical properties of heat-treated 316L stainless steel, Materials & Design, 204 (2021) 109684.
[55] Q. Chao, S. Thomas, N. Birbilis, P. Cizek, P.D. Hodgson, D. Fabijanic, The effect of post-processing heat treatment on the microstructure, residual stress and mechanical properties of selective laser melted 316L stainless steel, Materials Science and Engineering: A, 821 (2021) 141611.
[56] D. Riabov, E. Hryha, M. Rashidi, S. Bengtsson, L. Nyborg, Effect of atomization on surface oxide composition in 316L stainless steel powders for additive manufacturing, Surface and Interface Analysis, 52 (2020) 694-706.
[57] E. Ura-Bińczyk, A. Dobkowska, P. Bazarnik, J. Ciftci, A. Krawczyńska, W. Chromiński, T. Wejrzanowski, R. Molak, R. Sitek, T. Płociński, J. Jaroszewicz, J. Mizera, Effect of annealing on the mechanical and corrosion properties of 316L stainless steel manufactured by laser powder bed fusion, Materials Science and Engineering: A, 860 (2022) 144263.

[58] T. Voisin, J.-B. Forien, A. Perron, S. Aubry, N. Bertin, A. Samanta, A. Baker, Y.M. Wang, New insights on cellular structures strengthening mechanisms and thermal stability of an austenitic stainless steel fabricated by laser powder-bed-fusion, Acta Materialia, 203 (2021) 116476.
[59] C. Zhou, S. Hu, Q. Shi, H. Tao, Y. Song, J. Zheng, P. Xu, L. Zhang, Improvement of corrosion resistance of SS316L manufactured by selective laser melting through subcritical annealing, Corrosion Science, 164 (2020) 108353.
[60] S. Waqar, J. Liu, Q. Sun, K. Guo, J. Sun, Effect of post-heat treatment cooling on microstructure and mechanical properties of selective laser melting manufactured austenitic 316L stainless steel, Rapid Prototyping Journal, (2020).
[61] M. Lodhi, K. Deen, M. Greenlee-Wacker, W. Haider, Additively manufactured 316L stainless steel with improved corrosion resistance and biological response for biomedical applications, Additive Manufacturing, 27 (2019) 8-19.
[62] C. Zhou, J. Wang, S. Hu, H. Tao, B. Fang, L. Li, J. Zheng, L. Zhang, Enhanced corrosion resistance of additively manufactured 316L stainless steel after heat treatment, J. Electrochem. Soc., 167 (2020) 141504.
[63] Y.M. Wang, T. Voisin, J.T. McKeown, J. Ye, N.P. Calta, Z. Li, Z. Zeng, Y. Zhang, W. Chen, T.T. Roehling, Additively manufactured hierarchical stainless steels with high strength and ductility, Nature materials, 17 (2018) 63-71.
[64] A. Aversa, A. Saboori, E. Librera, M. de Chirico, S. Biamino, M. Lombardi, P. Fino, The Role of Directed Energy Deposition Atmosphere Mode on the Microstructure and Mechanical Properties of 316L Samples, Additive Manufacturing, (2020) 101274.
[65] E.M. Dematteis, N. Berti, F. Cuevas, M. Latroche, M. Baricco, Substitutional effects in TiFe for hydrogen storage: a comprehensive review, Materials Advances, 2 (2021) 2524-2560.
[66] G. Requena, K. Bugelnig, F. Sket, S. Milenkovic, G. Rödler, A. Weisheit, J. Gussone, J. Haubrich, P. Barriobero-Vila, T. Pusztai, Ultrafine Fe-Fe2Ti eutectics by directed energy deposition: Insights into microstructure formation based on experimental techniques and phase field modelling, Additive Manufacturing, 33 (2020) 101133.
[67] A. Durga, N.H. Pettersson, S.B.A. Malladi, Z. Chen, S. Guo, L. Nyborg, G. Lindwall, Grain refinement in additively manufactured ferritic stainless steel by in situ inoculation using pre-alloyed powder, Scripta Materialia, 194 (2021) 113690.
[68] Z. Fan, C. Li, H. Yang, Z. Liu, Effects of TiC nanoparticle inoculation on the hot-tearing cracks and grain refinement of additively-manufactured AA2024 Al alloys, Journal of Materials Research and Technology, (2022).
[69] F. Kies, P. Köhnen, M.B. Wilms, F. Brasche, K.G. Pradeep, A. Schwedt, S. Richter, A. Weisheit, J.H. Schleifenbaum, C. Haase, Design of high-manganese steels for additive manufacturing applications with energy-absorption functionality, Materials & Design, 160 (2018) 1250-1264.
[70] J. Delahaye, J.T. Tchuindjang, J. Lecomte-Beckers, O. Rigo, A. Habraken, A. Mertens, Influence of Si precipitates on fracture mechanisms of AlSi10Mg parts processed by Selective Laser Melting, Acta Materialia, 175 (2019) 160-170.
[71] T.-H. Park, M.-S. Baek, H. Hyer, Y. Sohn, K.-A. Lee, Effect of direct aging on the microstructure and tensile properties of AlSi10Mg alloy manufactured by selective laser melting process, Materials Characterization, 176 (2021) 111113.
[72] X. Liu, C. Zhao, X. Zhou, Z. Shen, W. Liu, Microstructure of selective laser melted AlSi10Mg alloy, Materials & Design, 168 (2019) 107677.
[73] A. Hadadzadeh, B.S. Amirkhiz, A. Odeshi, J. Li, M. Mohammadi, Role of hierarchical microstructure of additively manufactured AlSi10Mg on dynamic loading behavior, Additive Manufacturing, 28 (2019) 1-13.
[74] V. Fallah, A. Korinek, B. Raeisinia, M. Gallerneault, S. Esmaeili, Early-stage precipitation phenomena and composition-dependent hardening in Al-Mg-Si-(Cu) alloys, in: Mater. Sci. Forum, Trans Tech Publ, 2014, pp. 933-938.
[75] A.H. Maamoun, M. Elbestawi, G.K. Dosbaeva, S.C. Veldhuis, Thermal post-processing of AlSi10Mg parts produced by Selective Laser Melting using recycled powder, Additive Manufacturing, 21 (2018) 234-247.
[76] N.T. Aboulkhair, I. Maskery, C. Tuck, I. Ashcroft, N.M. Everitt, Improving the fatigue behaviour of a selectively laser melted aluminium alloy: Influence of heat treatment and surface quality, Materials & Design, 104 (2016) 174-182.

[77] W. Li, S. Li, J. Liu, A. Zhang, Y. Zhou, Q. Wei, C. Yan, Y. Shi, Effect of heat treatment on AlSi10Mg alloy fabricated by selective laser melting: Microstructure evolution, mechanical properties and fracture mechanism, Materials Science and Engineering: A, 663 (2016) 116-125.
[78] T. Kimura, T. Nakamoto, Microstructures and mechanical properties of A356 (AlSi7Mg0. 3) aluminum alloy fabricated by selective laser melting, Materials & Design, 89 (2016) 1294-1301.
[79] Q. Tan, J. Zhang, N. Mo, Z. Fan, Y. Yin, M. Bermingham, Y. Liu, H. Huang, M.-X. Zhang, A novel method to 3D-print fine-grained AlSi10Mg alloy with isotropic properties via inoculation with LaB6 nanoparticles, Additive Manufacturing, 32 (2020) 101034.
[80] A.S. Konopatsky, D.G. Kvashnin, S. Corthay, I. Boyarintsev, K.L. Firestein, A. Orekhov, N. Arkharova, D.V. Golberg, D.V. Shtansky, Microstructure evolution during AlSi10Mg molten alloy/BN microflake interactions in metal matrix composites obtained through 3D printing, Journal of Alloys and Compounds, 859 (2021) 157765.
[81] Y. Chen, S. Song, S. Zhu, X. Cui, F. Zhao, Selective laser remelting of in-situ Al2O3 particles reinforced AlSi10Mg matrix composite: Densification, microstructure and microhardness, Vacuum, (2021) 110365.
[82] Y. Xiao, Z. Bian, Y. Wu, G. Ji, Y. Li, M. Li, Q. Lian, Z. Chen, A. Addad, H. Wang, Effect of nano-TiB2 particles on the anisotropy in an AlSi10Mg alloy processed by selective laser melting, Journal of Alloys and Compounds, 798 (2019) 644-655.
[83] M.L. Montero-Sistiaga, M. Godino-Martinez, K. Boschmans, J.-P. Kruth, J. Van Humbeeck, K. Vanmeensel, Microstructure evolution of 316L produced by HP-SLM (high power selective laser melting), Additive Manufacturing, 23 (2018) 402-410.
[84] Z. Zhao, P. Bai, R. Misra, M. Dong, R. Guan, Y. Li, J. Zhang, L. Tan, J. Gao, T. Ding, AlSi10Mg alloy nanocomposites reinforced with aluminum-coated graphene: selective laser melting, interfacial microstructure and property analysis, Journal of Alloys and Compounds, 792 (2019) 203-214.
[85] L. Jiang, T. Liu, C. Zhang, K. Zhang, M. Li, T. Ma, W. Liao, Preparation and mechanical properties of CNTs-AlSi10Mg composite fabricated via selective laser melting, Materials Science and Engineering: A, 734 (2018) 171-177.
[86] C. Li, S. Sun, C. Liu, Q. Lu, P. Ma, Y. Wang, Microstructure and mechanical properties of TiC/AlSi10Mg alloy fabricated by laser additive manufacturing under high-frequency micro-vibration, Journal of Alloys and Compounds, 794 (2019) 236-246.
[87] P. Rometsch, Q. Jia, K.V. Yang, X. Wu, Aluminum alloys for selective laser melting–towards improved performance, in: Additive Manufacturing for the Aerospace Industry, Elsevier, 2019, pp. 301-325.
[88] M. Wang, B. Song, Q. Wei, Y. Zhang, Y. Shi, Effects of annealing on the microstructure and mechanical properties of selective laser melted AlSi7Mg alloy, Materials Science and Engineering: A, 739 (2019) 463-472.
[89] S. Tang, R. Ummethala, C. Suryanarayana, J. Eckert, K.G. Prashanth, Z. Wang, Additive Manufacturing of Aluminum-Based Metal Matrix Composites—A Review, Advanced Engineering Materials, (2021) 2100053.
[90] H. Liao, J. Zhu, S. Chang, G. Xue, J. Pang, H. Zhu, Lunar regolith-AlSi10Mg composite fabricated by selective laser melting, Vacuum, 187 (2021) 110122.
[91] J. Jue, D. Gu, Selective laser melting additive manufacturing of in situ Al2Si4O10/Al composites: Microstructural characteristics and mechanical properties, J. Compos. Mater., 51 (2017) 519-532.
[92] D. Gu, H. Wang, D. Dai, F. Chang, W. Meiners, Y.-C. Hagedorn, K. Wissenbach, I. Kelbassa, R. Poprawe, Densification behavior, microstructure evolution, and wear property of TiC nanoparticle reinforced AlSi10Mg bulk-form nanocomposites prepared by selective laser melting, Journal of Laser Applications, 27 (2015) S17003.
[93] M.-S. Baek, R. Kreethi, T.-H. Park, Y. Sohn, K.-A. Lee, Influence of heat treatment on the high-cycle fatigue properties and fatigue damage mechanism of selective laser melted AlSi10Mg alloy, Materials Science and Engineering: A, (2021) 141486.
[94] Y. Wang, J. Shi, Effect of hot isostatic pressing on nanoparticles reinforced AlSi10Mg produced by selective laser melting, Materials Science and Engineering: A, 788 (2020) 139570.
[95] L. Xi, D. Gu, K. Lin, S. Guo, Y. Liu, Y. Li, M. Guo, Effect of ceramic particle size on densification behavior, microstructure formation, and performance of TiB2-reinforced Al-based composites prepared by selective laser melting, J. Mater. Res., 35 (2020) 559-570.

[96] Y.K. Xiao, Z.Y. Bian, Y. Wu, G. Ji, Y.Q. Li, M.J. Li, Q. Lian, Z. Chen, A. Addad, H.W. Wang, Effect of nano-TiB2 particles on the anisotropy in an AlSi10Mg alloy processed by selective laser melting, Journal of Alloys and Compounds, 798 (2019) 644-655.
[97] S. Luo, R. Li, P. He, H. Yue, J. Gu, Investigation on the Microstructure and Mechanical Properties of CNTs-AlSi10Mg Composites Fabricated by Selective Laser Melting, Materials, 14 (2021) 838.
[98] G. Xue, L. Ke, H. Zhu, H. Liao, J. Zhu, X. Zeng, Influence of processing parameters on selective laser melted SiCp/AlSi10Mg composites: Densification, microstructure and mechanical properties, Materials Science and Engineering: A, 764 (2019) 138155.
[99] Z. Wang, L. Zhuo, E. Yin, Z. Zhao, Microstructure evolution and properties of nanoparticulate SiC modified AlSi10Mg alloys, Materials Science and Engineering: A, 808 (2021) 140864.
[100] P. He, H. Kong, Q. Liu, M. Ferry, J.J. Kruzic, X. Li, Elevated temperature mechanical properties of TiCN reinforced AlSi10Mg fabricated by laser powder bed fusion additive manufacturing, Materials Science and Engineering: A, 811 (2021) 141025.
[101] H.R. Ezatpour, S.A. Sajjadi, M.H. Sabzevar, Y. Huang, Investigation of microstructure and mechanical properties of Al6061-nanocomposite fabricated by stir casting, Materials & Design, 55 (2014) 921-928.
[102] M.M.E.-S. Seleman, M.M. Sabbah Ataya, A.M. Hassan, F.H. Latief, K. Hajlaoui, A.E. El-Nikhaily, M.I. Habba, The Additive Manufacturing of Aluminum Matrix Nano Al2O3 Composites Produced via Friction Stir Deposition Using Different Initial Material Conditions, Materials, 15 (2022).
[103] M. Ghayoor, S. Mirzababaei, K. Lee, Y. He, C.-h. Chang, B.K. Paul, S. Pasebani, Strengthening of 304L stainless steel by addition of yttrium oxide and grain refinement during selective laser melting, in: 2019 International Solid Freeform Fabrication Symposium, University of Texas at Austin, 2019.
[104] I.-T. Ho, T.-H. Hsu, Y.-J. Chang, C.-W. Li, K.-C. Chang, S. Tin, K. Kakehi, A.-C. Yeh, Effects of CoAl2O4 inoculants on microstructure and mechanical properties of IN718 processed by selective laser melting, Additive Manufacturing, 35 (2020) 101328.
[105] Q. Wang, K. Zhang, D. Qiu, W. Niu, Additive manufacturing of high-strength commercially pure titanium through lanthanum oxide addition, Materials Characterization, 176 (2021) 111074.
[106] S. Sun, D. Yi, Y. Chen, C. Wu, Thermodynamic properties of binary alloys of Al-Er and Si-Er, Chin. J. Nonferr. Metals, 19 (2009) 1580-1586.
[107] J. Gröbner, D. Kevorkov, R. Schmid-Fetzer, Thermodynamic calculation of Al-Gd and Al-Gd-Mg phase equilibria checked by key experiments, International Journal of Materials Research, 92 (2001) 22-27.
[108] G. Miranda, S. Faria, F. Bartolomeu, E. Pinto, S. Madeira, A. Mateus, P. Carreira, N. Alves, F. Silva, O. Carvalho, Predictive models for physical and mechanical properties of 316L stainless steel produced by selective laser melting, Materials Science and Engineering: A, 657 (2016) 43-56.
[109] L. Löber, C. Flache, R. Petters, U. Kühn, J. Eckert, Comparison of different post processing technologies for SLM generated 316l steel parts, Rapid Prototyping Journal, (2013).
[110] Y. Zhang, J. Zhang, Modeling of solidification microstructure evolution in laser powder bed fusion fabricated 316L stainless steel using combined computational fluid dynamics and cellular automata, Additive Manufacturing, 28 (2019) 750-765.
[111] K.V. Yang, P. Rometsch, T. Jarvis, J. Rao, S. Cao, C. Davies, X. Wu, Porosity formation mechanisms and fatigue response in Al-Si-Mg alloys made by selective laser melting, Materials Science and Engineering: A, 712 (2018) 166-174.
[112] T. Heeling, K. Wegener, The effect of multi-beam strategies on selective laser melting of stainless steel 316L, Additive Manufacturing, 22 (2018) 334-342.
[113] O. Andreau, I. Koutiri, P. Peyre, J.-D. Penot, N. Saintier, E. Pessard, T. De Terris, C. Dupuy, T. Baudin, Texture control of 316L parts by modulation of the melt pool morphology in selective laser melting, Journal of Materials Processing Technology, 264 (2019) 21-31.
[114] R. Shi, S.A. Khairallah, T.T. Roehling, T.W. Heo, J.T. McKeown, M.J. Matthews, Microstructural control in metal laser powder bed fusion additive manufacturing using laser beam shaping strategy, Acta Materialia, 184 (2020) 284-305.
[115] U. Scipioni Bertoli, B.E. MacDonald, J.M. Schoenung, Stability of cellular microstructure in laser powder bed fusion of 316L stainless steel, Materials Science and Engineering: A, 739 (2019) 109-117.

[116] K. Saeidi, X. Gao, Y. Zhong, Z.J. Shen, Hardened austenite steel with columnar sub-grain structure formed by laser melting, Materials Science and Engineering: A, 625 (2015) 221-229.
[117] A. Saboori, G. Piscopo, M. Lai, A. Salmi, S. Biamino, An investigation on the effect of deposition pattern on the microstructure, mechanical properties and residual stress of 316L produced by Directed Energy Deposition, Materials Science and Engineering: A, 780 (2020) 139179.
[118] H.S. Kim, Y. Kobayashi, S. Tsukamoto, K. Nagai, Effect of cooling rate on microstructure evolution of rapidly cooled high-impurity steels, Materials Science and Engineering: A, 403 (2005) 311-317.
[119] H. Yin, S. Felicelli, Dendrite growth simulation during solidification in the LENS process, Acta Materialia, 58 (2010) 1455-1465.
[120] P. HOCHNADEL, M.J. Cola, Pulsed Laser Beam Welding of 304 to 304L Stainless Steel: Effects of Welding Parameters on Cracking and Phase Transformations, in, Los Alamos National Lab., NM (US), 2001.
[121] M. Ma, Z. Wang, X. Zeng, A comparison on metallurgical behaviors of 316L stainless steel by selective laser melting and laser cladding deposition, Materials Science and Engineering: A, 685 (2017) 265-273.
[122] C. Man, C. Dong, T. Liu, D. Kong, D. Wang, X. Li, The enhancement of microstructure on the passive and pitting behaviors of selective laser melting 316L SS in simulated body fluid, Applied Surface Science, 467-468 (2019) 193-205.
[123] Y. Zhong, L. Liu, S. Wikman, D. Cui, Z. Shen, Intragranular cellular segregation network structure strengthening 316L stainless steel prepared by selective laser melting, Journal of Nuclear Materials, 470 (2016) 170-178.
[124] K. Bertsch, G.M. de Bellefon, B. Kuehl, D. Thoma, Origin of dislocation structures in an additively manufactured austenitic stainless steel 316L, Acta Materialia, 199 (2020) 19-33.
[125] B. Kocabekir, R. Kaçar, S. Gündüz, F. Hayat, An effect of heat input, weld atmosphere and weld cooling conditions on the resistance spot weldability of 316L austenitic stainless steel, Journal of Materials Processing Technology, 195 (2008) 327-335.
[126] P. Guo, B. Zou, C. Huang, H. Gao, Study on microstructure, mechanical properties and machinability of efficiently additive manufactured AISI 316L stainless steel by high-power direct laser deposition, Journal of Materials Processing Technology, 240 (2017) 12-22.
[127] A. Saboori, A. Aversa, F. Bosio, E. Bassini, E. Librera, M. De Chirico, S. Biamino, D. Ugues, P. Fino, M. Lombardi, An investigation on the effect of powder recycling on the microstructure and mechanical properties of AISI 316L produced by Directed Energy Deposition, Materials Science and Engineering: A, 766 (2019) 138360.
[128] O. Salman, C. Gammer, A. Chaubey, J. Eckert, S. Scudino, Effect of heat treatment on microstructure and mechanical properties of 316L steel synthesized by selective laser melting, Materials Science and Engineering: A, 748 (2019) 205-212.
[129] B. Barkia, P. Aubry, P. Haghi-Ashtiani, T. Auger, L. Gosmain, F. Schuster, H. Maskrot, On the origin of the high tensile strength and ductility of additively manufactured 316L stainless steel: Multiscale investigation, Journal of Materials Science & Technology, 41 (2020) 209-218.
[130] H. Choo, K.-L. Sham, J. Bohling, A. Ngo, X. Xiao, Y. Ren, P. Depond, M. Matthews, E. Garlea, Effect of laser power on defect, texture, and microstructure of a laser powder bed fusion processed 316L stainless steel, Materials & Design, 164 (2018).
[131] E. Garlea, H. Choo, C.C. Sluss, M.R. Koehler, R.L. Bridges, X. Xiao, Y. Ren, B.H. Jared, Variation of elastic mechanical properties with texture, porosity, and defect characteristics in laser powder bed fusion 316L stainless steel, Materials Science and Engineering: A, 763 (2019) 138032.
[132] M. Ghayoor, K. Lee, Y. He, C.-h. Chang, B.K. Paul, S. Pasebani, Selective laser melting of 304L stainless steel: Role of volumetric energy density on the microstructure, texture and mechanical properties, Additive Manufacturing, 32 (2020) 101011.
[133] M. Godec, S. Zaefferer, B. Podgornik, M. Šinko, E. Tchernychova, Quantitative multiscale correlative microstructure analysis of additive manufacturing of stainless steel 316L processed by selective laser melting, Materials Characterization, 160 (2020) 110074.
[134] Z. Sun, X. Tan, S.B. Tor, C.K. Chua, Simultaneously enhanced strength and ductility for 3D-printed stainless steel 316L by selective laser melting, NPG Asia Materials, 10 (2018) 127-136.

[135] H. Pouraliakbar, M.R. Jandaghi, G. Khalaj, Constrained groove pressing and subsequent annealing of Al-Mn-Si alloy: Microstructure evolutions, crystallographic transformations, mechanical properties, electrical conductivity and corrosion resistance, Materials & Design, (2017).
[136] P. Krakhmalev, I. Yadroitsava, G. Fredriksson, I. Yadroitsev, Microstructural and thermal stability of selective laser melted 316L stainless steel single tracks, South African Journal of Industrial Engineering, 28 (2017).
[137] A. Saboori, M. Toushekhah, A. Aversa, M. Lai, M. Lombardi, S. Biamino, P. Fino, Critical features in the microstructural analysis of AISI 316L produced by metal additive manufacturing, Metallography, Microstructure, and Analysis, 9 (2020) 92-96.
[138] P. Deng, M. Karadge, R.B. Rebak, V.K. Gupta, B.C. Prorok, X. Lou, The origin and formation of oxygen inclusions in austenitic stainless steels manufactured by laser powder bed fusion, Additive Manufacturing, 35 (2020) 101334.
[139] A.J. Pinkerton, L. Li, Direct additive laser manufacturing using gas- and water-atomised H13 tool steel powders, The International Journal of Advanced Manufacturing Technology, 25 (2005) 471-479.
[140] J.H. Tan, W.L.E. Wong, K.W. Dalgarno, An overview of powder granulometry on feedstock and part performance in the selective laser melting process, Additive Manufacturing, 18 (2017) 228-255.
[141] T. Talako, A. Letsko, Modern Tendencies in Production of Metal Powders for Additive Manufacturing, (2017) 95-102.
[142] M. Abdelwahed, S. Bengtsson, R. Casati, A. Larsson, S. Petrella, M. Vedani, Effect of water atomization on properties of type 4130 steel processed by L-PBF, Materials & Design, 210 (2021) 110085.
[143] Y. Hedberg, O. Karlsson, P. Szakalos, I.O. Wallinder, Ultrafine 316L stainless steel particles with frozen-in magnetic structures characterized by means of electron backscattered diffraction, Materials Letters, 65 (2011) 2089-2092.
[144] M. Ghayoor, S. Badwe, H. Irrinki, S. Atre, S. Pasebani, Water Atomized 17-4 PH Stainless Steel Powder as a Cheaper Alternative Powder Feedstock for Selective Laser Melting, Materials Science Forum, 941 (2018) 698-703.
[145] J. Yu, M. Rombouts, G. Maes, Cracking behavior and mechanical properties of austenitic stainless steel parts produced by laser metal deposition, Materials & Design, 45 (2013) 228-235.
[146] T.F. Murphy, C.T. Schade, 6 - Measurement of powder characteristics and quality for additive manufacturing in aerospace alloys, in: F. Froes, R. Boyer (Eds.) Additive Manufacturing for the Aerospace Industry, Elsevier, 2019, pp. 99-142.
[147] A. Pinkerton, L. Li, Process characteristics and effects of gas- and water-atomized stainless steel powders in laser-based rapid tooling, Journal of Laser Applications, 15 (2003) 172-178.
[148] Y. Zhang, F. Ensheng, W. Mo, Y. Lv, R. Ma, S. Ye, P. Yu, On the Microstructures and Fatigue Behaviors of 316L Stainless Steel Metal Injection Molded with Gas- and Water-Atomized Powders, Metals, 8 (2018) 893.
[149] D. Kong, C. Dong, X. Ni, Z. Liang, X. Li, In-situ observation of asymmetrical deformation around inclusion in a heterogeneous additively manufactured 316L stainless steel, Journal of Materials Science & Technology, 89 (2021) 133-140.
[150] N. Sridharan, M. Gussev, R. Seibert, C. Parish, M. Norfolk, K. Terrani, S.S. Babu, Rationalization of anisotropic mechanical properties of Al-6061 fabricated using ultrasonic additive manufacturing, Acta Materialia, 117 (2016) 228-237.
[151] V. Chaudhary, N.M. Sai Kiran Kumar Yadav, S.A. Mantri, S. Dasari, A. Jagetia, R.V. Ramanujan, R. Banerjee, Additive manufacturing of functionally graded Co–Fe and Ni–Fe magnetic materials, Journal of Alloys and Compounds, 823 (2020) 153817.
[152] D. Lin, L. Xu, H. Jing, Y. Han, L. Zhao, Y. Zhang, H. Li, A strong, ductile, high-entropy FeCoCrNi alloy with fine grains fabricated via additive manufacturing and a single cold deformation and annealing cycle, Additive Manufacturing, 36 (2020) 101591.
[153] S. Peng, S. Mooraj, R. Feng, L. Liu, J. Ren, Y. Liu, F. Kong, Z. Xiao, C. Zhu, P.K. Liaw, Additive manufacturing of three-dimensional (3D)-architected CoCrFeNiMn high-entropy alloy with great energy absorption, scripta materialia, 190 (2021) 46-51.

[154] N. Sridharan, P. Wolcott, M. Dapino, S.S. Babu, Microstructure and texture evolution in aluminum and commercially pure titanium dissimilar welds fabricated using ultrasonic additive manufacturing, Scripta Materialia, 117 (2016) 1-5.
[155] M.E.J. Perry, R.J. Griffiths, D. Garcia, J.M. Sietins, Y. Zhu, H.Z. Yu, Morphological and microstructural investigation of the non-planar interface formed in solid-state metal additive manufacturing by additive friction stir deposition, Additive Manufacturing, 35 (2020) 101293.
[156] P. Niu, R. Li, S. Zhu, M. Wang, C. Chen, T. Yuan, Hot cracking, crystal orientation and compressive strength of an equimolar CoCrFeMnNi high-entropy alloy printed by selective laser melting, Optics & Laser Technology, 127 (2020) 106147.
[157] N. Sridharan, M. Norfolk, S.S. Babu, Characterization of steel-Ta dissimilar metal builds made using very high power ultrasonic additive manufacturing (VHP-UAM), Metallurgical and Materials Transactions A, 47 (2016) 2517-2528.
[158] Y. Zhao, K. Li, M. Gargani, W. Xiong, A comparative analysis of Inconel 718 made by additive manufacturing and suction casting: Microstructure evolution in homogenization, Additive Manufacturing, 36 (2020) 101404.
[159] M. Pitchandi, A.K. V, P. Pi, V. Ramachandran, S. Manwatkar, S. Rao, N. Svs, D. Sivakumar, P. Narayanan, On the anisotropy in room-temperature mechanical properties of laser powder bed fusion processed Ti6Al4V-ELI alloy for aerospace applications, Journal of Materials Science, (2022).
[160] B. Hausnerova, B.N. Mukund, D. Sanetrnik, Rheological properties of gas and water atomized 17-4PH stainless steel MIM feedstocks: Effect of powder shape and size, Powder Technology, 312 (2017) 152-158.
[161] D.A. Hughes, N. Hansen, The microstructural origin of work hardening stages, Acta Materialia, 148 (2018) 374-383.
[162] M.E. Orazem, B. Tribollet, Electrochemical impedance spectroscopy, New Jersey, (2008) 383-389.
[163] K. Santhy, K.H. Kumar, Thermodynamic modelling of magnetic laves phase in Fe–Ti system using first principle method, Intermetallics, 128 (2021) 106978.
[164] T. Jing, H. Zheng, Q. Liao, L. Song, H. Peng, Y. Wen, Homogeneously introducing more and thinner nanotwins by engineering annealing twin boundaries: A TWIP steel as an example, Materials Science and Engineering: A, 840 (2022) 142908.
[165] C. Lee, Y. Lee, C. Lee, S. Hong, Precipitation behavior of the sigma phase with Ni and Mn content variations in superaustenitic stainless steel weld metal, Materials Characterization, 144 (2018) 148-154.
[166] C.-C. Hsieh, W. Wu, Overview of Intermetallic Sigma (?) Phase Precipitation in Stainless Steels, ISRN Metallurgy, 2012 (2012).
[167] W. Zhai, W. Zhou, S.M.L. Nai, Grain refinement of 316L stainless steel through in-situ alloying with Ti in additive manufacturing, Materials Science and Engineering: A, 840 (2022) 142912.
[168] T.V. Charlu, O.J. Kleppa, T.B. Reed, High-temperature combustion calorimetry III. Enthalpies of formation of titanium oxides, The Journal of Chemical Thermodynamics, 6 (1974) 1065-1074.
[169] K. Xiang, L. Ding, Z. Jia, X. Yang, Q. Liu, Z. Hao, Phase transition induced by synchroshear in Al-Zn-Mg-Cu alloy, Scripta Materialia, 212 (2022) 114577.
[170] J. Guénolé, F.-Z. Mouhib, L. Huber, B. Grabowski, S. Korte-Kerzel, Basal slip in Laves phases: The synchroshear dislocation, Scripta Materialia, 166 (2019) 134-138.
[171] N. Wang, Y. Chen, G. Wu, Q. Zhao, Z. Zhang, L. Zhu, J. Luo, Non-equivalence contribution of geometrically necessary dislocation and statistically stored dislocation in work-hardened metals, Materials Science and Engineering: A, 836 (2022) 142728.
[172] A. Aversa, M. Lorusso, G. Cattano, D. Manfredi, F. Calignano, E.P. Ambrosio, S. Biamino, P. Fino, M. Lombardi, M. Pavese, A study of the microstructure and the mechanical properties of an AlSiNi alloy produced via selective laser melting, Journal of Alloys and Compounds, 695 (2017) 1470-1478.
[173] H. Pouraliakbar, S. Firooz, M.R. Jandaghi, G. Khalaj, A. Amirafshar, Combined effect of heat treatment and rolling on pre-strained and SPDed aluminum sheet, Materials Science and Engineering: A, 612 (2014) 371-379.
[174] I. ASTM, Standard test methods for tension testing of metallic materials 1, in, Astm.
[175] W. Pei, W. Zhengying, C. Zhen, L. Junfeng, Z. Shuzhe, D. Jun, Numerical simulation and parametric analysis of selective laser melting process of AlSi10Mg powder, Appl. Phys. A, 123 (2017) 1-15.

[176] J. Guan, Y. Jiang, X. Zhang, X. Chong, Microstructural evolution and EBSD analysis of AlSi10Mg alloy fabricated by selective laser remelting, Materials Characterization, 161 (2020) 110079.
[177] C. Liu, C. Li, Z. Zhang, S. Sun, M. Zeng, F. Wang, Y. Guo, J. Wang, Modeling of thermal behavior and microstructure evolution during laser cladding of AlSi10Mg alloys, Optics & Laser Technology, 123 (2020) 105926.
[178] B. Straumal, O. Kogtenkova, P. Zięba, Wetting transition of grain-boundary triple junctions, Acta materialia, 56 (2008) 925-933.
[179] T. Yu, H. Hyer, Y. Sohn, Y. Bai, D. Wu, Structure-property relationship in high strength and lightweight AlSi10Mg microlattices fabricated by selective laser melting, Materials & Design, 182 (2019) 108062.
[180] F. Alghamdi, X. Song, A. Hadadzadeh, B. Shalchi-Amirkhiz, M. Mohammadi, M. Haghshenas, Post heat treatment of additive manufactured AlSi10Mg: On silicon morphology, texture and small-scale properties, Materials Science and Engineering: A, 783 (2020) 139296.
[181] P. Yang, M.A. Rodriguez, L.A. Deibler, B.H. Jared, J. Griego, A. Kilgo, A. Allen, D.K. Stefan, Effect of thermal annealing on microstructure evolution and mechanical behavior of an additive manufactured AlSi10Mg part, J. Mater. Res., 33 (2018) 1701-1712.
[182] T. Maconachie, M. Leary, J. Zhang, A. Medvedev, A. Sarker, D. Ruan, G. Lu, O. Faruque, M. Brandt, Effect of build orientation on the quasi-static and dynamic response of SLM AlSi10Mg, Materials Science and Engineering: A, 788 (2020) 139445.
[183] T. Wang, S. Dai, H. Liao, H. Zhu, Pores and the formation mechanisms of SLMed AlSi10Mg, Rapid Prototyping Journal, (2020).
[184] P. Wang, C. Gammer, F. Brenne, K.G. Prashanth, R.G. Mendes, M.H. Rümmeli, T. Gemming, J. Eckert, S. Scudino, Microstructure and mechanical properties of a heat-treatable Al-3.5 Cu-1.5 Mg-1Si alloy produced by selective laser melting, Materials Science and Engineering: A, 711 (2018) 562-570.
[185] S.A. Khairallah, A.T. Anderson, A. Rubenchik, W.E. King, Laser powder-bed fusion additive manufacturing: Physics of complex melt flow and formation mechanisms of pores, spatter, and denudation zones, Acta Materialia, 108 (2016) 36-45.
[186] H. Wang, D. Gu, Nanometric TiC reinforced AlSi10Mg nanocomposites: Powder preparation by high-energy ball milling and consolidation by selective laser melting, J. Compos. Mater., 49 (2015) 1639-1651.
[187] X.P. Li, G. Ji, Z. Chen, A. Addad, Y. Wu, H. Wang, J. Vleugels, J. Van Humbeeck, J.-P. Kruth, Selective laser melting of nano-TiB2 decorated AlSi10Mg alloy with high fracture strength and ductility, Acta Materialia, 129 (2017) 183-193.
[188] A. Mandal, J.K. Tiwari, N. Sathish, A.K. Srivastava, Microstructural and mechanical properties evaluation of graphene reinforced stainless steel composite produced via selective laser melting, Materials Science and Engineering: A, (2020) 138936.
[189] P. Van Cauwenbergh, V. Samaee, L. Thijs, J. Nejezchlebová, P. Sedlak, A. Iveković, D. Schryvers, B. Van Hooreweder, K. Vanmeensel, Unravelling the multi-scale structure–property relationship of laser powder bed fusion processed and heat-treated AlSi10Mg, Scientific reports, 11 (2021) 1-15.
[190] Z. Fan, X. Yan, Z. Fu, B. Niu, J. Chen, Y. Hu, C. Chang, J. Yi, In situ formation of D022-Al3Ti during selective laser melting of nano-TiC/AlSi10Mg alloy prepared by electrostatic self-assembly, Vacuum, 188 (2021) 110179.
[191] M.R. Jandaghi, A. Saboori, L. Iuliano, M. Pavese, On the effect of rapid annealing on the microstructure and mechanical behavior of additively manufactured stainless steel by Laser Powder Bed Fusion, Materials Science and Engineering: A, (2021) 142109.
[192] R. Drissi-Daoudi, V. Pandiyan, R. Logé, S. Shevchik, G. Masinelli, H. Ghasemi-Tabasi, A. Parrilli, K. Wasmer, Differentiation of materials and laser powder bed fusion processing regimes from airborne acoustic emission combined with machine learning, Virtual and Physical Prototyping, 17 (2022) 181-204.
[193] H. Zhang, D. Gu, D. Dai, Laser printing path and its influence on molten pool configuration, microstructure and mechanical properties of laser powder bed fusion processed rare earth element modified Al-Mg alloy, Virtual and Physical Prototyping, 17 (2022) 308-328.
[194] F. Lambiase, A. Di Ilio, A closed-form solution for thermal and deformation fields in laser bending process of different materials, The International Journal of Advanced Manufacturing Technology, 69 (2013) 849-861.

[195] P. Yang, L.A. Deibler, D.R. Bradley, D.K. Stefan, J.D. Carroll, Microstructure evolution and thermal properties of an additively manufactured, solution treatable AlSi10Mg part, Journal of Materials Research, 33 (2018) 4040-4052.
[196] R. Dargis, D. Williams, R. Smith, E. Arkun, R. Roucka, A. Clark, M. Lebby, Structural and thermal properties of single crystalline epitaxial Gd2O3 and Er2O3 grown on Si (111), ECS Journal of Solid State Science and Technology, 1 (2012) N24.
[197] D. Dai, D. Gu, Influence of thermodynamics within molten pool on migration and distribution state of reinforcement during selective laser melting of AlN/AlSi10Mg composites, International Journal of Machine Tools and Manufacture, 100 (2016) 14-24.
[198] F.V. Braga, D.P. Escobar, N.J.L. de Oliveira, M.S. Andrade, Hot deformation behavior of a ferritic stainless steel stabilized with Nb during hot rolling simulation at different temperature ranges, J. Mater. Res., 31 (2016) 635-645.
[199] A. Chaudhuri, A. Sarkar, S. Suwas, Investigation of stress-strain response, microstructure and texture of hot deformed pure molybdenum, Int. J. Refract. Met. Hard Mater., 73 (2018) 168-182.
[200] H. Okamoto, Al-Er (aluminum-erbium), Journal of phase equilibria and diffusion, 32 (2011) 261-262.
[201] H. Okamoto, Supplemental Literature Review of Binary Phase Diagrams: Al-Bi, Al-Dy, Al-Gd, Al-Tb, C-Mn, Co-Ga, Cr-Hf, Cr-Na, Er-H, Er-Zr, H-Zr, and Ni-Pb, Journal of Phase Equilibria and Diffusion, 35 (2014) 343-354.
[202] M. Liu, K. Wei, X. Yue, G. Huang, J. Deng, X. Zeng, High power laser powder bed fusion of AlSi10Mg alloy: Effect of laser beam mode, Journal of Alloys and Compounds, 909 (2022) 164779.
[203] S. Huang, R.L. Narayan, J.H.K. Tan, S.L. Sing, W.Y. Yeong, Resolving the porosity-unmelted inclusion dilemma during in-situ alloying of Ti34Nb via laser powder bed fusion, Acta Materialia, 204 (2021) 116522.
[204] D. Ben, Y. Ma, H. Yang, L. Meng, X. Shao, H. Liu, S. Wang, Q. Duan, Z. Zhang, Heterogeneous microstructure and voids dependence of tensile deformation in a selective laser melted AlSi10Mg alloy, Materials Science and Engineering: A, 798 (2020) 140109.
[205] P. Li, Y. Kim, A. Bobel, L. Hector Jr, A. Sachdev, S. Kumar, A. Bower, Microstructural origin of the anisotropic flow stress of laser powder bed fused AlSi10Mg, Acta Materialia, (2021) 117346.
[206] A. Kempf, K. Hilgenberg, Influence of sub-cell structure on the mechanical properties of AlSi10Mg manufactured by laser powder bed fusion, Materials Science and Engineering: A, 776 (2020) 138976.
[207] Z.-w. Chen, Z. He, W.-q. Jie, Growth restriction effects during solidification of aluminium alloys, Transactions of Nonferrous Metals Society of China, 19 (2009) 410-413.
[208] Y. Ou, Q. Zhang, Y. Wei, Y. Hu, S. Sui, J. Chen, X. Wang, W. Li, Evolution of Heterogeneous Microstructure and its Effects on Tensile Properties of Selective Laser Melted AlSi10Mg Alloy, Journal of Materials Engineering and Performance, 30 (2021) 4341-4355.
[209] M. Dong, W. Zhou, K. Kamata, N. Nomura, Microstructure and mechanical property of graphene oxide/AlSi10Mg composites fabricated by laser additive manufacturing, Materials Characterization, 170 (2020) 110678.
[210] W. Chen, L. Xu, Y. Zhang, Y. Han, L. Zhao, H. Jing, Additive manufacturing of high-performance 15-5PH stainless steel matrix composites, Virtual and Physical Prototyping, 17 (2022) 366-381.
[211] I. Pelevin, A. Nalivaiko, D. Ozherelkov, A. Shinkaryov, S. Chernyshikhin, A. Arnautov, S. Zmanovsky, A. Gromov, Selective Laser Melting of Al-Based Matrix Composites with Al2O3 Reinforcement: Features and Advantages, Materials, 14 (2021) 2648.
[212] J. Jue, D. Gu, K. Chang, D. Dai, Microstructure evolution and mechanical properties of Al-Al2O3 composites fabricated by selective laser melting, Powder Technol., 310 (2016).
[213] X. Zhao, B. Song, W. Fan, Y. Zhang, Y. Shi, Selective laser melting of carbon/AlSi10Mg composites: Microstructure, mechanical and electronical properties, Journal of Alloys and Compounds, 665 (2016) 271-281.
[214] J.K. Tiwari, A. Mandal, N. Sathish, A.K. Agrawal, A.K. Srivastava, Investigation of porosity, microstructure and mechanical properties of additively manufactured graphene reinforced AlSi10Mg composite, Additive Manufacturing, 33 (2020) 101095.
[215] L. Wan, S. Shi, Z. Xia, T. Shi, Y. Zou, K. Li, X. Chen, Directed energy deposition of CNTs/AlSi10Mg nanocomposites: Powder preparation, temperature field, forming, and properties, Optics & Laser Technology, 139 (2021) 106984.

[216] T. Yu, J. Liu, Y. He, J. Tian, M. Chen, Y. Wang, Microstructure and wear characterization of carbon nanotubes (CNTs) reinforced aluminum matrix nanocomposites manufactured using selective laser melting, Wear, 476 (2021) 203581.
[217] L. Wu, Z. Zhao, P. Bai, W. Zhao, Y. Li, M. Liang, H. Liao, P. Huo, J. Li, Wear resistance of graphene nano-platelets (GNPs) reinforced AlSi10Mg matrix composite prepared by SLM, Applied Surface Science, 503 (2020) 144156.
[218] D. Gu, X. Rao, D. Dai, C. Ma, L. Xi, K. Lin, Laser additive manufacturing of carbon nanotubes (CNTs) reinforced aluminum matrix nanocomposites: Processing optimization, microstructure evolution and mechanical properties, Additive Manufacturing, 29 (2019) 100801.
[219] T. Wang, Q. Meng, S. Araby, G. Yang, P. Li, R. Cai, S. Han, W. Wang, Non-oxidized graphene/metal composites by laser deposition additive manufacturing, Journal of Alloys and Compounds, 882 (2021) 160724.
[220] S. Luo, R. Li, P. He, H. Yue, J. Gu, Investigation on the Microstructure and Mechanical Properties of CNTs-AlSi10Mg Composites Fabricated by Selective Laser Melting, Materials, 14 (2021) 838.
[221] X. Xi, B. Chen, C. Tan, X. Song, J. Feng, Microstructure and mechanical properties of SiC reinforced AlSi10Mg composites fabricated by laser metal deposition, Journal of Manufacturing Processes, 58 (2020) 763-774.
[222] Y. Meng, Z. Yu, P. Rong, G. Li, Densification behavior, microstructure evolution, and tensile properties of selective laser melting additive manufactured TiB2/AlSi10Mg composite, Journal of Laser Applications, 32 (2020) 022007.
[223] L. Xi, D. Gu, S. Guo, M. Guo, K. Lin, Microstructure development, tribological property and underlying mechanism of laser additive manufactured submicro-TiB2 reinforced Al-based composites, Journal of Alloys and Compounds, 819 (2019) 152980.
[224] Y. Liu, R. Wang, C. Peng, Z. Cai, Z. Zhou, X. Li, X. Cao, Microstructural evolution and mechanical performance of in-situ TiB2/AlSi10Mg composite manufactured by selective laser melting, Journal of Alloys and Compounds, 853 (2021) 157287.
[225] J. Yi, X. Zhang, J.H. Rao, J. Xiao, Y. Jiang, In-situ chemical reaction mechanism and non-equilibrium microstructural evolution of (TiB2 + TiC)/AlSi10Mg composites prepared by SLM-CS processing, Journal of Alloys and Compounds, 857 (2021) 157553.
[226] Y. Li, D. Gu, H. Zhang, L. Xi, Effect of Trace Addition of Ceramic on Microstructure Development and Mechanical Properties of Selective Laser Melted AlSi10Mg Alloy, Chinese Journal of Mechanical Engineering, 33 (2020) 33.
[227] D. Gu, H. Wang, F. Chang, D. Dai, P. Yuan, Y.-C. Hagedorn, W. Meiners, Selective Laser Melting Additive Manufacturing of TiC/AlSi10Mg Bulk-form Nanocomposites with Tailored Microstructures and Properties, Physics Procedia, 56 (2014) 108–116.
[228] C. Li, S. Sun, Y. Zhang, C. Liu, P. Deng, M. Zeng, F. Wang, P. Ma, W. Li, Y. Wang, Effects of laser processing parameters on microstructure and mechanical properties of additively manufactured AlSi10Mg alloys reinforced by TiC, The International Journal of Advanced Manufacturing Technology, 103 (2019) 3235-3246.
[229] H. Wang, D. Gu, Nanometric TiC reinforced AlSi10Mg nanocomposites: Powder preparation by high-energy ball milling and consolidation by selective laser melting, J. Compos. Mater., 49 (2014).
[230] S. Zhou, Z. Wang, Y. Su, H. Wang, G. Liu, T. Song, M. Yan, Effects of Micron/Submicron TiC on Additively Manufactured AlSi10Mg: A Comprehensive Study from Computer Simulation to Mechanical and Microstructural Analysis, JOM, 72 (2020).
[231] C. ma, D. Gu, D. Dai, W. Chen, F. Chang, P. Yuan, Y. Shen, Aluminum-based nanocomposites with hybrid reinforcements prepared by mechanical alloying and selective laser melting consolidation, J. Mater. Res., 30 (2015) 2816-2828.
[232] C. Gao, Z. Wang, Z. Xiao, D. You, K. Wong, A.H. Akbarzadeh, Selective laser melting of TiN nanoparticle-reinforced AlSi10Mg composite: Microstructural, interfacial, and mechanical properties, Journal of Materials Processing Technology, 281 (2020) 116618.
[233] C. Gao, Z. Liu, Z. Xiao, W. Zhang, K. Wong, A. Akbarzadeh, Effect of heat treatment on SLM-fabricated TiN/AlSi10Mg composites: Microstructural evolution and mechanical properties, Journal of Alloys and Compounds, 853 (2021) 156722.

[234] X. Teng, G. Zhang, J. Liang, H. Li, Q. Liu, Y. Cui, T. Cui, L. Jiang, Parameter optimization and microhardness experiment of AlSi10Mg alloy prepared by selective laser melting, Materials Research Express, 6 (2019) 086592.
[235] L. Zhou, A. Mehta, E. Schulz, B. McWilliams, K. Cho, Y. Sohn, Microstructure, precipitates and hardness of selectively laser melted AlSi10Mg alloy before and after heat treatment, Materials Characterization, 143 (2018) 5-17.
[236] L.-z. Wang, S. Wang, X. Hong, Pulsed SLM-manufactured AlSi10Mg alloy: Mechanical properties and microstructural effects of designed laser energy densities, Journal of Manufacturing Processes, 35 (2018) 492-499.
[237] Z. Dong, M. Xu, H. Guo, X. Fei, Y. Liu, B. Gong, G. Ju, Microstructural evolution and characterization of AlSi10Mg alloy manufactured by selective laser melting, Journal of Materials Research and Technology, 17 (2022) 2343-2354.